Fusion of human monocarboxylate transporter 1 with basigin and expression in *S. cerevisiae*: Is basigin more than a chaperone?

Dissertation zur Erlangung des Doktorgrades
der Mathematisch-Naturwissenschaftlichen Fakultät
der Christian-Albrechts-Universität zu Kiel

vorgelegt von
Anna-Lena Köpnick

Kiel, 2021

Erster Gutachter:	Prof. Dr. Eric Beitz
Zweiter Gutachter:	Prof. Dr. Axel Scheidig
Tag der mündlichen Prüfung:	17.05.2021

Contents

Abbreviations

ACF	Acriflavine	EDTA	Ethylenediaminetetraacetic acid
ALT	Alanine transaminase	Eh	*Entamoeba histolytica*
Amp	Ampicillin	EM	Electron microscopy
APC	Allophycocyanin	EMB	Embigin
APS	Ammonium persulfate	EMMPRIN	Extracellular matrix metalloproteinase inducer
AQP	Aquaporin		
ATP	Adenosine-5'-triphosphate	EPR	Electron paramagnetic resonance
BCECF	2'-7'-Bis-(carboxyethyl)-5-6-carboxy-fluorescein	EtBr	Ethidium bromide
		FC	Flow cytometry
BMGY	Buffered complex glycerol medium	FM	Feeding mixture
		FNT	Formate-nitrite transporter
BMMY	Buffered complex methanol medium	FRET	Fluorescence resonance energy transfer
BMTS	Benzyl methanethiosulfonate	FSC	Forward scatter
BSA	Bovine serum albumin	GFP	Green fluorescent protein
BSG	Basigin	Gluc	Glucose
CA	Carbonic anhydrase	GTP	Guanosine-5'-triphosphate
CD	Cluster of differentiation	HA	Hemagglutinin
CECF	Continuous exchange cell-free	HEPES	4-(2-Hydroxyethyl)-1-piperazineethanesulfonic acid
CHC	α-Cyano-4-hydroxycinnamate		
CoV	Corona virus	HIF-1	Hypoxia-inducible factor 1
cpm	counts per minute	HPLC	High-performance liquid chromatography
CTP	Cytidine-5'-triphosphate		
D-CF	Detergent-based cell-free	HRP	Horseradish peroxidase
ddH_2O	double-distilled H_2O	IC_{50}	Half maximal inhibitory concentration
DDM	*n*-Dodecyl-β-D-maltopyranoside		
DIDS	4,4'-Diisothiocyano-2,2'-stilbenedisulfonic acid	Ig	Immunoglobulin
		IMAC	Immobilized metal affinity chromatography
DMSO	Dimethyl sulfoxide		
DNA	Deoxyribonucleic acid	KLF4	Kruppel-like factor 4
DOPG	1,2-Dioleoyl-*sn*-glycero-3-phospho-(1'-*rac*-glycerol)	Lac	Lactate
		LB	Lennox broth
DTNB	5,5′-Dithiobis(2-nitro-benzoic acid)	LDH	Lactate dehydrogenase
		MCS	Multiple cloning site
DTT	Dithiothreitol	MCT	Monocarboxylate transporter
ECL	Enhanced chemiluminescence	MES	2-(*N*-morpholino)ethanesulfonic acid

0 Abbreviations

MM	Master mix
MMTS	Methyl methanethiosulfonate
MPC	Mitochondrial pyruvate carrier
MSP	Membrane Scaffold Protein
MTSES	2-Sulfonatoethyl methanethiosulfonate
MWCO	Molecular weight cut-off
NAD	Nicotinamide adenine dinucleotide
NADP	Nicotinamide adenine dinucleotide phosphate
ND-CF	Nanodisc-based cell-free
NF-κB	Nuclear factor kappa-light-chain-enhancer of activated B cells
NMR	Nuclear magnetic resonance
NTA	Nitrilotriacetic acid
NTP	Nucleoside triphosphate
OD_{600}	Optical density at 600 nm
ORF	Open reading frame
OXPHOS	Oxidative phosphorylation
PAGE	Polyacrylamide gel electrophoresis
PBS	Phosphate-buffered saline
pCMBS	*p*-Chloromercuribenzene sulfonate
PCR	Polymerase chain reaction
PDH	Pyruvate dehydrogenase
PEG	Polyethylene glycol
PEP	Phosphoenolpyruvic acid
Pf	*Plasmodium falciparum*
Pfu	*Pyrococcus furiosus*
Pma	Plasma membrane H^+-ATPase
PMCA	Plasma membrane Ca^{2+}-ATPase
PMTS	Propyl methanethiosulfonate
POPG	1-Palmitoyl-2-oleoyl-*sn*-glycero-3-phospho-(1'-*rac*-glycerol)
PP	Pentose phosphate
RM	Reaction mixture
RNA	Ribonucleic acid
RT	Room temperature
SARS	Severe acute respiratory syndrome
SC	Scintillation cocktail
SD	Synthetic drop-out
SDS	Sodium dodecyl sulfate
SEC	Size-exclusion chromatography
SEM	Standard error of the mean
SfMCT	*Syntrophobacter fumaroxidans* monocarboxylate transporter
SLC	Solute carrier
SSC	Side scatter
TAE	Tris-acetate-EDTA
TAT1	T-type amino acid transporter 1
TBS	Tris-buffered saline
TCA	Tricarboxylic acid
TEM	Transmission electron microscopy
TEMED	*N*,*N*,*N*′,*N*′-Tetramethylethane-1,2-diamine
Tg	*Toxoplasma gondii*
TM	Transmembrane
Tris	Tris(hydroxymethyl)aminomethane
TTP	Thymidine-5'-triphosphate
UTP	Uridine-5'-triphosphate
YNB	Yeast nitrogen base
YPD	Yeast extract peptone dextrose

Abstract

Lactate is a key metabolite in human cells. A regulated transport across membranes is vital for cellular function while deregulated transport is a hallmark of cancer. In tumor cells, glycolysis as the main route for ATP synthesis even in the presence of oxygen (Warburg effect) demands rapid lactate clearance to avoid acidification. Oxygenic cancer cells, in turn, rely on an efficient retrieval of extracellular lactate to fuel the citric acid cycle (reverse Warburg effect). To maintain an active interchange between cells, four monocarboxylate transporters (MCT1−4) manage bi-directional, proton-coupled transport across plasma membranes. For its translocation to the plasma membrane, MCT1 demands chaperoning by a member of the immunoglobulin superfamily, namely basigin. Both proteins remain complexed at the plasma membrane. Although frequently suggested, a direct effect of the chaperone on MCT1-mediated transport is not resolvable in commonly used expression systems. In this study, MCT1 expression in *S. cerevisiae* Δ*jen1* Δ*ady2* profited from a basigin-independent translocation in a system with zero background from endogenous monocarboxylate transporters or basigin homologs. The molecular fusion with truncated basigin constructs revealed an effect on transmembrane L-lactate distribution at the domain level. In zero-trans influx experiments using ^{14}C-labeled substrate, the presence of basigin's extracellular Ig-I domain permitted a 4.5-fold intracellular L-lactate accumulation in the transport equilibrium. At near-neutral pH, cytosolic L-lactate concentrations greatly exceeded those provided with the buffer. The absence of the basigin Ig-I domain due to truncation or misfolding reversed this effect. The identification of patches of positive and negative surface potentials and evidence from charge-resolving point mutations indicated an electrostatic attraction of L-lactate anions and protons. This thesis deduces a substrate harvesting function of basigin that creates a "microenvironment" of locally increased concentrations and drives L-lactate influx according to Le Chatelier's principle. This influx was physiologically relevant and promoted cell growth on L-lactate medium. According to classical and reverse Warburg effects, highly adapted tumor cells require a fine-tuned transmembrane L-lactate distribution and basigin might be an important determinant. Hereof, MCTs are promising targets in the anti-tumor therapy. The basigin-MCT1 fusion set-up from this study further revealed two known MCT1 inhibitors, AZD3965 and *p*-chloromercuribenzene sulfonate (pCMBS), as direct and basigin-independent modifiers. Cys159 in the transporter cavity was revealed as selectively targetable by pCMBS leading to a complete transport inhibition. Smaller cysteine-modifiers had a less prominent effect and lacked site-specificity. Cys159 is proposed to constitute a hinge region of the alternating access transporter and a wedge-like modification locks MCT1 in the outward open conformation. This reveals a target region for inhibitor design and in the future, Cys159 might serve as a natural anchor to introduce distinct labels and report on physicochemical modalities in a most critical part of the transporter.

Zusammenfassung

Laktat ist ein zentraler Metabolit in menschlichen Zellen, dessen regulierter Transport durch Zellmembranen Bedingung für die Aufrechterhaltung vieler Zellfunktionen ist. Ein deregulierter Laktataustausch zwischen Zelle und Zellumgebung ist für Tumoren kennzeichnend. In Tumorzellen erfordert die auch unter aeroben Bedingungen verstärkte Glykolyse (Warburg-Effekt) einen effizienten Export von Laktat, um einer Zellübersäuerung entgegenzuwirken. Oxidative Tumorzellen nehmen hingegen extrazelluläres Laktat auf und führen es dem Citratzyklus zu (reverser Warburg-Effekt). Vier Monocarboxylat-Transporter (MCT1−4) ermöglichen den bidirektionalen, protonengekoppelten Transport von Laktat. Die Translokation von MCT1 zur Membran erfordert die Interaktion mit Basigin, einem Vertreter der Immunoglobulin-Superfamilie. Obwohl beide Proteine an der Membran assoziiert bleiben, konnte ein direkter Effekt des Chaperons auf den MCT1-vermittelten Transport in gängigen Systemen nie belegt werden. In dieser Arbeit wurde MCT1 in *S. cerevisiae* Δ*jen1* Δ*ady2*-Zellen exprimiert, um von einer Basigin-unabhängigen Translokation und einem System ohne endogene Laktat-Transporter oder Basigin-Homologe zu profitieren. Durch Fusion mit verkürzten Basigin-Konstrukten und Messungen des Einstroms von ^{14}C-markiertem Laktat konnte gezeigt werden, dass Basigins extrazelluläre Ig-I-Domäne im Transport-Gleichgewicht eine 4,5-fache Laktat-Anreicherung im Zellinneren ermöglicht. Im annähernd neutralen pH-Bereich konnten dadurch höhere intrazelluläre Laktatkonzentrationen erreicht werden, als es die extrazellulären Pufferbedingungen erlauben würden. Das Fehlen einer korrekt gefalteten Ig-I-Domäne hob diesen Effekt auf. Die Identifizierung von positiven und negativen Oberflächenpotentialen und der Effekt von ladungskompensierenden Mutationen deuteten auf eine elektrostatische Anziehung von Laktat-Ionen und Protonen hin. Diese Arbeit schreibt der Ig-I-Domäne von Basigin eine substratkonzentrierende Funktion am Transportereingang zu, die nach dem Prinzip von Le Chatelier den Substrateinstrom in die Zellen begünstigt. Dieser Einstrom war physiologisch bedeutend und förderte das Zellwachstum auf Laktatmedium. Spezialisierte Tumorzellen bedürfen eines regulierten Laktataustauschs und Basigin könnte einen bestimmenden Faktor darstellen. Die Basigin-MCT1-Fusion dieser Arbeit konnte weiter genutzt werden, um zwei bekannte MCT1-Inhibitoren, AZD3965 und 4-Chlormercuribenzolsulfonat (pCMBS), als direkte und Basigin-unabhängige Modifikatoren zu enthüllen. pCMBS adressierte Cys159 selektiv und blockierte den Laktattransport vollständig. Kleinere Cystein-Modifikatoren erwiesen sich als ineffizient und nicht selektiv. Diese Arbeit zeigt Cys159 in einem „MCT1-Scharnier“ und eine sperrige Modifikation scheint den Transporter in der *outward open*-Konformation festzusetzen. Dies offenbart eine neue Zielregion für Inhibitoren und könnte künftig als Bindestelle für Markierungsstudien dienen, um physikochemische Eigenschaften in einer wichtigen Region des Transporters aufzuklären.

1. Introduction

Cells are the smallest functional units of prokaryotic and eukaryotic organisms [1]. A cellular organization establishes a microenvironment in which physiological processes are separated from the environmental entourage. To achieve physical enclosure, biological membranes constitute a barrier and isolate the cytoplasmic interior as well as establish individual compartments within a cell. Cell membranes are semipermeable and only freely diffusible by small uncharged molecules and water [2]. For larger solutes, e.g. metabolic precursors and waste products, membranes are less passable and an exchange between in- and outside depends on specific transmembrane proteins that span the membrane and allow controlled permeability and transport [2]. Roughly 10 % of the human proteome constitute proteins for transmembrane transport and mediate the permeability of ions, signal transducers, drugs, essential nutrients, metabolites and metabolic waste (refer to the Human Protein Atlas, data from 03/12/2021, [3, 4]) [5]. One of these key metabolites in need for efficient transport across biological membranes is lactate.

1.1. L-Lactate: a key metabolite in healthy and in tumor cells

1.1.1. L-Lactate metabolism: formation and clearance in human cells

Lactic acid is a chiral monocarboxylic acid and a key substrate in human metabolism. The L(+)-lactic acid is the physiological abundant enantiomer and with a pK_a value of 3.86, it is largely deprotonated and anionic under physiological conditions. As extensively reviewed by Adeva-Andany *et al.*, the metabolic routes of L-lactate are widespread ranging from its relevance as a mere waste product of anaerobic glycolysis to its significance as a substrate for gluconeogenesis and as an energy source via oxidation in mitochondria [6]. L-Lactate metabolism centers around the enzymatic conversion from pyruvate via the lactate dehydrogenase (LDH) in the cytosol (Figure 1.1). In humans, the reversible reduction of pyruvate to L-lactate using nicotinamide adenine dinucleotide (NADH) is the main route of L-lactate formation and recovers NAD^+ essential for sustaining glycolysis under anaerobic conditions [1]. In that regard, the endogenous formation of L-lactate is tightly linked to pyruvate metabolism. Pyruvate itself is mainly formed by two routes: the metabolic breakdown of glucose via the above-mentioned anaerobic glycolysis or the pentose phosphate pathway, and alanine metabolism via the alanine transaminase (ALT)-catalyzed conversion to pyruvate [1]. L-Lactate consumption profits from the reverse LDH-catalyzed oxidation to pyruvate which then serves as a substrate for numerous metabolic pathways. In each case, pyruvate is rapidly transported to the mitochondria by mitochondrial pyruvate carriers MPC1 and 2 [7] and

converted to either acetyl coenzyme A by the pyruvate dehydrogenase (PDH) complex or to oxaloacetate via the action of pyruvate carboxylase [1]. Acetyl coenzyme A then fuels the TCA cycle and ATP synthesis via oxidative phosphorylation, or serves as a direct substrate for lipogenesis [1]. Oxaloacetate, on the other hand, feeds the gluconeogenesis which has been shown as one of the main routes for metabolic L-lactate clearance [8]. The disturbance of one of the rate-limiting steps of L-lactate clearance leads to the accumulation well above the physiological concentration of around 1 mM which demands non-metabolic clearance of access L-lactate by a rapid efflux from cells and manifests a hallmark in several physiological conditions including cancer [9–12].

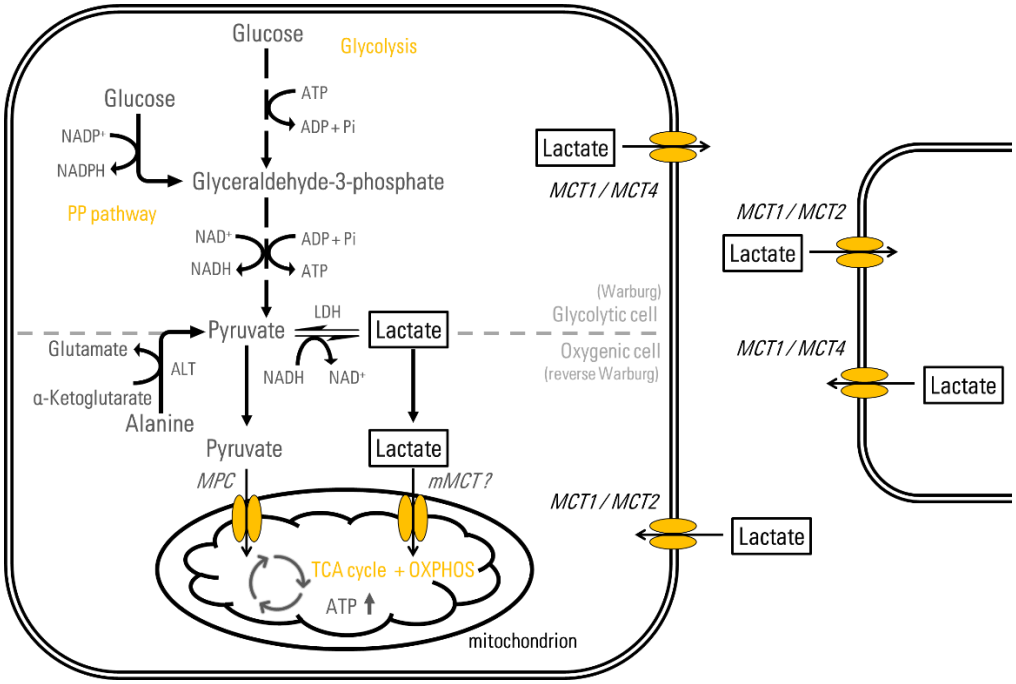

Figure 1.1. L-Lactate metabolism and transport in human cells. L-Lactate metabolism centers around the reversible conversion from/to pyruvate by LDH action. L-Lactate is mainly formed as product of glucose breakdown and anerobic glycolysis which outlines the main pathway for ATP synthesis in highly glycolytic cancer cells (Warburg). In normal cells as well as in oxygenic cancer cells (reverse Warburg), pyruvate and L-lactate (via conversion to pyruvate) are fueled into the TCA cycle for oxidative phosphorylation (OXPHOS) and ATP synthesis. Inter- and intracellular shuttling of L-lactate is managed by monocarboxylate transporters (MCT1−4) and mitochondrial pyruvate carriers (MPCs). For simplicity, metabolic pathways are not stoichiometrically balanced. Detailed information can be found in the main text. ADP/ATP, adenosine di/triphosphate; ALT, alanine transaminase; LDH, lactate dehydrogenase; OXPHOS, oxidative phosphorylation; TCA, tricarboxylic acid; MCT, monocarboxylate transporter; mMCT, mitochondrial MCT; MPC, mitochondrial pyruvate carrier; NAD^+/NADH, nicotinamide adenine dinucleotide; $NADP^+$/NADPH, nicotinamide adenine dinucleotide phosphate; PP, pentose phosphate.

1.1.2. L-Lactate metabolism in cancer: the (reverse) Warburg effect

Cancer cells are known to be highly adapted to changing metabolic requirements and deregulated cell energetics secure rapid cell growth, proliferation and angiogenesis (reviewed in [13]).

In normal cells, pyruvate from glucose breakdown is fed into the TCA cycle and processed to carbon dioxide for an effective ATP synthesis under aerobic conditions. Only at O_2 deprivation, cells rely on an anaerobic glycolysis and a NAD^+ recovery by L-lactate formation. In 1927, Warburg *et al.* described a metabolic switch of tumor cells to glycolysis even under normoxic conditions and a rapid formation and accumulation of L-lactate as a waste product. This is nowadays termed as the Warburg effect [14] (Figure 1.1). The metabolic shift of tumor cells to "aerobic glycolysis" is thereby partly accomplished by an oncogenic induction of gene expression for enzymes of the glycolytic machinery [15, 16]. Over the years, various explanations for the metabolic switch of tumor cells to the less effective glycolytic ATP production have been proposed. First, although generating less equivalents of ATP per glucose molecule, ATP synthesis rates for glycolysis are much faster enabling cells to rapidly consume limited glucose resources [17, 18]. And second, an accelerated glucose breakdown provides biosynthetic precursors including glycerol and citrate for fatty acid synthesis, non-essential amino acids and, via the pentose phosphate pathway, NADPH as an essential component for rapid cell growth and proliferation [19]. Strikingly, beyond highly glycolytic tumor cells producing vast amounts of L-lactate as a waste product, other cancerous cells have recently been shown to actively feed on external L-lactate that enters the TCA cycle for ATP production (Figure 1.1, called "reverse Warburg") [20]. Moreover, other studies indicate L-lactate as the preferred substrate that overrules the glucose contribution as a fuel for the TCA cycle possibly by sparing effort for the synthesis of glycolytic enzymes [21, 22].

Beside its deep involvement in cancer energy metabolism, L-lactate has additionally been revealed as a key player in the tumorigenic signal transduction to promote migration, cell growth and survival, and immunosuppression [23–25]. Thereof, L-lactate has been shown to regulate G protein-coupled receptor 81 (GPR81) signaling [24] and affect the expression of tumor-promoting transcription factors including hypoxia-inducible factor 1 (HIF-1), Kruppel-like factor 4 (KLF4) and NF-κB [26, 27, 23].

1.2. L-Lactate transport across cell membranes: an overview

To maintain L-lactate homoeostasis and to enable an efficient metabolic exchange of L-lactate between glycolytic and oxygenic cells, several L-lactate/pyruvate transporters have been identified that sustain L-lactate shuttling between cells and intracellular compartments. Respective transporters can roughly be divided into sodium-coupled monocarboxylate transporters (SMCTs; SLC5a family), proton-coupled transporters of the SLC16a family (MCTs) and mitochondrial pyruvate carriers (MPCs) (reviewed in [9]).

The electrogenic, Na^+-coupled transport of monocarboxylates including L-lactate, pyruvate, short-chain fatty acids and ketone bodies by two members of the SLC5a family, namely SMCT1 (SLC5a8) and SMCT2 (SLC5a12), has been shown to allow an active metabolite resorption and is therefore largely restricted to the epithelial cell lining in the kidney tubules and intestine [28–31]. In most cases, L-lactate transport is accomplished by the expression of MCTs of the SLC16a family (Figure 1.1). Individual members with a broad range of transport characteristics and specifications are expressed at the plasma membrane of numerous cell types. All of them mediate proton-coupled, bi-directional transport and allow a dynamic substrate shuttling between cells [9]. MCTs are discussed in detail in section 1.3. Finally, monocarboxylates (i.e. L-lactate) taken up by cells need subsequent intracellular shuttling and transport into mitochondria. Generally, L-lactate is converted to pyruvate which enters via specific mitochondrial pyruvate carriers (MPCs) [7] (Figure 1.1). MPCs have been shown to be expressed at the mitochondrial membrane and mediate the transport of pyruvate and other monocarboxylic acids including α-ketoacids with a very low affinity for L-lactate [32, 33]. More recently, MCTs have also been localized at the inner mitochondrial membrane to presumably fuel L-lactate directly into the TCA cycle [34, 35].

1.3. Human monocarboxylate transporters (MCTs)

1.3.1. MCTs: members of the SLC16a solute carrier family

According to the solute carrier (SLC) gene tables (SLC Tables, http://slc.bioparadigms.org, [36]), the SLC family of proteins includes over 65 subfamilies and at least 400 transporter genes sharing a sequence identity of 20−25 % [37]. All family members facilitate passive diffusion or mediate secondary active transport of solutes across membranes [38]. The SLC16a family, also known as the monocarboxylate transporter (MCT) family, consists of 14 members of which four have been revealed as genuine monocarboxylate transporters (MCT1, 2, 3 and 4; corresponding to members SLC16a1, 7, 8 and 3, respectively) and are found in all examined eukaryotic organisms (refer to the SLC Tables [36]). Most remaining members are referred to as orphan transporters with no substantial insight on functionality and substrates. Only SLC16a10 (TAT1, aromatic acid transporter [39]) and SLC16a2 (MCT8, thyroid hormone transporter [40]) have been expressed and characterized in detail. For MCT6, 7 and 9, recent studies suggest them as genuine transporters involved in the flux of drugs, ketone bodies in hepatocytes, and carnitine, respectively, although information on the function and physiological relevance is sparse [41–43].

1.3.2. Discovery and functional characteristics

The discovery and characterization of genuine monocarboxylate transporters can largely be attributed to the work of A. P. Halestrap and coworkers in the 1990s. From a historical perspective, Poole *et al.* purified a protein of 35−50 kDa from rat and rabbit erythrocytes that enabled the transport of pyruvate and L-lactate [44, 45]. Several related studies including an N-terminal sequencing identified the protein as a monocarboxylate transporter homolog and named it MCT1 [46, 47]. Extensive functional characterization determined MCT1 to 4 as bi-directional, proton-coupled but electroneutral transporters that mediate the secondary active transport of a various spectrum of substrates including L-lactate, pyruvate, short-chain fatty acids and ketone bodies (reviewed in [48]). The substrate spectrum and transport kinetics as well as the tissue distribution differ between the MCT isoforms designating distinct physiological roles. Whereas the MCT3 expression is less systemic and restricted to the retinal pigment epithelium [49], MCT1 is ubiquitously expressed. With a K_m of 3.5 mM for L-lactate [50], it was found to mediate both the in- and efflux of L-lactate with directionality determined by the substrate and proton availability and gradients (Figure 1.1). MCT2 as a high-affinity isoform (K_m of 0.74 mM for L-lactate [51]) is thought to be more destined for L-lactate uptake whereas MCT4 (K_m = 28 mM [52]) is dedicated to the efflux from highly glycolytic cells (Figure 1.1).

1.3.3. Structural characteristics and transport mechanism

Based on topology plots, proteolytic digestion [53] and the recently published structures of a bacterial MCT homolog (SfMCT, 25 % sequence identity with MCT1) [54] and human MCT2 [55], MCTs were confirmed to consist of 12 highly conserved α-helical transmembrane domains (TMs) of which some are discontinuous (depending on MCT member) (Figure 1.2A). Accordingly, MCTs display intracellular N- and C-termini and a long, flexible linker between TM6 and 7 prone to proteolytic digestion [53]. MCTs form two distinct domains of six helices each (TM1−6 and TM7−12) which are arranged with a pseudo-two-fold symmetry.

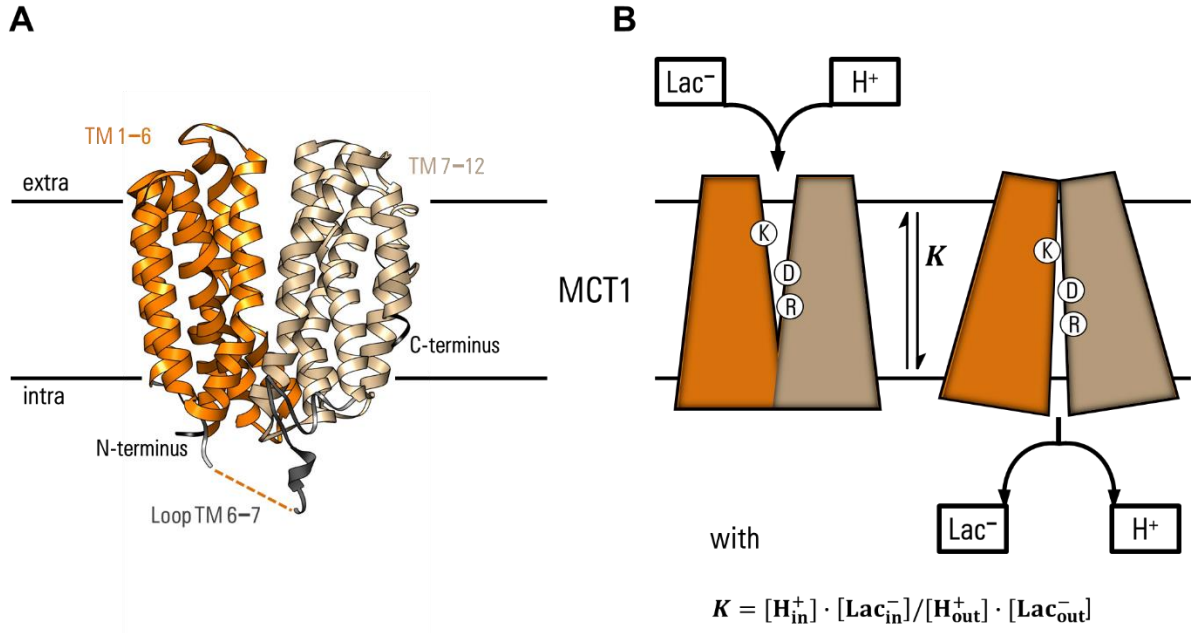

Figure 1.2. Structure and translocation cycle of human MCT1. **(A)** Structure model for human MCT1 in the outward open conformation. The model was calculated with SWISS-MODEL based on the crystal structure for SfMCT (PDB #6HCL) and visualized with Chimera. TM1−6 and TM7−12 form distinct subunits connected by a long, flexible loop (orange dashed line, not resolved in the SfMCT crystal structure). Intracellular N- and C-termini are indicated in black and truncated due to lacking structure data. **(B)** Illustration of the proposed alternating access translocation cycle of MCTs (based on [56]). The secondary active transport of L-lactate is coupled to proton co-transport. Critical residues for proton and substrate binding (K38, D309 and R313) are indicated. The process is reversible with direction determined by the equilibrium constant K, intra-/extracellular substrate concentrations and pH.

Movement and rearrangement of both domains is thought to mediate conformational changes (Figure 1.2B). The existence of two conformations constituting an alternating access mechanism was initially proposed by Wilson *et al.* and Manoharan *et al.* and based on homology models using the crystal structure of *E. coli* glycerol-3-phosphate transporter

(10−15 % sequence identity with MCTs) [56, 57]. Indeed, the resolved structures for SfMCT and MCT2 were captured in two distinct conformations proposing a transport mechanism in which MCTs toggle between an outward open and an inward open state. MCTs have very early been emphasized as pH-sensitive H^+/monocarboxylate co-transporters with an electroneutral substrate/proton stoichiometry of 1:1 [58–60]. Even before revelation of the molecular identity of MCTs, a transport mechanism involving extensive kinetic measurements on cellular monocarboxylate transport postulated an alternating access model and a distinct translocation cycle. According to Bruijne *et al.*, in influx, the co-transported H^+ protonates an exposed residue in the transporter cavity generating a positive charge suitable for substrate anion attraction. Further passage of the substrate anion leads to electrostatic rearrangements and a transporter swiveling to the inward open conformation and release of first the substrate and second the accompanying proton [61, 62] (Figure 1.2B). This process is reversible with directionality determined by the transporter kinetics and the prevailing substrate concentrations and pH. The transporter's return to the original position is known as the rate-limiting step of transport and can be promoted by a substrate exchange from the opposite side of the membrane termed transacceleration [63, 64]. In the course of time, structural, mechanistic and mutational analyses unveiled distinct residues some of which found reoccurring importance in the translocation cycle. For simplicity, the numberings for the below described residues from publications for other MCT members are translated to the corresponding positions in the human MCT1 sequence. Initially, Wilson *et al.* suggested Lys38 as the primary proton acceptor and consecutive substrate anion attractor in the outward open state with an Asp309/Arg313 ion pair guiding the passage of H^+/L-lactate through the transport path [56, 57, 65] (Figure 1.2B). Mutational analyses showed that the substitution of Phe367 in the binding pocket by smaller residues allowed the passage of bulkier monocarboxylates attributing a relevance in substrate selectivity [47]. More recent studies confirmed the importance of Lys38, Arg313, Asp309 and, lately, Asp414 attributing a role in pH dependency and substrate recognition, respectively [54, 55, 66, 67]. Further, Zhang *et al.* presented a three-dimensional inward open conformation of MCT2 and proposed Asp309 as the cytosolic proton binding site with residues Arg313, Tyr34, Phe367 and Ser371 forming a network for substrate binding from the cytosolic side [55].

1.3.4. Basigin: a member of the immunoglobulin superfamily and a chaperone for MCTs

Although being a non-glycosylated protein, MCT1 associates with a glycosylated protein for targeting to the plasma membrane. Generally, MCTs interact with one of two glycoproteins of the immunoglobulin (Ig) superfamily, namely basigin and embigin. Although first evidence from rat erythrocytes revealed an association of MCT1 with embigin [68], further investigations confirmed human MCT1 and 4 to preferably associate with basigin [69] presumably accepting

embigin as a secondary, alternative partner. Contrary, MCT2 relies on the interaction with embigin [70]. In the absence of basigin/embigin, MCTs reside in the perinuclear compartment suggesting their interaction to be crucial for intracellular trafficking and cell surface expression [69, 71].

Basigin and embigin both belong to the so called basigin superfamily and share structural similarity with a sequence identity of 24 %. All basigin (four isoforms) and embigin variants (two isoforms) consist of a single transmembrane domain and one to three immunoglobulin folds in the N-terminal, extracellular portion [72, 73] (Figure 1.3).

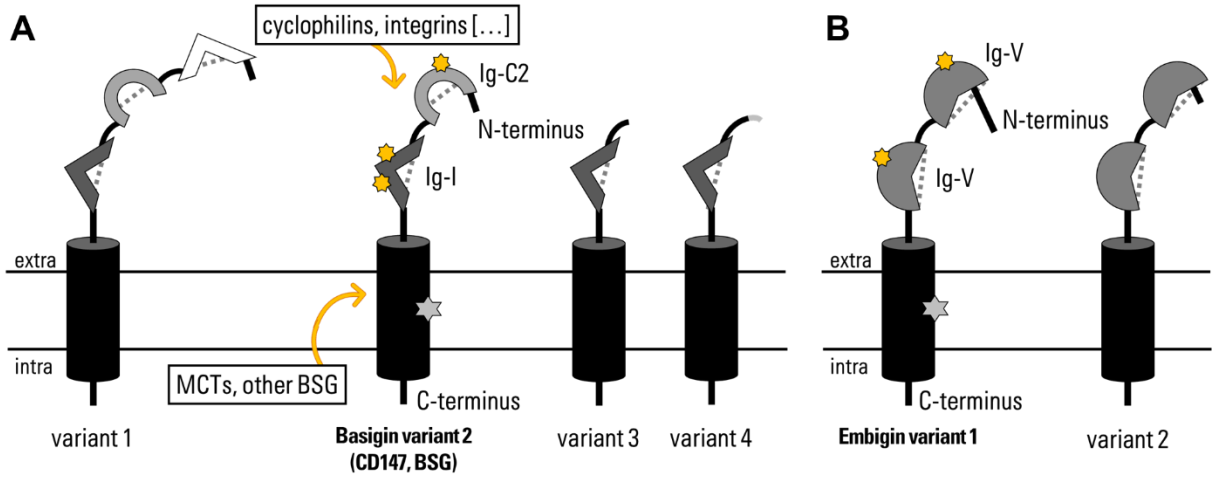

Figure 1.3. Structure of different basigin and embigin isoforms. All basigin/embigin isoforms display an extracellular N-terminus, an intracellular C-terminus, and a single transmembrane (TM) helix domain (black). Isoforms differ in the number and type of extracellular Ig-like domains (I-, C2- or V-type, gray to white) and are a result of alternative promoter usage or splicing. The proper folding of the Ig-like domains depends on the formation of disulfide bridges (dotted lines). Exemplary, the Ig-like domain types (labeled), glycosylation sites (orange stars) and the highly conserved glutamate in the TM (gray star) are indicated for the most prevalent isoform of basigin/embigin. **(A)** Basigin isoforms 1−4 are displayed. Beside MCTs, basigin interacts with cyclophilins, integrins and other basigin isoforms for intracellular signaling processes (see text for details). **(B)** Embigin isoforms 1 and 2 are shown. Isoforms differ in the N-terminal sequences (1−50 missing in embigin variant 2).

The amino acids 1−21 in basigin splice variant 2 (1−32 in embigin variant 1) designate a putative signal peptide for proper trafficking [74]. Both isoforms of embigin consist of two Ig-like domains of the V-type [75]. Similarly, the most prevalent and investigated basigin splice variant 2 (also named BSG, basigin-2, CD147, EMMPRIN) displays two Ig-like domains. X-ray diffraction of the extracellular domain of basigin variant 2 confirmed the specific folds for an N-terminal C2-type and a membrane-proximal I-type domain [76]. The full-length, retinal-

specific isoform 1 of basigin harbors a third N-terminal Ig-like domain and is associated with retinoblastoma [77]. The basigin variants 3 and 4 share the membrane-adjacent Ig-I domain but lack an additional Ig-like domain. These isoforms are, along with basigin variant 2, expressed in various human cell lines and may be upregulated in cancer [73]. The functional differences between basigin isoforms are not completely understood although basigin variant 3 has been found to inhibit tumor cell proliferation and invasion, and form homo- and heterodimers to regulate basigin variant 2 function in tumor progression [73]. Basigin variant 2 is the most abundant, functionally characterized isoform and MCT studies mainly concentrate on this variant. Beside its interaction with MCTs, basigin variant 2 is a receptor for integrins and cyclophilins and associated with cell adhesion and inflammation [78–80] (Figure 1.3). Via the induction of matrix metalloproteinases, basigin variant 2 is also involved in tumor invasion and progression [74, 81]. The physiological importance of basigin and its interaction partners were reviewed in detail by Muramatsu [82]. Underlining the wide network of cellular processes basigin variant 2 is involved in, it is additionally proposed to be essential for host invasion by *Plasmodium falciparum* and common viruses including the immunodeficiency virus (HIV) and the severe acute respiratory syndrome (SARS) coronavirus (CoV) [83–85].

In the context of MCTs, the role of basigin has been limited to its action as a chaperone that facilitates trafficking. Most MCT-related studies of basigin concentrated on the investigation of the exact mode of interaction of both proteins and the physiological relevance of its disturbance. Basigin has been confirmed to form dimers via its extracellular domain [76, 86], and earlier studies using fluorescence resonance energy transfer (FRET) revealed a basigin-MCT1 interaction stoichiometry of a basigin dimer associating with two MCT1 monomers [87]. To gather information on the mode of interaction between MCT1 and basigin, Kirk *et al.* constructed chimeras of basigin and a close relative and member of the immunoglobulin superfamily (cluster of differentiation 2, CD2) and found that the transmembrane domain and/or the C-terminal end of basigin are sufficient for proper interaction [69]. Indeed, the transmembrane domain of basigin displays an unusual but highly conserved charged residue (Glu218 in basigin variant 2) prone for electrostatic hydrogen bonding to a suitable residue in MCT1 [57]. This interaction is assumed to persist at the plasma membrane [69, 87], and several studies indicated that basigin further regulates MCT activity beyond chaperoning [88, 89]. Indeed, at least the activity or efficiency of common MCT inhibitors has occasionally been linked to basigin (see next chapter). Information on a more direct effect on the MCT functionality is scarce and evidence suffers from the tight dependence of MCTs on basigin to reach the plasma membrane in the first place.

1.3.5. MCT1 as a drug target: physiological relevance and inhibition

MCTs as the key mediators of L-lactate transport across membranes enable a metabolite exchange between not only cancer cells but also in the brain (astrocytes and neurons) and in skeletal muscle (white and red fibers) (reviewed in [90, 91]). The deep involvement of MCTs in lactate homeostasis and lactate being a key metabolite in energy metabolism link a deregulated MCT expression to several pathophysiological conditions including exercise-induced hyperinsulinemia or cryptic exercise intolerance (reviewed in [48]). Most importantly, in cancerous tissue, MCTs permit a substrate exchange between the L-lactate-producing, glycolytic (Warburg) and the L-lactate consuming, oxygenic tumor cells and are therefore recognized as essential for tumor progression [22, 92]. Hence, an increased expression of several MCT members is a diagnostic marker of common malignancies [93–95]. The overexpression of MCTs has been shown to be under extensive regulation ranging from transcriptional to posttranslational mechanisms and mediated by hypoxic conditions or tumor-related signaling pathways (reviewed in [22]). In most cases, oxidative tumor cells predominantly express MCT1 whereas glycolytic cells rely on the expression of MCT4 to enforce export [52, 92].

Due to the metabolic dependency of tumor survival and progression, MCTs are recognized as potential therapeutic targets. In that respect, several studies determined the feasibility of inhibiting MCT function as treatment approach. They elucidated a vulnerability of cancer cells to intracellular acidification and suppressed energetics in glycolytic cells on one hand, and decreased lactate-fueled respiration in oxygenic tumor cells on the other hand overall reducing tumor growth [92, 96]. Thereof, several more or less specific inhibitors have been found and tested some of which already entered clinical testing. Generally, most inhibitors are non-specific and target several MCT members or other transporters. These include the competitive, aromatic monocarboxylate α-cyano-4-hydroxycinnamate (CHC), stilbene disulphonates (i.e. 4,4'-diisothiocyano-2,2'-stilbenedisulphonic acid (DIDS)), and bioflavonoids (i.e. phloretin, quercetin) (reviewed in [48, 97]). Further unspecific inhibitors were suggested to target the associated basigin and mediate an indirect inhibition of MCTs. Among those are acriflavine (Figure 1.4A) and, most knowingly, *p*-chloromercuribenzene sulfonate (pCMBS) (Figure 1.4B) [70, 98]. Both have been proposed as basigin modifiers to avoid the basigin-MCT interaction. Although proven effective in tumor therapy [96], targeting basigin as an abundant protein that is linked to numerous signaling pathways might cause adverse side effects. Most recently, AstraZeneca developed two compounds, namely AR-C155858 and AZD3965 (Figure 1.4C, D), that selectively inhibit MCT1 and, to a lesser extent, MCT2 [99]. Both substances are closely related and exhibit a high affinity for MCT1 (K_i of 1.6 nM (AZD3965) and 2.3 nM (AR-C155858)) with only slight differences in the pharmacokinetic properties [100, 101]. AR-C155858 has been studied more intensively with respect to the molecular basis of inhibition

and has been suggested to bind from the cytosolic side of the transporter involving residues already elucidated as crucial for transport [102]. Although similarly potent, AZD3965 exhibits more favorable pharmacokinetics including the oral bioavailability [100]. It is currently tested in a phase I clinical trial to treat advanced solid tumors and lymphomas (www.ClinicalTrials.gov, identifier: NCT01791595).

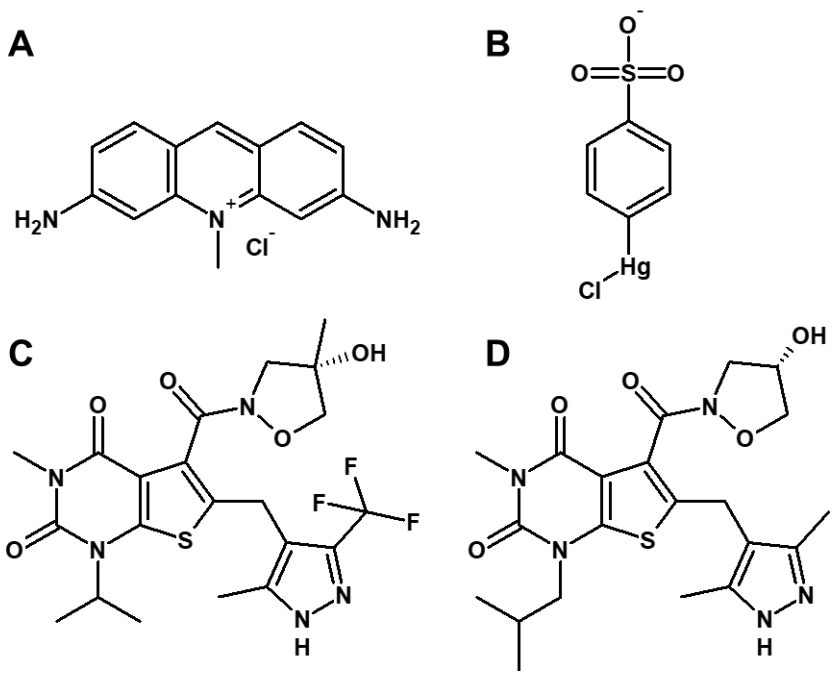

Figure 1.4. Chemical structures of the basigin/MCT inhibitors acriflavine **(A)**, *p*-chloromercuribenzene sulfonate (pCMBS) **(B)**, AZD3965 **(C)** and AR-C155858 **(D)**.

In the stage of finalizing this thesis, MCT1 structures in complex with basigin and in the inward and outward open conformation have been resolved using cryo electron microscopy [103]. These located AZD3965 in the substrate binding pocket proposing an inhibitory mechanism in which AZD3965 locks the transporter in the outward open conformation. In line with the previous literature, the substrate binding site was confirmed to consist of residues Tyr34, Lys38, Asp309, Arg313, Phe367 and Ser371. The authors further examined the basigin-MCT1 interaction and identified Asn187 of MCT's TM6 as the long-sought residue that forms a hydrogen bond with Glu218 of basigin and confers complexation. They reported lead evidence on the spatial organization of MCT1 and basigin although data on a functional relevance of basigin in MCT1 transport is still missing [103].

1.4. The aim: basigin-MCT1 fusion and functional characterization in yeast

The expression of human MCT1 is tightly linked to its association with basigin. In commonly used mammalian and *Xenopus* oocyte expression systems, MCT1 depends on basigin for translocation to the plasma membrane as the site of action. Therefore, studies on the MCT1 functionality regardless of basigin effects are hardly possible.

This thesis aims at determining unbiased functional and inhibitory characteristics of MCT1-mediated L-lactate transport and at revealing a long hypothesized direct modulation by basigin. For this purpose, MCT1 is expressed alone and in molecular fusion with basigin in the eukaryotic yeast *Saccharomyces cerevisiae*. The protein fusion profits from a constant close association of both proteins in a stoichiometric manner. The yeast-based expression system employs several advantages in functional studies on MCTs. First, earlier studies with *S. cerevisiae* confirmed the unique property to translocate MCTs to the plasma membrane in the absence of basigin [88, 104]. Second, a *jen1 ady2* knockout strain is devoid of any L-lactate transport activity [105, 106] and does not express endogenous basigin homologs [107]. In glucose-rich conditions, the yeast's end product of glucose breakdown is CO_2 (respiration) or ethanol (fermentation) [108]. L-Lactate formation and metabolism is virtually absent. These properties lay the foundation to examine the transport characteristics of unbiased MCT1 devoid of metabolic interference. Using a ^{14}C-based transport assay, the L-lactate influx via MCT1 will be monitored in a zero-trans set-up as well as in the equilibrium state while changing external modalities including pH, substrate availability and inhibitor treatment. Primarily, the molecular fusion to truncated basigin constructs seeks to examine respective basigin-mediated effects at the domain level. The functional expression of fusion proteins will finally be used for large scale protein synthesis to promote a structural understanding of the basigin-MCT1 complex using electron microscopy.

2. Materials

The following listing summarizes materials used in this project. The list is grouped into coding sequences, plasmids and oligonucleotides, cell strains, antibodies, chemicals and enzymes, and kits. It further describes the preparation of used buffers and solutions, and lists lab equipment and software. Individual compositions and corresponding producers are specified.

2.1. Coding sequences, plasmids, and oligonucleotides

2.1.1. Coding sequences

The coding sequences for human MCT1, basigin splice variant 1 and embigin splice variant 1 were purchased as ORF clones in pcDNA3.1+/C-(K)DYK (GenScript, Leiden, Netherlands) and the respective open reading frames (ORF) are listed below. Stop codons (italic) were removed by the supplier. Restriction sites PflMI/BspEI in the ORF of human MCT1 used for initial subcloning into pDRTXaLK vector (see section 2.1.2) are highlighted (bold). Customized coding sequences for basigin mutant constructs BSG Ig-I Glu→Gln and BSG Ig-I Lys,Arg→Ala + R166A including additional, flanking restriction sites were purchased as DNA constructs in vector pUC57. Restriction sites used for subcloning (bold) and respective base exchanges (small letters) are highlighted.

MCT1, ORF (GenBank NM_001166496):

```
1       ATGCCA**CCAG CAGTTGG**AGG TCCAGTTGGA TACACCCCCC CAGATGGAGG CTGGGGCTGG
61      GCAGTGGTAA TTGGAGCTTT CATTTCCATC GGCTTCTCTT ATGCATTTCC CAAATCAATT
121     ACTGTCTTCT TCAAAGAGAT TGAAGGTATA TTCCATGCCA CCACCAGCGA AGTGTCATGG
181     ATATCCTCCA TAATGTTGGC TGTCATGTAT GGTGGAGGTC CTATCAGCAG TATCCTGGTG
241     AATAAATATG GAAGTCGTAT AGTCATGATT GTTGGTGGCT GCTTGTCAGG CTGTGGCTTG
301     ATTGCAGCTT CTTTCTGTAA CACCGTACAG CAACTATACG TCTGTATTGG AGTCATTGGA
361     GGTCTTGGGC TTGCCTTCAA CTTGAATCCA GCTCTGACCA TGATTGGCAA GTATTTCTAC
421     AAGAGGCGAC CATTGGCCAA CGGACTGGCC ATGGCAGGCA GCCCTGTGTT CCTCTGTACT
481     CTGGCCCCCC TCAATCAGGT TTTCTTCGGT ATCTTTGGAT GGAGAGGAAG CTTTCTAATT
541     CTTGGGGGCT TGCTACTAAA CTGCTGTGTT GCTGGAGCCC TCATGCGACC AATCGGGCCC
601     AAGCCAACCA AGGCAGGGAA AGATAAGTCT AAAGCATCCC TTGAGAAAGC TGGAAAATCT
661     GGTGTGAAAA AAGATCTGCA TGATGCAAAT ACAGATCTTA TTGGAAGACA CCCTAAACAA
721     GAGAAACGAT CAGTCTTCCA AACAATTAAT CAGTTCCTGG ACTTAACCCT ATTCACCCAC
781     AGAGGCTTTT TGCTATACCT CTCTGGAAAT GTGATCATGT TTTTTGGACT CTTTGCACCT
841     TTGGTGTTTC TTAGTAGTTA TGGGAAGAGT CAGCATTATT CTAGTGAGAA GTCTGCCTTC
901     CTTCTTTCCA TTCTGGCTTT TGTTGACATG GTAGCCCGAC CATCTATGGG ACTTGTAGCC
961     AACACAAAGC CAATAAGACC TCGAATTCAG TATTTCTTTG CGGCTTCCGT TGTTGCAAAT
1021    GGAGTGTGTC ATATGCTAGC ACCTTTATCC ACTACCTATG TTGGATTCTG TGTCTATGCG
1081    GGATTCTTTG GATTTGCCTT CGGGTGGCTC AGCTCCGTAT TGTTTGAAAC ATTGATGGAC
1141    CTTGTTGGAC CCCAGAGGTT CTCCAGCGCT GTGGGATTGG TGACCATTGT GGAATGCTGT
1201    CCTGTCCTCC TGGGGCCACC ACTTTTAGGT CGGCTCAATG ACATGTATGG AGACTACAAA
1261    TACACATACT GGGCATGTGG CGTCGTCCTA ATTATTTCAG GTATCTATCT CTTCATTGGC
1321    ATGGGCATCA ATTATCGACT TTTGGCAAAA GAACAGAAAG CAAACGAGCA GAAAAAGGAA
1381    AGTAAAGAGG AAGAGACCAG TATAGATGTT GCTGGGAAGC CAAATGAAGT TACCAAAGCA
1441    GCAGAATC**TC CGGA**CCAGAA AGACACAGAT GGAGGGCCCA AGGAGGAGGA AAGTCCAGTC
1501    *TGA*
```

Basigin splice variant 1, ORF (GenBank NM_001728):

```
1       ATGGCGGCTG CGCTGTTCGT GCTGCTGGGA TTCGCGCTGC TGGGCACCCA CGGAGCCTCC
61      GGGGCTGCCG GCTTCGTCCA GGCGCCGCTG TCCCAGCAGA GGTGGGTGGG GGGCAGTGTG
121     GAGCTGCACT GCGAGGCCGT GGGCAGCCCG GTGCCCGAGA TCCAGTGGTG GTTTGAAGGG
181     CAGGGTCCCA ACGACACCTG CTCCCAGCTC TGGGACGGCG CCCGGCTGGA CCGCGTCCAC
241     ATCCACGCCA CCTACCACCA GCACGCGGCC AGCACCATCT CCATCGACAC GCTCGTGGAG
301     GAGGACACGG GCACTTACGA GTGCCGGGCC AGCAACGACC CGGATCGCAA CCACCTGACC
361     CGGGCGCCCA GGGTCAAGTG GGTCCGCGCC CAGGCAGTCG TGCTAGTCCT GGAACCCGGC
421     ACAGTCTTCA CTACCGTAGA AGACCTTGGC TCCAAGATAC TCCTCACCTG CTCCTTGAAT
481     GACAGCGCCA CAGAGGTCAC AGGGCACCGC TGGCTGAAGG GGGGCGTGGT GCTGAAGGAG
541     GACGCGCTGC CCGGCCAGAA AACGGAGTTC AAGGTGGACT CCGACGACCA GTGGGGAGAG
601     TACTCCTGCG TCTTCCTCCC CGAGCCCATG GGCACGGCCA ACATCCAGCT CCACGGGCCT
661     CCCAGAGTGA AGGCTGTGAA GTCGTCAGAA CACATCAACG AGGGGGAGAC GGCCATGCTG
721     GTCTGCAAGT CAGAGTCCGT GCCACCTGTC ACTGACTGGG CCTGGTACAA GATCACTGAC
781     TCTGAGGACA AGGCCCTCAT GAACGGCTCC GAGAGCAGGT TCTTCGTGAG TTCCTCGCAG
841     GGCCGGTCAG AGCTACACAT TGAGAACCTG AACATGGAGG CCGACCCCGG CCAGTACCGG
901     TGCAACGGCA CCAGCTCCAA GGGCTCCGAC CAGGCCATCA TCACGCTCCG CGTGCGCAGC
961     CACCTGGCCG CCCTCTGGCC CTTCCTGGGC ATCGTGGCTG AGGTGCTGGT GCTGGTCACC
1021    ATCATCTTCA TCTACGAGAA GCGCCGGAAG CCCGAGGACG TCCTGGATGA TGACGACGCC
1081    GGCTCTGCAC CCCTGAAGAG CAGCGGGCAG CACCAGAATG ACAAAGGCAA GAACGTCCGC
1141    CAGAGGAACT CTTCC*TGA*
```

Embigin splice variant 1, ORF (GenBank NM_198449):

```
1       ATGCGCGCCC TCCCCGGCCT GCTGGAGGCC AGGGCGCGTA CGCCCCGGCT GCTCCTCCTC
61      CAGTGCCTTC TCGCTGCCGC GCGCCCAAGC TCGGCGGACG GCAGTGCCCC AGATTCGCCT
121     TTTACAAGTC CACCTCTCAG AGAAGAAATA ATGGCAAATA ACTTTTCCTT GGAGAGTCAT
181     AACATATCAC TGACTGAACA TTCTAGTATG CCAGTAGAAA AAAATATCAC TTTAGAAAGG
241     CCTTCTAATG TAAATCTCAC ATGCCAGTTC ACAACATCTG GGGATTTGAA TGCAGTAAAT
301     GTGACTTGGA AAAAAGATGG TGAACAACTT GAGAATAATT ATCTTGTCAG TGCAACAGGA
361     AGCACCTTGT ATACCCAATA CAGGTTCACC ATCATTAATA GCAAACAAAT GGGAAGTTAT
421     TCTTGTTTCT TTCGAGAGGA AAAGGAACAA AGGGGAACAT TTAATTTCAA AGTCCCTGAA
481     CTTCATGGGA AAAACAAGCC ATTGATCTCT TACGTAGGGG ATTCTACTGT CTTGACATGT
541     AAATGTCAAA ATTGTTTTCC TTTAAATTGG ACCTGGTACA GTAGTAATGG GAGTGTAAAG
601     GTTCCTGTTG GTGTTCAAAT GAATAAATAT GTGATCAATG GAACATATGC TAACGAAACA
661     AAGCTGAAGA TAACACAACT TTTGGAGGAA GATGGGGAAT CTTACTGGTG CCGTGCACTA
721     TTCCAATTAG GCGAGAGTGA AGAACACATT GAGCTTGTGG TGCTGAGCTA TTTGGTGCCC
781     CTCAAACCAT TTCTTGTAAT AGTGGCTGAG GTGATTCTTT TAGTGGCCAC CATTCTGCTT
841     TGTGAAAAGT ACACACAAAA GAAAAAGAAG CACTCAGATG AGGGGAAAGA ATTTGAGCAG
901     ATTGAACAGC TGAAATCAGA TGATAGCAAT GGTATAGAAA ATAATGTCCC CAGGCATAGA
961     AAAAATGAGT CTCTGGGCCA G*TGA*
```

BSG Ig-I Glu→Gln (E114,118,120,168,172Q)*:*

```
1       ACTAGTATGC CCAGAGTGAA GGCTGTGAAG TCGTCAcAAC ACATCAACcA GGGGcAGACG
61      GCCATGCTGG TCTGCAAGTC AGAGTCCGTG CCACCTGTCA CTGACTGGGC CTGGTACAAG
121     ATCACTGACT CTGAGGACAA GGCCCTCATG AACGGCTCCG AGAGCAGGTT CTTCGTGAGT
181     TCCTCGCAGG GCCGGTCAcA GCTACACATT cAGAACCTGA ACATGGAGGC CGACCCCGGC
241     CAGTACCGGT GCAACGGCAC CAGCTCCAAG GGCTCCGACC AGGCCATCAT CACGCTCCGC
301     GTGCGCAGCC ACCTGGCCGC CCTCTGGCCC TTCCTGGGCA TCGTGGCTGA GGTGCTGGTG
361     CTGGTCACCA TCATCTTCAT CTACGAGAAG CGCCGGAAGC CCGAGGACGT CCTGGATGAT
421     GACGACGCCG GCTCTGCACC CCTGAAGAGC AGCGGGCAGC ACCAGAATGA CAAAGGCAAG
481     AACGTCCGCC AGAGGAACTC TTCCGGATCC CTGCAG
```

BSG Ig-I Lys,Arg→Ala + R166A (K108,111,127A / R166,201,203A):

```
1       ACTAGTATGC CCAGAGTGgc GGCTGTGgcG TCGTCAGAAC ACATCAACGA GGGGGAGACG
61      GCCATGCTGG TCTGCgcGTC AGAGTCCGTG CCACCTGTCA CTGACTGGGC CTGGTACAAG
121     ATCACTGACT CTGAGGACAA GGCCCTCATG AACGGCTCCG AGAGCAGGTT CTTCGTGAGT
181     TCCTCGCAGG GCgcGTCAGA GCTACACATT GAGAACCTGA ACATGGAGGC CGACCCCGGC
241     CAGTACCGGT GCAACGGCAC CAGCTCCAAG GGCTCCGACC AGGCCATCAT CACGCTCgcC
301     GTGgcCAGCC ACCTGGCCGC CCTCTGGCCC TTCCTGGGCA TCGTGGCTGA GGTGCTGGTG
361     CTGGTCACCA TCATCTTCAT CTACGAGAAG CGCCGGAAGC CCGAGGACGT CCTGGATGAT
421     GACGACGCCG GCTCTGCACC CCTGAAGAGC AGCGGGCAGC ACCAGAATGA CAAAGGCAAG
481     AACGTCCGCC AGAGGAACTC TTCCGGATCC CTGCAG
```

Sequences for fusion constructs as well as additional basigin and embigin variants were produced by molecular cloning techniques using the above-mentioned sequences as template and are described in section 3.1.1.
The expression construct for the plasmodial formate-nitrite transporter (PfFNT) in the yeast expression vector pDRTXa has been described earlier [109] and was kindly provided by Marie Wiechert.

2.1.2. Expression plasmids

For the recombinant expression in *S. cerevisiae*, coding sequences were cloned into the expression vectors pDRTXa, pDRTXaLK and pUG35 (U. Güldener and J. H. Hegemann, University of Düsseldorf, Germany) (Figure 2.1A, B). The plasmid pDRTXaLK resulted from two-step modification of commercial plasmid vector pDR196 [110] (Addgene #36029). First, the previously described introduction of an N-terminal HA-tag and a C-terminal His-tag gave rise to plasmid pDRTXa [109]. Further modification in this study introduced additional restriction sites via a linker sequence (pDRTXaLK, see section 3.1.1 for protocol). The multiple cloning sites (MCS) of pDRTXa and pDRTXaLK including respective restriction sites are displayed in Figure 2.1A. For the expression in *P. pastoris*, constructs were subcloned into a modified pPink-HC vector of the PichiaPink™ Expression System (Invitrogen). The modification has previously been described (see dissertation of J. Holm-Bertelsen [111]) and included the insertion of a C-terminal His-tag and additional restriction sites. pPink-HC carrying optPfFNT was kindly provided by L. Petersen and was used as a template for further cloning purposes (Figure 2.1C). Cell-free expression was induced from the vectors pIVEX2.3w or pIVEX2.3w-GFPΔM1 (Figure 2.1D, E) which are modified versions of the commercially available vector pIVEX2.3 (Roche). Modifications have been introduced previously and are described elsewhere (see dissertation A. Müller-Lucks [112, 113]). The sequences of the MCS of all vector plasmids (from promoter to terminator) are attached in the supplementary data.

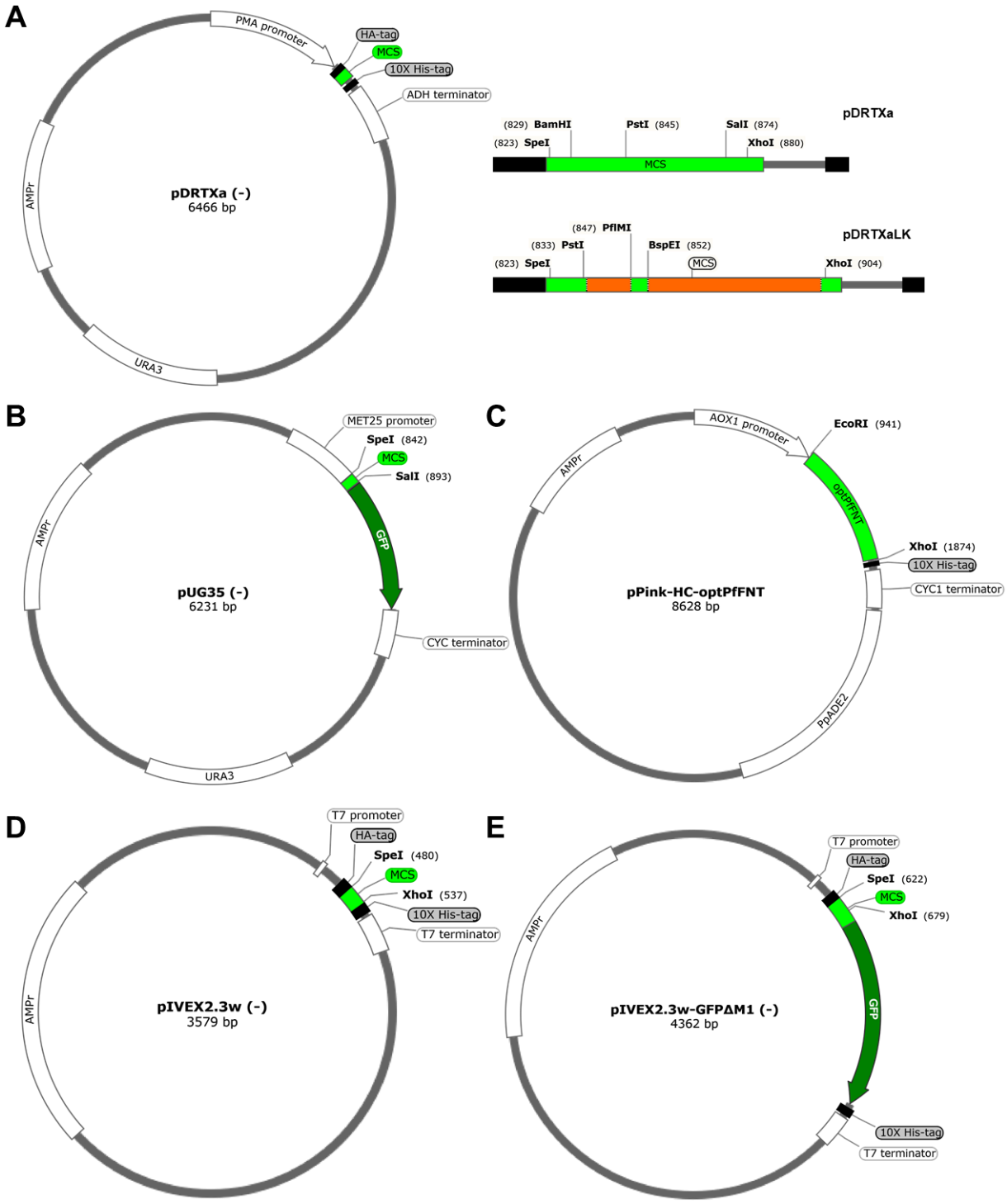

Figure 2.1. Vector maps. Shown are maps for the yeast expression vectors pDRTXa/pDRTXaLK including magnified excerpts of corresponding multiple cloning sites (MCS) **(A)**, pUG35 **(B)** and pPink-HC carrying PfFNT as insert **(C)**. The MCS of pDRTXaLK contains N- and C-terminal sequences complementing PflMI/BspEI-inserted MCT1 (orange). **(D, E)** Maps for cell-free expression plasmid pIVEX2.3w with and without the coding sequence for green fluorescent protein (GFP). The endogenous start-methionine of GFP was deleted (see dissertation S. Bock [114]). In all maps, promoter/terminator sequences, selection genes (AMPr, ampicillin resistance; URA3, Orotidine-5'-phosphate decarboxylase; ADE2, phosphoribosylaminoimidazole carboxylase), potential tags (HA, hemagglutinin) and relevant restriction sites are highlighted. Vector maps were generated with SnapGene® Viewer.

2.1.3. Oligonucleotides

Oligonucleotides for molecular cloning, site-directed mutagenesis and sequencing purposes are summarized in Table 2.1, Table 2.2 and Table 2.3, respectively. All oligonucleotides were purchased from Thermo Fisher Scientific (Schwerte, Germany) and dissolved in ddH_2O to a final concentration of 100 µM.

For constructing full-length and truncated basigin and embigin constructs, oligonucleotides were designed to introduce a start-methionine and suitable restriction sites for cloning purposes (Table 2.1). Relevant restriction sites (bold) and codons for start-methionines (italic) are highlighted. Bases complementary to BSG or MCT1 template DNA are written in capitals. Oligonucleotide descriptions include the construct identifier used in this work and specify deleted DNA segments for each construct (in brackets; numbering refers to full-length sequence of BSG var1 or EMB var1).

Table 2.1. Oligonucleotides for cloning purposes. s, sense; as, antisense.

Description	Oligonucleotide sequence (5'→3')
MCT1 linker, s	ctagtctgcagATGCCACCAGCAGTTGGTCCGGACCAGAAA GACACAGATGGAGGGCCCAAGGAGGAGGAAAGTCCAGTCC
MCT1 linker, as	tcgaGGACTGGACTTTCCTCCTCCTTGGGCCCTCCATCTGT GTCTTTCTGGTCCGGACCAACTGCTGGTGGCATctgcaga
BSGΔIg (Δ1-308), s	tt**actagt***atg*TCCGACCAGGCCATCATCACGC
BSG Ig-I(Δ1-220), s	tt**actagt***atg*CCCAGAGTGAAGGCTGTGAAGT
BSG Ig-I/C2 (Δ1-139), s	tt**actagt***atg*gctgccGGCACAGTCTTCACTACCGTAG
BSG var2 (Δ24-139), s	tt**actagt***atg*gcggctgcgctgttcgtgctgctgggattc gcgctgctgggcacccacggagcctccggggctgccgGCAC AGTCTTCACTACCGTAG
BSG var1, s	tt**actagt***atg*GCGGCTGCGCTGTTCGTGC
BSG, as	tt**ctgcagggatcc**GGAAGAGTTCCTCTGGCGGACG
EMBΔIg (Δ1-239), s	gg**actagt***atg*CTATTCCAATTAGGCGAGAGTG
EMB, s	tt**actagt***atg*CGCGCCCTCCCCGG
EMB, as	tt**ctgcag**GGATCCCTGGCCCAGAGACTCATTT

Oligonucleotides for site-directed *in vitro* mutagenesis of basigin and MCT1 are listed in Table 2.2. Base exchanges for the introduction of point mutations are written in lower case letters.

Table 2.2. Oligonucleotides for *in vitro* mutagenesis. s, sense; as, antisense.

Description	**Oligonucleotide sequence (5'→3')**
BSG Ig-I K108,111A, s	GCCCAGAGTGgcGGCTGTGgcGTCGTCAGAAC
BSG Ig-I K108,111A, as	CACTCTGGGCATACTAGTGTCCGCGTAGTCAGG
BSG Ig-I R201,203A, s	CATCACGCTCgcCGTGgcCAGCCACCTGG
BSG Ig-I R201,203A, as	GAGCGTGATGATGGCCTGGTCGGAGCCCTTGG
BSG Ig-I A166R, s	CCTCGCAGGGCcgGTCAGAGCTACACATTG
BSG Ig-I A166R, as	GCCCTGCGAGGAACTCACGAAGAACCTGC
BSG E(27)R, s	CTGGGCATCGTGGCTagaGTGCTGGTGCTG
BSG E(27)R, as	AGCCACGATGCCCAGGAAGGGCCAGAGG
BSG Ig-I C23S, s	ACGGCCATGCTGGTCTcCAAGTCAGAGTCCGTG
BSG Ig-I C23S, as	GACCAGCATGGCCGTCTCCCCCTCGTTGAT
BSG Ig-I C82S, s	GGCCAGTACCGGTcCAACGGCACCAGCTCCAA
BSG Ig-I C82S, as	CCGGTACTGGCCGGGGTCGGCCTCCATGTT
MCT1 C159S, s	AGCCCTGTGTTCCTCTcTACTCTGGCCCCCCTC
MCT1 C159S, as	GAGGAACACAGGGCTGCCTGCCATGGCCAG
MCT1 C399S, s	GTGACCATTGTGGAAagcTGTCCTGTCCTCCTG
MCT1 C399,400S, s	GTGACCATTGTGGAAagctctCCTGTCCTCCTG
MCT1 C400S, s	GTGACCATTGTGGAATGCtctCCTGTCCTCCTG
MCT1 C399,400S, as	TTCCACAATGGTCACCAATCCCACAGCGCT

Oligonucleotides for sequencing purposes are listed in Table 2.3. Oligonucleotides include vector- and insert-specific complementary sequences to cover full-length coding regions and ensure gapless sequence verifications. Complementary sequences are written in capital letters.

Table 2.3. Oligonucleotides for DNA sequencing.

Description	**Oligonucleotide sequence (5'→3')**
PMA	CTCTCTTTTATACACACATTC
ADH	CATAAATCATAAGAAATTCGC
MET25	AGTAAAGCGTCTGTTAGAAAGG
AOX1	CGACTGGTTCCAATTGACAAGC
CYC1	GGAGGGCGTGAATGTAAGCG
BSG_139, s	ttactagtatgCCCGGCACAGTCTTCACTACCG
BSG_208, s	GAGCCCATGGGCACGGCCAACAT
BSG_190, as	GAACTCCGTTTTCTGGCCGGG
EMB_64, s	CTGACTGAACATTCTAGTATGCC
EMB_158, s	atactagtatgGTCCCTGAACTTCATGGG
MCT1 F367D, s	TTCTTTGGATTTGCCgaCGGGTGGCTCAGCTC
MCT1 F367D, as	GGCAAATCCAAAGAATCCCGCATAGACACA
MCT1 R313N, s	GTTGACATGGTAGCCaatCCATCTATGGGACTT

2.2. Organisms and strains

This work includes work with bacteria and yeasts. The following list specifies the individual strains and their respective genotypes (Table 2.4).

Table 2.4. Organisms, strains and relevant genotype.

Organism (Strain)	**Genotype**	**Source**
Escherichia coli (DH5α)	F$^-$ *φ*80*lac*ZΔM15 Δ(*lac*ZYA-*arg*F)U169 *rec*A1 *end*A1 *hsd*R17(rK$^-$, mK$^-$) *pho*A *sup*E44 λ$^-$ *thi*-1 *gyr*A96 *rel*A1	-
Saccharomyces cerevisiae (W303-1A)	MATa, *can1-100*, *ade2-1*^{oc}, *his3-11-15*, *leu2-3,-112*, *trp1-1-1*, *ura3-1*, *jen1::kanMX4*, *ady2::hphMX4* *(Δjen1 Δady2)*	M. Casal (Braga, Portugal) [115]
Pichia pastoris (PichiaPink™ Strain 1)	Δ*ade*2	Invitrogen (Carlsbad, USA)

2.3. Antibodies

The following table lists primary and secondary antibodies used in this project (Table 2.5).

Table 2.5. Antibodies for Western blot and flow cytometry.

Antibody	**Host**	**Producer**	**Cat. Nr.**	**Purpose**
Penta-His antibody, BSA free (0.2 mg/ml)	Mouse	Qiagen	34660	Western blot
Anti-GFP (FL) antibody (0.2 mg/ml)	Rabbit	Santa Cruz Biotechnology	sc-8334	Western blot
Peroxidase AffiniPure Goat anti-Mouse IgG, HRP conjugate (0.4 mg/ml)	Goat	Jackson Immuno Research	115-035-174	Western blot
Peroxidase AffiniPure Goat anti-Rabbit IgG, HRP conjugate (0.4 mg/ml)	Goat	Jackson Immuno Research	111-035-003	Western blot
MCT1 antibody (0.5 mg/ml)	Rabbit	Biorbyt	orb312305	Flow cytometry
Goat anti-Rabbit IgG, APC conjugate (0.5 mg/ml)	Goat	Southern Biotech	4050-11S	Flow cytometry

2.4. Chemicals and enzymes

Chemicals and enzymes are listed below (Table 2.6). Corresponding manufacturers are indicated. For cell-free protein synthesis, S30 cell extracts and the T7 RNA polymerase were produced in-house. Respective protocols were adapted from Schwarz *et al.* [116] and were described in detail by A. Müller-Lucks [112]. S30 extracts were produced under the technical guidance of L. Petersen and B. Höger and the T7 polymerase was kindly provided by F. Helmstetter. MSP1E3D1-DOPG/POPG-nanodiscs were produced by C. Hansen according to protocols adapted from Rues *et al.* [117].

Table 2.6. Chemicals and enzymes, and respective suppliers.

Substance	Producer
Acetic acid	J.T. Baker, München
Acetyl phosphate (Li^+/K^+ salt)	Sigma Aldrich, München
Acriflavine	Sigma Aldrich, München
Adenine hemisulfate salt	Sigma Aldrich, München
Adenosine-5'-triphosphate disodium salt (ATP, hydrate)	Sigma Aldrich, München
Agar bacteriological	Oxoid, Basingstoke, USA
Agarose LE	Genaxxon BioScience, Ulm
L-Alanine	Fluka Chemie, Buchs, Switzerland
Ammonium persulfate	Carl Roth, Karlsruhe
Ampicillin (Na^+ salt)	Genaxxon BioScience, Ulm
L-Arginine monohydrochloride	Sigma Aldrich, München
L-Asparagine (monohydrate)	Sigma Aldrich, München
L-Aspartic acid (Na^+ salt, monohydrate)	Sigma Aldrich, München
AZD3965 (MCT1 inhibitor)	Hycultec, Beutelsbach, Germany
Bacto™ Peptone	BD Biosciences, San Jose, USA
Bacto™ Yeast Extract	BD Biosciences, San Jose, USA
Benzyl methanethiosulfonate (BMTS)	Interchim, Montluçon, France
Bovine albumin fraction V (pH 7.0)	Genaxxon BioScience, Ulm
Brij®35	AppliChem, Darmstadt
Brij®58	AppliChem, Darmstadt
Brij®78	Sigma Aldrich, München
Brij®98	Sigma Aldrich, München
Bromophenol Blue (Na^+ salt)	Carl Roth, Karlsruhe
Calcium chloride (dihydrate, ≥ 99 %)	Carl Roth, Karlsruhe

p-Chloromercuribenzene sulfonate (Na^+ salt, pCMBS)	Toronto Research Chemicals Inc., North York, Canada
Clarity™ ECL Western blotting substrate	Bio-Rad, München
Cloned *Pfu* reaction buffer (10X)	Agilent Technologies, Waldbronn
cOmplete™ protease inhibitor cocktail (EDTA-free)	Roche Diagnostics, Mannheim
L-Cysteine	Sigma Aldrich, München
Cytidin-5'-triphosphate disodium salt (CTP)	Sigma Aldrich, München
Deoxyribonucleic acid (Na^+ salt, single-stranded, from salmon testes)	Sigma Aldrich, München
2'-Deoxyadenosine-5'-triphosphate (dATP, 100 mM)	Thermo Fisher Scientific, Schwerte
2'-Deoxycytidine-5'-triphosphate (dCTP, 100 mM)	Thermo Fisher Scientific, Schwerte
2'-Deoxyguanosine-5'-triphosphate (dGTP, 100 mM)	Thermo Fisher Scientific, Schwerte
2'-Deoxythymidine-5'-triphosphate (dTTP, 100 mM)	Thermo Fisher Scientific, Schwerte
Difco™ Yeast Nitrogen Base w/o amino acids and ammonium sulfate	BD Biosciences, San Jose, USA
Dimethyl sulphoxide (DMSO, ≥ 99.8 %)	Sigma Aldrich, München
Dipotassium hydrogen phosphate (K_2HPO_4)	Carl Roth, Karlsruhe
Disodium hydrogen phosphate (Na_2HPO_4, dihydrate)	Carl Roth, Karlsruhe
Dithiothreitol (DTT)	Carl Roth, Karlsruhe
n-Dodecyl-β-D-maltopyranoside (DDM)	Anatrace, Maumee, USA
E. coli S30 extract	Beitz lab, CAU Kiel
Ethanol (≥ 99.8 %)	Carl Roth, Karlsruhe
Ethidium bromide (EtBr)	MP Biomedicals, Illkirch, France
Ethylenediaminetetraacetic acid (EDTA, ≥ 99 %)	Carl Roth, Karlsruhe
Ethylenediaminetetraacetic acid disodium salt (Na_2-EDTA, dihydrate, ≥ 99 %)	Carl Roth, Karlsruhe
Ethylenediaminetetraacetic acid disodium salt solution (Na_2-EDTA, 0.5 M)	Sigma Aldrich, München
FastAP Thermosensitive Alkaline Phosphatase (1 U μl^{-1})	Thermo Fisher Scientific, Schwerte
2-[(5-Fluoresceinyl)aminocarbonyl]ethyl methanethiosulfonate (MTS-4-Fluorescein)	Interchim, Montluçon, France
Folinic acid (Ca^{2+} salt)	Sigma Aldrich, München
G153 developer and fixation solution	Agfa-Gevaert, Mortsel, Belgium
D(+)-Glucose (monohydrate)	Carl Roth, Karlsruhe
L-Glutamic acid (K^+ salt, monohydrate)	Fluka Chemie, Buchs, Switzerland
L-Glutamine	Sigma Aldrich, München
Glycerol (≥ 98 %, anhydrous)	Carl Roth, Karlsruhe
Glycine	Carl Roth, Karlsruhe
Guanosine 5′-triphosphate sodium salt (hydrate, GTP)	Sigma Aldrich, München
L-Histidine monohydrochloride (monohydrate)	Sigma Aldrich, München

Hydrochloric acid	J. T. Baker, München
4-(2-Hydroxyethyl)-1-piperazineethanesulfonic acid (HEPES, ≥ 99.5 %)	Carl Roth, Karlsruhe
Imidazole	Sigma Aldrich, München
L-Isoleucine	Sigma Aldrich, München
Isopropyl alcohol (≥ 99.8 %)	Carl Roth, Karlsruhe
L(+)-Lactate (Na^+ salt)	AppliChem, Darmstadt
L-[$^{1\text{-}14}$C]-Lactic acid (sodium salt, 0.1 mCi ml^{-1}, 55 mCi $mmol^{-1}$)	Hartmann Analytic, Braunschweig
Lambda DNA	Thermo Fisher Scientific, Schwerte
LB agar (Lennox)	Carl Roth, Karlsruhe
LB medium (Lennox)	Carl Roth, Karlsruhe
L-Leucine	Carl Roth, Karlsruhe
Lithium acetate (> 99 %)	Carl Roth, Karlsruhe
L-Lysine monohydrochloride	Sigma Aldrich, München
Magnesium acetate (tetrahydrate)	Sigma Aldrich, München
Methanol (HPLC grade)	J. T. Baker, München
L-Methionine	Sigma Aldrich, München
Methyl methanethiosulfonate (MMTS)	Sigma Aldrich, München
Milk powder (blotting grade)	Carl Roth, Karlsruhe
2-(*N*-morpholino)ethanesulfonic acid (MES)	Carl Roth, Karlsruhe
MSP1E3D1-DOPG/POPG-nanodiscs	C. Hansen, Beitz lab, CAU Kiel
Ni^{2+}-NTA agarose	Qiagen, Hilden
OneTaq® DNA polymerase (5 U μl^{-1})	New England Biolabs, Frankfurt a. M.
OneTaq® Standard Reaction Buffer (5X)	New England Biolabs, Frankfurt a. M.
Orange G	Carl Roth, Karlsruhe
PeqGOLD Protein Marker III (prestained)	Peqlab, Erlangen
PfuTurbo DNA polymerase (2.5 U μl^{-1})	Agilent Technologies, Waldbronn
L-Phenylalanine	Sigma Aldrich, München
Phosphoenolpyruvate (K^+ salt, PEP)	AppliChem, Darmstadt
Polyethylenglycol (PEG) 3350	Sigma Aldrich, München
Polyethylenglycol (PEG) 8000	Sigma Aldrich, München
Potassium acetate	Carl Roth, Karlsruhe
Potassium chloride	Carl Roth, Karlsruhe
Potassium dihydrogenphosphate (KH_2PO_4)	Carl Roth, Karlsruhe
Potassium hydroxide	AppliChem, Darmstadt
L-Proline	Carl Roth, Karlsruhe

Propyl methanethiosulfonate (PMTS)	Interchim, Montluçon, France
Pyruvate kinase (10 mg ml^{-1})	Roche Diagnostics, Mannheim
Restriction Endonuclease Buffers (Orange, Green, Tango, 10X)	Thermo Fisher Scientific, Schwerte
Restriction Endonucleases (various, 10 U μl^{-1})	Thermo Fisher Scientific, Schwerte
RiboLock RNase inhibitor (40 U μl^{-1})	Thermo Fisher Scientific, Schwerte
Roti®-Quant concentrate (5X)	Carl Roth, Karlsruhe
Rotiphorese® Blue R concentrate	Carl Roth, Karlsruhe
Rotiphorese® Gel 40 (40 %, 29:1)	Carl Roth, Karlsruhe
Scintillation cocktail (Quicksafe A)	Zinsser Analytic, Frankfurt
L-Serine	Fluka Chemie, Buchs, Switzerland
Sodium acetate buffer solution (3 M, pH 5.2)	Sigma Aldrich, München
Sodium azide (NaN_3)	Carl Roth, Karlsruhe
Sodium chloride (NaCl)	Carl Roth, Karlsruhe
Sodium dihydrogen phosphate (NaH_2PO_4, monohydrate)	Carl Roth, Karlsruhe
Sodium dodecyl sulfate (SDS)	AppliChem, Darmstadt
Sodium hydroxide	Carl Roth, Karlsruhe
D-Sorbitol (≥ 98 %)	Carl Roth, Karlsruhe
2-Sulfonatoethyl methanethiosulfonate (MTSES)	Biotrend Chemikalien GmbH, Köln
T4 DNA ligase (5 U μl^{-1})	Thermo Fisher Scientific, Schwerte
T4 DNA ligase buffer	Thermo Fisher Scientific, Schwerte
T4 DNA polymerase (5 U μl^{-1})	Thermo Fisher Scientific, Schwerte
T7 RNA polymerase	Beitz lab, CAU Kiel
N,N,N′,N′-tetramethylethane-1,2-diamine (TEMED)	Genaxxon bioscience, Ulm
L-Threonine	Sigma Aldrich, München
Tris(hydroxymethyl)aminomethane	Carl Roth, Karlsruhe
Triton X-100	Carl Roth, Karlsruhe
tRNA (*E. coli*, MRE 600)	Roche Diagnostics, Mannheim
L-Tryptophan	Sigma Aldrich, München
Tween® 20	AppliChem, Darmstadt
L-Tyrosine	Sigma Aldrich, München
Uridine-5’-triphosphate trisodium salt (UTP, hydrate)	Sigma Aldrich, München
L-Valine	Sigma Aldrich, München

2.5. Consumables and kits

The following table lists consumables and commercially available kits used in this work (Table 2.7).

Table 2.7. Consumables and kits, and respective suppliers.

Consumable or kit	Producer
Amersham™ Hybond™ P 0.45 PVDF membrane	GE Healthcare, Freiburg
Amersham™ Hyperfilm ECL chemiluminescence films	GE Healthcare, Freiburg
Amicon Ultra-4 PLTK Ultracel-PL Membrane (30 kDa)	Merck, Darmstadt
Centrifuge tubes (15 ml and 50 ml)	Sarstedt, Nümbrecht
Conical flasks for cell culture (various sizes)	Schott AG, Mainz
Cuvettes, polystyrol (10 x 4 x 45 mm)	Sarstedt, Nümbrecht
Cuvettes, precision cells of quartz, 10 mm	Hellma, Jena
Dialysis tubing, Visking® (14 kDa MWCO)	Carl Roth, Karlsruhe
Falcon™ polypropylene round-bottom tube (5 ml, flow cytometry)	Corning Inc., Corning, USA
FluoroDish™	World Precision Instruments, Friedberg
Gene Pulser® Electroporation Cuvettes, 0.2 cm gap	Bio-Rad, München
GenomeLab™ DTCS Quick Start Kit	Beckman Coulter, Krefeld
Glass beads (acid-washed, Ø 425-600 µm)	Sigma Aldrich, München
HiYield® PCR Clean-up / Gel Extraction Kit	Süd-Laborbedarf, Gauting
Micro tubes (1.5 ml, 2 ml)	Sarstedt, Nümbrecht
NORM-JECT® syringes	Eydam, Kiel
NucleoBond® PC 500	Macherey-Nagel, Düren
Parafilm “M”	American National Can, Chicago, USA
PCR strips (8-strip opt. clear flat caps)	Sarstedt, Nümbrecht
PCR tubes Multiply®-Pro 0.2 ml, PP	Sarstedt, Nümbrecht
Pipette tips (various sizes)	Sarstedt, Nümbrecht
Poly-Prep® Chromatography Columns	Bio-Rad, München
Polypropylene tubes (1.5 ml, ultracentrifuge)	Beckman Coulter, Krefeld
Quick Start™ Bradford Protein Assay	Bio-Rad, München
QuikChange Site-Directed Mutagenesis Kit	Agilent, Santa Clara, USA
Scintillation vials, Snaptwist® (6.5 ml, HDPE tube)	VWR, Darmstadt
Serological pipettes	Sarstedt, Nümbrecht
Slide-A-Lyzer™ Dialysis Cassettes (10 kDa MWCO, 3 ml)	Thermo Fisher Scientific, Schwerte

Sterile filter, Filtropur S 0.2	Sarstedt, Nümbrecht
Sterile filter, Filtropur S 0.45	Sarstedt, Nümbrecht
Whatman Grade GF/C Glass Micro-fiber filter (25 mm).	GE Healthcare, Freiburg
Whatman™ Grade 3MM CHR Blotting Paper	GE Healthcare, Freiburg
Wizard® Plus SV Minipreps DNA Purification System	Promega, Mannheim

2.6. Preparation of buffers, solutions, and cell culture media

The following sections list the specifications, compositions, and recipes for used buffers, stock solutions and cell culture media. Utilized chemicals and their suppliers are listed in chapter 2.4.

2.6.1. Molecular biological methods

TAE buffer (50X)

Tris base	242 g (≙ 2 M)
Na_2-EDTA (0.5 M)	100 ml (≙ 0.05 M)
glacial acetic acid	57.1 ml (≙ 1 M)
ddH_2O	ad 1 l
(final pH 8.5)	

TAE buffer (1X)

TAE (50X)	20 ml
ddH_2O	ad 1 l
(final 40 mM Tris-acetate, 1 mM EDTA)	

Orange G loading buffer (10X)

Orange G	0.04 g (≙ 0.4 %)
Glycerol (≥ 98 %)	3 ml (≙ 30 %)
Na_2-EDTA (0.5 M)	2 ml (≙ 100 mM)
ddH_2O	ad 10 ml
(stored at 4 °C)	

EtBr (10 mg ml^{-1})

Ethidium bromide	5 tablets (à 0.1 µg)
ddH_2O	ad 50 ml
(stored at 4 °C)	

Na_2-EDTA (100 mM)

Na_2-EDTA (0.5 M)	10 ml
ddH_2O	ad 50 ml

dNTP mix (2.5 mM)

dATP (100 mM)	0.25 ml
dGTP (100 mM)	0.25 ml
dCTP (100 mM)	0.25 ml
dTTP (100 mM)	0.25 ml
ddH_2O	9 ml

Lambda DNA PstI digest

Lambda DNA	200 µl
Buffer Orange (10X)	108 µl
PstI restriction enzyme	12 µl
ddH_2O	760 µl
(incubated overnight, 37 °C)	

After digestion, 120 µl of Orange G loading buffer were added. Stored at −20 °C.

2.6.2. Cell culture, transformation, and storage

LB medium

LB medium (Lennox)	20 g
ddH_2O	ad 1 l
(autoclaved)	

LB agar plates

LB agar (Lennox)	35 g
ddH_2O	ad 1 l
(autoclaved)	

For LB Amp selection media, media were supplemented with 1 ml 1000X ampicillin (1 g ad 10 ml ddH_2O, filter sterilized) to a final concentration of 100 µg ml^{-1}.

YPD medium

Bacto™ Peptone	20 g
Bacto™ Yeast Extract	10 g
D-Glucose	20 g
ddH_2O	ad 1 l
(autoclaved)	

YPD agar plates

Bacto™ Peptone	20 g
Bacto™ Yeast Extract	10 g
D-Glucose	20 g
Agar bacteriological	20 g
ddH_2O	ad 1 l
(autoclaved)	

SD medium (+ AHLW)

Difco™ Yeast Nitrogen Base (w/o ammonium sulfate and amino acids)	1.7 g
Ammonium sulfate	5.0 g
D-Glucose	20 g
(pH adjusted to 5.6 with NaOH)	
ddH_2O	ad 1 l
(autoclaved)	

SD agar plates (+ AHLW)

Difco™ Yeast Nitrogen Base (w/o ammonium sulfate and amino acids)	1.7 g
Ammonium sulfate	5.0 g
D-Glucose	20 g
(pH adjusted to 5.6 with NaOH)	
Agar bacteriological	20 g
ddH_2O	ad 1 l
(autoclaved)	

For SD AHLW media and agar plates, 5 ml 200X adenine (≙ final 25 mg l^{-1}), 1 ml 1000X L-histidine (≙ final 20 mg l^{-1}), 5 ml 200X L-leucine (≙ final 100 mg l^{-1}) and 2 ml 500X L-tryptophan (≙ final 10 mg l^{-1}) were added after autoclaving.

Adenine (200X)

Adenine hemisulfate salt	1 g (≙ 5 g l^{-1})
ddH_2O	ad 200 ml
(filter sterilized)	

L-Histidine (1000X)

L-Histidine monohydro-chloride (monohydrate)	4 g (≙ 20 g l^{-1})
ddH_2O	ad 200 ml
(filter sterilized, stored at 4 °C)	

L-Leucine (200X)

L-Leucine	4 g (≙ 20 g l^{-1})
ddH_2O	ad 200 ml
(filter sterilized)	

L-Tryptophan (500X)

L-Tryptophan	1 g (≙ 5 g l^{-1})
ddH_2O	ad 200 ml
(filter sterilized, stored at 4 °C)	

L-Lactate medium (1 %, pH 6.0)

Difco™ Yeast Nitrogen Base (w/o ammonium sulfate and amino acids)	1.7 g
Ammonium sulfate	5 g
MES (1 M, pH 6.0)	50 ml (≙ 50 mM)
ddH_2O	ad 850 ml
(autoclaved)	

After autoclaving, add 150 ml of L-lactate (66.7 g l^{-1}, filter sterilized) and 5 ml 200X adenine (≙ final 25 mg l^{-1}), 1 ml 1000X L-histidine (≙ final 20 mg l^{-1}), 5 ml 200X L-leucine (≙ final 100 mg l^{-1}) and 2 ml 500X L-tryptophan (≙ final 10 mg l^{-1}).

L-Lactate agar plates (2 %, pH 5.8 or 6.8)

Difco™ Yeast Nitrogen Base (w/o ammonium sulfate and amino acids)	1.7 g
Ammonium sulfate	5 g
MES	9.76 g (≙ 50 mM)
Agar bacteriological	20 g
ddH_2O	ad 900 ml
(pH adjusted to 5.8 or 6.8 with NaOH, autoclaved)	

After autoclaving, add 100 ml of L-lactate (200 g l^{-1}, filter sterilized) and 5 ml 200X adenine (≙ final 25 mg l^{-1}), 1 ml 1000X L-histidine (≙ final 20 mg l^{-1}), 5 ml 200X L-leucine (≙ final 100 mg l^{-1}) and 2 ml 500X L-tryptophan (≙ final 10 mg l^{-1}).

MES (1 M, pH 6.0)

MES	195.2 g
ddH_2O	ad 1 l
(pH adjusted to 6.0)	

YNB (10X)

Difco™ Yeast Nitrogen Base (w/o ammonium sulfate and amino acids)	34 g
Ammonium sulfate	100 g
ddH_2O	ad 1 l
(filter sterilized)	

BMGY medium

Peptone / yeast extract	700 ml
Phosphate buffer	100 ml
(1 M, pH 6.0)	
Glycerol (10X)	100 ml
YNB (10X)	100 ml

BMMY medium

Peptone / yeast extract	700 ml
Phosphate buffer	100 ml
(1 M, pH 6.0)	
Methanol (10X)	100 ml
YNB (10X)	100 ml

Peptone / yeast extract

Bacto™ Peptone	20 g
Bacto™ Yeast Extract	10 g
ddH_2O	ad 700 ml
(autoclaved)	

Phosphate buffer (1 M, pH 6.0)

K_2HPO_4 (1 M)	132 ml
KH_2PO_4 (1 M)	868 ml
(pH adjusted to 6.0, autoclaved)	

Glycerol (10X, ≙ 10 %)

Glycerol (≥ 98 %)	100 ml
ddH_2O	ad 1 l
(filter sterilized)	

Methanol (10X, ≙ 5 %)

Methanol	12.5 ml
ddH_2O	ad 250 ml
(filter sterilized, stored at 4 °C)	

Single-stranded carrier DNA (2 mg ml^{-1})

DNA (single-stranded, from salmon testes)	200 mg
TE buffer	ad 100 ml
(stored at −20 °C)	

TE buffer

Tris base	121 mg (≙ 10 mM)
EDTA	29.2 mg (≙ 1 mM)
ddH_2O	ad 100 ml
(pH adjusted to 8.0, autoclaved)	

PEG 3350 (50 % w/v)

Polyethylenglycol 3350	50 g
ddH_2O	ad 100 ml
(autoclaved)	

Glycerol (80 % w/v)

Glycerol (≥ 98 %)	80 g
ddH_2O	ad 100 ml
(autoclaved)	

LiAc (1 M)

Lithium acetate	33 g
ddH_2O	ad 500 ml
(autoclaved, final pH 8.4−8.9)	

Sorbitol (1 M)

D-Sorbitol	18.2 g
ddH_2O	ad 100 ml
(autoclaved)	

YPD (+ 25 % glycerol)

YPD medium	17.2 ml
Glycerol (80 %)	7.8 ml

YPDS

Bacto™ Peptone	20 g
Bacto™ Yeast Extract	10 g
D-Glucose	20 g
D-Sorbitol	182.2 g
ddH_2O	ad 1 l
(autoclaved)	

$CaCl_2$ (0.1 M / 0.2 M)

Calcium chloride (dihydrate)	7.35 g
ddH_2O	ad 500 ml / 250 ml
(autoclaved, stored at 4 °C)	

$CaCl_2$ (+ 20 % glycerol)

$CaCl_2$ (0.2 M)	25 ml
Glycerol (40 %)	25 ml

2.6.3. Biophysical transport assay using ^{14}C-labeled substrates

HEPES/Tris assay buffer (50 mM, pH 6.8)	
Tris base	606 mg (≙ 50 mM)
HEPES	1192 mg (≙ 50 mM)
ddH_2O	ad 100 ml
(pH adjusted to 6.8 ± 0.1, filter sterilized)	

MES/Tris assay buffer (50 mM, pH 5.8)	
Tris base	606 mg (≙ 50 mM)
MES	976 mg (≙ 50 mM)
ddH_2O	ad 100 ml
(pH adjusted to 5.8 ± 0.1, filter sterilized)	

L-Lactate stock (0.25 M)	
L-Lactate (Na^+ salt)	0.2801 g
ddH_2O (sterile)	ad 10 ml
(stored at 4 °C)	

L-Lactate stock (0.05 M)	
L-Lactate (0.25 M)	0.2 ml
Assay buffer (pH 5.8 or pH 6.8)	0.8 ml
(stored at 4 °C)	

Substrate solution (5X), for uptake over time and inhibition	
L-Lactate stock (0.05 M)	2 µl (≙ 5 mM)
L-[$^{1\text{-}14}$C]-Lactic acid (Na^+ salt, 0.1 mCi ml^{-1}, 55 mCi $mmol^{-1}$)	0.4 µl (≙ 0.04 µCi)
Assay buffer (pH 5.8 or pH 6.8)	ad 20 µl

Substrate solution (5X), for kinetic measurements	
L-Lactate stock (0.05 M or 0.25 M)	2−12 µl (≙ 5−50 mM)
L-[$^{1\text{-}14}$C]-Lactic acid (Na^+ salt, 0.1 mCi ml^{-1}, 55 mCi $mmol^{-1}$)	1 µl (≙ 0.1 µCi)
Assay buffer (pH 5.8 or pH 6.8)	ad 20 µl

Preparations are exemplary for a single probe. Substrate solutions were always prepared as master mix for a total number of probes. In each assay, L-lactate is finally diluted 1:5 with cell suspension leading to a final L-lactate concentration of 1−10 mM.

2 % Glucose (for washing)	
D-Glucose (monohydrate)	10 g
ddH_2O	ad 500 ml
(filter sterilized)	

HEPES/Tris assay buffer (2 % glucose, 50 mM, pH 6.8)	
D-Glucose (monohydrate)	0.5 g (≙ 110 mM)
Assay buffer (pH 6.8)	ad 25 ml

2.6.4. Flow cytometry

Phosphate Buffered Saline (PBS, 1X)

NaCl	8 g (≙ 137 mM)
KCl	0.2 g (≙ 2.7 mM)
$Na_2HPO_4 \cdot 2\ H_2O$	1.78 g (≙ 10 mM)
KH_2PO_4	0.27 g (≙ 2 mM)
ddH_2O	ad 1 l
(pH adjusted to 7.4, autoclaved)	

FC buffer (1 % BSA)

Bovine serum albumin	1 g
PBS (1X)	ad 100 ml
(stored at 4 °C)	

2.6.5. Cell lysis, SDS-PAGE, Coomassie staining, and Western blot

Extraction Buffer

Tris base	3 g (≙ 25 mM)
Na_2-EDTA (0.5 M)	10 ml (≙ 5 mM)
ddH_2O	ad 1 l
(pH adjusted to 7.5 with HCl, autoclaved)	

Solubilization Buffer (pH 8.0)

Na_2HPO_4 (1 M)	93.2 ml
NaH_2PO_4 (1 M)	6.8 ml
NaCl	2.9 g (≙ 50 mM)
ddH_2O	ad 1 l
(pH adjusted to 8.0, final 100 mM sodium phosphate, autoclaved)	

Electrophoresis buffer (10X)

Glycine	144 g (≙ 1.92 M)
Tris base	30.3 g (≙ 0.25 M)
SDS	10 g (≙ 1 %)
ddH_2O	ad 1 l
(pH at 8.2−8.6)	

Electrophoresis buffer (1X)

Electrophoresis buffer (10X)	100 ml
ddH_2O	ad 1 l
(final 0.192 M glycine, 25 mM Tris, 0.1 % SDS)	

SDS loading buffer (4X)

Tris base (1 M, pH 6.8)	2.5 ml (≙ 0.25 M)
Glycerol (≥ 98 %)	4 ml (≙ 40 %)
Bromophenol Blue	2 mg (≙ 0.02 %)
SDS	0.8 g (≙ 8 %)
DTT	0.62 g (≙ 400 mM)
ddH_2O	ad 10 ml
(stored at −20 °C)	

APS (10 %)

Ammonium persulfate	5 g
ddH_2O	ad 50 ml
(stored at −20 °C)	

Separation gel buffer (4X)

Tris base	18.2 g (≙ 1.5 M)
SDS	0.4 g (≙ 0.4 %)
ddH_2O	ad 100 ml
(pH adjusted to 8.8)	

Stacking gel buffer (4X)

Tris base	12.1 g (≙ 0.5 M)
SDS	0.8 g (≙ 0.4 %)
ddH_2O	ad 200 ml
(pH adjusted to 6.8)	

Rotiphorese® Blue R solution

Rotiphorese® Blue R concentrate	600.0 ml
ddH_2O	397.5 ml

Destaining solution

Acetic acid	100 ml (≙ 10 % v/v)
Ethanol (≥ 99.8 %)	300 ml (≙ 30 % v/v)
ddH_2O	ad 1 l

Transfer buffer (5X)

Tris base	7.6 g (≙ 0.125 M)
Glycine	36.0 g (≙ 0.96 M)
SDS	0.934 g (≙ 0.19 %)
ddH_2O	ad 500 ml

Transfer buffer (1X)

Transfer buffer (5X)	10 ml
Methanol	10 ml
ddH_2O	ad 50 ml
(final 25 mM Tris, 192 mM glycine and 0.038 % SDS)	

Tris-buffered saline (TBS, 10X)

NaCl	80 g (≙ 1.35 M)
Tris base	24.3 g (≙ 0.2 M)
ddH_2O	ad 1 l
(pH adjusted to 7.6)	

TBS-T (1X)

TBS (10X)	100 ml
ddH_2O	900 ml
Tween® 20	1 ml
(final 135 mM NaCl and 20 mM Tris)	

3 % Milk powder in TBS-T

Milk powder	1.2 g
TBS-T (1X)	ad 40 ml
(stored at 4 °C)	

2.6.6. Cell-free protein synthesis

All stocks and solutions used for cell-free protein synthesis were kindly prepared and provided by B. Höger and C. Hansen.

NaN_3 (10 %)

Sodium azide	100 mg
ddH_2O (sterile)	ad 1 ml
(filter sterilized, stored at −20 °C)	

PEG 8000 (40 %)

PEG 8000	20 g
ddH_2O (sterile)	ad 50 ml

COmplete™ protease inhibitor (50X)

COmplete™ protease inhibitor	1 tablet
ddH_2O (sterile)	ad 1 ml
(stored at −20 °C)	

NTP mix (75 X)

ATP	409.7 mg (≙ 90 mM)
GTP	251.1 mg (≙ 60 mM)
CTP	253.0 mg (≙ 60 mM)
UTP	272.6 mg (≙ 60 mM)
ddH_2O (sterile)	ad 8 ml
(pH adjusted to 7, filter sterilized, stored at −20 °C)	

PEP (1000 mM)

Phosphoenolpyruvate (K^+ salt)	412.2 mg
ddH_2O (sterile)	ad 2 ml
(pH adjusted to 7, stored at −20 °C)	

tRNA (*E. coli*, 40 mg ml^{-1})

tRNA (*E. coli*)	46 mg
ddH_2O (sterile)	ad 1.15 ml
(filter sterilized, stored at −20 °C)	

AcP (1000 mM)

Acetyl phosphate (Li^+/K^+ salt)	368.2 mg
ddH_2O (sterile)	ad 2 ml
(pH adjusted to 7, stored at −20 °C)	

Folinic acid (10 mg ml^{-1})

Folinic acid	10 mg
ddH_2O (sterile)	ad 1 ml
(stored at −20 °C)	

DTT (500 mM)

Dithiothreitol	154 mg
ddH_2O (sterile)	ad 2 ml
(filter sterilized, stored at −20 °C)	

KOAc (4000 mM)

Potassium acetate	19.63 g
ddH_2O (sterile)	ad 50 ml
(filter sterilized, stored at −20 °C)	

$Mg(OAc)_2$ (1000 mM)

Magnesium acetate (tetrahydrate)	3.21 g
ddH_2O (sterile)	ad 15 ml

(filter sterilized, stored at −20 °C)

Amino acid stocks

L-Arginine	316.1 mg
L-Asparagine	225.3 mg
L-Alanine	133.6 mg
L-Aspartate	259.7 mg
L-Glutamate	304.9 mg
L-Glutamine	219.2 mg
Glycine	112.6 mg
L-Histidine	314.4 mg
L-Isoleucine	196.8 mg
L-Leucine	196.8 mg
L-Phenylalanine	247.8 mg
L-Proline	172.7 mg
L-Lysine	274.1 mg
L-Serine	157.7 mg
L-Tryptophan	306.3 mg
L-Threonine	178.7 mg
L-Valine	175.7 mg
L-Cysteine	181.8 mg
L-Methionine	223.8 mg

(dissolved in 15 ml sterile ddH_2O each, final 100 mM)

L-Tyrosine	181.2 mg

(dissolved in 50 ml sterile ddH_2O, final 20 mM)

20-Amino acid mix

For preparation of the final 20-Amino acid mix, 2 ml of amino acid stock solutions (10 ml for L-tyrosine) were combined to a final volume of 50 ml. Final concentration: 4 mM each.
(filter sterilized, stored at −20 °C)

6-Amino acid mix (RCWMDE)

For preparation of the final 6-Amino acid mix, 4 ml of amino acid stock solutions (R, C, W, M, D and E only) were combined to a final volume of 24 ml. Final concentration: 16.7 mM each.
(filter sterilized, stored at −20 °C)

HEPES/EDTA buffer (24X)

HEPES	28.6 g (≙ 2.4 M)
EDTA	0.372 g (≙ 0.02 M)
ddH_2O	ad 50 ml

(pH adjusted to 8 with KOH, filter sterilized, stored at −20 °C)

S30 buffer (50X)

Tris base	60.6 g (≙ 500 mM)
Magnesium acetate (tetrahydrate)	150.1 g (≙ 700 mM)
Potassium acetate	2.9 g (≙ 30 mM)
ddH_2O	ad 1 l

(pH adjusted to 8.2 with acetic acid, filter sterilized)
For cell-free synthesis, 50X buffer was diluted to 1X with ddH_2O to final 10 mM Tris, 14 mM $Mg(OAc)_2$ and 0.6 mM KOAc.

Purification buffer (1X)

Tris	0.02 M
NaCl	0.15 M
optional:	
for detergent screen:	0.05 % DDM (w/v)
for detergent-based synthesis:	0.05 % Brij®78 (w/v)
for nanodiscs-guided synthesis:	no detergent

(pH adjusted to 8.0, 4 °C, filter sterilized)

Purification buffer (1X, + imidazole)

Tris	0.02 M
NaCl	0.15 M
Imidazole	0.02−0.5 M
optional:	
for detergent screen:	0.05 % DDM (w/v)
for detergent-based synthesis:	0.05 % Brij®78 (w/v)
for nanodiscs-guided synthesis:	no detergent

(pH adjusted to 8.0, 4 °C, filter sterilized)

Eluent for SEC

As eluent for size-exclusion chromatography, the respective 1X purification buffer was used.

2.7. Lab equipment and software

Equipment and devices used in this project are listed in Table 2.8.

Table 2.8. Lab equipment and corresponding manufacturer.

Lab equipment	Manufacturer
ÄKTApurifier™ 10	GE Healthcare, Freiburg
Analytical balance ABS 120-4	Kern & Sohn, Balingen
Analytical balance CP225D	Sartorius, Göttingen
Battery-powered pipette controller accu-jet® *pro*	Brand GmbH + CO. KG, Wertheim
Gallios 3L Flow Cytometer	Beckman Coulter, Krefeld
BioPhotometer 6131	Eppendorf, Hamburg
CAWO ABS cassette (for film exposure)	CAWO, Schrobenhausen
Cell-free reaction chamber (analytic)	Beitz lab, CAU Kiel
Cell-free reaction chamber (preparative)	Beitz lab, CAU Kiel
Centrifuge Biofuge™ Pico	Heraeus, Hanau
Chemostar Touch ECL & Fluorescence Imager	INTAS Science Imaging Instruments, Göttingen
Climate Chamber Incubator WTC Binder 9010-0021	Binder, Tuttlingen
Digital pH meter Lab 850	Schott Instruments, Mainz
DNA Sequencer CEQ™ 8000	Beckman Coulter, Krefeld
DNA SpeedVac® DNA110	Savant Instruments, Farmingdale, USA
Elektrophoresis Power Supply EPS 300	Pharmacia Biotech, Stockholm, Sweden
Gene Pulser® II Electroporation System	Bio-Rad, München
Heating block Dri-Block DB20	Techne, Stone, Great Britain
Heraguard Clean Bench	Heraus, Hanau
Image Document Analyzer Raytest IDA	Elysia-Raytest, Straubenhardt
Incubator Kelvitron® t	Heraeus, Hanau
Incubator Shaker Minitron	Infors HT, Bottmingen
JEM-1400 Plus Transmission Electron Microscope	JEOL, Peabody, USA
Leica SP5 confocal microscope (HCX PL APO CS 63.0×1.40 Oil objective)	Leica Microsystems, Wetzlar
Lumi Imager™ F1	Roche Diagnostics, Mannheim
Magnetic stirrer Ikamag® Ret-GS	IKA-Werke, Staufen
PerfectBlue Dual Gel System Twin S w/ casting base	Peqlab, Erlangen
Power Pac 200 Electrophoresis Power Supply	Bio-Rad, München
Precision balance PB3002-S Delta Ranger	Mettler-Toledo, Gießen

Refrigerated benchtop centrifuge 5424 R	Eppendorf, Hamburg
Refrigerated benchtop centrifuge Multifuge 1S-R	Heraeus, Hanau
Refrigerated benchtop centrifuge PerfectSpin 24 R	Peqlab, Erlangen
Rocking Shaker WS 10	Edmund Bühler, Hechingen
Rotator Grant Bio PTR-30 360-degree	Keison International, Essex, Great Britain
Rotator TC-7	New Brunswick Scientific, Edison, USA
Scintillation Counter Tri-Carb 2900TR	Packard, Downers Grove, USA
Shaking table Certomat® MO	Sartorius, Göttingen
Single channel pipettes	Gilson, Middleton, USA
Superdex 200 10/30 GL	GE Healthcare, Freiburg
Thermocycler Primus HT 25	Clemens, Waldbüttelbrunn
Trans-Blot® SD Semi-Dry Transfer Cell	Bio-Rad, München
Ultracentrifuge Optima™ XL-80 K	Beckman Coulter, Krefeld
Ultracentrifuge Rotor Type 50.2 Ti	Beckman Coulter, Krefeld
UV-Transluminator UVT-20 S/M	Herolab Laborgeräte, Wiesloch
Vacuum pump type 400171 (chemically resistant)	Ilmvac, Ilmenau
Vortex Genie® 2	Scientific Industries, Bohemia, USA
Water bath	Gesellschaft für Labortechnik, Burgwedel
Water purification system Puranity TU	VWR, Darmstadt

This work was written using Microsoft Office. Data analysis was done with SigmaPlot, Kaluza and ImageJ, and generation, analysis and visualization of protein structures was conducted with Chimera and PyMOL.

Table 2.9. Software and corresponding manufacturer.

Software	Producer
Microsoft Office 365, Version 2010	Microsoft Corporation
SigmaPlot 11.0	Systat Software Inc.
Chimera 1.15	Resource for Biocomputing, Visualization, and Informatics at the University of California [118]
PyMOL 1.7.4.1	Schrödinger, LLC
ImageJ 1.52p	National Health Institute USA
Kaluza Analysis 1.3	Beckman Coulter
SnapGene® Viewer 5.2.3	GSL Biotech LLC
Lasergene 7.2.1	DNASTAR®
Photoshop® Elements 11.0	Adobe Systems Inc.
ChemSketch	ACD/Labs

3. Methods

3.1. Molecular biological methods

3.1.1. General cloning strategy for basigin/embigin-MCT1 fusion constructs

This section outlines the general cloning approaches for MCT1 constructs in this work. Individual methodic protocols are described in detail in later sections.

For the recombinant expression of MCT1 constructs in yeast, coding sequences (see 2.1.1) were cloned into the modified expression vector pDR196 (pDRTXa, see 2.1.2). To introduce suitable restriction sites, the multiple cloning site of pDRTXa was modified by a specific linker generating plasmid vector pDRTXaLK. In short, a complementary pair of oligonucleotides (Table 2.1, “MCT1 linker”) carrying restrictions sites for PflMI, BspEI and PstI, as well as N- and C-terminal flanking sequences of MCT1 (see Figure 2.1A for illustration) was annealed and resulting SpeI/XhoI overhangs were ligated into the pDRTXa vector. Subsequently, the coding sequence for MCT1 (lacking the respective N- and C-terminal ends) was introduced via internal PflMI/BspEI restriction sites. The basigin/embigin variants BSGΔIg/EMBΔIg, BSG Ig-I, BSG-Ig-I/C2, BSG var2 and BSG var1/EMB var1 including suitable SpeI and PstI restriction sites were produced via PCR using basigin/embigin splice variant 1 as a template (see Table 2.1 for respective oligonucleotides). To generate BSG/EMB-MCT1 fusion constructs, respective basigin/embigin variants were inserted upstream of MCT1 using SpeI/PstI restriction sites. Mutations in coding sequences for basigin and MCT1 were introduced via site-directed mutagenesis. All constructs were sequenced for verification.

Additional basigin mutant constructs BSG Ig-I K108,111A and BSG Ig-I R201,203A were generated via site-directed mutagenesis using BSG Ig-I as a template (see Table 2.2 for oligonucleotides, conducted by K. Geistlinger). The basigin constructs BSG Ig-I E114,118, 120,168,172Q (BSG Ig-I Glu→Gln) and BSG Ig-I K108,111,127A / R166,201,203A (Lys,Arg→Ala + R166A) including SpeI and PstI restriction sites were purchased as synthetic DNA fragments (GenScript, Leiden, Netherlands; see section 2.1.1) and inserted upstream of MCT1. The putative salt-bridge associated Arg166 was reintroduced via site-directed mutagenesis generating BSG Ig-I Lys,Arg→Ala (Table 2.2, “BSG Ig-I A166R”, conducted by K. Geistlinger). All constructs were sequenced for verification.

See Figure 3.1 for the protein sequences derived from basigin fusion constructs.

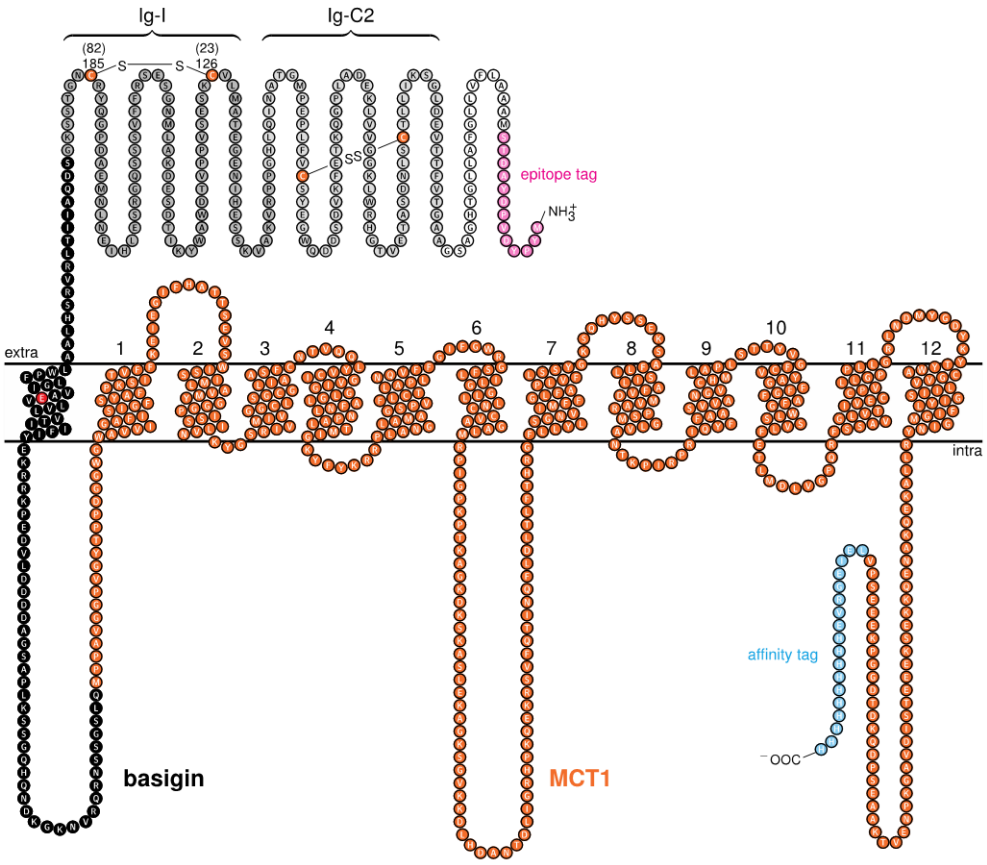

Figure 3.1. Topology and protein sequence of the BSG var2-MCT1 fusion construct. Highlighted are the N-terminal hemagglutinin epitope tag (pink) and the C-terminal His_{10} affinity tag (blue), the cysteine residues forming disulfide bridges in the Ig-like domains Ig-I (dark gray) and Ig-C2 (light gray), and the glutamate in the transmembrane helix of basigin (red). The N-terminal signal peptide present in BSG var2 is shaded white. The expression constructs of this study were generated by truncations at the sites of changed gray levels between the extracellular domains (BSGΔIg, BSG Ig-I, BSG Ig-I/C2, BSG var2); or lacked the basigin fusion altogether (MCT1).

To express fusion constructs with C-terminal green fluorescent protein (GFP) in yeast, the open reading frames were inserted into the SpeI and XhoI-compatible SalI sites of the pUG35 plasmid (Figure 2.1B). For the expression in *P. pastoris*, coding sequences were cloned into the pPink-HC vector using blunted upstream SpeI (coding sequence in pDRTXaLK) or EcoRI (MCS in pPink-HC) and downstream XhoI restriction sites. For the cell-free expression, coding sequences were cloned into the pIVEX2.3w(-GFPΔM1) vectors using SpeI/XhoI restriction sites. For the cell-free expression of the BSG var2-MCT1 fusion protein, the ORF was modified by C. Hansen to introduce a Factor Xa restriction site between basigin and MCT1 (see Master's thesis of C. Hansen for protocol [119]).

3.1.2. Oligonucleotide annealing

To anneal two single-stranded oligonucleotides with complementary sequences, the oligonucleotides were dissolved in double-distilled water (ddH_2O) to a final concentration of 2 µM. An equal volume of both oligonucleotides was combined in a PCR tube (total volume of 50 µl) and annealed using a suitable thermal profile. In a thermocycler, secondary structures were disrupted by heat (95 °C, 2 min) and annealing was achieved by a step-wise decrease of temperature to 8 °C (0.5 °C s^{-1}).

3.1.3. Polymerase chain reaction (PCR)

To amplify specific DNA sequences, to introduce additional restriction sites and to construct individual basigin variants, polymerase chain reactions (PCR) with suitable oligonucleotide primers (Table 2.1) were conducted. 1−2.5 ng of plasmid DNA were used as a template (Table 3.1) for amplification in a thermocycler (Table 3.2). The PCR products were later cloned into target vectors and verified by sequencing.

Table 3.1. Components of standard PCR reactions.

Component	Amount
Plasmid DNA (200-500 µg ml^{-1}, 1:100 diluted)	0.5 µl
dNTPs (2.5 mM each)	4.0 µl
Oligonucleotide primer (25 µM)	each 1.5 µl
OneTaq DNA polymerase (5 U $µl^{-1}$)	0.5 µl
OneTaq Standard Reaction Buffer (5X)	10.0 µl
ddH_2O	ad 50.0 µl

Table 3.2. Thermal profile of standard PCR reactions.

Step	Temp.	Duration	
Initial Denaturation	94 °C	5.0 min	
Denaturation	94 °C	0.5 min	30 cycles
Annealing	*55-70 °C	1.0 min	
Elongation	68 °C	†1−1.5 min	
Final Elongation	68 °C	5.0 min	
Storage	8 °C	∞	

* annealing temperature was calculated with $T_{annealing} = 60 + 0.41 \cdot \mathrm{GC}\,(\%) - (\frac{600}{\mathrm{bp\ (primer)}})$

† depending on product size (1 min per 1-2 kilobases)

3.1.4. Colony-PCR

To confirm the successful integration of plasmids in *P. pastoris*, white colonies of yeast transformants were resuspended in 10 µl ddH_2O. 1.5 µl of resuspended cells were lysed by heat and released DNA was used as a template to perform target insert-specific PCR (Table 3.3, Table 3.4). The successful integration was subsequently evaluated using agarose gel electrophoresis.

Table 3.3. Components of colony PCR reactions.

Component	Amount
Template	1.5 µl
dNTPs (2.5 mM each)	4.0 µl
Oligonucleotide primer “AOX1” (25 µM)	0.5 µl
Oligonucleotide primer “CYC1” (25 µM)	0.5 µl
OneTaq DNA polymerase (5 U $µl^{-1}$)	0.5 µl
OneTaq Standard Reaction Buffer (5X)	10.0 µl
ddH_2O	ad 50.0 µl

Table 3.4. Thermal profile of colony PCR reactions.

Step	Temp.	Duration	
Initial Denaturation	94 °C	5.0 min	
Denaturation	94 °C	1.0 min	30 cycles
Annealing	54 °C	1.0 min	
Elongation	68 °C	†1.0−3.0 min	
Final Elongation	68 °C	5.0 min	
Storage	8 °C	∞	

† depending on product size (1 min per 1-2 kilobases)

3.1.5. Site-directed mutagenesis

In vitro mutagenesis was based on the QuikChange Site-Directed Mutagenesis Kit (Agilent). In short, plasmid DNA encoding the protein of interest was used as a template to conduct a complete plasmid amplification. For site-specific base substitutions, the forward oligonucleotide primers contained respective nucleotide exchanges. The reverse oligonucleotide primers were designed to complementary bind sequences flanking the mutation region. See Table 2.2 for the respective oligonucleotide primer pairs. The plasmid amplification was conducted using the high fidelity *PfuTurbo* DNA polymerase (Table 3.5, Table 3.6).

Table 3.5. Components of PCR reactions for *in vitro* mutagenesis.

Component	Amount
Plasmid DNA (200-500 µg ml^{-1}, 1:100 diluted)	1.0 µl
dNTPs (2.5 mM each)	4.0 µl
Oligonucleotide primer (25 µM)	each 1.5 µl
PfuTurbo DNA polymerase (2.5 U µl^{-1})	0.8 µl
Pfu Standard Reaction Buffer (10X)	5.0 µl
ddH_2O	ad 50.0 µl

Table 3.6. Thermal profile of PCR reactions for *in vitro* mutagenesis.

Step	Temp.	Duration	
Initial Denaturation	94 °C	0.5 min	
Denaturation	94 °C	0.5 min	16 cycles
Annealing	*55-70 °C	1.0 min	
Elongation	72 °C	†~16.0 min	
Final Elongation	72 °C	20.0 min	
Storage	8 °C	∞	

* annealing temperature was calculated with $T_{annealing} = 60 + 0.41 \cdot \mathrm{GC}\,(\%) - (\frac{600}{\mathrm{bp\ (primer)}})$

† depending on product size (1 min per kilobase)

After thermocycling, the PCR products were DpnI-digested to eliminate *E. coli*-methylated template DNA. Subsequently, competent *E. coli* DH5α cells were transformed with the nicked plasmid DNA. Sequences and mutations were confirmed by sequencing and subcloned into verified vectors.

3.1.6. Restriction digest

For the subcloning of PCR products and target sequences, DNA was digested using suitable restriction enzymes. Approximately 1 µg of plasmid DNA / 16 µl of purified PCR product were digested in compatible, commercial buffers using 2−10 U of restriction enzymes (10−20 µl total volume). Usually, digestions were conducted at 37 °C (3 h to overnight). The digestion with non-compatible restriction enzymes was conducted in a two-step process including DNA purification (by PCR Clean-up, see 3.1.9) followed by buffer and digest condition adjustments. For later ligation of non-compatible overhangs, digested sticky ends were blunted by the action of T4 DNA polymerase. In short, sticky overhangs of restriction digests (10 µl) were “filled in” by topping up to a final volume of 20 µl to introduce 5 U of T4 DNA polymerase and dNTP mix (0.25 mM each). The restriction digest buffer conditions were preserved. The reactions were incubated for 5 min at room temperature.

3.1.7. Dephosphorylation of linearized plasmid vectors

To increase the cloning efficiency and avoid background vector re-circulation, the 5'-phosphate ends of linearized vectors were enzymatically removed by the action of FastAP Alkaline Phosphatase. In short, 1 µl (1 U) of phosphatase was added to restriction digests and cleavage was induced by incubation at 37 °C (10 min). Prior to following fragment ligation steps, the phosphatase was heat-inactivated (5 min, 75 °C).

3.1.8. Agarose gel electrophoresis

To visualize and analyze DNA fragments, the samples were separated by size using agarose gel electrophoresis. The gels were prepared by dissolving agarose powder (final 1 % w/v) in 50 ml TAE buffer (1X) in a microwave and adding 1 µl of DNA-intercalating ethidium bromide (10 mg ml^{-1}). The DNA samples were mixed 1:10 with Orange G loading buffer (10X), and up to 20 µl were loaded per lane and separated in an electric field (120 V, 20−40 min). The DNA was visualized by exciting ethidium bromide fluorescence at 312 nm using a UV transilluminator. Fragment sizes were estimated using PstI-digested lambda phage DNA (5 µl per lane) as size standard.

3.1.9. DNA purification and isolation from agarose gels

For the DNA recovery from agarose gel electrophoresis and PCR, the HiYield® PCR Clean-up/Gel Extraction kit was used according to the manufacturer's protocol (Süd-Laborbedarf). For the isolation from agarose gels, gel sections of interest were excised using a scalpel and dissolved according to the producer's guidelines. Purified DNA was finally eluted using 15−20 µl of ddH_2O.

3.1.10. Ligation of DNA fragments

The ligation of sticky and blunt ends after restriction digestions or oligonucleotide annealing with sticky overhangs was based on the enzymatic action of T4 DNA ligase. DNA fragments (e.g. linearized plasmid, ORFs, PCR products, annealed oligonucleotides) with compatible ends were ligated in a final volume of 10 µl of 1X T4 DNA ligase buffer (Table 3.7). The ligation reactions were incubated for 20−30 min at room temperature.

Table 3.7. Components of DNA fragment ligation.

Component	Amount
Plasmid DNA, linearized	1.0 / 3.0 µl
Insert	7.0 / 5.0 µl
T4 DNA ligase buffer (10X)	1.0 µl
T4 DNA ligase (5 U μl^{-1})	1.0 µl

3.1.11. Preparation of competent *E. coli* strains

E. coli competent cells were prepared by technical assistant A. Fuchs using the previously described calcium chloride method. Briefly, *E. coli* DH5α cells were grown overnight on LB agar plates (37 °C) and inoculated in 5 ml liquid LB media. After approximately 9 h, the cells were inoculated in a 100 ml main culture (LB) and incubated overnight at 20 °C on a shaker (200 rpm). The cells were harvested at an optical density (OD_{600}) of 0.4−0.6 by centrifugation (2,000 *g*, 4 °C, 10 min). The cells were resuspended in 30 ml of ice-cold $CaCl_2$-solution (0.1 M) by swirling and gently shaking for 10 min and kept on ice for additional 10 min. The cells were again pelleted (2,000 *g*, 4 °C, 10 min) and resuspended first in 20 ml ice-cold 0.1 M $CaCl_2$ and cooled on ice (20 min), and secondly in 10 ml ice-cold 0.1 M $CaCl_2$ additionally containing 20 % glycerol. The cells were kept on ice for at least 4 h and stored at −80 °C (100 µl aliquots).

3.1.12. Transformation of *E. coli* strains

To amplify and store plasmid DNA, competent *E. coli* cells were transformed with respective plasmids. The competent cells were gently thawed on ice (~3 min), 10 µl of DNA (e.g. ligation reactions) were subsequently added and the cells were incubated on ice (30 min). The transformation was induced by a heat shock (42 °C, 45 s) and the cells were cooled down on ice. 900 µl of LB medium were added and the cells were rotated at 37 °C for 45−60 min. Finally, the cells were centrifuged at maximum speed (21,000 *g*, 30 s), resuspended in 100 µl of supernatant and 50−100 µl were plated and grown on ampicillin-containing LB agar plates.
For the transformation of cells with purified, highly concentrated plasmid DNA, the protocol was simplified. Thawed cells (100 µl) were incubated with 0.5 µl of DNA (15 min, on ice) and immediately plated on selection medium.

3.1.13. Long-term plasmid storage and glycerol stocks of *E. coli* transformants

Cells on solid agar medium were inoculated in 5 ml liquid LB Amp medium, grown overnight (37 °C, under rotation) and stored in 27 % glycerol at −80 °C (1 ml cell culture + 0.5 ml 80 % glycerol).

3.1.14. Plasmid isolation from *E. coli* strains

Small-scale isolation of plasmid DNA (yielding ~10−25 µg) from transformed *E. coli* was done using the Wizard® Plus SV Minipreps DNA Purification kit (Promega). To recover DNA from glycerol stocks, the cells were initially plated on LB Amp agar medium using a sterile pipette tip. Subsequently, single cell colonies from solid medium (glycerol stocks or transformants) were inoculated in 5 ml of liquid LB Amp medium and grown overnight (37 °C, under rotation). Plasmid DNA was finally isolated according to the manufacturer's protocol (the alkaline protease step was skipped) and purified DNA was eluted using 50 µl of ddH_2O.
Large-scale isolation of plasmid DNA (yielding ~50−100 µg) was done with the NucleoBond™ PC 500 kit (Macherey-Nagel). Again, the cells from LB Amp agar plates were inoculated in 5 ml LB Amp liquid media and grown under rotation for approximately 6 h at 37 °C. Subsequently, a 250 ml-main culture was inoculated and incubated overnight on a rotary shaker (37 °C). Finally, plasmid DNA was isolated according to the manufacturer's protocol, and the purified, air-dried DNA was resuspended in 50−100 µl ddH_2O.
DNA concentrations were determined by measuring the absorbance at 260 nm and employing the correlation that an absorbance of A_{260} = 1.0 equals 50 µg ml^{-1} (equation 1).

$$\text{DNA concentration } (\mu g\ ml^{-1}) = 50\ (\mu g\ ml^{-1}) \cdot A_{260} \cdot \text{dilution factor} \quad (1)$$

The DNA purity was evaluated by determining the absorbance ratio A_{260}/A_{280} with ratios of 1.7−2.0 confirming high quality.

3.1.15. Sanger sequencing

The sequencing of distinct DNA segments (PCR, mutagenesis) was either done externally or in-house using the DTCS Quick Start Kit.
For external sequencing, the DNA was diluted to a final concentration of 100 µg ml^{-1} and 3 µl of DNA sample were mixed with 1 µl of a suitable oligonucleotide primer (4.8 µM). The probes were sent to the Institute of Clinical Molecular Biology, Kiel for Sanger sequencing.
In-house sequencing relied on the DTCS Quick Start Kit. Generally, DNA segments were PCR-amplified using suitable oligonucleotide primers as well as deoxynucleotides (dNTPs) and fluorescently labeled dideoxynucleotides (ddNTPs). The incorporation of ddNTPs resulted in synthesis termination giving partially replicated DNA fragments of different size fluorescently

labeled according to the terminating nucleotide. The DNA fragments were size-separated via capillary electrophoresis and sequences were traced back using the DNA Sequencer CEQ™ 8000. Based on the manufacturer's protocol, 50−150 fmoles of DNA in ddH_2O (total volume of 9.5 µl) were preheated in a thermocycler (5 min, 86 °C) and cooled down to 8 °C. Subsequently, the preheated DNA template was mixed with a suitable oligonucleotide primer and DTCS Quick Start Master Mix containing all essential components for sequencing PCR reactions and DNA template extension was finally induced using the depicted thermal profile (Table 3.8, Table 3.9).

Table 3.8. Components of sequencing reactions.

Component	Amount
DNA template, preheated	9.5 µl
Oligonucleotide primer (5 µM)	1.5 µl
DTCS Quick Start Master Mix	2.0 µl

Table 3.9. Thermal profile of sequencing reactions.

Step	Temp.	Duration	
Denaturation	96 °C	20 s	30 cycles
Annealing	50 °C	20 s	
Elongation	60 °C	4.0 min	
Storage	8 °C	∞	

Reactions were stopped by the addition of 5 µl of stop solution/glycogen mixture containing 2 µl of 3 M sodium acetate buffer solution (pH 5.2), 2 µl of 100 mM Na_2-EDTA (pH 8.0) and 1 µl of 20 mg ml^{-1} glycogen on ice. Finally, DNA fragments were precipitated by adding 60 µl of 95 % (v/v) ethanol (ice-cold) and by centrifugation (18,000 *g*, 4 °C, 15 min), and washed twice with 200 µl of 70 % (v/v) ethanol (ice-cold). For each rinse, the samples were centrifuged at 18,000 *g* (4 °C, 5 min). The supernatant was discarded, and the DNA pellet was dried by centrifugation under vacuum (up to 30 min) and resuspended in 30 µl of manufacturer's sample loading solution. The samples were kept at 4 °C until analyzed by technical assistant B. Henke using the DNA Sequencer CEQ™ 8000.

3.2. Recombinant expression and functionality in *S. cerevisiae*

3.2.1. Transformation of *S. cerevisiae*, and storage

For recombinant expression in *S. cerevisiae*, cells were transformed with pDRTXa/pUG35 plasmids encoding the protein of interest using a protocol adapted from the previously described LiAc/single-stranded carrier DNA/PEG method [120].

First, the naive yeast strain was plated on a YPD agar plate and grown for 3-5 days (29 °C). A single colony was inoculated into 5 ml liquid YPD medium and incubated overnight in a rotary shaker (29 °C, 220 rpm). Next day, the cells were inoculated in a 50 ml main culture with an initial OD_{600} of 0.2 and incubated on a rotary shaker (29 °C, 220 rpm) to a final OD_{600} of 0.6. The cells were harvested by centrifugation (2,500 *g*, 4 °C, 5 min) and washed once with 25 ml of sterile water. The cell pellet was resuspended in 1 ml of sterile water and aliquoted (100 µl per transformation). The cells were again pelleted (21,000 *g*, 30 s) and resuspended in 360 µl of transformation mix (Table 3.10). For each transformation, 0.5 µl of target plasmid were added and the samples were mixed by vortexing. Transformation was induced by incubation in a heating block (42 °C, 45−60 min). The transformation mix was removed by centrifugation (21,000 *g*, 30 s) and the cells were resuspended in 1 ml of sterile water. Approximately 100 µl of 1:10-dilutions were finally plated on SD AHLW selection agar and grown for 3-4 days in a 29 °C-incubator.

Table 3.10. Transformation mix.

Component	Amount
PEG 3500 (50 % w/v)	240 µl
LiAc (1 M)	36 µl
Single-stranded carrier DNA (boiled*, 2 mg ml^{-1})	50 µl
Sterile water	34 µl

*Single-stranded carrier DNA was boiled at 100 °C for 5 min prior to use

For the long-term storage of transformed cells, glycerol stocks of transformants were prepared. Single colonies were inoculated in 5 ml liquid SD AHLW medium, grown overnight (29 °C, under rotation) and stored in 40 % glycerol at −80 °C (0.5 ml cell culture + 0.5 ml 80 % glycerol).

3.2.2. Cell culture

To induce recombinant expression and prepare expressing cells for analyses including transport assays, confocal microscopy and flow cytometry, the transformed cells were inoculated in 5 ml SD AHLW and incubated as 20−24 h-precultures. After up to two precultures, 50−100 ml-main cultures were inoculated and grown in SD AHLW medium to a final OD_{600} of 1.0 ± 0.1. Finally, the cells were immediately harvested by centrifugation (4,000 *g*, 4 °C, 5 min) and prepared for further analyses (see sections 3.2.3 to 3.2.15).

3.2.3. Cell lysis and protein extraction from *S. cerevisiae*

To evaluate protein synthesis and expression in yeast, the harvested cell cultures from section 3.2.2 (50 ml-main cultures) were washed once with 50 ml of ice-cold water and once with 10 ml of cold extraction buffer (25 mM Tris, pH 7.5, 5 mM EDTA). For each washing step, the cells were pelleted by centrifugation at 4,000 *g* (4 °C, 5 min). After removal of supernatant, the pelleted cells were frozen at −80 °C for at least 30 min (up to several weeks) and finally resuspended in 0.5 ml of extraction buffer (on ice). Roughly 0.5 g of acid-washed glass beads (~0.5 mm in diameter) were added, and the cells were broken by 10−15 intervals of vortexing (30 s) and cooling down (1 min, on ice). The cell extracts were separated from glass beads by centrifugation (1,000 *g*, 4 °C, 5 min) and transferred to a micro tube. Remaining glass beads and non-broken cells were washed with 0.5 µl of extraction buffer and subject to a second round of 10−15 cycles of vortexing. The cell extracts from both vortexing intervals were combined (total volume of 1 ml) and larger cell compartments and cell debris (mitochondria, nuclei, larger plasma membrane fractions) were separated by centrifugation at 10,000 *g* (4 °C, 5 min). The supernatants were transferred to ultracentrifuge tubes and the microsomal fractions were isolated from cytosolic components by centrifugation at 100,000 *g* (4 °C, 45 min). The isolated fractions were resuspended in 100 µl of solubilization buffer (100 mM sodium phosphate, pH 8.0, 50 mM NaCl) on ice.

3.2.4. Biophysical transport assay using ^{14}C-radiolabeled substrates

The functional analysis of expressing cells was based on the uptake of ^{14}C-radiolabeled substrates via functional transporters. ^{14}C is an instable radioisotope going through radioactive low-energy beta decay to stable ^{14}N with a half-life of 5,730 years [121, 122]. Cells expressing L-lactate-transporting proteins were extracellularly exposed to L-lactate solutions spiked with ^{14}C-labeled L-lactate. Active transporters led to the accumulation of radioisotopes inside the cells and emitted beta particles were quantified by detecting the light emission from excited scintillation molecules (Figure 3.2).

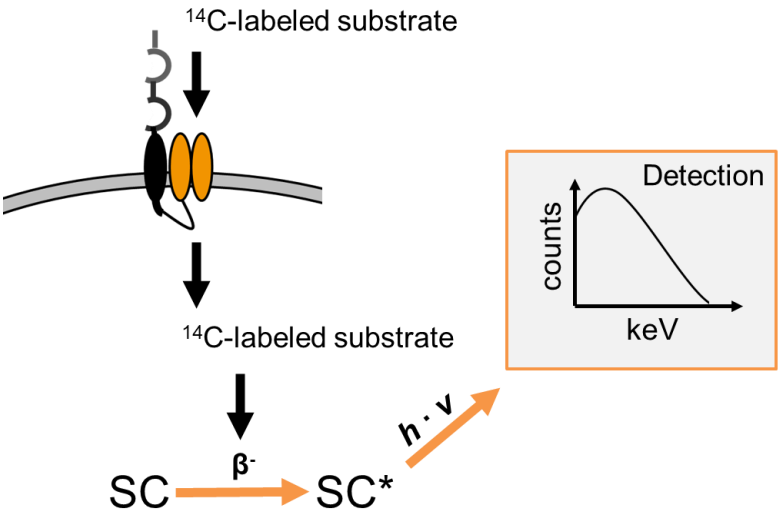

Figure 3.2. Transport assay using ^{14}C-radiolabeled substrates. A ^{14}C-labeled substrate is transported into cells by transporters. Intracellularly accumulated ^{14}C-labeled substrate emits beta particles that excite scintillation (SC) molecules. Excited SC molecules relax under the emission of light. Signals are multiplied by a photomultiplier and detected as counts per minute and kilo-electron volts.

The characterization and evaluation of transport properties of recombinantly expressed proteins in yeast was based on a protocol established in-house by J. Rambow [123] and B. Wu [109]. Generally, uptake experiments were conducted as follows. Specifications for each individual experimental setting are indicated in sections hereinafter. Unless otherwise indicated, harvested cells (see 3.2.2) were washed with 50 ml of ddH_2O and centrifuged (4,000 *g*, 4 °C, 5 min) to remove the supernatant. The dried pellets were kept on ice (0.5 to 3 h) and resuspended in ice-cold HEPES/Tris (50 mM, pH 6.8) or MES/Tris (50 mM, pH 5.8) assay buffer to a final OD_{600} of 50 ± 5 just prior to conducting the uptake assay and kept on ice until the experiment was started. Common to all individual assay methods, 80 µl of cell suspension (± inhibitor/modifying reagent, prewarmed) were subject to 20 µl of substrate solution (5X, in respective assay buffer, spiked with ^{14}C-labeled substrate) in 1.5 ml tubes and mixed by pipetting. The probes were incubated (non-shaken) for various time periods, and the uptake was abruptly stopped by the addition of 1 ml ice-cold water and immediate transfer to GF/C™ glass microfiber filters. The cells were cleared from excess substrate solution by vacuum filtration. To reduce background, substrate adhesion to filters / cells was minimized by washing with 7 ml of ice-cold water. The dried filters were transferred to 3 ml of scintillation cocktail (Quicksafe A, Zinsser Analytic) and the cells were left to dissolve over 20−24 h in scintillation vials. The light emission from scintillation molecules excited by beta particles from ^{14}C-decay was detected via a photomultiplier and events were counted over 2 min using the Scintillation Counter Tri-Carb 2900TR (Packard). Data was collected as counts per minute (cpm) in an energy range of 4−156 keV. In the following sections, the specifications of individual experimental settings are summarized.

3.2.5. Transport parameters, data conversion and normalization

Data collected as counts per minute (cpm) were translated to molar quantities of substrate (in nmol) to estimate the absolute substrate uptake. For each experiment, 20 µl of ^{14}C-spiked substrate solution were transferred to 3 ml of scintillation cocktail to get an estimate of maximal activity resulting from complete substrate uptake into cells. The maximum activity was determined for each individual experiment and was measured in triplicates. The determination of absolute molar quantities per sample (→ nmol) was based on equation 2.

$$\text{substrate (nmol)} = \frac{\text{sample activity (cpm)}}{\text{max. activity (cpm)}} \cdot \text{max. substrate (nmol)} \quad (2)$$

Total molar quantities of substrate were ultimately normalized to the cell mass per sample. To get an estimate, the cells from section 3.2.2 were collected, washed once with 50 ml of sterile water and finally resuspended in sterile water to a final OD_{600} of 40 ± 4 (this equals the final OD_{600} of samples after addition of substrate solution in uptake assays, see section 3.2.4). For accuracy, 1 ml of cell suspension was centrifuged (21,000 *g*, 5 min) and the supernatant was carefully discarded. The cell pellets were weighed and referred to 100 µl sample volumes. The determined weights from a total of 8 samples from 4 individual cell cultures was averaged obtaining a mean of 5.6 mg of cell mass per 100 µl sample volumes in uptake assays. The factor of 5.6 mg was finally used to normalize molar quantities of substrate to 1 mg of cells (→ nmol mg^{-1}).

3.2.6. Substrate uptake over time

To monitor L-lactate uptake over time, cells resuspended in assay buffer of desired pH (see section 3.2.4) were prewarmed to either room temperature (19 ± 1 °C, for 10−15 min) or 30 °C (heating block, for 5 min). Uptake was initiated by a final 1 mM inward gradient of L-lactate (spiked with 0.04 µCi of ^{14}C-labeled L-lactate) and monitored for 0.5 min to 32 min at the given assay temperature. For each time point, the cells were left undisturbed over the respective time span.

The background leakage into cells was estimated by monitoring the uptake of non-expressing cells transformed with empty vectors. The uptake was corrected for filter adhesion by subtracting values determined for 20 µl substrate solution pipetted directly onto filters. For the uptake of expressing cells after each time point, the determined uptake of non-expressing cells was subtracted as background. Uptake-over-time curves were fitted according to the equation $f(t) = a \cdot (1 - e^{-kt})$. Initial transport rates as nmol min^{-1} mg^{-1} were determined as the slope at $t = 0$. Maximal uptake capacities in nmol mg^{-1} result from the determination of the upper limit of each curve ($\lim_{t\to\infty} f(t) = a$). The curves for non-active transporters were fitted linearly. Unless

otherwise indicated, curves depict mean ± SEM (standard error of the mean) of three biological replicates where each replicate itself is an average of duplicate or triplicate measurements. The calculations on the initial transport rate and the uptake capacity result from individual fits for each biological replicate and represent mean ± SEM.
In individual cases (indicated in the respective figure legends), the initial transport rates from mutant constructs lacking a resolved uptake-over-time curve were determined via single time point measurements in the initial phase of transport (2 min for human MCT1-related mutant constructs; 4 min for rat MCT1).

3.2.7. Impact of increasing preparation times on the transport activity of cells

To estimate cell fitness and transport activity drop over time, harvested cells resuspended in assay buffer (pH 6.8) (see section 3.2.4) were prewarmed to RT for 5, 15 and 30 min just prior to conducting the assay. Transport was subsequently initiated by adding substrate solution (1 mM L-lactate spiked with 0.04 µCi ^{14}C-L-lactate) and transport rates were determined by monitoring uptake over 2−4 min. The rates per minute were calculated and averaged as mean ± SEM of three biological replicates each resulting from technical triplicates. The background of non-expressing cells was subtracted.

3.2.8. Determination of intracellular L-lactate concentrations

To estimate achieved intracellular L-lactate concentrations, the correlation of 0.28 nmol mg^{-1} equaling a cytosolic concentration of 1 mM (see results section 4.1.7) determined by A. Jansen was used to translate uptake capacities in nmol mg^{-1} to molar concentrations in mM using equation 3.

$$\text{concentration (mM)} = \text{capacity (nmol mg}^{-1}\text{)} \frac{1\ \text{mM}}{0.28\ \text{nmol mg}^{-1}} \quad (3)$$

The results were averaged as mean ± SEM from the conversion of uptake capacities for each individual biological replicate.

3.2.9. Determination of Michaelis-Menten kinetics

For kinetic measurements, cells resuspended in assay buffer (pH 6.8) (see section 3.2.4) were prewarmed to RT (10−15 min) and zero-trans influx was initiated with inward L-lactate gradients ranging from 1 mM to 10 mM (each supplemented with 0.1 µCi ^{14}C-L-lactate). Transport rates in nmol min^{-1} mg^{-1} were calculated via single time point measurements in the initial phase of transport (2 min for all examined transporters). For each individual concentration, the uptake of non-expressing cells was subtracted as background. Curves were

fitted according to the equation $f(x) = a \cdot (1 - e^{-kx})$. Maximum transport velocities result from the determination of the upper limit of each curve ($\lim_{x\to\infty}(f(x)) = a = v_{max}$). K_m values result from the determination of respective concentrations for $f(x) = 0.5\,a$. The curves depict mean ± SEM of three biological replicates where each replicate itself is an average of duplicate measurements. Calculations on the kinetic parameters result from individual fits for each biological replicate and represent mean ± SEM.

3.2.10. Determination of transport inhibition and IC_{50} values

The protocol for inhibitory studies was adapted from A. Golldack [124]. Cells resuspended in assay buffer (pH 6.8) (see section 3.2.4) were subject to preincubation with several compounds to estimate their inhibitory potential. In general, the compounds were dissolved in suitable solvent (ddH_2O / DMSO) to an 80X stock concentration. In a 1.5 ml-tube, 1 µl of 80X compound solution were joined with 80 µl of cell suspension, mixed by vortexing and preincubated for 15 min. After incubation, L-lactate uptake was immediately determined by single time point measurements in the initial phase of transport dependent on the examined transport protein (see figure legends for details; pH 6.8, RT, 1 mM inward gradient, spiked with 0.04 µCi of ^{14}C-L-lactate). The residual transport activities in % of compound-exposed cells expressing the protein of interest were determined by subtracting the background of non-expressing cells (solvent-exposed; control for 0 % activity) and referring to expressing cells lacking compound treatment (solvent-exposed; 100 % activity).

IC_{50} curves were determined by calculating the % activity after pretreatment with up to six increasing compound concentrations. The % activity for each concentration was measured in technical triplicates and averaged. The mean ± SEM was plotted over compound concentration and resulting curves were fitted according to the Hill equation. The IC_{50} values were calculated as the concentration leading to 50 % of residual activity and were confirmed with three biological replicates.

The compound concentrations and the durations of pretreatment for all tested compounds are summarized in Table 3.11. The final concentration of DMSO was kept at 1.25 %.

Table 3.11. Concentration and solvent of tested compounds.

Compound	Solvent	Stock conc. (80X)	Final conc. (1X)	Duration of treatment
AZD3965	DMSO	800−160,000 nM	10–2,000 nM	15 min
DTT	ddH_2O	80 mM / 800 mM	1 mM / 10 mM	15 min
ACF	ddH_2O	80 mM	1 mM	15 min

3.2.11. Transporter modification by cysteine-reactive agents

The relevance of cysteine residues in MCT1 were investigated by cysteine-modifying compounds including *p*-chloromercuribenzene sulfonate (pCMBS) and methanethiosulfonate (MTS) reagents. Whereas pCMBS targets thiols via its mercurial portion, MTS reagents form disulfides with targetable cysteine residues under mild conditions (Figure 3.3).

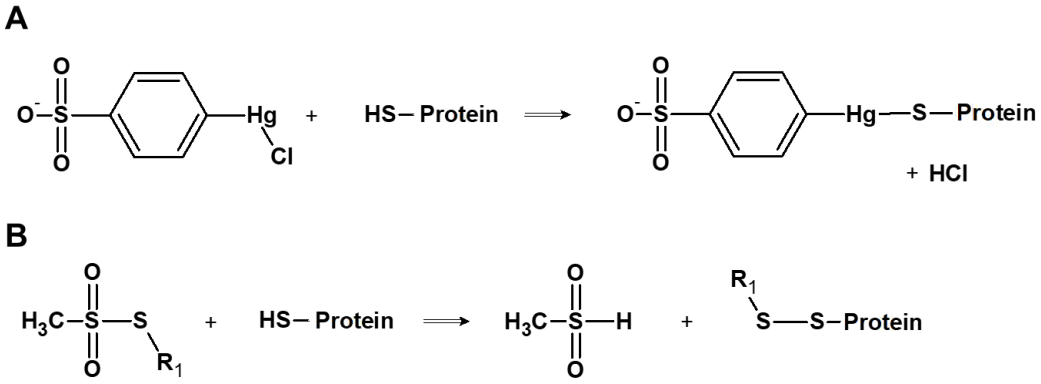

Figure 3.3. Reaction equations of cysteine modification by *p*-chloromercuribenzene sulfonate (pCMBS) **(A)** and methanethiosulfonate (MTS) reagents **(B)**. Residue R_1 defines the transferred group and differs between individual MTS reagents.

According to the supplier (Interchim), the covalent modification with MTS reagents under mild conditions is irreversible in the absence of reducing agents and the complete conversion is usually achieved within 5 min and with concentrations of 1 mM to 10 mM.

In this work, the cysteine modification was done according to the above-mentioned protocol for transport inhibition (see section 3.2.10). A time-dependent inhibition was achieved by pretreatment with compounds for 5−15 min. The concentrations and solvents for all compounds can be found in Table 3.12. L-Lactate transport activity was immediately determined by single time point measurements (see figure legends for details) and at a 1 mM inward gradient of L-lactate (spiked with 0.04 µCi of ^{14}C-L-lactate, pH 6.8, RT). For each treatment duration, controls were treated similarly with compounds substituted by the corresponding solvent.

To test for covalent and irreversible modification via MMTS, the protocol was slightly modified to remove excess reagent prior to determining L-lactate uptake activities. After compound pretreatment for 5 min (1 mM, RT, technical replicates were pretreated in a bulk), the cells were centrifuged at top speed (12,225 *g*, RT, 1 min) and washed twice with respective volumes of assay buffer. The cells were subsequently resuspended in a respective volume of assay buffer (RT), split into 80 µl-aliquots and transport was initiated (1 mM, 0.04 µCi of ^{14}C-L-lactate, pH 6.8, RT). For respective controls, compound treatment was substituted by water.

To examine pCMBS inhibition after the modification with MTS reagents, the cells were first pretreated with MTS reagents (1 mM, RT, 5 min, replicates were treated in a bulk). Excess compound was removed by centrifugation (see above) and the cells were split into 80 µl-aliquots. The cells were subsequently exposed to further treatment with pCMBS (final 30 µM, RT, 15 min) or solvent (100 % controls). For 0 % activity controls (non-expressing cells), both treatment steps were conducted with solvent. Transport activity was again determined with a 1 mM inward gradient of L-lactate (0.04 µCi of ^{14}C-L-lactate, pH 6.8, RT).
In all cases, transport activities in % are averages from three biological replicates (mean ± SEM) with each replicate itself determined in technical triplicates.

Table 3.12. Concentration and solvent of cysteine-modifying reagents.

Compound	Solvent	Stock conc. (80X)	Final conc. (1X)	Duration of treatment
pCMBS	ddH_2O	2.4 mM	0.03 mM	5 / 15 min
MMTS	ddH_2O	80 mM	1 mM	5 / 15 min
MTSES	ddH_2O	80 mM	1 mM	5 min
PMTS	DMSO	80 mM	1 mM	5 min
BMTS	DMSO	80 mM	1 mM	5 min
MTS-4-fluorescein	DMSO	80 mM	1 mM	5 min

3.2.12. Determination of glucose effects on transport

To determine the impact of glucose on L-lactate transport, the cells from 3.2.2 were alternatively washed with 50 ml of 2 % glucose (in ddH_2O) and resuspended in glucose-supplemented assay buffer (2 % glucose, HEPES/Tris 50 mM, pH 6.8). Transport was initiated by adding 1 mM L-lactate (spiked with 0.04 µCi ^{14}C-L-lactate) in the presence of 2 % glucose.
To analyze the direct inhibitory potential of glucose on L-lactate transport, glucose was employed just prior to conducting the uptake assay and according to the general protocol for transport inhibition (see 3.2.10). In short, expressing cells were preincubated (15 min, RT) with 1 µl of 80X glucose stock solution (final concentration 25 mM). Transport was initiated by employing a 1 mM inward gradient of L-lactate (spiked with 0.04 µCi of ^{14}C-L-lactate, RT) and monitored for 2 min (initial phase) and 8 min (equilibrium state).

3.2.13. Phenotypic transport assay (solid and liquid)

To estimate the metabolic turnover of L-lactate and the ability of cells to adapt to glucose-deprived conditions dependent on L-lactate as sole carbon source, cells were initially prepared under glucose-rich conditions as described in section 3.2.2. 1 ml of main culture

(OD_{600} = 1.0 ± 0.1) was harvested and washed twice with 1 ml of sterile water to thoroughly remove excess glucose (centrifugation at 4,000 *g*, 4 °C, 5 min). Finally, the 1 ml-cell suspension was inoculated in 50 ml of 1 % L-lactate medium (MES-buffered to pH 6.0) and incubated at 29 °C in a rotary shaker (220 rpm). The cell growth was monitored by regular OD_{600} determinations over a time span of 9 days.

To evaluate metabolic advantages of cells expressing functional L-lactate transporters when subject to L-lactate as sole carbon source, 20 ml of main cultures prepared in section 3.2.2 were harvested (4,000 *g*, 4 °C, 5 min) and washed twice with 10 ml of sterile water. Collected cell pellets (4,000 *g*, 4 °C, 5 min) were kept on ice for at least 30 min to delay cell proliferation and metabolism and resuspended in sterile water to an OD_{600} of 1.00 ± 0.05. Finally, 5 µl of cell suspensions as well as two serial, ten-fold dilutions were spotted on agar plates supplemented with 2 % L-lactate (MES-buffered to pH 6.8 or pH 5.8) or 2 % glucose (SD AHLW agar plates, growth control) and grown for up to 12 days (29 °C). The plates were visualized using a commercial scanner and images were edited using Photoshop® Elements to improve contrast.

3.2.14. Confocal live-cell imaging of GFP fusion proteins

Confocal live-cell imaging was done in close cooperation with Christine Desel (Institute of Biochemistry, CAU Kiel, Germany). Cells transformed with pUG35 plasmids encoding the protein of interest were prepared as described in section 3.2.2. The cells were harvested and washed with 50 ml of sterile water and the cell pellet was kept on ice until ready for imaging. Just prior to confocal imaging, the cells were resuspended in 1 ml sterile water and transferred to a confocal dish. Proteins with C-terminally fused GFP were imaged at a Leica SP5 confocal microscope system with a HCX PL APO CS 63.0x1.40 OIL objective. For quantification, fluorophores were excited by an argon laser line at 488 nm (14 % LP power). The emission was detected at 500 nm to 540 nm. Z stacks including up to 8 layers were taken in a window of 27.39x27.39 µm and over a depth of 5.879 µm to 7.904 µm (512x512, 8-Bit). Up to five stacks of different regions were imaged for each sample. Estimations on relative transporter amounts at the cell surface were done using the ImageJ 1.52p software (Java 1.8.0_172). Layers capturing cells in a central plane were chosen from each stack. The mean gray value per pixel (normalized to 1 µm depth) of single cells was determined on a line manually drawn on the cellular border as determined by corresponding bright field images. At least ten individual cells of highest intensities and up to five different areas were analyzed and averaged to obtain an averaged mean gray value per pixel on the cellular surface. The amounts of transporter present at the cell surface were derived from confocal GFP intensity of the basigin fusion constructs relative to unfused MCT1 of which the mean gray value per pixel at 1 µm confocal depth was set to 1.

3.2.15. Flow cytometry

The protocol for flow cytometric (FC) analyses was modified from [125]. The harvested cells from section 3.2.2 (50 ml-main cultures) were washed once with 10 ml PBS and the pellets were cleared from supernatant by centrifugation (4,000 *g*, 4 °C, 5 min). The cells were kept on ice for at least 30 min to delay cell proliferation and were finally resuspended in 20 ml of FC buffer (1 % BSA in PBS). The number of cells was determined by OD_{600} measurements (with OD_{600} = 1 equaling $1.6 \cdot 10^7$ cells ml^{-1}, correlation determined by J. Rambow) and $2 \cdot 10^6$ cells (non-expressing cells, i.e. controls lacking primary antibody treatment) or 10^7 cells ((non-)expressing cells with primary antibody treatment) were transferred to 1.5 ml-tubes. The cell suspensions were cleared by centrifugation (4,000 *g*, 4 °C, 5 min) and resuspended in FC buffer ± primary antibody (orb312305, 1 µg per sample) to a final volume of 100 µl. The samples were incubated on ice for 50 min. The cells were again cleared from excess antibody (4000 *g*, 4 °C, 5 min) and washed twice with 1 ml of FC buffer. The cells were resuspended in FC buffer ± APC-conjugated secondary antibody (Goat anti-Rabbit IgG, 4050-11S, 1 µg per sample) to a final volume of 100 µl and incubated for 50 min under the exclusion of light (on ice). The cells were washed twice with 1 ml PBS and finally resuspended in 500 µl PBS. The samples were transferred to FC tubes, analyzed in cooperation with S. Riethmüller (Pharmaceutical Biology, CAU Kiel) using the Gallios 3L Flow Cytometer, and evaluated using the Kaluza Analysis software.

3.3. Recombinant expression in *P. pastoris*

3.3.1. Preparation of plasmid DNA for transformations

For the transformation of *P. pastoris* strains, the target plasmid DNA (pPink-HC vector including the coding DNA for the protein of interest) was prepared by linearization. In short, 10 µg of purified plasmid DNA were digested with SpeI restriction enzyme in a total volume of 30 µl (30 U, 37 °C, overnight). The digestion was stopped by adding 8 µl of 100 mM Na_2-EDTA (pH 8.0; final concentration: 20 mM) in a final volume of 40 µl. The linearization was evaluated by agarose gel electrophoresis. DNA was finally precipitated by adding 4 µl of 3 M sodium acetate buffer solution (pH 5.2) and 100 µl of ethanol (95 %) and centrifugation (21,000 *g*, 4 °C, 15 min). The DNA was purified by gentle rinsing with 100 µl of 70 % ethanol done twice. The DNA was carefully cleared from supernatant and dried by vacuum centrifugation for approximately 30 min. The linearized DNA was resuspended in 10 µl of ddH_2O and stored at −20 °C until usage.

3.3.2. Transformation of *P. pastoris* by electroporation, and storage

The protocol for transformation of *P. pastoris* strains was adapted from the PichiaPink™ Expression System (Invitrogen). The commercially purchased native strains were first streaked on YPD complete medium and cultivated for 3−5 days (29 °C) for distinct colony formation. Around 1−3 colonies were inoculated in precultures of 5−10 ml of respective medium and grown for 20−24 h (29 °C, 220 rpm, rotary shaker). The precultures were used to inoculate main cultures (100 ml, 1 l-flask) and were grown to an optical density OD_{600} of 1.3−1.5 (16−20 h, 29 °C, 220 rpm). The cell cultures were harvested by centrifugation (1,500 *g*, 4 °C, 5 min) and washed first with 250 ml, and second with 50 ml of ice-cold, sterile water. For each step of washing, the cells were cleared from supernatant by centrifugation (1,500 *g*, 4 °C, 5 min). The cells were subsequently washed with 10 ml of ice-cold sorbitol (1 M) and finally resuspended in 0.3 ml thereof. In a micro tube, 80 µl of prepared cells were mixed with 10 µl of linearized target plasmid (see above), transferred to a precooled electroporation cuvette, and kept on ice for 5 min. The cells were instantly pulsed in an electroporator for approximately 4−5 ms (200 Ω, 2 kV, 25 µF). The cells were immediately supplied with 1 ml of YPDS medium and incubated for 2−4 h inside the cuvettes (29 °C). Finally, 100−300 µl of pulsed cells were plated on SD selection agar and incubated for 3−10 days (29 °C). Single white colonies from transformations were again streaked on SD plates to achieve proper colony separation. The plasmid integration was confirmed by colony PCR (see section 3.1.4) and suitable colonies were used for induced protein production by *P. pastoris*.

For the long-term storage of successful transformants, single colonies were inoculated in 10 ml of YPD medium, cultivated for 20−24 h (29 °C, 220 rpm) and used to inoculate

100 ml-main cultures (in YPD). The cultures were grown to an OD_{600} of 2.0−2.5 (29 °C, 220 rpm) and harvested by centrifugation (1,500 g, 4 °C, 5 min). The harvested cells were resuspended in 25 % glycerol (in YPD) to a final OD_{600} of 100 and stored at −80 °C.

3.3.3. Cell culture and induction of gene expression

The protocol for induction of gene expression in *P. pastoris* was again adapted and modified from the PichiaPink™ Expression System (Invitrogen). For inducing gene expression and protein synthesis in transformed *P. pastoris* cells, single colonies of successful transformants (see sections 3.1.4 and 3.3.2) were picked and inoculated in precultures of 10 ml glycerol-based BMGY medium (29 °C, 220 rpm, 20−24 h).

For small-scale production of BSG var1-MCT1 fusion protein, the cells were inoculated in 50 ml-main cultures and grown to an OD_{600} of 5.0 ± 0.5 (identical growth conditions). The cells were harvested by centrifugation (1,500 *g*, RT, 5 min) and resuspended in 50 ml of methanol-based BMMY medium to induce protein production (OD_{600} = 2 at induction; 500 ml-flasks).

For medium-scale production of MCT1 alone and under optimized growth and induction conditions, precultures from above were used to inoculate 200 ml-main cultures. The cells were grown to an OD_{600} of 2.0 ± 0.1, harvested (1,500 *g*, RT, 5 min) and resuspended in 40 ml of methanol-based BMMY medium to induce protein production (OD_{600} = 10 at induction; 500 ml-flasks).

After 24 h, methanol was added to a final concentration of 0.5 % to compensate for metabolization and vaporization. The cells were finally harvested 30−40 h after induction of protein biosynthesis by centrifugation (4,000 *g*, 4 °C, 5 min) and the protein production was evaluated by cell lysis (see section 3.3.4) and protein detection methods.

3.3.4. Cell lysis and protein extraction from *P. pastoris*

To evaluate protein production in the *P. pastoris* expression system, the protein extraction protocol was adapted from *S. cerevisiae* (see section 3.2.3). Due to larger cell cultures and higher obtained cell masses, the procedure was upscaled and the cells were resuspended in 1 ml (small scale) or 2 ml (medium scale) of extraction buffer and cell breakage was done with 1 g (small scale) or 2 g (medium scale) of acid-washed glass beads. All other steps remained unaltered.

3.4. Protein synthesis by detergent- and nanodisc-based cell-free techniques

3.4.1. General strategy for cell-free protein synthesis

Cell-free synthesis of proteins in the continuous exchange cell-free (CECF) system was adapted from [116] and established in the Beitz lab by A. Müller-Lucks [112] and S. Bock [114]. The expression in the CECF system uses two compartments separated by a semipermeable membrane. The gene transcription as well as the translation take place in the reaction mixture (RM) compartment and the diffusion of low-molecular weight compounds across the membrane allows continuous exchange of limited reaction precursors and amino acids from and constant removal of reaction-impeding byproducts to the feeding mixture (FM) compartment. During cell-free synthesis, membrane proteins demand solubilization of transmembrane domain structures for stabilization and proper folding.

The CECF system used in this work relied on the *in vitro* transcription and translation from plasmid vectors pIVEX2.3w and pIVEX2.3w-GFPΔM1 encoding the gene of interest. The gene expression was under the control of the T7 promoter from T7 bacteriophage and is only induced in the presence of the T7 RNA polymerase. The necessary cell machinery (i.e. ribosomes and transcription/translation factors) for *in vitro* protein synthesis was obtained by the fermentation of *E. coli* BL21 (DE3) cells and the sedimentation of cell extracts at 30,000 *g* (S30 extract). The S30 extracts were kindly provided by L. Petersen and B. Höger and the protocols are described in detail elsewhere [112].

The protein solubilization was achieved by detergent-based (D-CF) and nanodisc-assisted (ND-CF) cell-free protein synthesis. The nanodiscs were produced by C. Hansen as part of his Master's thesis and the methodic development and realization are described in detail therein [119]. In general, the protocol for preparation and assembly was adapted from Rues *et al.* [117]. The nanodiscs were produced using recombinantly expressed membrane scaffold protein 1E3D1 (MSP1E3D1) to encapsulate the anionic lipids 1,2-dioleoyl-*sn*-glycero-3-phospho-(1'-*rac*-glycerol) (DOPG) or 1-palmitoyl-2-oleoyl-*sn*-glycero-3-phospho-(1'-*rac*-glycerol) (POPG) with a final nanodisc diameter of 12.1 nm [126, 127]. The assembled nanodiscs were added to the CECF protein synthesis reactions for co-translational reconstitution. The nanodisc-based cell-free protein synthesis of MCT1 constructs in this study was done in close cooperation with C. Hansen and in equal participation.

3.4.2. Cell-free protein synthesis (analytical scale)

The cell-free protein synthesis in an analytical scale allowed for estimations on optimal methodical conditions and detergent/nanodisc concentrations for an ideal protein reconstitution and solubilization. To evaluate successful reconstitution, GFP fusion proteins (pIVEX2.3w-GFPΔM1 plasmids) were synthesized with C-terminal GFP serving as an indicator

for proper protein folding [113]. The reaction chambers for CECF synthesis in analytical scale were adapted from [116] and designed in-house. A small cylindric container was sealed at the lower end with a dialysis membrane (14 kDa MWCO, hydrated in sterile ddH_2O) secured by a small Teflon ring and served as the reaction mixture compartment. This compartment was mounted in 12-well plates containing the feeding mixture and allowed contact of both compartments via the semipermeable membrane. The reaction (RM) and feeding mixtures (FM) were prepared on ice according to Table 3.13 and Table 3.14.

Table 3.13. Pipetting scheme for CECF synthesis in an analytical scale. Listed volumes are exemplary for a total of (10+1) tested conditions and were accordingly adjusted for different sample amounts.

	Stock conc.	Final conc.	Volume (µl)
MM-M			
NaN_3	10 %	0.05 %	50.8
PEG 8000	40 %	2 %	508.3
KOAc	4000 mM	150.8 mM	383.2
$Mg(OAc)_2$†	1000 mM	5.1 mM	51.8
HEPES/EDTA buffer	24X	1X	372.7
COmplete™ protease inhibitor	50X	1X	203.3
Folinic acid	10 mg ml^{-1}	0.1 mg ml^{-1}	101.7
DTT	500 mM	2.0 mM	40.7
NTP	75X	1X	135.5
PEP	1000 mM	20 mM	203.3
AcP	1000 mM	20 mM	203.3
20-Amino acid mix	4 mM	0.5 mM	1270.6
6-Amino acid mix (RCWMDE)	16.67 mM	1 mM	609.9
Final volume			4135.1
MM-R			
MM-M			290.9
DNA template*	variable	0.015 mg ml^{-1}	X
tRNA (E. coli)	40 mg ml^{-1}	0.7 mg ml^{-1}	12.5
T7 RNA polymerase	350 U $µl^{-1}$	15.0 U $µl^{-1}$	30.6
RiboLock RNase inhibitor	40 U $µl^{-1}$	0.3 U $µl^{-1}$	5.4
Pyruvate kinase	10 mg ml^{-1}	0.08 mg ml^{-1}	5.7
S30 extract	1X	0.35X	250.3
ddH_2O (sterile)			ad 715.0‡
MM-F			
MM-M			3844.2
20-Amino acid mix	4 mM	1.05 mM	1299.0
S30 buffer	1X	0.35X	3308.0
ddH_2O (sterile)			ad 9450.0

*For analytical scale, pIVEX2.3w-GFPΔM1 plasmids were used as template. The DNA template volumes used varied among plasmid preparations. †The optimal magnesium concentration for the S30 extract was determined beforehand by L. Petersen and B. Höger and adjusted to 10 mM. The final K^+ concentration was set to 290 mM. ‡ddH_2O was only added in the detergent-based cell-free protein synthesis.

Table 3.14. Preparation of reaction (RM) and feeding mixes (FM) including detergent/nanodisc supplementation. Listed volumes are exemplary for duplicate tests of each condition.

Detergents					
	Brij®35 (5 %)	Brij®58 (15 %)	Brij®78 (15 %)	Brij®98 (5 %)	DDM (2.5 %)
Final conc. (%)	0.2	1.5	0.8	0.2	0.1
RM					
MM-R (µl)	118.4	118.4	118.4	118.4	118.4
Detergent (µl)	5.2	13.0	6.9	5.2	6.5
ddH_2O (sterile)	ad 130 µl				
FM					
MM-F (µl)	1614	1614	1614	1614	1614
Detergent (µl)	72.0	180.0	96.0	72.0	72.0
ddH_2O (sterile)	ad 1800 µl				

Nanodiscs*							
	DOPG-ND (320 µM)			POPG-ND (290 µM)			Brij®78 (15 %)
Final conc. (µM)	15	30	60	15	30	60	0.8 %
RM							
MM-R (µl)	99.7	99.7	99.7	99.7	99.7	99.7	99.7
Nanodiscs / detergent (µl)	6.1	12.2	24.4	6.7	13.5	26.9	6.9
ddH_2O (sterile)	ad 130 µl						
FM							
MM-F (µl)	1614	1614	1614	1614	1614	1614	1614
Nanodiscs / detergent (µl)	-	-	-	-	-	-	96
ddH_2O (sterile)	ad 1800 µl						

*MSP1E3D1-DOPG/POPG-nanodiscs were produced and kindly provided by C. Hansen. The nanodiscs were only added to the RM.

Generally, a shared master mix containing components for both mixes (MM-M) was prepared. The individual master mixes for reaction and feeding mixes (MM-R and MM-F) were prepared by completing MM-M master mixes by specific compounds. For testing the reconstitution with different detergent and nanodisc concentrations, respective MM-F and MM-R mixes were supplemented with varying amounts of detergent/nanodiscs (Table 3.14).

For each test condition, 55 µl of finalized reaction mixture were gently pipetted onto the semipermeable membrane in the reaction mixture chamber and immerged air-bubble free in 850 µl of feeding mixture (volume FM:RM at 15:1). The reaction chambers were covered with parafilm and the protein synthesis was started by incubation at 30 °C in a shaking water bath (20−24 h). After synthesis, the reaction mixtures were transferred to a micro tube and kept on ice for roughly 1 h to finalize protein folding.

3.4.3. Cell-free protein synthesis (preparative scale)

The CECF protein synthesis in a preparative scale was again adapted from [116] and the protocol and reaction chambers from analytical scale were upscaled for the synthesis of larger protein yields and further structural analysis of proteins. The reaction mixture volumes were adjusted for a total volume of 0.7−1.0 ml. For a preparative scale, pIVEX2.3w plasmid vectors encoding MCT1 constructs without C-terminal GFP were used as the DNA template.

The reaction chambers containing the feeding mixture were constructed in-house and were built to fit Slide-A-Lyzer™ dialysis cassettes (10 kDa MWCO, 3 ml) that served as the reaction mixture compartment. The feeding (15.3−17.0 ml) and reaction mixtures (0.7−1.0 ml) were pipetted into the respective compartments (volume FM:RM at 22:1−17:1) and were incubated for 20−24 h at 30 °C in a shaking water bath. The reaction mixture was transferred to 15 ml-tubes and kept on ice for roughly 1 h. Pipetting schemes for the preparation of the reaction and feeding mixtures are summarized in Table 3.15.

Table 3.15. Pipetting scheme for CECF synthesis in a preparative scale. Listed volumes are exemplary for a final reaction mixture volume of 1 ml and were accordingly adjusted for different sample volumes.

	Stock conc.	Final conc.	Volume (µl)
MM-M			
NaN_3	10 %	0.05 %	90.0
PEG 8000	40 %	2 %	900.0
KOAc	4000 mM	150.8 mM	678.6
$Mg(OAc)_2$†	1000 mM	5.1 mM	91.8
HEPES/EDTA buffer	24X	1X	660.0
COmplete™ protease inhibitor	50X	1X	360.0
Folinic acid	10 mg ml^{-1}	0.1 mg ml^{-1}	180.0
DTT	500 mM	2.0 mM	72.0
NTP	75X	1X	240.0
PEP	1000 mM	20 mM	360.0
AcP	1000 mM	20 mM	360.0
20-Amino acid mix	4 mM	0.5 mM	2250.0
6-Amino acid mix (RCWMDE)	16.67 mM	1 mM	1080.0
Detergent (Brij®78)	15 %	0.8 %	‡960.0 / 0.0
Final volume			‡8282.4 / 7322.4
MM-R (→RM)			
MM-M			‡460.1 / 406.8
DNA template*	variable	0.023 mg ml^{-1}	X
tRNA (E. coli)	40 mg ml^{-1}	0.7 mg ml^{-1}	17.5
T7 RNA polymerase	350 U $µl^{-1}$	15.0 U $µl^{-1}$	42.9
RiboLock RNase inhibitor	40 U $µl^{-1}$	0.3 U $µl^{-1}$	7.5
Pyruvate kinase	10 mg ml^{-1}	0.08 mg ml^{-1}	8.0
S30 extract	1X	0.35X	350.0
Nanodiscs	220 µM	30 µM	‡136.4
ddH_2O (sterile)			ad 1000.0
MM-F (→FM)			
MM-M			‡7822.3 / 6916.0
20-Amino acid mix	4 mM	1.05 mM	2338.0
S30 buffer	1X	0.35X	5950.0
ddH_2O (sterile)			17000.0

*For preparative scale, pIVEX2.3w plasmids were used as template. The DNA template volumes used varied among plasmid preparations. †The optimal magnesium concentration for the S30 extract was determined beforehand by L. Petersen and B. Höger and adjusted to 10 mM. The final K^+ concentration was set to 290 mM. ‡For the detergent-based synthesis, Brij®78 was used and added to RM and FM (in MM-M). For the respective reactions of nanodisc-assisted synthesis, MSP1E3D1-POPG nanodiscs (provided by C. Hansen) were only added to the RM. The volumes for both approaches are indicated and separated by a slash.

3.4.4. Immobilized metal affinity chromatography (IMAC)

For the purification of proteins carrying a C-terminal His-tag, a Ni^{2+}-NTA affinity chromatography was carried out. The preparation of used purification buffers and respective specifications of individual buffers for detergent- or nanodisc-based analytical and preparative CECF synthesis are listed in detail in section 2.6.6.

For the purification of synthesized protein in the analytical scale, 15 µl of Ni^{2+}-NTA agarose bead slurry were transferred to purification columns (column volume: 7.5 µl) and washed twice with 1 ml of 1X purification puffer. The beads were suspended in 0.4−0.5 ml of 1X purification buffer and mixed with the reaction mixtures from the analytical CECF synthesis. The protein binding to Ni^{2+}-NTA beads was achieved overnight (4 °C, under rotation). In purification columns, the beads were cleared from the purification buffer and the respective flow through was collected. The beads were washed twice with 75 µl of 20 mM imidazole-containing purification buffer to elute non-specifically bound proteins. The beads were finally incubated with (15 min, RT) and the protein was eluted by 80 µl of 400 mM imidazole-containing purification buffer. The remaining beads were finally suspended in 80 µl of 1X purification buffer and collected as the bead fraction.

For the purification of synthesized protein in the preparative scale, 300 µl of Ni^{2+}-NTA agarose bead slurry were transferred to Poly-Prep® chromatography columns (column volume: 150 µl; Bio-Rad) and washed twice with 1 ml of 1X purification buffer (no detergent). The beads were suspended in 4 ml of 1X purification buffer, added to the reaction mixtures from the preparative CECF synthesis and the samples were incubated overnight (4 °C, under rotation). In Poly-Prep® chromatography columns, the beads were cleared from purification buffer and the flow through was collected. For stepwise purification, the beads were first washed with 3 ml of 20 mM imidazole-containing purification buffer and finally with 0.75 ml of purification buffers of increasing imidazole concentrations (60−400 mM). The remaining beads were suspended in 0.75 ml of 400 mM imidazole-containing purification buffer and collected as the bead fraction. The collected fractions were finally denatured with SDS and evaluated by SDS-PAGE and in-gel fluorescence, Coomassie staining or Western blotting, or further purified by size-exclusion chromatography for structural analyses.

3.4.5. Size-exclusion chromatography (SEC)

The protein purification with size-exclusion chromatography was carried out with the ÄKTApurifier™ and a Superdex 200 10/30 GL column.

Prior to injection, the fractions from IMAC including the highly purified protein of interest were merged and diluted with purification buffer to decrease the total imidazole concentration to below 100 mM. The protein was concentrated by centrifugation at 5,000 *g* (4 °C, 5 min) to a final volume of roughly 0.5 ml using Amicon Ultra-4 PLTK Ultracel-PL membranes (Merck)

yielding concentrations of roughly 0.6−2.2 mg ml^{-1}. The protein samples were centrifuged at 10,000 *g* (4 °C, 10 min) to precipitate aggregates and larger particles, and finally injected for size-exclusion chromatography (flow rate: 0.35 ml min^{-1}; eluent: 20 mM Tris, pH 8.0, 150 mM NaCl (+ 0.05 % Brij®78)). The protein was detected by absorbance at 280 nm.

3.4.6. Transmission electron microscopy (TEM)

For the structural elucidation by negative-staining room temperature transmission electron microscopy (TEM), fractions from SEC were collected and analyzed by P. Arnold (Anatomical Institute, CAU Kiel) [128].

The samples were transferred to negative flow discharged continuous carbon grids and excess volume was removed. The probes were negatively stained with 1 % (w/v) uranyl acetate solution and air-dried. Images were obtained at 50,000-fold magnification (2048 x 2048 pixels) using the JEOL JEM-1400 Plus electron microscope (acceleration voltage at 100 kV) and a TVIPS F416 4 kx4 k camera. Single particles were analyzed using the EMAN2 image processing suite [129] and categorized into class-sums. The class-sum images contained 128 x 128 pixels with an edge length of 4.58 Å per pixel.

3.5. Further protein methods

3.5.1. Determination of protein concentrations

To quantify protein amounts and yields in cell lysates as well as after cell-free protein synthesis, the Quick Start™ Bradford Protein Assay (Bio-Rad) was used. In short, 2-8 µl of protein-containing samples were diluted with ddH_2O (final volume of 800 µl) and mixed with 200 µl of Roti®-Quant concentrate (5X). The samples were mixed by vortexing and incubated for 5 min at RT. The absorbance of samples against the zero value (solubilization buffer instead of protein sample) was measured at 595 nm. The quantification of protein amounts was based on a calibration curve of BSA standard solutions ranging from 1−14 µg ml^{-1}.

3.5.2. SDS-PAGE

Protein samples were size-separated by discontinuous, vertical sodium dodecyl sulfate polyacrylamide gel electrophoresis (SDS-PAGE).
Polyacrylamide gels were produced in-house between a glass and a ceramic plate separated by spacers. First, a separation gel (see Table 3.16, pH 8.8, 12.5 % acrylamide) was cast into the mold and sealed by isopropyl alcohol. After polymerization, the alcohol was removed and the stacking gel was cast onto the separation gel (see Table 3.16, pH 6.8, 6 % acrylamide). A sample comb was inserted to generate sample pockets (10-12 pockets per gel). After complete polymerization, the comb was removed, and the gel was covered with electrophoresis buffer. For protein sample preparation and denaturation, the samples were mixed 3:1 with 4X SDS-containing sample loading buffer and incubated for 30 min at 37 °C. The prepared samples (2−30 µl, depending on pocket size and sample protein concentrations) were loaded into the gel pockets and concentrated in the stacking gel (160 V, 10−15 min). The proteins were finally size-separated by migration in an electric field (200 V, 75−90 min). As a molecular weight size marker, 5 µl of prestained PeqGOLD Protein Marker III (Peqlab) were loaded. After separation, the gels were removed from the electrophoresis chamber, the stacking gel was detached and proteins were detected in the separation gel using several staining and visualization methods (see sections 3.5.3, 3.5.4 and 3.5.5).

Table 3.16. Preparation of separation and stacking gels (for two gels).

Component	Stacking gel	Separation gel
ddH_2O	2.4 ml	5.25 ml
stacking gel / separation gel buffer (4X)	1 ml	3 ml
ROTIPHORESE® Gel 40	0.6 ml	3.75 ml
TEMED	6 µl	10 µl
APS (10 %)	25 µl	80 µl

3.5.3. In-gel fluorescence detection

Protein samples including GFP fusion proteins were analyzed with in-gel fluorescence to evaluate the correct folding of synthesized proteins [113]. Gels from SDS-PAGE were transferred to thin glass plates and imaged with the Chemostar Touch ECL & Fluorescence Imager (INTAS Science Imaging Instruments, Göttingen) or the Lumi Imager™ F1 (Roche Diagnostics, Mannheim) by an excitation at 475 nm and the detection of fluorescence emission at 520 nm.

3.5.4. Coomassie staining

For the unspecific detection of proteins in gels from SDS-PAGE, the gels were submerged in Rotiphorese® Blue R solution and incubated for roughly 1 h (RT, under shaking). The gels were washed with destaining solution (10−30 min, RT, under shaking) to decrease background staining and finally rinsed with ddH_2O (up to several hours) to sharpen the protein bands. The gels were visualized with a commercial scanner and images were modified by Photoshop® Elements to optimize contrast.

3.5.5. Western blot

For the specific detection of target proteins, the gels from SDS-PAGE were blotted onto PVDF membranes in a semi-dry procedure. The gels and methanol-activated (30 s) PVDF membranes were stacked between three layers of Whatman™ papers and soaked in transfer buffer. Blotting occurred in an electric field (17 V) for 60 min. The PVDF membranes carrying the transferred protein bands were subsequently submerged in 20 ml of 3 % milk powder in TBS-T (1 h, RT, under shaking) to block non-specific binding of antibodies. The blots were incubated with 10 ml of a dilution of protein-specific primary antibody overnight (4 °C, under shaking), rinsed three times with 10−15 ml of TBS-T (15 min per rinse, RT) and finally incubated with 10 ml of a dilution of horseradish peroxidase (HRP)-conjugated secondary antibody (1 h, RT, under shaking). All antibodies were diluted in 3 % milk powder in TBS-T (Penta-His antibody, 1:5,000; GFP antibody, 1:10,000; Goat anti-Mouse, 1:5,000; Goat anti-Rabbit, 1:10,000). The blots were again rinsed three times and coated with 1 ml of Clarity™ ECL Western blotting substrate (1:1, Bio-Rad). The luminescence was finally detected using the Chemostar Touch ECL & Fluorescence Imager (INTAS Science Imaging Instruments, Göttingen) or the Lumi Imager™ F1 (Roche Diagnostics, Mannheim). For the manual detection and film exposure (*P. pastoris*-related Western blots), ECL chemiluminescence films were pressed onto Western blots in a commercial CAWO ABS cassette and the exposure times were manually adjusted. The exposed films were submerged in G153 developer and fixation solutions (Agfa-Gevaert, Mortsel, Belgium), dried and scanned for further analysis.

3.6. Bioinformatics and statistics

3.6.1. Sequence analysis, topology plots and protein structure models

The DNA and protein sequences for analyses and sequence alignments were derived from the NCBI gene and protein databases, respectively [130]. Sequences were aligned using the respective tools in the NCBI database (BLAST, https://blast.ncbi.nlm.nih.gov/Blast.cgi, [130, 131]) or in the Universal Protein Resource (Uniprot, https://www.uniprot.org/align/, [132]). The topology plots were generated in TEXtopo [133]. The protein structure data for SfMCT (PDB #6HCL [54]), human MCT2 (PDB #7BP3 [55]), basigin (PDB #3B5H [76]), and MCT1 (PDB #7CKO and PDB #6LZ0 [103]) were received from the RCSB Protein Data Bank [134, 135] and visualized with the PyMOL Molecular Graphics System, Version 1.7.4.1 (Schrödinger, LLC.) and the Chimera 1.14 software [118]. The MCT1 structure models were calculated using SWISS-MODEL [136, 137].

3.6.2. Calculation of surface potentials

The calculations of the electrostatic surface potential were done using the PDB structure file #3B5H [76] for the extracellular domain of basigin variant 2. For the Poisson-Boltzmann electrostatics, the PDB2PQR [138, 139] and APBS tools [140] were used from within Chimera. The pH was set to 7.0, the protonation state assignment was done by PROPKA, and the PARSE forcefield was applied. Visualization was done using the Chimera 1.14 software [118].

3.6.3. Data evaluation and statistics

The data handling for individual experiments is described in detail in each chapter. Generally, the biological triplicates from yeast experiments represent three independent yeast transformations. The technical replicates represent repetitions within the same experiment. The curve fittings were done with SigmaPlot (Systat Software) and the individual equations are stated in the corresponding chapters. Statistical significance was tested by unpaired, two-tailed t-tests with significance indicated as *$p < 0.05$, **$p < 0.01$ and ***$p < 0.001$.

4. Results

4.1. Basigin acts as an extracellular proton and substrate antenna and drives intracellular L-lactate accumulation via monocarboxylate transporter 1

Basigin acts as a chaperone to guide human monocarboxylate transporter 1 (MCT1) to the plasma membrane. Additionally, basigin has been suggested as a direct modulator of transport via MCTs although commonly used expression systems and techniques failed to confirm previous speculations. In this study, human MCT1 alone and in fusion with several distinct basigin variants were expressed in *Saccharomyces cerevisiae* to elucidate basigin effects at the domain level. Generally, an expression in *S. cerevisiae* profits from an easy-to-handle and easy-to-manipulate expression system that has already been shown to express monocarboxylate transporters at the plasma membrane even in the absence of an accessory protein [88, 104]. Moreover, a suitable Δ*jen1* Δ*ady2* knock out strain is devoid of endogenous monocarboxylate transporters [105, 106] and – by nature – homologs of the basigin family [107]. To evaluate and compare transport characteristics of MCT1 with and without fusion to basigin, a radiolabeling-based technique was used to investigate L-lactate uptake capacities in the equilibrium state, transport velocities and Michaelis-Menten kinetics.

4.1.1. Expression of human MCT1 in *S. cerevisiae*

For the expression of human monocarboxylate transporter 1 in *S. cerevisiae*, the open reading frame (ORF) was cloned into a pDRTXa expression vector (see section 2.1.2) that allows for constitutive expression from the *pma* (plasma membrane H^+-ATPase) promoter. The transformation of cells resulted in the expression of functional transporter even in the absence of an accessory protein (Figure 4.1A−C). MCT1 was present in the microsomal fraction and appeared as a discrete band at the calculated 58 kDa in a Western blot with a faint band of lower molecular weight hinting at minor protein fragmentation (Figure 4.1A and B). The protein detection with antibodies targeting the C-terminal His-tag (Figure 4.1A) and the N-terminal HA-tag (Figure 4.1B) confirmed full translation and the presence of full-length protein.

With the use of ^{14}C-labeled substrate, the uptake of L-lactate was monitored over a time span of 32 min. MCT1-expressing cells gave mean values of 200 counts per minute (cpm) (0.5 min uptake) to 579 cpm (32 min uptake). Following data conversion (see section 3.2.5 for calculations) and background subtraction, this allowed for a maximum uptake of 0.11 ± 0.01 nmol mg^{-1} at an initial transport rate of 0.049 ± 0.005 nmol min^{-1} mg^{-1} at a near-neutral pH and an inward-directed gradient of 1 mM (Figure 4.1C). Control cells (−) indicated minor background substrate leakage into cells (mean of 104 cpm (0.5−32 min) in raw data).

All derived data for MCT1 and further constructs and experiments from following sections are summarized in Table 4.1.

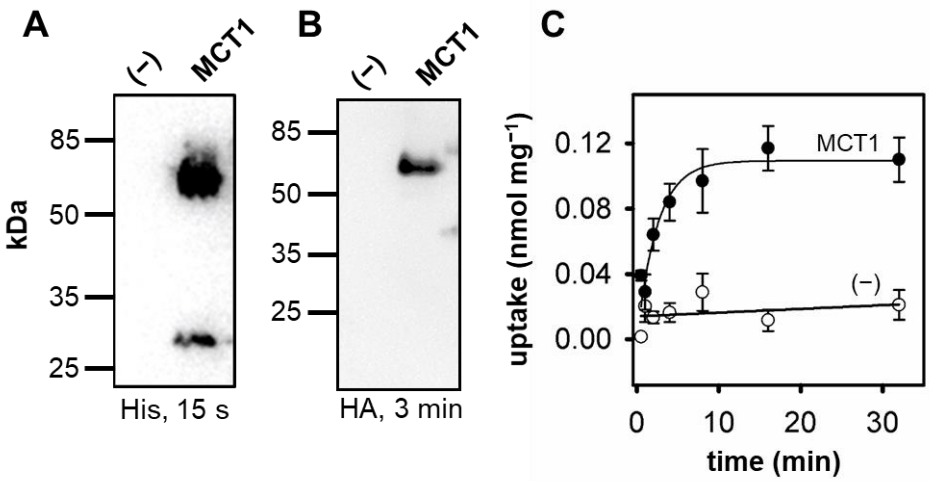

Figure 4.1. Expression and functionality of human MCT1 in *S. cerevisiae*. **(A, B)** Expression of human MCT1 (58 kDa) in the microsomal fraction was evaluated with SDS-PAGE and Western blotting. Protein was detected using a His-tag- **(A)** and a hemagglutinin-(HA-)tag-targeting **(B)** antibody. 30 µg **(A)** and 5 µg **(B)** of total protein were loaded per lane. Microsomal fractions of non-expressing yeast cells were used as negative control (−). Exposure times are indicated. **(C)** L-Lactate uptake over time into Δ*jen1* Δ*ady2* yeast cells at pH 6.8 and a 1 mM inward gradient. Shown are curves for non-expressing cells (background, (○), corrected for L-lactate adhesion to filters) and cells expressing MCT1 (●). Data is normalized to 1 mg of cells and the background of non-expressing cells was subtracted from uptake curves for MCT1. Data represent mean ± SEM of three biological replicates.

Table 4.1. Kinetic parameters ± SEM of MCT1 / basigin fusion constructs (nD: not determined).

Construct	**uptake rate*** nmol min^{-1} mg^{-1}	**uptake capacity**† nmol mg^{-1} & (mM)	**K_m**† mM	**v_{max}*** nmol min^{-1} mg^{-1}	**membrane localization** relative intensity
MCT1	0.049 ± 0.005	0.11 ± 0.01 (0.39 ± 0.05)	2.8 ± 0.2	0.187 ± 0.009	1.00 ± 0.13
+ BSGΔIg	0.037 ± 0.004	0.11 ± 0.01 (0.39 ± 0.03)	2.4 ± 0.7	0.125 ± 0.037	0.59 ± 0.07
+ BSG Ig-I	0.105 ± 0.008	0.50 ± 0.01 (1.77 ± 0.04)	3.9 ± 0.1	0.419 ± 0.024	1.66 ± 0.11
+ BSG Ig-I C23S	0.012 ± 0.001	0.12 ± 0.02 (0.44 ± 0.07)	nD	nD	nD
+ BSG Ig-I C82S	0.007 ± 0.002	0.05 ± 0.01 (0.18 ± 0.05)	nD	nD	nD
+ BSG Ig-I/C2	0.098 ± 0.013	0.59 ± 0.01 (2.11 ± 0.02)	6.8 ± 3.1	0.431 ± 0.175	0.79 ± 0.06
+ BSG var2	0.021 ± 0.002	0.51 ± 0.06 (1.82 ± 0.20)	1.2 ± 0.2	0.041 ± 0.006	0.58 ± 0.07
+ BSG Glu→Gln	0.069 ± 0.006	0.25 ± 0.01 (0.89 ± 0.04)	nD	nD	nD
+ BSG Lys/Arg→Ala	0.005 ± 0.001	0.11 ± 0.01 (0.39 ± 0.03)	nD	nD	nD
+ BSG Lys108,111Ala	0.133 ± 0.031	0.47 ± 0.07 (1.70 ± 0.24)	nD	nD	nD
+ BSG Arg201,203Ala	0.013 ± 0.002	0.25 ± 0.01 (0.91 ± 0.01)	nD	nD	nD

* dependent on the number of active transporters at the plasma membrane
† independent of the number of active transporters

4.1.2. Transport parameters and their validity

In *S. cerevisiae*, the metabolism and the formation of L-lactate is virtually absent resulting in a generally low endogenous intracellular concentration [108]. This allows for monitoring substrate influx in a so-called zero-trans setting. In a zero-trans experiment, an externally applied substrate gradient drives inward transport into non-loaded cells. Two main parameters characterize the substrate uptake over time: the initial transport rate and the maximal amount of substrate taken up by cells (see section 4.1.1 for values for MCT1). The initial transport rate ultimately depends on the existing substrate gradient, the amount of transporter present at the cell surface and transporter kinetics. A transporter capable of in- and outward-directed transport (e.g. the MCTs) will – over time – establish a steady-state of transport in which equal transport rates for in- and efflux result in equilibrium concentrations and a maximal L-lactate load inside cells. This would appear as the upper limit of a resolved uptake-over-time curve. In contrast to transport rates, the position of equilibrium and resulting equilibrium concentrations are independent of the amount of transporter available at the plasma membrane. This gives a transport characteristic comparable between differentially expressed constructs.

In common mammalian expression systems and transport assays, cellular metabolism, cell viability, and technical difficulties restrict prolonged assay times (reviewed in [9]). Studies on the equilibrium positions are hardly possible. As a consequence, the transporter characterization is limited to initial transport rates. To validate and approve the feasibility of this study's assay set-up, the methodic parameters were validated with respect to enduring transport activities and a repressed L-lactate metabolism, and the gathered results on transport characteristics were verified in different settings.

In the yeast system, L-lactate metabolism is repressed by glucose [141]. Affirmatively, glucose-adapted, MCT1-expressing cells from this study were transferred to medium with L-lactate as sole carbon source. The determined lag phase of up to 4 days (Figure 4.2A) confirmed their inability to rapidly metabolize L-lactate and set grounds to monitor L-lactate accumulation for the required longer time periods. Secondly, estimations on equilibrium positions demand enduring cell viability and fitness over the required time span. To confirm an adequate cell viability and transport activity in the applied assay conditions and buffers (19 °C, pH 6.8), the L-lactate uptake rates of cells subject to varying time delays in the glucose-free assay buffer were compared (Figure 4.2B). Although the transport rates decreased over time, cells were still active even after a 30 min-delay leading to a transport rate of 0.015 nmol min^{-1} mg^{-1} (33 % compared to 0.046 nmol min^{-1} mg^{-1} after 5 min).

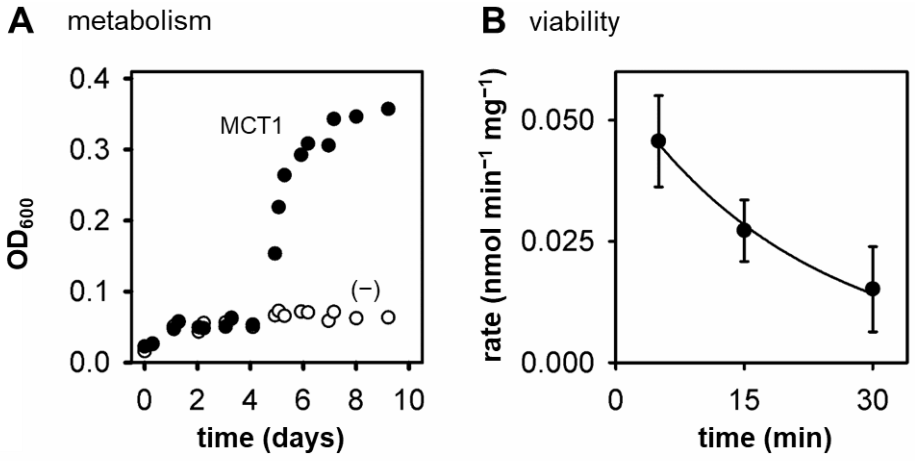

Figure 4.2. L-Lactate metabolism and viability / transport activity of *S. cerevisiae* Δ*jen1* Δ*ady2* cells. **(A)** Growth (optical density at 600 nm) of cells expressing MCT1 (●) with 1 % L-lactate as sole carbon source. Growth of cells not expressing an L-lactate transporter (○) were monitored as control. **(B)** Transport rates per minute (pH 6.8, 1 mM L-lactate) of MCT1-expressing cells after 5, 15 and 30 min of preincubation at room temperature. Data was normalized to 1 mg cell weight and background of non-expressing cells was subtracted. Data represent mean ± SEM of three biological replicates.

To experimentally test the validity of the determined equilibrium position for MCT1 at room temperature, the uptake of L-lactate over time was additionally monitored at 30 °C (Figure 4.3). As expected, the equilibrium of transport was achieved slightly faster (~ 6 min) but allowed for a comparable total L-lactate load of 0.07 nmol mg^{-1} (compare to Figure 4.1C) confirming the determined equilibrium position at room temperature and the validity of the assay.

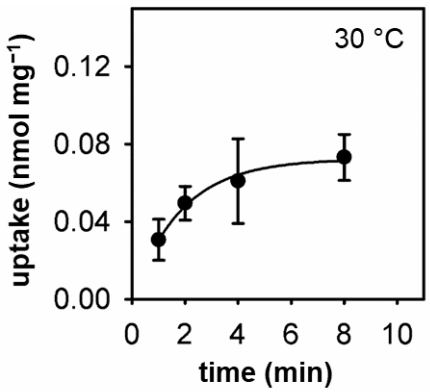

Figure 4.3. L-Lactate uptake over time by MCT1-expressing cells at 30 °C. Uptake was measured at a pH of 6.8 and a 1 mM inward gradient of L-lactate. Data represent mean ± SEM of three technical replicates. Data was normalized to 1 mg cell weight and the background of non-expressing cells was subtracted.

In contrast, initial uptake rates depend on the number of transporters available. First attempts on the quantification of surface MCT1 protein via flow cytometry failed due to the lack of a yeast cell-approved specific MCT1-antibody. Yeast cells were successfully gated with an efficiency of 98.8 % (Figure 4.4A). Unfortunately, control cells not expressing MCT1 that were subject to primary and secondary antibody treatment showed fluorescence intensities comparable to those achieved by MCT1-expressing cells (Figure 4.4B). Treatment with the secondary antibody alone gave no signal indicating a non-specific adhesion of the primary antibody to the examined cells.

To enable a direct comparison of initial rates between differentially expressed constructs, the membrane localization of MCT1 was finally estimated using confocal microscopy (Figure 4.4C). C-terminally fused green fluorescent protein (GFP) served as a detectable label. The confocal microscopy of a layer in the central plane of cells (as estimated by bright field images) showed a distribution of soluble GFP throughout the cell ((−), Figure 4.4C). Only a small, circular compartment, presumably representing the vacuole, excluded GFP. In contrast, MCT1-GFP resided mainly at the cellular rim confirming the translocation to the plasma membrane (MCT1, Figure 4.4C). Nonetheless, a substantial portion of MCT1-GFP appeared trapped at intracellular membranes. A numerical quantification at the plasma membrane was based on the determination of mean gray values per pixel at an ellipsoid line at the cellular rim.

To estimate the membrane localization differences, the resulting value for MCT1 was set to 1 and the quantification for additional constructs is relative to MCT1 (Table 4.1, see following sections). Strikingly, the C-terminal fusion with GFP led to membrane-resident but non-functional protein. Although the trafficking seemed unaffected, a protein fusion to the C-terminal end of MCT1 was not tolerated elucidating a substantial role in transporter function (Figure 4.4D).

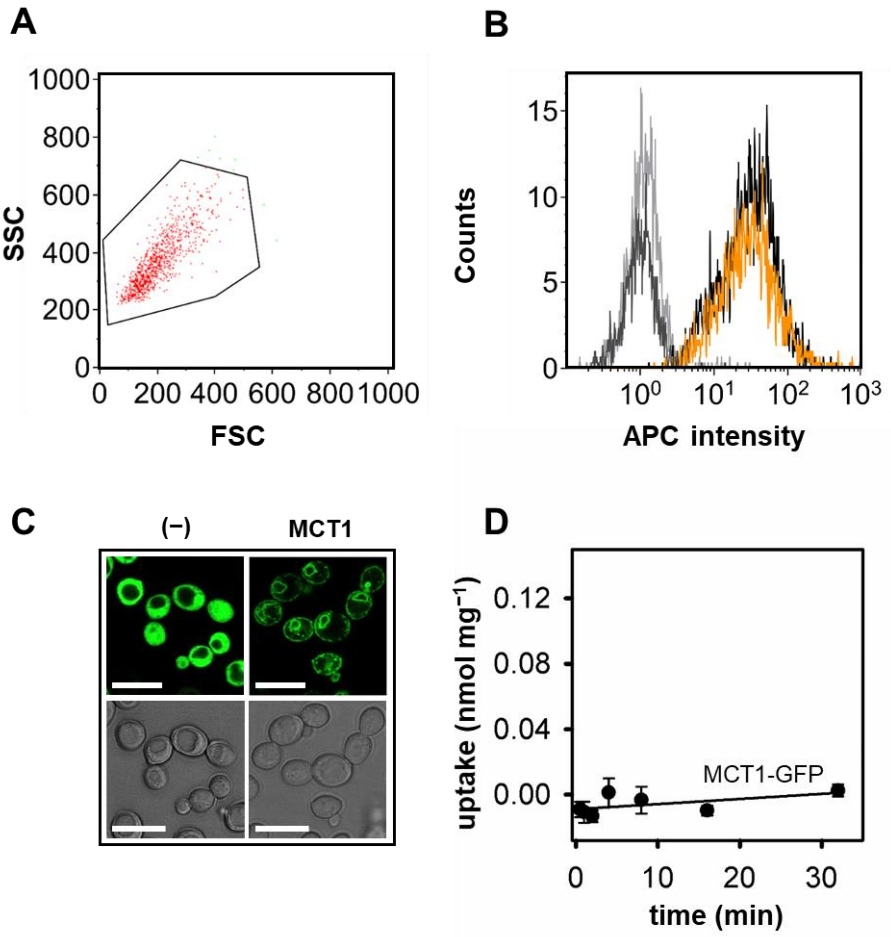

Figure 4.4. Quantification of MCT1 at the plasma membrane. **(A, B)** Flow cytometry of MCT1-expressing cells. **(A)** SSC/FSC dot plot and gating of non-expressing *S. cerevisiae* Δ*jen1* Δ*ady2* cells. Side scatter (SSC, cell volume) is plotted against forward scatter (FSC, granularity) and cells gated for analysis are outlined (red). The gating efficiency was 98.8 %. **(B)** Histogram illustrating the counts per fluorescence intensity. Non-expressing (black) and MCT1-expressing (orange) cells were labeled with an anti-MCT1 primary antibody (orb312305) and an allophycocyanin (APC)-labeled secondary antibody. As control, non-expressing cells lacked any antibody treatment (dark gray) or were only subject to secondary antibody (light gray). **(C)** Visualization of MCT1-GFP at the plasma membrane via live-cell confocal microscopy. Cells expressing soluble GFP (−) and GFP fused to the C-terminus of MCT1 are shown. Bright field images are in the bottom row. The white scale bar indicates 10 µm. **(D)** L-Lactate uptake via the MCT1-GFP fusion construct over time (pH 6.8, 1 mM inward gradient). Background of non-expressing cells was subtracted, and data was normalized to 1 mg of cells. Data represent mean ± SEM of three biological replicates.

4.1.3. Fusion of MCT1 with its accessory protein

The here confirmed MCT1 activity in the absence of basigin in yeast was an excellent and unique prerequisite to investigate the interaction and more importantly further effects on the transport activity of MCT1 induced via basigin. Generally, the fusion of two functionally and structurally different proteins enables the expression in a stoichiometric manner and excludes background from one of the partners acting alone. In order to investigate effects of the accessory protein (basigin in particular) on the transporter functionality, and additionally reveal the importance of the distinct domains, various fusion proteins of human MCT1 and basigin were generated. Starting from a minimalistic variant harboring only the transmembrane domain and C-terminus (named BSGΔIg), the TM-associated extracellular Ig-like domain (Ig-I type, named BSG Ig-I), the N-terminal C2-type domain (named BSG Ig-I/C2) and finally the N-terminal signal peptide were sequentially added to give rise to the full-length, wildtype basigin splice variant 2 (BSG var2). All produced constructs are depicted in Figure 4.5 and are based on structure models for MCT1, and the crystal structure for the extracellular domain and schematic illustrations for the TM-region of basigin. In all cases, the C-terminus of basigin was fused to the N-terminal portion of MCT1. Secondary structure predictions for basigin and the recently published crystal structure for a bacterial MCT homolog [54] suggested a resulting flexible linker of a total of around 60 amino acids ensuring enough flexibility to enable a functional protein interaction (see Figure 3.1 for additional topology plot).

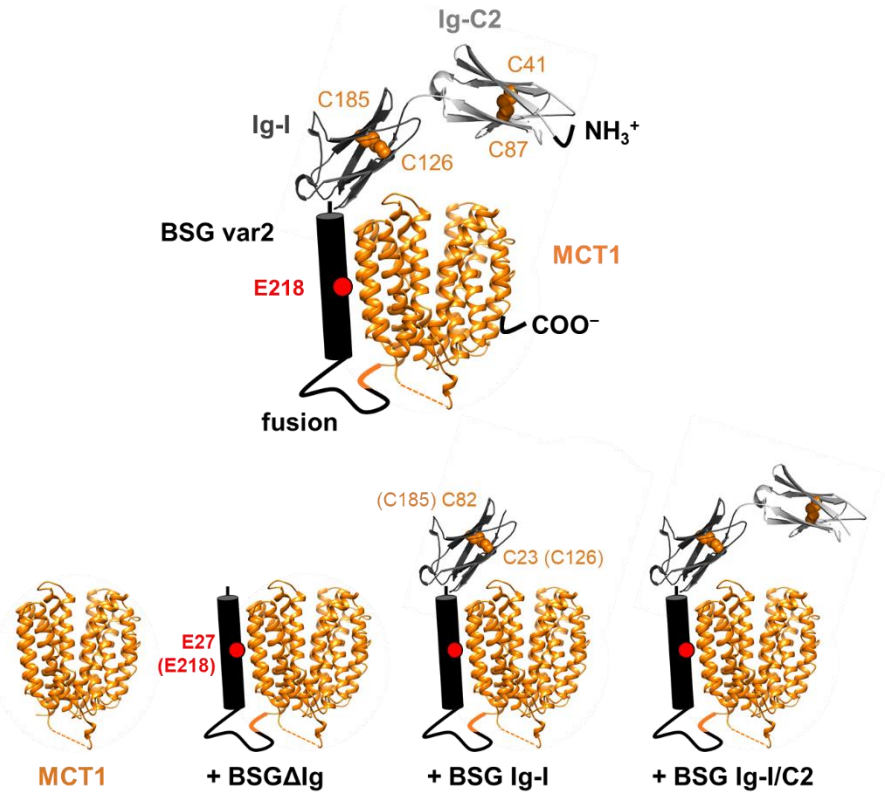

Figure 4.5. Schematic models of basigin-MCT1 fusion constructs. Fusion constructs of basigin (black/gray; PDB #3B5H; the transmembrane domain as schematic illustration) with MCT1 (orange; structure model based on SfMCT, PDB #6HCL). Disulfide bridges in the extracellular domain of basigin are shown as orange spheres and relevant cysteines are labeled. Glu218 (Glu27 in BSGΔIg) in the transmembrane domain of basigin is highlighted in red. The N- and C-terminal sequences of constructs are indicated and additionally include a hemagglutinin- and a His-tag, respectively (not shown).

4.1.4. The transmembrane domain of basigin associates with MCT1

The fusion of the minimalistic BSGΔIg construct to human MCT1 resulted in almost identical expression patterns, levels and membrane localization (Figure 4.6A, B; Table 4.1). The BSGΔIg fusion led to an expected band shift in the Western blot and the fusion protein was detected at a higher molecular weight of 67 kDa. Most importantly, the fusion of both proteins did not alter L-lactate uptake into cells. The maximal uptake capacity as well as the initial transport rate corresponded to values determined for MCT1 alone – especially when considering slight differences in membrane localization (Figure 4.6C, Table 4.1). To investigate whether basigin and MCT1 were in fact interacting, Glu27 in the transmembrane domain (corresponding to Glu218 in basigin splice variant 2) was mutated to a positively charged arginine. Previous literature proposed Glu218 to engage in the association with MCT1 and E218R mutants failed to interact with MCT1 [57]. In this study, the expression of a BSGΔIg E27R-MCT1 fusion protein failed to mediate L-lactate transport although the protein was

expressed and reached the plasma membrane (Figure 4.6A−C). This effect could not be rescued by an analogous mutation in full-length basigin variants (Figure 4.6D).

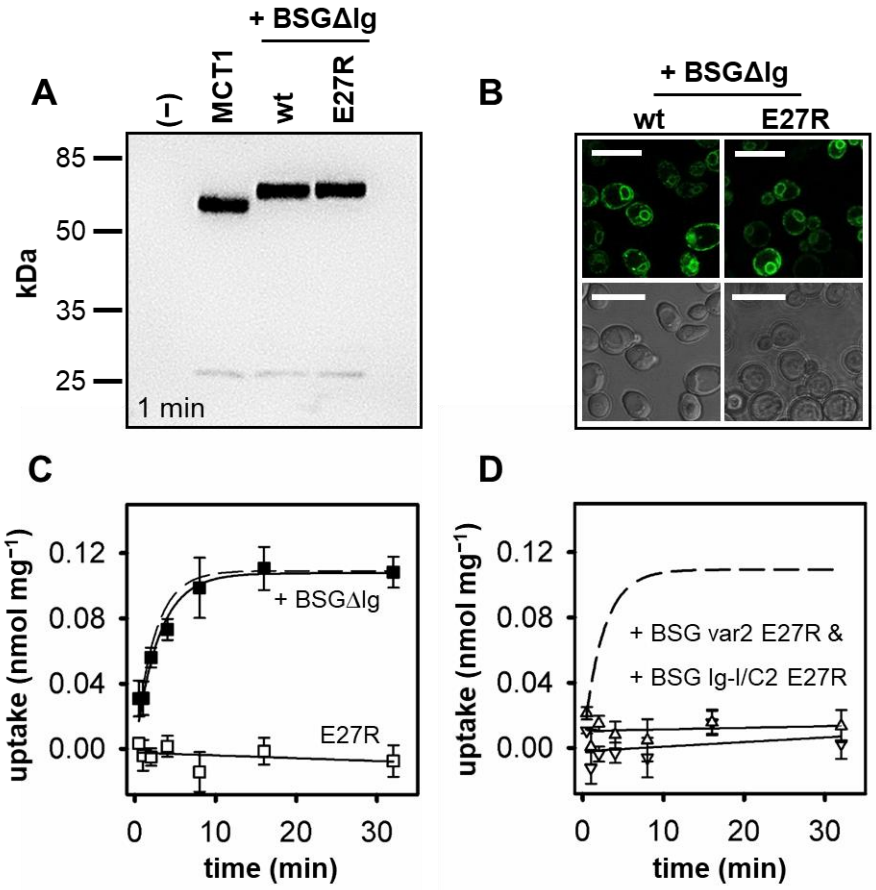

Figure 4.6. Expression and functionality of BSGΔIg-MCT1 fusion constructs. **(A)** Western blot of microsomal fractions showing the expression of MCT1 alone (58 kDa) and fused with wildtype BSGΔIg (67 kDa) or the E27R point mutant. 4−6 µg of total protein were loaded per lane and protein was detected via a His-tag-targeting antibody. Microsomal fractions of non-expressing cells were blotted as control. Exposure time is indicated. **(B)** Confocal microscopy of the BSGΔIg-MCT1-GFP fusion constructs carrying C-terminal GFP. Cells expressing MCT1-GFP in fusion with wildtype BSGΔIg or the E27R point mutant are shown. Bright field images are in the bottom row. The white scale bar indicates 10 µm. **(C, D)** L-Lactate uptake over time (pH 6.8, 1 mM inward gradient). Shown are curves for MCT1 fused to wildtype BSGΔIg (C, ■), BSGΔIg E27R (C, □), and full length basigin variants BSG Ig-I/C2 (D, ▽) and BSG var2 (D, △) carrying the corresponding point mutant (E27 ≙ E198 in BSG Ig-I/C2 and E218 in BSG var2). Data was normalized to 1 mg cell weight and background of non-expressing cells was subtracted. As a reference, uptake via MCT1 alone is indicated as dashed line. Data represent mean ± SEM of three biological replicates.

The abolishment of transporter function via a mutation in the adjacent basigin, e.g. due to an induced conformational change, demonstrated the importance of proper transmembrane interaction in the basigin-MCT1 fusion protein. Nonetheless, an effect on transport via MCT1 was not observable.

Strikingly, the fusion to a minimalistic variant of embigin as the not preferred but alternative partner of MCT1 led to only marginally expressed MCT1 (Figure 4.7A). The resulting low transport rates facilitated minimal L-lactate uptake over time obstructing further analyses (Figure 4.7B).

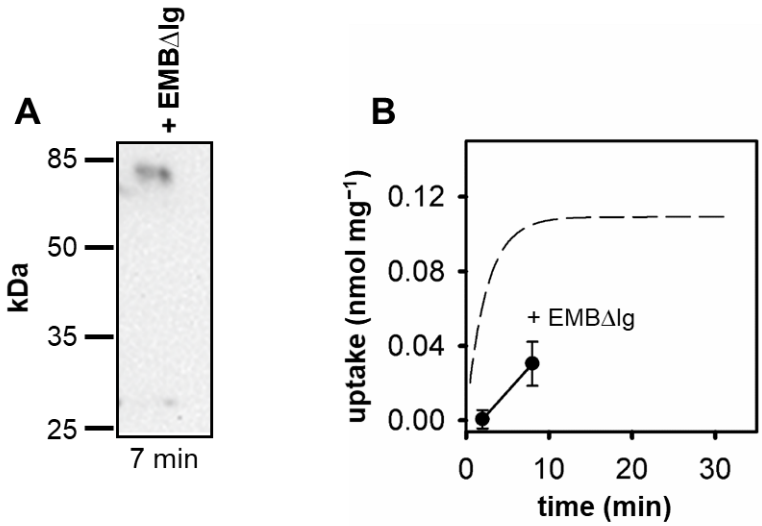

Figure 4.7. Expression and functionality of EMBΔIg-MCT1 fusion constructs. **(A)** Western blot (30 µg of total protein per lane, detection via a His-tag-targeting antibody, exposure time is indicated) and **(B)** L-lactate uptake (pH 6.8, 1 mM inward gradient) of MCT1 fused to a minimalistic variant of embigin (+ EMBΔIg, 68 kDa). Data was normalized to 1 mg cell weight and background of non-expressing cells was subtracted. As a reference, uptake via MCT1 alone is indicated as dashed line. Data represent mean ± SEM of three technical replicates.

4.1.5. The Ig-I domain of basigin drives inward-directed transport via MCT1

Next, the membrane-proximal Ig-I and the N-terminal Ig-C2 domains of basigin were sequentially added to investigate whether an effect on MCT1 transport depends on the presence of basigin's extracellular domains. The generated fusion proteins were less well expressed but reached the plasma membrane (Figure 4.8A, B). Generally, the MCT1 fusion to basigin variants led to a more or less apparent shift to higher molecular weights (Figure 4.8A). The calculated molecular weights expected for each construct can be found in the figure legend. In addition to the expected protein fragment at around 30 kDa, additional bands mirroring MCT1 alone hints at a minor breakage in the linking sequence between both proteins. The amount of transporter located at the plasma membrane was quantified with confocal

microscopy (Figure 4.8B, Table 4.1). The apparent differences largely account for differences in the determined initial transport rates (Figure 4.8C, D, summarized in Table 4.1). Strikingly, the presence of the TM-adjacent Ig-I domain (+ BSG Ig-I) led to an altered L-lactate transport profile manifesting in a 4.5-fold total uptake into the cells compared to MCT1 alone (0.50 nmol mg^{-1}, Figure 4.8C, Table 4.1). Noteworthy, despite differences in the transport rates, the constructs including the second, N-terminal Ig-like domain (BSG Ig-I/C2 and BSG var2) allowed for almost identical L-lactate loads accumulated within the cells (Figure 4.8D, Table 4.1). Due to low expression levels at the cell surface and low transport rates (see Figure 4.8B, Table 4.1), the uptake capacity for BSG var2 was extrapolated.

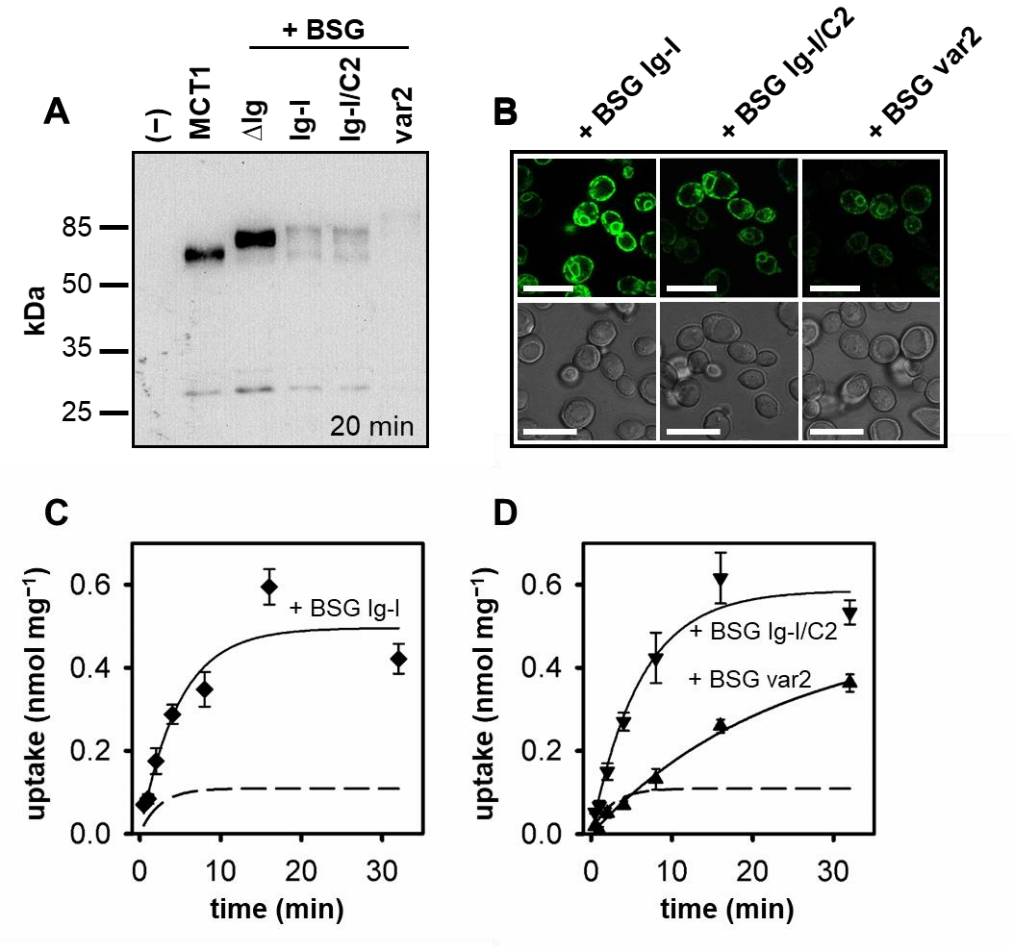

Figure 4.8. Expression and functionality of BSG-MCT1 fusion constructs carrying the extracellular Ig-I domain. **(A)** Western blot of microsomal fractions showing expression of MCT1 alone (58 kDa) and fused to BSGΔIg (67 kDa), BSG Ig-I (77 kDa), BSG Ig-I/C2 (85 kDa) and BSG var2 (87 kDa). 5 µg of total protein were loaded per lane. Protein was detected via a His-tag-targeting antibody. Microsomal fractions of non-expressing cells were used as control. Exposure time is indicated. **(B)** Visualization of the BSG-MCT1 fusion constructs at the plasma membrane via live-cell confocal microscopy and C-terminally fused GFP. Bright field images are in the bottom row. The white scale bar indicates 10 µm. **(C, D)** Uptake of L-lactate into cells over time (pH 6.8, 1 mM inward gradient). Shown are curves for MCT1 fused to BSG Ig-I (C, ♦), BSG Ig-I/C2 (D, ▼) and BSG var2 (D, ▲). Data was normalized to 1 mg cell weight and background of non-expressing cells was subtracted. As a reference, uptake via MCT1 alone is indicated as dashed line. Note the different scaling when comparing to Figure 4.1C and Figure 4.6C. Data represent mean ± SEM of three biological replicates.

An additional, less prevalent basigin splice variant (BSG var1) that carries a third Ig-like domain was poorly expressed and showed only residual transport activity (Figure 4.9A and B). A fusion construct with full-length embigin variant 1 was equally low in activity which obstructed analyses on embigin as an alternative MCT1 regulator.

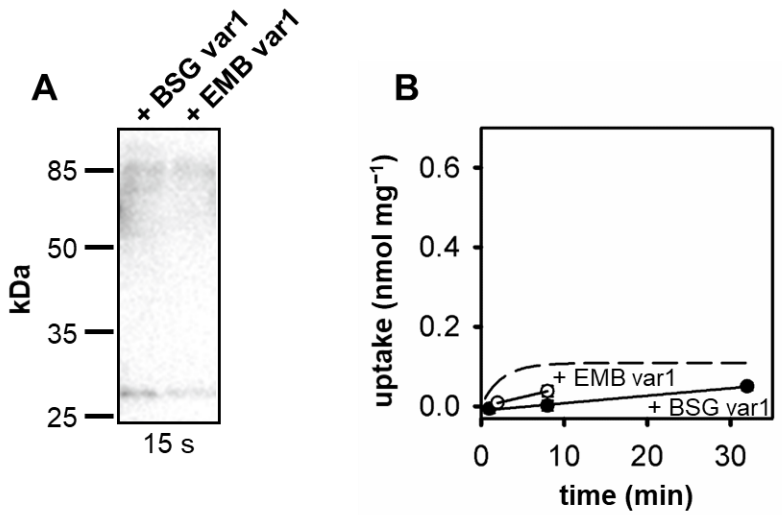

Figure 4.9. Expression and functionality of BSG var1/EMB var1-MCT1 fusion constructs. **(A)** Western blot (30 µg of total protein per lane, detection via a His-tag-targeting antibody, exposure time is indicated) and **(B)** L-lactate uptake over time (pH 6.8, 1 mM inward gradient) of MCT1 fused to BSG var1 (●, 100 kDa) and full-length EMB var1 (○, 95 kDa). Data was normalized to 1 mg cell weight and background of non-expressing cells was subtracted. As a reference, uptake via MCT1 alone is indicated as dashed line. Data represent mean ± SEM of three biological (BSG var1) or technical (EMB var1) replicates.

In conclusion, the presence of the extracellular Ig-I domain of basigin increased the intracellular load of L-lactate that was achieved in the equilibrium state of transport. To corroborate the results, several attempts were made to prevent a basigin-MCT1 interaction and reverse basigin-mediated effects. Acriflavine is a chemical agent that has been shown to bind to the extracellular domain of basigin leading to the inability to interact with MCTs [98]. Here, BSG Ig-I-MCT1-expressing cells were pretreated with acriflavine. Nonetheless, acriflavine failed to modulate the basigin-related effect on MCT1 functionality in this study (Figure 4.10A). Although acriflavine reduced the amount of L-lactate that was taken up after 4 min, the cells expressing MCT1 alone and in fusion with BSG Ig-I were similarly affected hinting at a non-specific, presumably yeast-toxic effect [142, 143].

The Ig-like domains of basigin have a distinct and functionally essential folding consisting of two β-sheets connected via a disulfide bridge (marked as orange sticks in Figure 4.5). The pretreatment with dithiothreitol (DTT) as a disulfide-reducing agent did also not decrease the capability of BSG Ig-I-MCT1-expressing cells to accumulate L-lactate (Figure 4.10B, compare to Table 4.1). The uptake of 0.172 nmol mg^{-1} after 4 min (10 mM DTT) was comparable to non-treated cells and much higher than the uptake capacities at all achievable by MCT1-expressing cells not interacting with basigin. Finally, single serine mutants of both cysteines involved in disulfide bridge formation in the BSG Ig-I construct (Cys23 and Cys82

corresponding to Cys126 and Cys185 in splice variant 2) were generated (Figure 4.10C, D). Although the mutants were well expressed (Figure 4.10C), the prevention of disulfide formation in basigin led to low intracellular L-lactate loads comparable to those obtained for MCT alone or in combination with the truncated BSGΔIg construct (Figure 4.10D, Table 4.1). This confirmed the necessity of a correctly folded Ig-I domain of basigin to drive cytosolic L-lactate accumulation via MCT1.

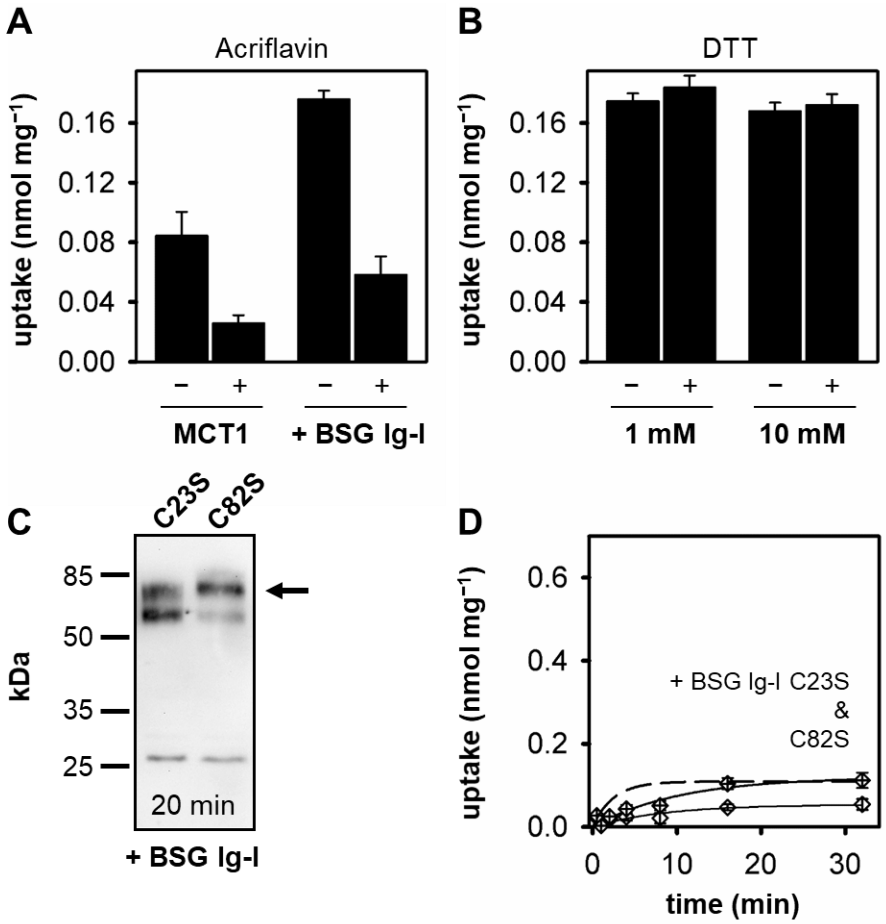

Figure 4.10. Reversal of BSG Ig-I-mediated effects on L-lactate uptake via MCT1. **(A)** Acriflavine treatment. Cells expressing MCT1 alone and in fusion with BSG Ig-I with (+) or without (−, solvent instead) acriflavine pretreatment (1 mM, 15 min, RT). **(B)** DTT treatment. Cells expressing the BSG Ig-I-MCT1 fusion construct with (+) or without (−, solvent instead) DTT pretreatment (1 mM / 10 mM, 15 min, RT). For **(A)** and **(B)**, bars delineate subsequent uptake of L-lactate (pH 6.8, 1 mM inward gradient) after 4 min. Data was normalized to 1 mg cell weight and background of non-expressing cells was subtracted. Data represent mean ± SEM of three technical replicates. **(C)** Western blot (5 µg of total protein per lane, detection via a His-tag-targeting antibody, exposure time is indicated) and **(D)** L-lactate uptake (pH 6.8, 1 mM inward gradient) of MCT1 fused to the BSG Ig-I mutants C23S (⏧) and C82S (◊) (77 kDa, arrow in Western blot). Data was normalized to 1 mg cell weight and background of non-expressing cells was subtracted. As a reference, uptake via MCT1 alone is indicated as dashed line. Data represent mean ± SEM of three biological replicates.

4.1.6. Michaelis-Menten kinetics and the use of protons

To investigate the nature of transport modulation by basigin, the Michaelis-Menten kinetics were determined for the zero-trans influx of L-lactate at pH 6.8 (Figure 4.11A, B). All obtained K_m and v_{max} values are summarized in Table 4.1. Due to low transport rates, estimations on the K_m value for BSG var2-MCT1 were largely error prone. For MCT1 alone, the obtained K_m value of 2.8 mM is comparable to previous literature (3.5 mM determined in *Xenopus* oocytes [50]). Of note, in *Xenopus* oocytes, endogenous basigin will be associated with MCT1. The fusion to BSG Ig-I led to a significant increase to a K_m of 3.9 mM ($p = 0.01$, unpaired, two-tailed t-test). Nonetheless, the required extrapolation of the curve's upper limits imply imprecise K_m determinations. To this end, accurate maximum velocity (v_{max}) determinations were likewise challenging but values appeared largely unaffected. The observed 2.2-fold increase in v_{max} (0.419 nmol min^{-1} mg^{-1} (+ BSG Ig-I) compared to 0.187 nmol min^{-1} mg^{-1} (MCT1)) is explainable by the almost equal difference in membrane localization (1.7-fold increase for + BSG Ig-I, Table 4.1). Yet, the apparent lower substrate affinity of MCT1 (higher K_m) when accompanied by BSG Ig-I points at an altered substrate availability with respect to the overall buffer concentrations.

As already mentioned, protons are the respected co-substrate of MCT1-mediated L-lactate transport. To estimate the overall pH gradient at the given extracellular pH, colleague N. H. Epalle loaded expressing cells with a fluorescent pH indicator (according to [144]) and determined a near-neutral cytosolic pH for all cells. Upon the addition of L-lactate, the pH stabilized at a cytosolic pH of 6.3−6.5 for all constructs demonstrating the efficient endogenous pH regulation of yeasts. The knowledge of the cytosolic pH revealed a slightly outward directed pH gradient (≈ 0.16 µM $[H^+]_{external}$ vs. ≈ 0.4 µM $[H^+]_{internal}$; outward gradient: 2.5). Lowering the outside buffer pH to 5.8 to provide more protons and generate an inward directed gradient led to a general increase of the intracellular L-lactate load according to Le Chatelier's principle (Figure 4.11C, 1.6 µM $[H^+]_{external}$; inward gradient: 4.0). Still, a fusion to BSG Ig-I favored L-lactate influx. Nonetheless, this effect was less prominent at pH 5.8 leading to an only 2.2-fold higher intracellular L-lactate load compared to MCT1 alone (Figure 4.11D; compare to 4.5-fold at pH 6.8) suggesting that basigin drives substrate influx especially at near-neutral pH conditions.

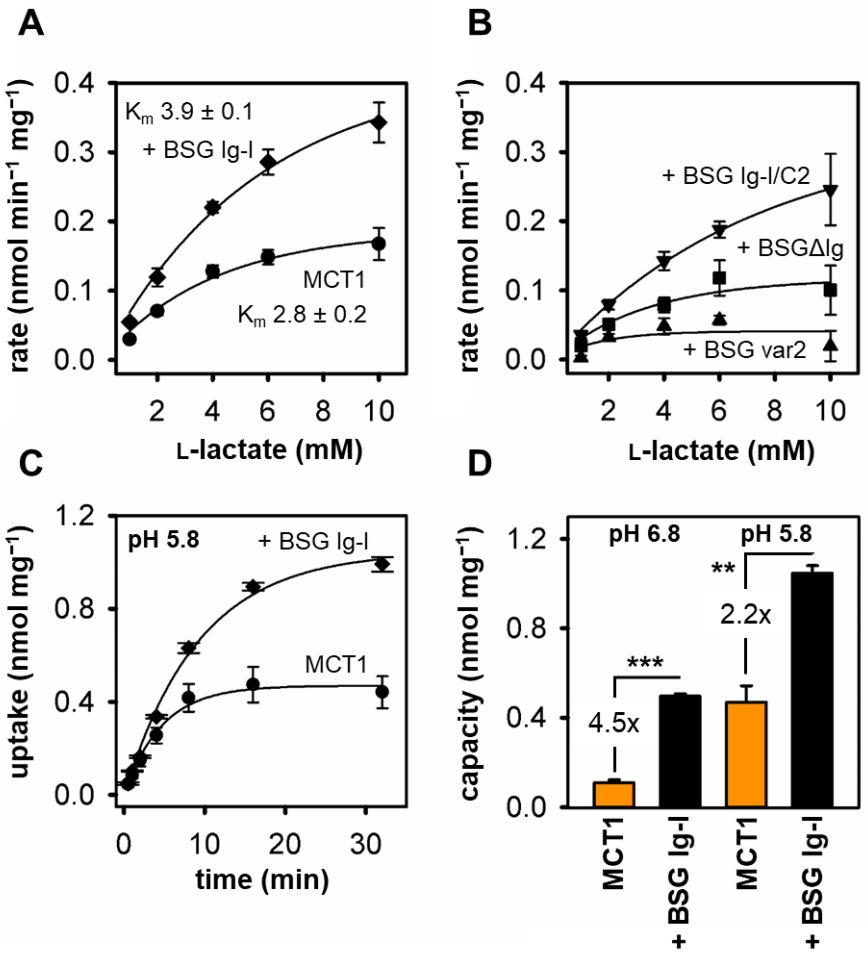

Figure 4.11. The effect of substrate and proton concentrations on MCT1-mediated transport. **(A, B)** Michaelis-Menten kinetics for **(A)** MCT1 alone (●) and fused to BSG Ig-I (♦) and **(B)** remaining basigin fusion constructs. Initial transport rates result from single time point measurements of L-lactate uptake for 2 min (pH 6.8, inward gradient from 1−10 mM). Data represent mean ± SEM of three biological replicates. K_m values (in mM) were determined by three independent exponential fits of three biological replicates and are given in mean ± SEM. **(C)** L-Lactate uptake via MCT1 alone and fused to BSG Ig-I at pH 5.8 (1 mM inward gradient). **(D)** Uptake capacities of cells expressing MCT1 alone (orange) and fused with BSG Ig-I (black) at pH 6.8 (based on data from Figure 4.1C and Figure 4.8C) and pH 5.8 (data from C). Significance was tested by an unpaired, two-tailed t-test (**p < 0.01, ***p < 0.001). In all cases, data was normalized to 1 mg of cell weight and background of non-expressing cells was subtracted. Data represent mean ± SEM of three biological replicates.

4.1.7. Basigin drives L-lactate uptake to concentrations exceeding the inward gradient

To estimate equilibrium substrate concentrations inside the cell, the uptake capacities in nmol mg^{-1} were translated to intracellular molar concentrations. As part of her dissertation, A. Jansen expressed two known and well-characterized glycerol-conducting channel proteins, namely murine and human aquaporins (AQP) 7 and 9, in *S. cerevisiae*. Channels facilitate the diffusion of neutral substrates to an equilibrium of equal concentrations in- and outside the cell

[145]. A. Jansen loaded cells with ^{14}C-labeled glycerol using a 1 mM inward gradient and determined an uptake capacity of 0.28 nmol mg^{-1} that corresponds to a cytosolic concentration of 1 mM. Using this correlation, the uptake capacities for L-lactate of all constructs in this study (from Table 4.1) were translated to cytosolic concentrations in mM. Assuming the outside buffer volume to be infinitely larger than the total cytosolic volume, the outside L-lactate concentration (1 mM) is considered constant. Accordingly, the equilibrium position for L-lactate for all constructs can be displayed as the ratio of internal and outside equilibrium concentrations (c_{eq_in} / c_{eq_ex}, Figure 4.12A). For MCT1 alone and in fusion with the truncated basigin variants, the intracellular accumulation of L-lactate reached concentration ratios between 0.18-0.44. Strikingly, the fusion with basigin constructs carrying the Ig-I domain enabled the cells to accumulate L-lactate to cytosolic concentrations higher than those accomplished by channel-facilitated diffusion and well above those achieved by MCT1 alone. An accumulation to concentrations exceeding the inward gradient for L-lactate (c_{eq_in} / c_{eq_ex} = 1.8–2.1, Table 4.1) demonstrates that basigin drives an intracellular accumulation of L-lactate via its Ig-I domain – possibly by affecting the local L-lactate and/or proton availability.

Considering the previously determined pH gradients (see section 4.1.6), the equilibrium constants K for all constructs were determined (Figure 4.12B). For MCT1 alone and in fusion with the basigin constructs lacking the Ig-I domain, the system was in equilibrium ($K \approx 1 = (c_{eq\_in} \cdot [H^+]_{eq\_in}) / (c_{eq\_ex} \cdot [H^+]_{eq\_ex})$). The presence of the membrane-proximal Ig-I domain of basigin led to a disturbance of the system and an apparent equilibrium constant $K_{apparent}$ of 4.5 (for BSG Ig-I-MCT1). Thermodynamically, such a disturbance would arise from basigin creating a microenvironment of locally increased proton/substrate availability at the extracellular site and above concentrations provided by the buffer.

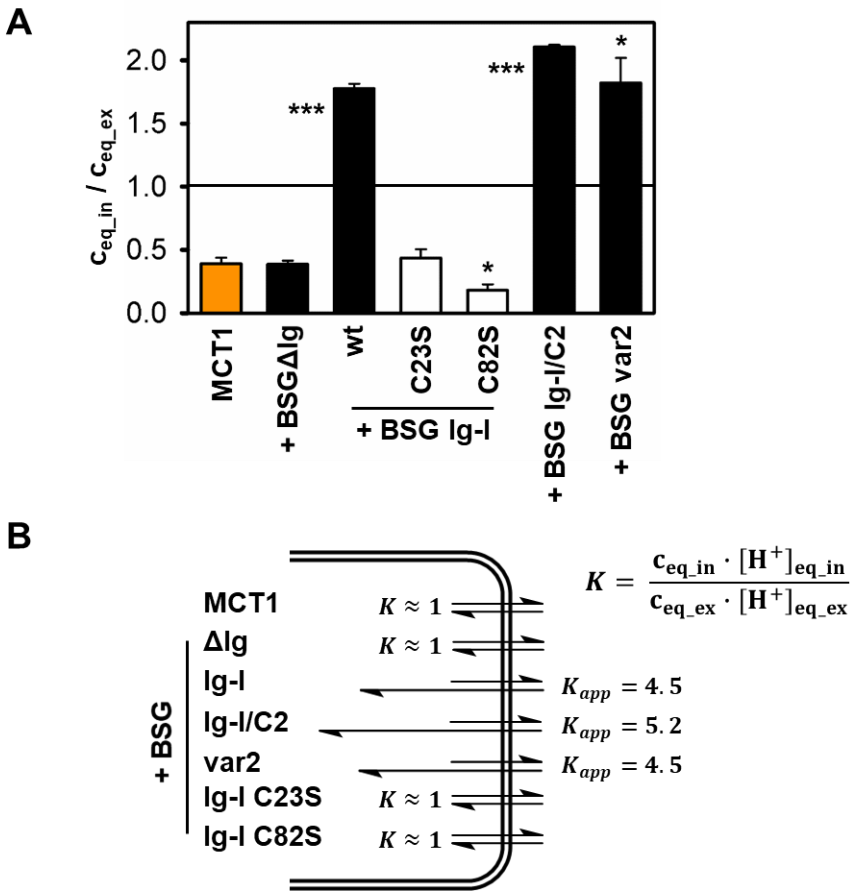

Figure 4.12. Shifted intracellular L-lactate concentrations and transport equilibrium. **(A)** L-Lactate transmembrane distribution generated by the expression of MCT1 alone (orange) and in fusion with basigin variants (black). Shown is the ratio of intracellular and extracellular molar L-lactate concentrations at equilibrium. Data represent mean ± SEM of three biological replicates. Significance in relation to MCT1 alone was determined by an unpaired, two-tailed t-test (*p < 0.05, ***p < 0.001). **(B)** Equilibrium constants. The internal and external L-lactate (c_{eq_in}, c_{eq_ex}) and proton concentrations ($[H^+]_{eq\_in}$, $[H^+]_{eq\_ex}$) determine the equilibrium constant K. Respective K values for basigin-MCT1 fusion constructs indicate an equilibrative ($K \approx 1$) or an accumulating effect ($K_{apparent} > 1$) on intracellular L-lactate with respect to the overall buffer concentrations.

To evaluate the physiological relevance, expressing cells were grown on media supplemented with L-lactate as sole carbon source (Figure 4.13). The growth was monitored over a time span of 12 days and showed only minor colony formation of cells expressing MCT1 alone or in association with the truncated or misfolded basigin variants (BSGΔIg, BSG Ig-I C23S/C82S) at pH 5.8 as well as pH 6.8. Moreover, the growth was comparable to control cells lacking L-lactate transporters. In line with the biophysical results, the presence of basigin variants containing the Ig-I domain boosted L-lactate uptake and promoted cell growth.

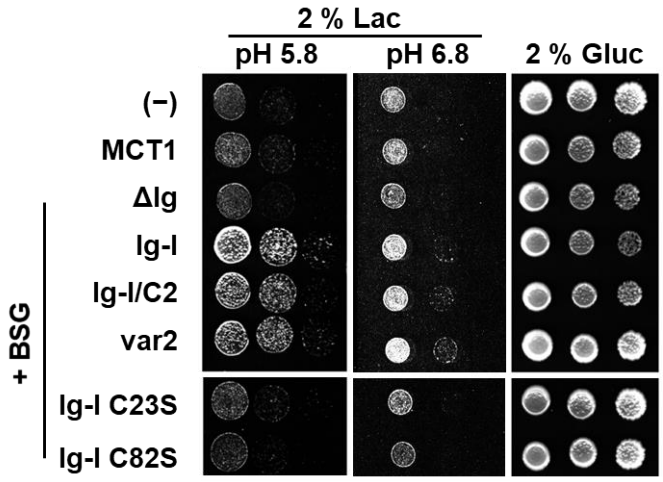

Figure 4.13. Physiological relevance of basigin-driven L-lactate influx. Growth of cells expressing MCT1 and basigin-MCT1 fusion variants on agar medium containing 2 % sodium L-lactate at pH 5.8 (left) and pH 6.8 (middle), or on 2 % glucose medium (growth control; right). Cell suspensions (5 µl) were spotted in ten-fold serial dilutions (left to right) from a starting OD_{600} of 1.

4.1.8. Impact of glucose on L-lactate transport via basigin-MCT1 fusion proteins

Glucose is the key substrate for glycolysis and energy metabolism in yeast. The metabolisms of glucose and L-lactate are tightly linked. As part of an attempt to ensure cellular fitness during transport assays (see section 4.1.2), the standard buffer compositions were supplemented with 2 % (= 110 mM) glucose. Although not prolonging cellular viability, the glucose availability during cell preparation and uptake measurements had an impact on L-lactate accumulation of cells (Figure 4.14A). The total uptake via MCT1 alone as well as in fusion with BSG Ig-I reached a maximum after 2 min leading to uptake capacities below those achieved in glucose-deprived conditions. For MCT1 alone, the L-lactate influx was only slightly altered giving a cytosolic load of 0.04 nmol mg^{-1}. The fusion to BSG Ig-I, in contrast, failed to promote the previously disclosed increased influx of substrate leading to uptake capacities almost identical to those of unfused MCT1. Strikingly, a short-term exposure (15 min) to more physiological glucose concentrations just prior to conducting the assay failed to affect the L-lactate uptake (Figure 4.14B). This excluded glucose as a direct MCT1 inhibitor or competitor and points at a presumably metabolism- or osmosis-driven phenomenon.

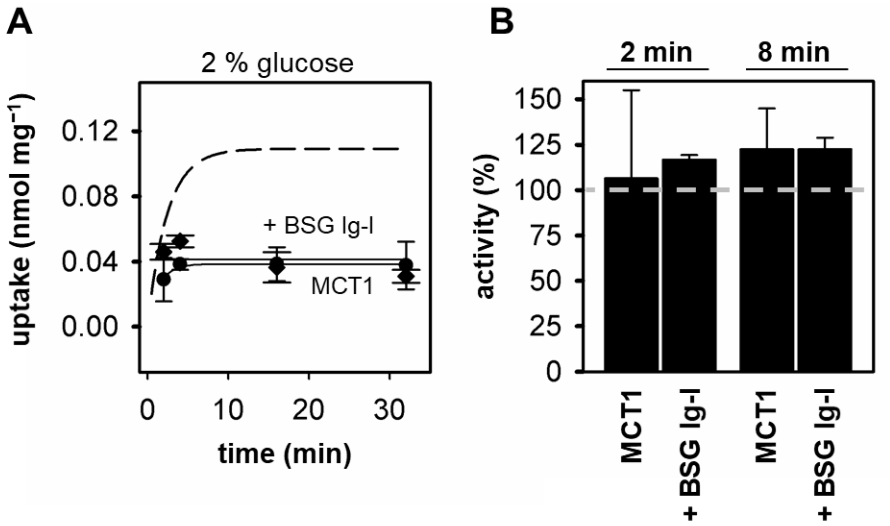

Figure 4.14. Impact of glucose on L-lactate uptake via MCT1. **(A)** L-Lactate uptake (pH 6.8, 1 mM inward gradient) via MCT1 alone (●) and in fusion with BSG Ig-I (♦). In contrast to previous measurements, cells were supplied with 2 % glucose during preparation and in the uptake assay. Data was normalized to 1 mg cell weight. As a reference, uptake via MCT1 alone under glucose-deprived conditions is indicated as dashed line. **(B)** Percental L-lactate uptake of expressing cells pretreated with 25 mM glucose (15 min, RT) compared to solvent-exposed cells. Shown are percentages for MCT1 alone and in fusion with BSG Ig-I after monitoring L-lactate uptake in the initial (2 min) and in the equilibrating (8 min) phase of transport. For **(A)** and **(B)**, background of non-expressing cells was subtracted, and data represent mean ± SEM of two technical replicates.

4.1.9. Basigin acts as an electrostatic proton and substrate antenna

To investigate how basigin modulates MCT1-driven L-lactate influx, the Poisson-Boltzmann electrostatics of the extracellular domain were calculated using the available crystal structure data (PDB #3B5H, Figure 4.15). The membrane-proximal Ig-I domain of basigin shows a negatively charged patch of five clustered glutamates (Glu114,118,120,168,172) suited for an electrostatic proton attraction (Figure 4.15, left). Strikingly, this domain displays another, positively charged patch consisting of up to six clustered arginine and lysine residues (Lys108,111,127 and Arg166,201,203) possibly suited to serve as an additional substrate antenna (Figure 4.15, right).

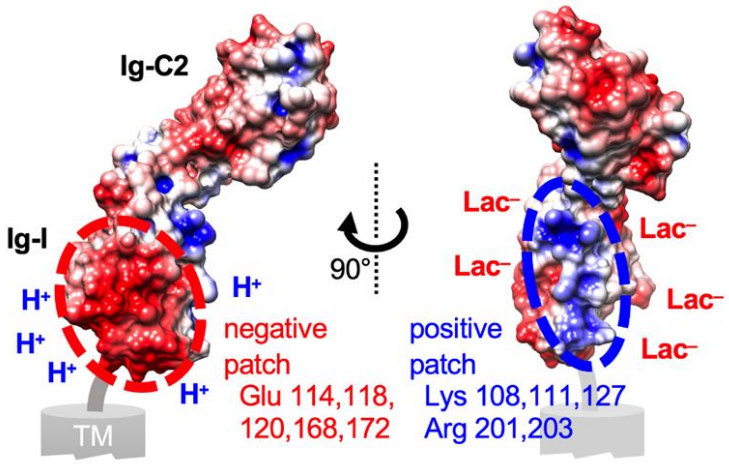

Figure 4.15. Electrostatic surface potential of the extracellular domain of basigin. The Poisson-Boltzmann electrostatic potential of the extracellular domain of BSG var2 (PDB #3B5H) reveals two oppositely charged surface patches suited for proton/L-lactate attraction in the BSG Ig-I domain. The red/blue scale covers the range of –3 kT/e to +3 kT/e. Relevant residues for each patch are indicated.

The mutation of the five glutamates to non-charged glutamines (BSG Ig-I Glu→Gln) neutralized the negative patch as displayed in Figure 4.16A. The mutant was functionally expressed but provoked a drop in the uptake capacity when fused to MCT1 (Figure 4.16A, B). The cytosolic concentration reached 0.89 mM L-lactate inside the cells (Table 4.1). This hinted at basigin as an electrostatic proton collector pooling the co-substrate at the transporter surface and driving inward-directed flux of the accompanied L-lactate. Notably, the removal of the negative charges did not fully decrease the uptake capacity to the MCT1 base level (lower dashed line of Figure 4.16A). This is suggestive of a second, additive effect probably deriving from the positive patch acting as a substrate harvesting antenna. Neutralizing the positive patch by mutating all respective lysines/arginines to alanines (named BSG Ig-I Lys/Arg→Ala + R166A) led to the expression of non-functional protein (Figure 4.16B, C). In cooperation with K. Geistlinger, the putative ion-bridge forming arginine at position 166 was reintroduced and reinstated functionality (Figure 4.16B, C). The resulting electrostatic surface potential of the corresponding BSG Ig-I Lys/Arg→Ala construct is shown in Figure 4.16C and highlights a strong negative overall charge of the BSG Ig-I domain. A removal of the positive patch fully decreased the uptake capacity to that achieved by non-fused MCT1 (Figure 4.16C, Table 4.1). A partial abrogation of the positive patch (constructs BSG Ig-I K108,111A and BSG Ig-I R201,203A) led to a partial decrease. Here, the membrane-proximal Arg201 and Arg203 unveiled as especially relevant (Figure 4.16D, Table 4.1, conducted by K. Geistlinger). Overall, the results ascribe a new role to basigin in MCT1 functionality. Apparently, the membrane-proximal Ig-I domain serves as a proton and substrate harvesting antenna to create a microenvironment that pools substrate and co-substrate at the extracellular transporter

surface and drives L-lactate influx according to Le Chatelier's principle. This allows for apparent thermodynamic equilibrium constants K > 1 driving L-lactate influx to concentrations well above those the buffer conditions would allow.

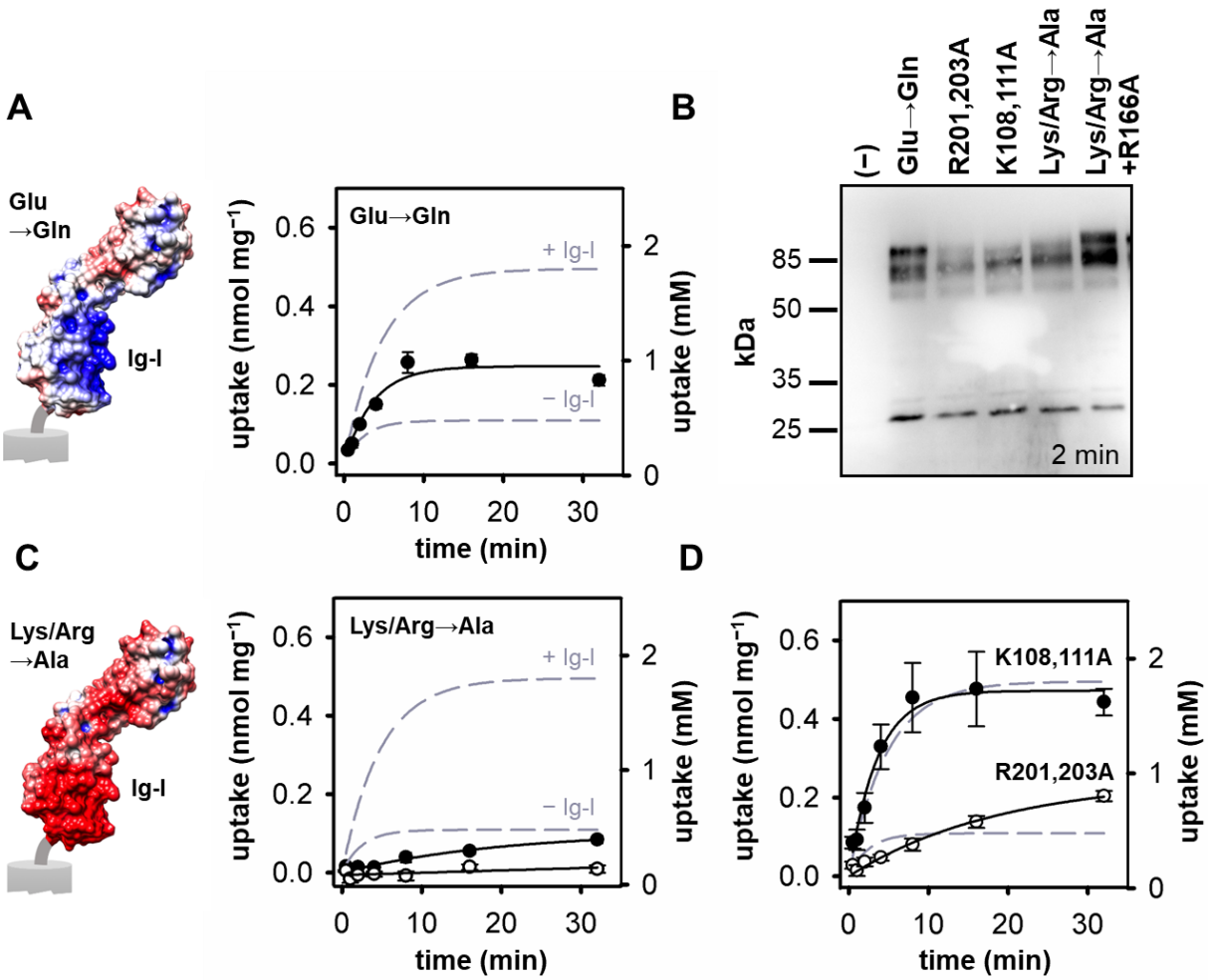

Figure 4.16. Effect of neutralizing the charged patches in the BSG Ig-I domain on overall surface potentials and L-lactate transport via fused MCT1. **(A)** The five Glu residues of the negative patch were mutated to Gln. The resulting surface potential as well as the L-lactate uptake of cells expressing BSG Ig-I Glu→Gln fused to MCT1 is shown. **(B)** Western blot (10 µl per lane) of the microsomal fractions for all mutant constructs. Protein was detected via a His-tag-targeting antibody. Microsomal fractions of non-expressing cells were used as control. The exposure time is indicated. **(C)** The Lys/Arg residues of the positive patch were mutated to Ala. The resulting surface potential as well as the L-lactate uptake of cells expressing MCT1 fused to the BSG Ig-I mutant Lys/Arg→Ala without (●) and including (o) the salt bridge-associated R166A mutation (+R166A) is shown. **(D)** Stepwise mutation of Lys/Arg residues of the positive patch and L-lactate uptake of MCT1 fused to the mutants BSG Ig-I K108,111A (●) and R201,203A (o). In all cases, L-lactate uptake over time was monitored (pH 6.8, 1 mM inward gradient) and displayed in nmol mg^{-1} (left axis) and mM (right axis). The dashed lines indicate the corridor between uptake of MCT1 alone (lower border) and fused to wildtype BSG Ig-I (upper border). Data represent mean ± SEM of three biological replicates. Data for constructs BSG Ig-I Lys/Arg→Ala, K108,111A and R201,203A was collected by K. Geistlinger.

4.2. Cys159: a target for cysteine-modifiers in the MCT1 hinge region

In common mammalian or *Xenopus* oocyte expression systems, either the expression of endogenous basigin variants or an insufficient targeting of MCTs in their absence interferes with resolving basigin-independent MCT1 characteristics. The results from section 4.1. have demonstrated a functional expression of human MCT1 in the absence of an accessory protein in *S. cerevisiae*. This gave the unique opportunity to investigate specific MCT1 characteristics and inhibitor sensitivities without basigin interference. The functional fusion to basigin then allowed to unveil the distinct involvement of basigin in MCT1 inhibitor efficacy. MCT1 alone and in fusion with basigin exhibited transport activities that allowed for inhibitory studies and the determination of initial transport rates from single time point measurements. According to the uptake-over-time curves from section 4.1., measurements after 2 min appeared most suitable. Transport activities in % were then derived from relating transport rates of substance-treated and solvent-treated cells. The testing for basigin effects was done with the most active BSG Ig-I/C2-MCT1 fusion construct carrying both Ig-like domains (see Figure 4.5) which is now referred to as BSG-MCT1.

4.2.1. AZD3965 and pCMBS are direct inhibitors of MCT1

AstraZeneca developed a potent inhibitor of human monocarboxylate transporter 1, namely AZD3965 [100]. To date, the specific mode of action was unresolved as well as the significance of basigin for inhibitor potency. Here, MCT1-expressing yeast cells were pretreated with increasing concentrations of AZD3965 and resulting transport rates were determined. The results identified AZD3965 as a potent and direct inhibitor of MCT1 with a determined IC_{50} value of 96 ± 2 nM (Figure 4.17A). Basigin as the interacting partner did not significantly affect inhibitor potency (IC_{50} at 118 ± 15 nM, see Figure 4.17B, unpaired, two-tailed t-test, $p > 0.05$). See Figure 4.17C for the chemical structure of AZD3965. The L-lactate transport via plasmodial transporter PfFNT was not affected (Figure 4.17D).

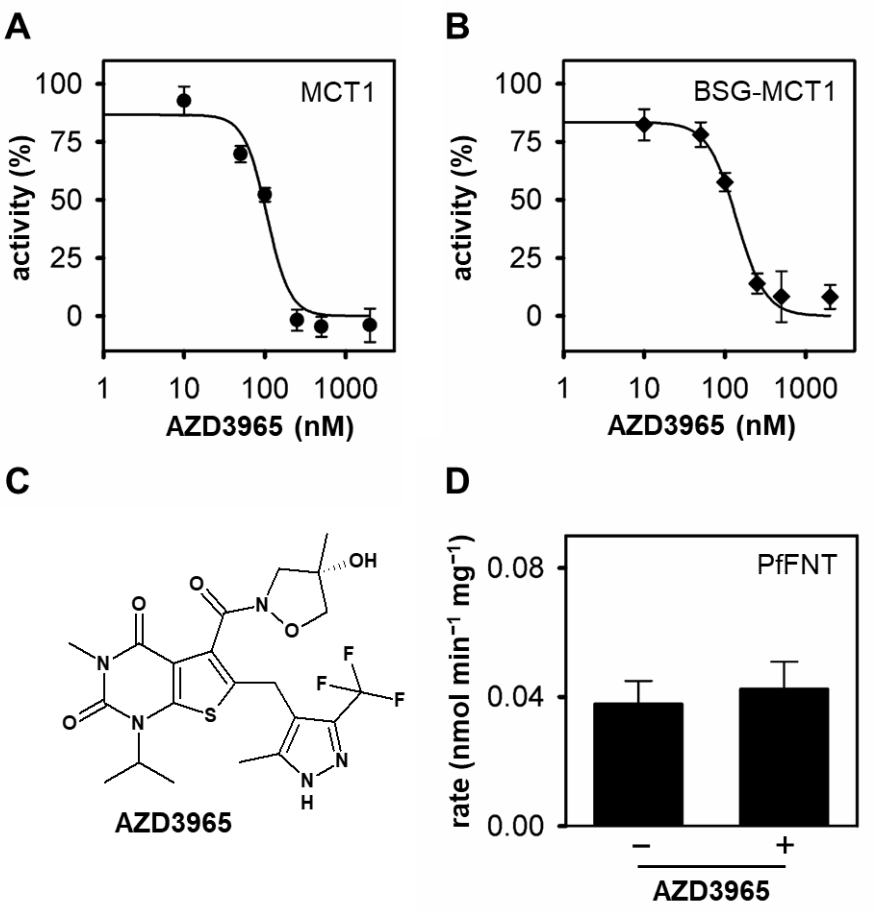

Figure 4.17. Inhibition of MCT1-mediated L-lactate transport by AZD3965. **(A, B)** IC_{50} curves showing the % activity of L-lactate transport by MCT1 alone **(A)** and fused to basigin **(B)**. Expressing cells were pretreated with increasing concentrations of AZD3965 (15 min, RT). L-lactate uptake rates were determined in the initial phase of transport (2 min). For % activities, transport rates of inhibitor-treated cells were related to solvent-exposed cells. Background of non-expressing cells was subtracted, and data represent mean ± SEM of three technical replicates. To confirm IC_{50} values, the activity at 100 nM represents mean ± SEM of 9 technical replicates including three biological replicates. **(C)** Chemical structure of the MCT1 inhibitor AZD3965. **(D)** L-Lactate uptake rates of cells expressing plasmodial PfFNT with (+) and without (−) pretreatment with AZD3965 (500 nM, 15 min). Background of non-expressing cells was subtracted, and data represent mean ± SEM of three biological replicates.

The organomercurial *p*-chloromercuribenzene sulfonate (pCMBS) (Figure 4.18A), on the other hand, has been suggested as an indirect inhibitor of MCT activity via covalent modification of its accessory protein basigin [70]. Noteworthy, pCMBS is known for the inhibition of transport via MCT1 and 4, but not MCT2 [146]. The exact mode of action remained unclear. In this study, the modification of MCT1-expressing cells revealed pCMBS as a direct inactivator of MCT1 (Figure 4.18B). In the absence of basigin, a time-dependent inhibition of L-lactate uptake resulted in an almost complete inactivation after 15 minutes. The fusion to basigin did not alter the inhibition profile negating the possibility of additive effects of indirect and direct inhibition

(Figure 4.18C). The advantage of basigin-independent MCT1 expression and functionality in yeast therefore allowed to reveal a sensitivity of MCT1 towards cysteine-modifying compounds – a piece of the puzzle not addressable in human or *Xenopus* oocyte-based expression systems.

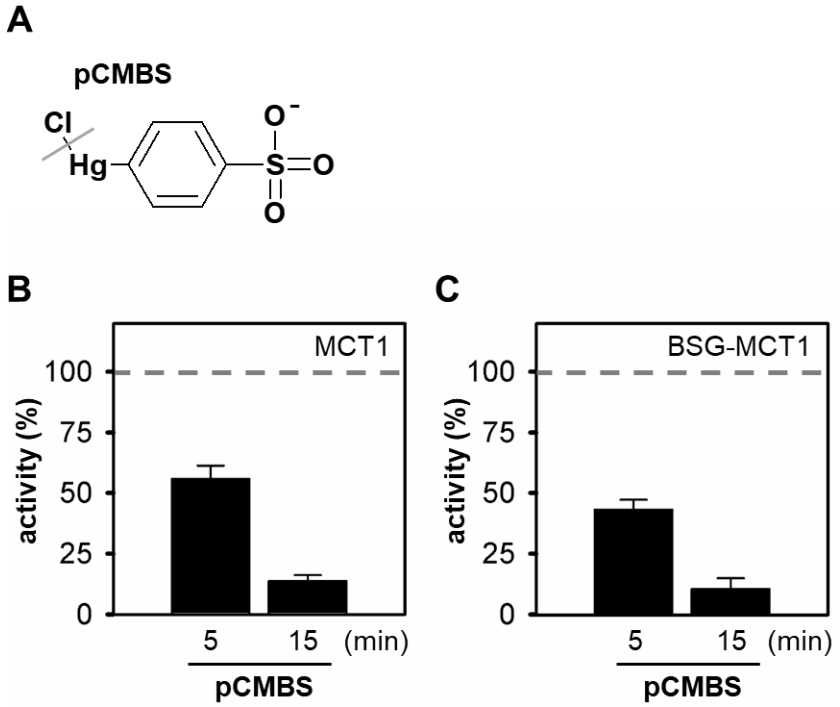

Figure 4.18. Inhibition of MCT1-mediated L-lactate transport by pCMBS. **(A)** Chemical structure of *p*-chloromercuribenzene sulfonate (pCMBS). **(B, C)** Cells expressing MCT1 alone **(B)** and in fusion with BSG **(C)** were preincubated with pCMBS (30 µM, RT) for 5 and 15 min**.** Shown is the percental L-lactate uptake activity in the initial phase of transport (2 min) compared to solvent-exposed cells. Background of non-expressing cells was subtracted, and data represent mean ± SEM of three biological replicates.

4.2.2. Cys159 of MCT1 is solvent-accessible and the sole target for pCMBS

The membrane-impermeable pCMBS is known for its reactivity and the covalent modification of solvent-accessible cysteine residues in proteins. MCT1 contains 12 cysteines in total (highlighted in red/blue/green in Figure 4.19). The exclusion of all cysteines previously disqualified as the target for pCMBS inhibition of MCT1 (Cys106,188,189 [70]; colored blue in Figure 4.19A) and limiting the potential cysteines to those existing in both pCMBS-sensitive MCT members MCT1 and 4 (see Figure 4.19B for sequence alignment) unveiled Cys159 (Figure 4.19A, green) as a likely candidate for modification by pCMBS.

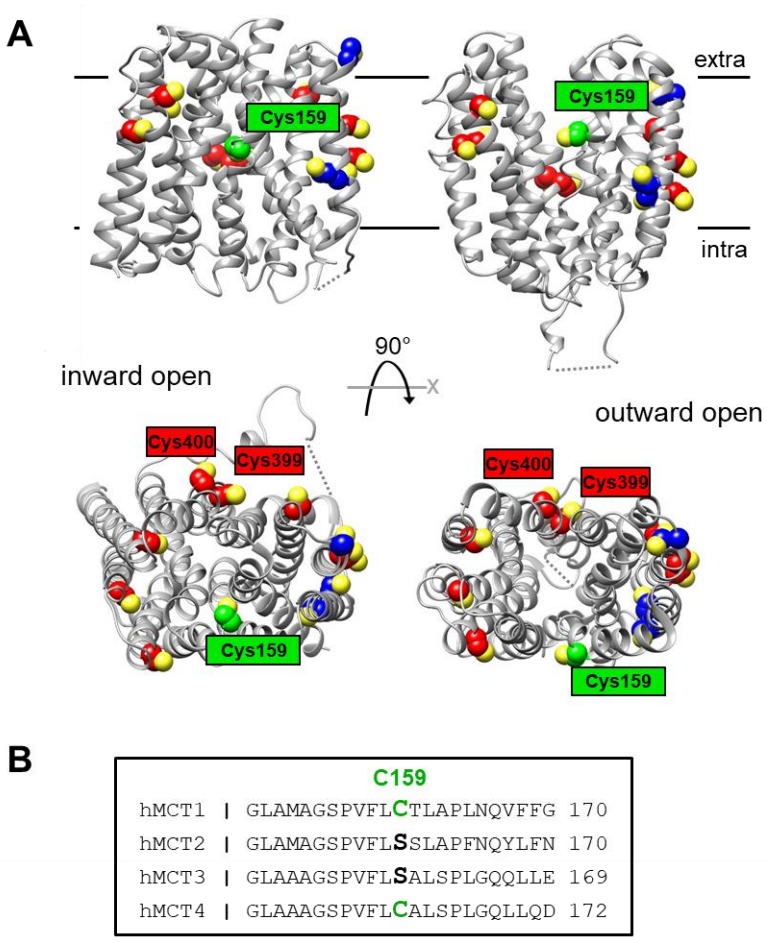

Figure 4.19. MCT1 structure models in the inward and outward open conformations. **(A)** MCT1 was modeled onto the cryo-EM/crystal structures of human MCT2 (inward open, PDB #7BP3, left) and the bacterial MCT homolog SfMCT (outward open, PDB #6HCL, right), respectively. Models are shown in side-view (from inside the plasma membrane, top) and in top-view (from the extracellular space, bottom). All existing cysteines are highlighted in red, blue (cysteines mutated in [70]) and green (Cys159). Sulfur atoms are colored yellow. **(B)** Sequence alignment of human MCT1−4. Cys159 in MCT1 is marked green and respective residues in other MCT members are highlighted in green/black.

The recently published structures of human MCT2 [55] and the bacterial homolog SfMCT [54] enabled structure modeling in the inward and outward open conformations. Strikingly, Cys159 sits in a central position of the extracellular binding pocket of MCT1 that appears as a possible hinge region of MCT1. Although buried in the closed conformation (MCT2-based model), structural reorientation exposes Cys159 as a solvent-accessible residue in the outward open conformation (SfMCT-based model). Cys159 was mutated to serine (C159S) in this study and the resulting protein expression levels and transport rates were comparable to the wildtype protein (Figure 4.20A and B; compare to Table 4.1). The slightly lower transport rates most likely arise from single time point deductions instead of accurate curve fittings.

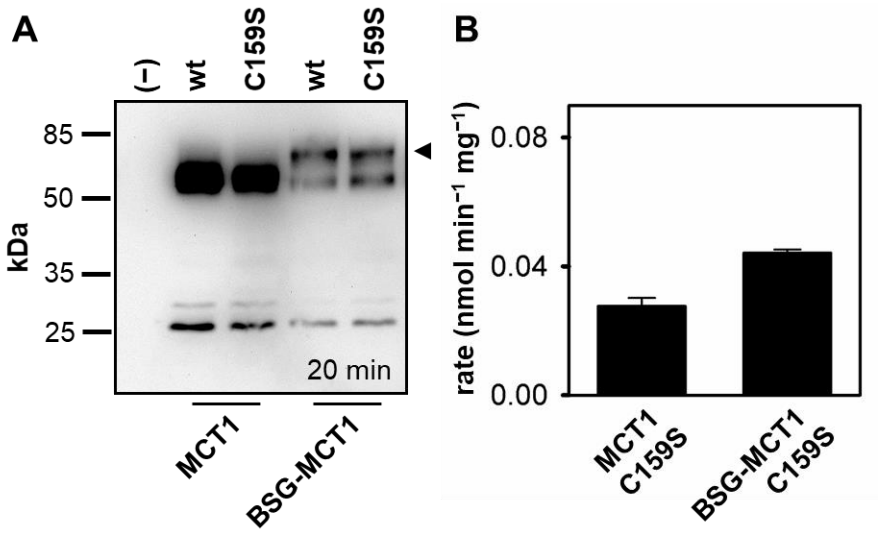

Figure 4.20. Expression and L-lactate transport of MCT1 Cys159 mutants. **(A)** Western blot of microsomal fractions from cells expressing wildtype MCT1 and C159S mutants alone and in fusion with BSG (arrowhead). 5 µg of total protein were loaded per lane. Protein was detected via a His-tag-targeting antibody. Microsomal fractions of non-expressing cells served as control. Exposure time is indicated. **(B)** Initial transport rates of cells expressing MCT1 C159S alone and in fusion with BSG. Rates for L-lactate uptake were determined in the initial phase of transport (2 min) and normalized to 1 mg cell weight. Background of non-expressing cells was subtracted. Data represent mean ± SEM of three biological replicates.

Strikingly, the C159S mutation rendered MCT1 insensitive to a modification by pCMBS (Figure 4.21). Even a prolonged incubation for 15 min did not reduce the transport activity. The fusion with basigin did not rescue inhibitor sensitivity again confirming its irrelevance for pCMBS inhibition.

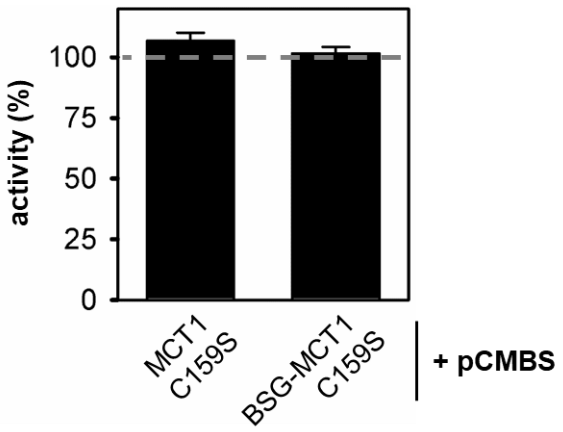

Figure 4.21. Treatment of MCT1 C159S mutants with pCMBS. Cells expressing the MCT1 C159S mutant alone and in fusion with BSG were preincubated with pCMBS (30 µM, RT) for 15 min**.** Shown is the percental L-lactate uptake activity in the initial phase of transport (2 min) compared to solvent-exposed cells. Background of non-expressing cells was subtracted, and data represent mean ± SEM of three biological replicates.

MCT1 in rat erythrocytes (rMCT1) has previously been shown as being non-reactive towards pCMBS [70]. This has been attributed to its close association with embigin rather than basigin. An alignment of rat and human MCT1 revealed rMCT1 as a natural C159S variant (Figure 4.22A). Rat MCT1 has already been shown to be functionally expressed in yeast [104]. Here, rMCT1 was expressed in *S. cerevisiae* although the minor expression level (Figure 4.22B) allowed a low initial transport rate of 0.004 ± 0.001 nmol min^{-1} mg^{-1} in the absence of an accessory protein (Figure 4.22C). Nonetheless, in contrast to human MCT1, rMCT1 was insensitive to pCMBS underlining the necessity of a cysteine at position 159 (Figure 4.22C).

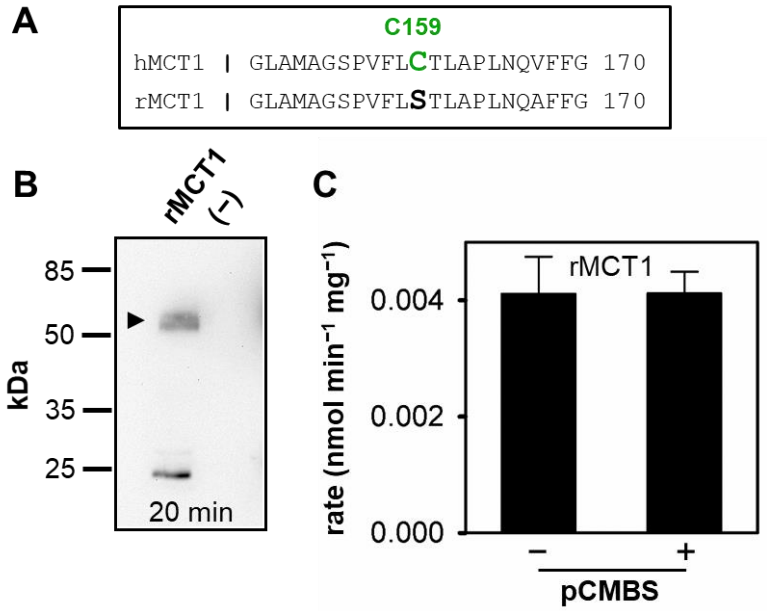

Figure 4.22. Expression, functionality, and treatment of rMCT1-expressing cells with pCMBS. **(A)** Sequence alignment of human and rat MCT1. Cys159 in MCT1 (green) and the respective serine in rat MCT1 (black) are indicated. **(B)** Western blot of microsomal fractions showing the expression of rMCT1 (arrowhead) in *S. cerevisiae*. 5 µg of total protein were loaded per lane. Protein was detected via a His-tag-targeting antibody. Microsomal fractions of non-expressing cells served as control. The exposure time is indicated. **(C)** Initial transport rates for L-lactate uptake of rMCT1-expressing cells with (+) and without (−, ddH_2O) pretreatment with pCMBS (30 µM, 15 min) were determined in the initial phase of transport (4 min) and normalized to 1 mg cell weight. Background of non-expressing cells was subtracted, and data represent mean ± SEM of three biological replicates.

4.2.3. Smaller thiosulfonates allow for only partial inhibition of MCT1

pCMBS as a very bulky compound blocked MCT1-mediated transport completely and demonstrated the reactivity of MCT1 towards cysteine-modifying reagents. The covalent

modification of reactive cysteines with a set of methanethiosulfonate (MTS) reagents differing in size, charge and membrane permeability is a common tool to directly alter protein characteristics and structural properties without dealing with changed expression levels that accompany amino acid substitutions. MTS reagents are usually applied at concentrations of 1 to 10 mM and allow for complete and – in the absence of reducing agents – irreversible conversion of reactive cysteines to the corresponding disulfide in a 1 to 5 min time range. Four non-charged MTS reagents of different size (Figure 4.23A) were tested to investigate their effect on MCT1-mediated L-lactate transport. Strikingly, all tested substances (1 mM, pretreatment for 5 min at RT) decreased the initial transport rates to a residual activity between 46-75 % (Figure 4.23B). The apparent differences in the efficacy most likely arise from varying reactivity and/or accessibility between compounds. Nonetheless, none of the substances was able to completely inactivate MCT1 at the applied assay conditions. 2-Sulfonatoethyl methanethiosulfonate (MTSES) as a medium-sized, negatively charged compound showed no activity towards MCT1. Most importantly, even methyl methanethiosulfonate (MMTS) as the smallest, non-charged member introducing only a thiomethyl group decreased the MCT1 activity to 57 ± 7 %. A prolonged incubation (up to 15 min) with MMTS did not have further effects indicating the complete conversion of cysteines. Thereby, a complete transporter inactivation could not be achieved with the small-sized MMTS. This hints at a mechanism in which a modification of the transporter hinge serves as a wedge and locks the transporter size-dependently in an outward open conformation.

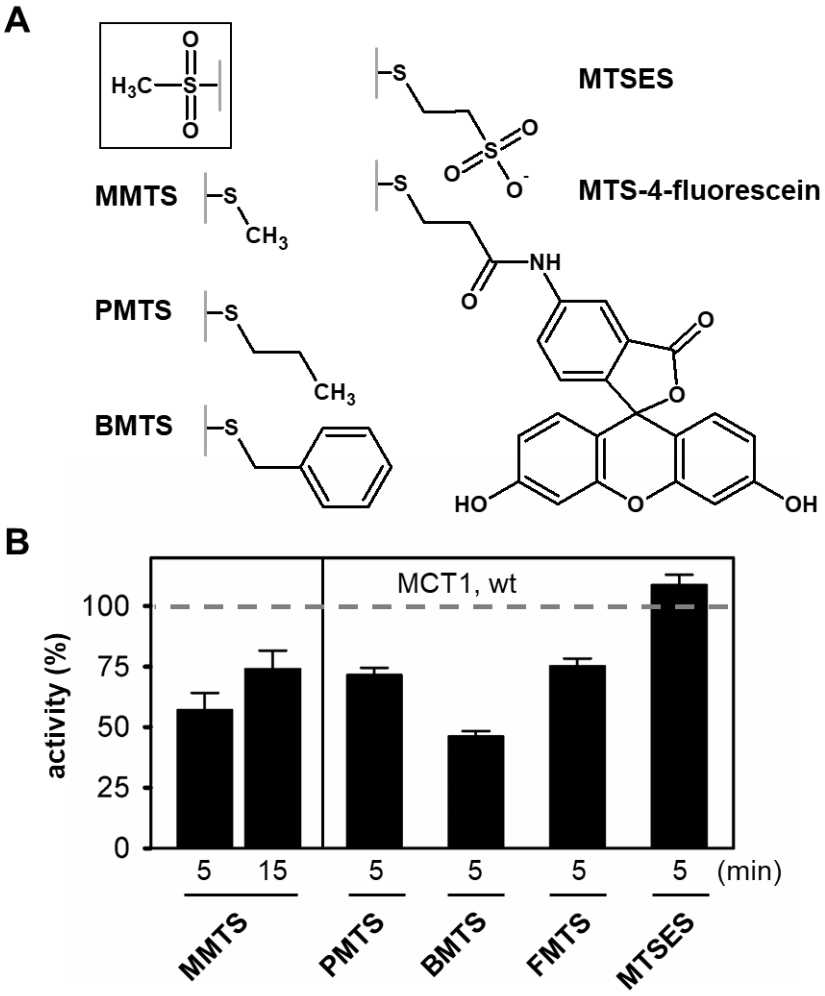

Figure 4.23. Treatment of MCT1-expressing cells with methanethiosulfonate (MTS) reagents. **(A)** Chemical structures of methyl MTS (MMTS), propyl MTS (PMTS), benzyl MTS (BMTS), 2-sulfonatoethyl MTS (MTSES) and MTS-4-fluorescein (FMTS). The mutual core structure (framed) and the respective cysteine-transferred moieties of each reagent are indicated. **(B)** Cells expressing wildtype MCT1 were preincubated with MTS reagents (1 mM, RT) for the time indicated**.** Shown is the percental L-lactate uptake activity in the initial phase of transport (2 min) compared to solvent-exposed cells. Background of non-expressing cells was subtracted, and data represent mean ± SEM of three biological replicates.

A persisting inhibition (30.3 % activity) even after the removal of non-reacted, excess MMTS prior to the L-lactate uptake assay confirmed a covalent modification and excluded unspecific competitive effects (Figure 4.24A). Cells expressing the plasmodial lactate transporter (PfFNT) with no apparent solvent-exposed, targetable cysteines were resistant to MMTS treatment confirming an MCT1-directed effect (Figure 4.24B).

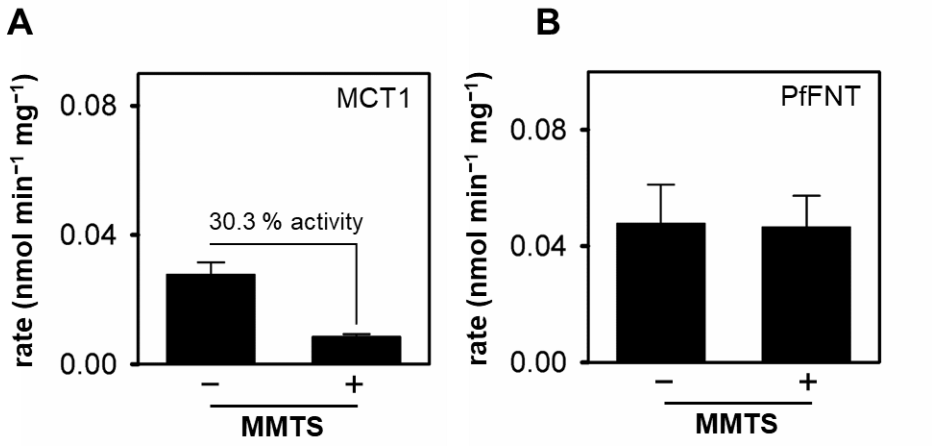

Figure 4.24. Modification by MMTS is covalent and MCT1-directed. **(A)** Cells expressing wildtype MCT1 were preincubated with MMTS (1 mM, 5 min, RT) and, in contrast to the previous protocol, non-reacted reagent was removed by centrifugation prior to determining L-lactate uptake rates. The graph depicts L-lactate uptake rates with (+) and without (−, ddH_2O) MMTS pretreatment. The % activity after MMTS treatment compared to solvent-exposed cells is indicated. **(B)** To confirm MCT1-specific inhibition, cells expressing PfFNT were preincubated with MMTS (1 mM, 5 min, RT, standard protocol). In both cases, rates were determined in the initial phase of transport (2 min). Background of non-expressing cells was subtracted, and data represent mean ± SEM of three biological replicates.

To test whether Cys159 was covalently modified by MMTS, the accessibility of Cys159 for pCMBS after MMTS treatment was examined (Figure 4.25A). Affirmatively, a MMTS pretreatment obstructed the inhibitory effect of pCMBS. The preincubation with non-inhibiting MTSES, on the other hand, still allowed a reactivity of pCMBS towards Cys159.

Strikingly, the mutation of Cys159 to serine did not confer resistance towards the MTS reagents (Figure 4.25B). As with the wildtype MCT1, MMTS inhibited transport via the C159S mutant to 50 ± 4 % activity suggesting that Cys159 is not the only target for MMTS.

The results demonstrate that although Cys159 was not decisive for inhibition, MMTS modified Cys159 among other relevant cysteines allowing for partial inhibition of the transporter function.

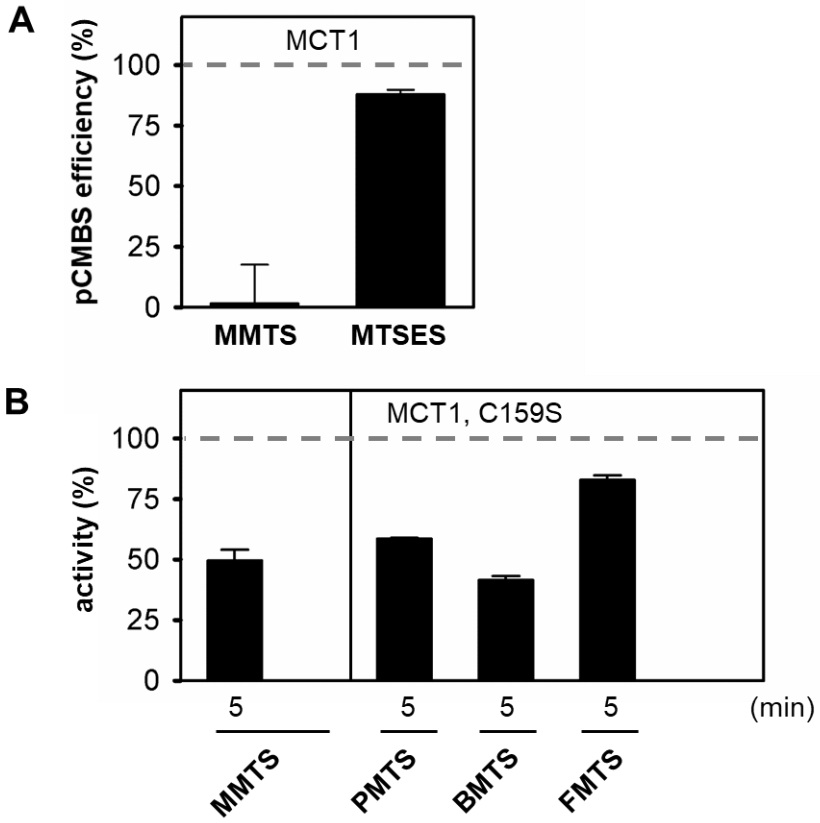

Figure 4.25. Site-specificity of MCT1 modification by MTS reagents. **(A)** Cells expressing wildtype MCT1 were preincubated with MMTS/MTSES (1 mM, 5 min, RT) and subsequently subject to further modification by pCMBS (30 µM, 15 min, RT). The L-lactate uptake activity in the initial phase of transport was compared to MMTS/MTSES-treated cells lacking the additional pCMBS modification (solvent-exposed). Efficiency was then determined as 100 %−% activity after pCMBS treatment. After MMTS/MTSES treatment, excess inhibitor was removed by centrifugation prior to modification with pCMBS. **(B)** Analogous to Figure 4.23, cells expressing the MCT1 C159S mutant were preincubated with MTS reagents (1 mM, RT) for 5 min**.** Shown is the percental L-lactate uptake activity in the initial phase of transport compared to solvent-exposed cells. In both cases, background of non-expressing cells was subtracted, and data represent mean ± SEM of three biological replicates.

Most cysteines of MCT1 outline a ring within the central plane of MCT1 with only Cys399 and Cys400 slightly extending into the transport path and therefore possibly accessible for the modification by MTS reagents (see Figure 4.19A). The MCT1 mutants C399S and C400S (as single and as C159S double mutants) were expressed and functional (Figure 4.26A, B). Noteworthy, a C399S/C400S double mutation was not tolerated leading to expressed but non-functional protein attributing these two additional cysteines a relevance in transporter function and/or folding (Figure 4.26A, B). Nonetheless, the C399S and C400S single mutants still showed sensitivity towards MMTS also in combination with the C159S mutant (42−59 % activity) (Figure 4.26C).

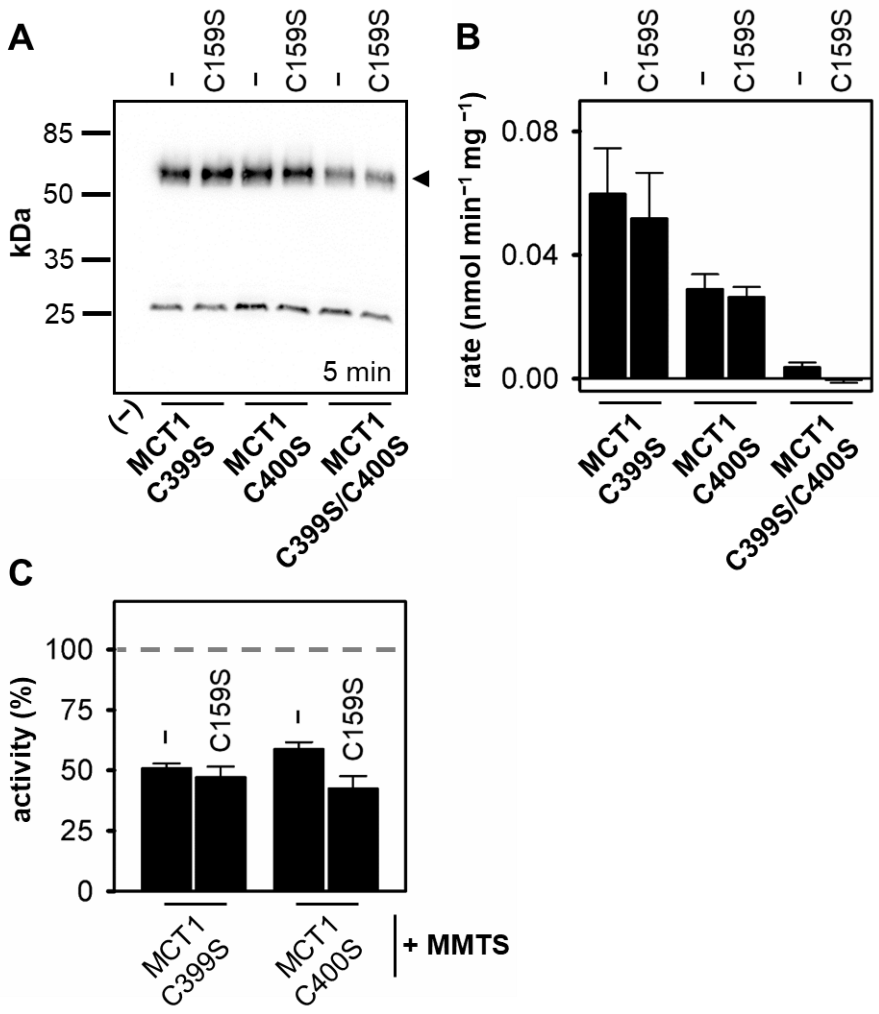

Figure 4.26. Expression, functionality, and inhibition of MCT1 mutants C399S and C400S by MMTS. **(A)** Western blot of microsomal fractions showing the expression of MCT1 C399S/C400S single, double and triple mutants in *S. cerevisiae* (arrowhead). 10 µg of total protein were loaded per lane. Protein was detected via a His-tag-targeting antibody. Microsomal fractions of non-expressing cells served as control. The exposure time is indicated. **(B)** Initial transport rates for L-lactate uptake of cells expressing the respective MCT1 mutants were determined in the initial phase of transport (2 min) and normalized to 1 mg cell weight. **(C)** Percental L-lactate uptake activity of MMTS-treated (1 mM, 5 min) compared to solvent-exposed cells. For **(B)** and **(C)**, background of non-expressing cells was subtracted, and data represent mean ± SEM of three biological replicates.

In conclusion, two known modifiers of MCT1, AZD3965 and pCMBS, were examined in the yeast system elucidating their action as MCT1-directed and basigin-independent. The organo-mercurial pCMBS inactivated MCT1 and revealed Cys159 as the critical residue. Introducing a smaller wedge, i.e. MMTS, substantially reduced the selectivity towards Cys159 and allowed for an only partial inhibition revealing this region as a potential transporter hinge.

4.3. Generation of samples for a structure elucidation of the basigin-MCT1 complex using electron microscopy

The expression of human MCT1 as fusion protein with its chaperone unveiled basigin as a direct transport modulator. The crystal structure of basigin's extracellular domain allowed the calculation of electrostatic surface potentials and enabled the elucidation of basigin as an extracellular substrate antenna that drives L-lactate influx via MCT1. To corroborate the results and better understand the exact mechanism, a cell-based and a cell-free strategy launched experiments on a structure elucidation of the basigin-MCT1 complex.

4.3.1. Expression of MCT1 constructs in *P. pastoris*

S. cerevisiae turned out to be a well-suited and valuable expression system for human MCT1. To profit from a system that allows for large-scale production and eukaryote-compatible posttranslational modification, *Pichia pastoris* was tested for recombinant expression of MCT1. The coding sequence of MCT1 alone and in fusion with basigin variant 1 (BSG var1; BSG var2 was not yet produced and available) was cloned into a suitable expression vector and electroporated into an adenine-auxotroph *P. pastoris* strain. The cells were grown on adenine dropout medium and transformants appeared as white colonies. The successful integration of the coding gene sequence of MCT1 constructs (MCT1: 1660 bp, + BSGvar1: 2821 bp) in selected colonies was confirmed via colony PCR with only one colony not carrying the coding DNA (Colony 3 of BSG var1-MCT1 transformed cells, Figure 4.27A, B).

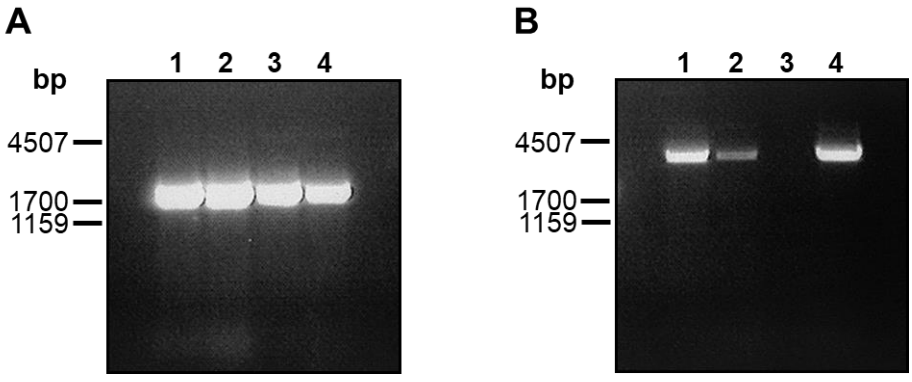

Figure 4.27. Colony PCR showing a successful transformation of *P. pastoris*. Transformants (1−4) were picked, and colony PCR was conducted using suitable primers to amplify successfully integrated coding sequences for MCT1 (**A**, 1660 bp) and BSG var1-MCT1 (**B**, 2821 bp). 10 µl of PCR products were separated via agarose gel electrophoresis and DNA was detected with intercalating ethidium bromide.

In several small- and medium-scale set-ups of different tested growth and induction conditions (see methods section 3.3.3), the transformants were cultivated and cell mass was produced in glycerol-based medium. The gene expression was induced by switching to methanol-based medium. Unfortunately, SDS-PAGE and Western blotting failed to show any expression of human MCT1 in three tested colonies (Figure 4.28A). The expression of the BSG var1-MCT1 fusion protein was equally inefficient with only faint fragmentary bands detectable (Figure 4.28B).

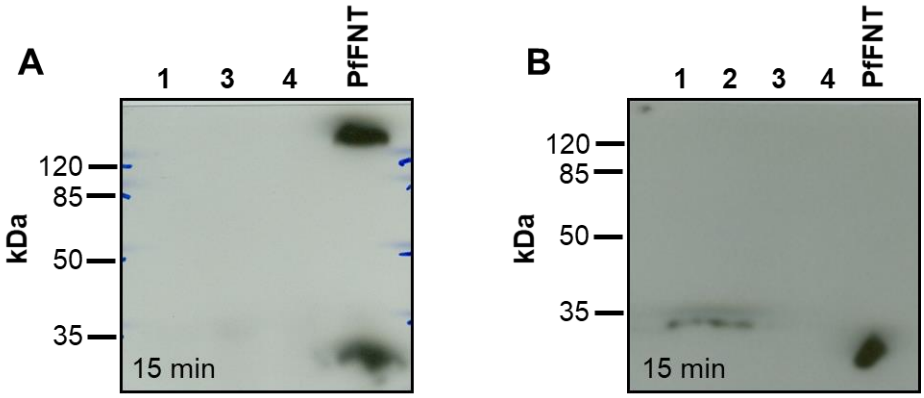

Figure 4.28. Western blot of lysed *P. pastoris* cells. After the induction of protein expression, cells were lysed, and protein (10,000 *g* fraction) was separated using SDS-PAGE. 70 µg **(A)** and 30 µg **(B)** of total protein were loaded per lane. Subsequent Western blotting enabled the detection of recombinant protein using a His-tag-targeting antibody. Shown are lysates for 3−4 colonies transformed with plasmids encoding MCT1 **(A)** or BSG var1-MCT1 **(B)** as well as plasmodial PfFNT. Exposure times for both blots are indicated.

In line with previous literature [147], the expression of the plasmodial PfFNT (monomer: 37 kDa, pentamer: 185 kDa) was successful (Figure 4.28A, B) and ensured a well-working protocol and an efficient induction of gene expression. In this study, in contrast to *S. cerevisiae*, *P. pastoris* emerged as non-suitable to express human MCT1 and excluded subsequent experiments for structure elucidation.

4.3.2. Detergent- and nanodisc-based cell-free synthesis of MCT1 constructs

The cell-free synthesis of recombinant proteins using a cell-extract-based technology profits from controllable and rapid production of proteins prone to proteolysis by a living host. The method used in this study relied on the transcription and translation from a DNA template encoding the protein of interest and using *E. coli*-based extracts and recombinantly produced components to complete the gene expression machinery *in vitro*. The specific synthesis of

membrane proteins, e.g. MCT1 and basigin, needed a supplementation by either detergents or protein-lipid nanodiscs to provide a membrane-mimicking environment and ensure a sufficient protein solubilization and correct folding.

Here, in a detergent-based, continuous-exchange cell-free system (CECF), MCT1 was initially produced as a GFP fusion protein to indicate correct folding of the synthesized protein [113] and screen for optimal detergent conditions. In a duplicate set-up using five different detergents, the MCT1-GFP fusion protein was synthesized and purified using Ni^{2+}-NTA affinity chromatography. The proteins were separated by SDS-PAGE and subsequently detected via Western blotting and in-gel fluorescence (Figure 4.29A, B). Whereas *n*-dodecyl-β-D-maltopyranoside (DDM) emerged as non-suitable, all four detergents of the Brij® family enabled the synthesis of human MCT1. Western blotting confirmed the synthesis of full-length MCT1-GFP fusion protein at around 85-100 kDa (theoretical molecular weight: 85 kDa). Despite differences in band intensities between duplicates, Brij®58 and Brij®78 enabled the synthesis of MCT1 most effectively. The in-gel fluorescence confirmed the detection of correctly folded fusion protein at 85 kDa indicating that a considerable amount of synthesized protein was misfolded (most bands in Western blots appeared at a slightly higher molecular weight). Only the Brij®58- and Brij®78-based synthesis resulted in the appearance of distinct bands at 85 kDa in the Western blots confirming Brij®58 and Brij®78 as suitable detergents for the cell-free synthesis and solubilization of MCT1.

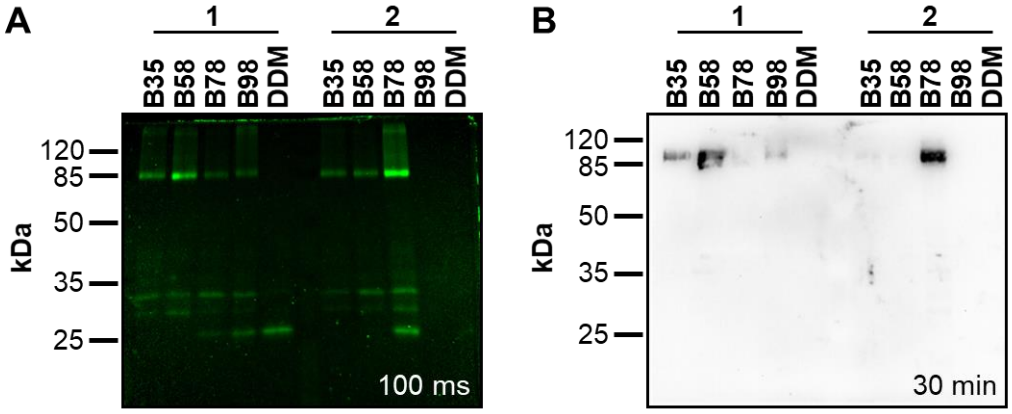

Figure 4.29. Cell-free synthesis of MCT1-GFP and detergent screen in analytical scale. Elution fractions (16 µl) from Ni^{2+}-NTA affinity purification were separated by SDS-PAGE and protein was detected via in-gel fluorescence **(A)** and Western blotting **(B)** (His-tag-targeting antibody). Four detergents of the Brij® series (B35─B98) and *n*-dodecyl-β-D-maltopyranoside (DDM) were tested as solubilizing agents. Each detergent was tested in a duplicate set-up (1 and 2). Exposure times are indicated.

The successful cell-free production of MCT1 alone laid the foundation of synthesizing MCT1 in fusion with basigin. Given the basigin splice variant 2 as the most prevalent variant in human cells and given its elucidated direct role in MCT1-mediated L-lactate transport, the BSG var2-MCT1 fusion construct was inserted into the cell-free expression vector and produced as a GFP fusion construct. Analogously to the functionality assay, the protein fusion aimed at a production in a stoichiometric manner and a close association of both proteins at all times.

Two techniques were tested to gain high yields of correctly folded BSG var2-MCT1 fusion protein: the detergent-based production using Brij®78 as solubilizing agent, and a nanodisc-based technology. The latter method was developed by C. Hansen who assembled 1,2-dioleoyl-*sn*-glycero-3-phospho-(1'-*rac*-glycerol) (DOPG)- and 1-palmitoyl-2-oleoyl-*sn*-glycero-3-phospho-(1'-*rac*-glycerol) (POPG)-based nanodiscs using MSP1E3D1 as membrane scaffold protein (see Master's thesis of C. Hansen [119]). These nanodiscs were here used to support a co-translational reconstitution of the basigin-MCT1 fusion protein. In contrast to detergent-based cell-free synthesis, the nanodisc technology mimics the natural lipid-bilayer environment of plasma membranes and is an emerging technique to optimize protein folding and integrity.

All following experiments on the protein production and structure elucidation were done in collaboration with C. Hansen. The figures shown can also be found in the Master's thesis of C. Hansen [119]. The synthesis of the BSG var2-MCT1-GFP fusion construct using Brij®78 and three increasing concentrations of DOPG- and POPG-nanodiscs for reconstitution was initially evaluated with SDS-PAGE and Western blotting (Figure 4.30A−D). In line with the results for MCT1 alone, Brij®78 enabled the synthesis of the fusion construct. The Western blot analysis using two specific antibodies detected the full-length construct as a distinct band just above 120 kDa. Strikingly, an additional band of higher molecular weight indicated either aggregates or the formation of protein dimers that had not been observable when producing MCT1 alone. In contrast, DOPG- and POPG-nanodisc-based synthesis resulted in a comparably low protein yield only detectable using the GFP-directed antibody and DOPG-based nanodiscs. A His-tag-directed antibody failed to detect the fusion protein. Bands just below 35 kDa represented the His-tag-carrying nanodisc belt proteins. The apparent high sensitivity of the GFP-targeted antibody allowed the detection of several weak bands indicating minor protein fragmentation in all approaches.

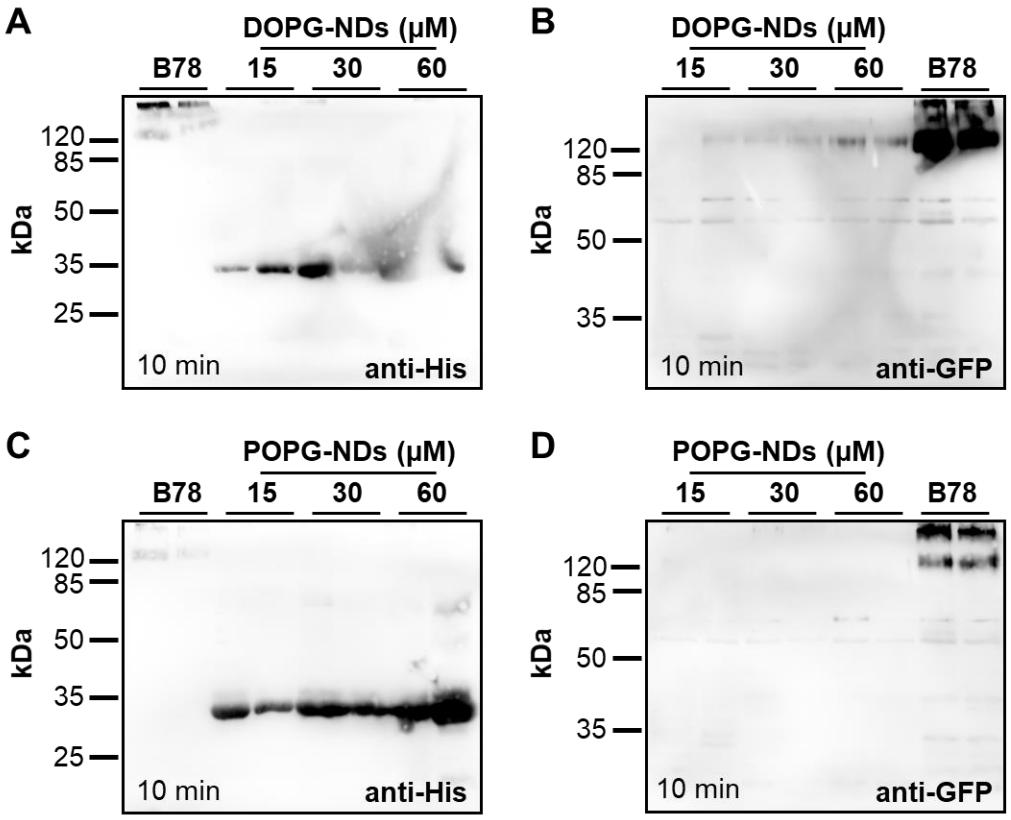

Figure 4.30. Brij®78- and nanodisc-based cell-free synthesis of BSG var2-MCT1-GFP fusion protein in analytical scale. Synthesized protein was Ni^{2+}-NTA-purified, and elution fractions (20 µl) were separated by SDS-PAGE. Protein was detected by Western blotting using a His-tag- (**(A)** and **(C)**) and a GFP- (**(B)** and **(D)**) targeting antibody. Brij®78 (0.8 %) and POPG/DOPG-nanodiscs in three elevating concentrations were compared as reconstituting agents. Exposure times are indicated.

In-gel fluorescence mirrored the results from synthesizing MCT1 alone and showed distinct bands at the expected molecular weights (Figure 4.31A and B). Although the nanodisc technology generally resulted in lower yields for the full-length fusion proteins (refer to Figure 4.30), the proportion of protein detected by in-gel fluorescence to Western blotting appeared higher for the nanodisc-based synthesis than for Brij®78-solubilized protein. This indicates a more efficient native folding in the nanodisc environment with more of the protein produced being correctly folded. Moreover, raising nanodisc concentrations favored higher yields.

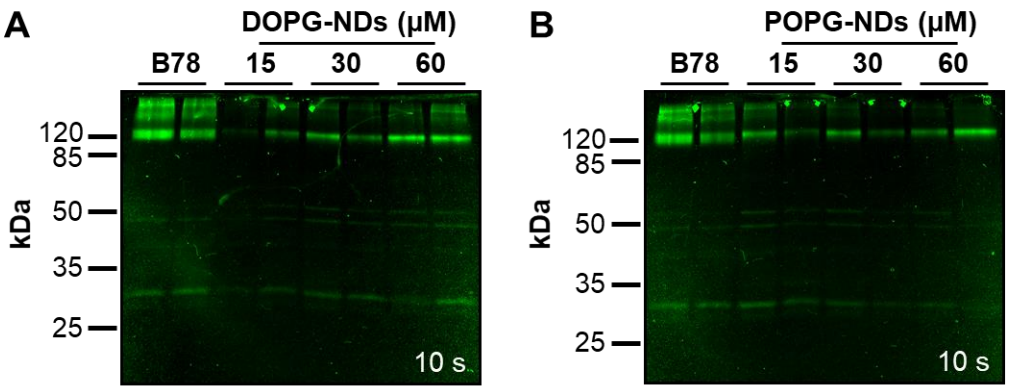

Figure 4.31. In-gel fluorescence of Brij®78- and nanodisc-based cell-free synthesis of BSG var2-MCT1-GFP. Gels used for Western blotting in Figure 4.30A and C were analyzed via in-gel fluorescence. Synthesized protein was Ni^{2+}-NTA-purified and elution fractions (20 µl) were separated by SDS-PAGE. Brij®78 (0.8 %) and DOPG- **(A)** and POPG- **(B)** nanodiscs in three elevating concentrations were compared as reconstituting agents. Exposure times are indicated.

In a large-scale, preparative set-up, the BSG var2-MCT1 fusion protein was produced without the C-terminal GFP to further purify and prepare protein for transmission electron microscopy (TEM). Both Brij®78 and POPG-nanodiscs allowed a sufficient protein synthesis (Figure 4.32). The elution fractions from step gradient Ni^{2+}-NTA affinity chromatography were separated by SDS-PAGE. Coomassie staining as well as Western blotting showed high protein yields with the target protein found at around 88 kDa (Figure 4.32).

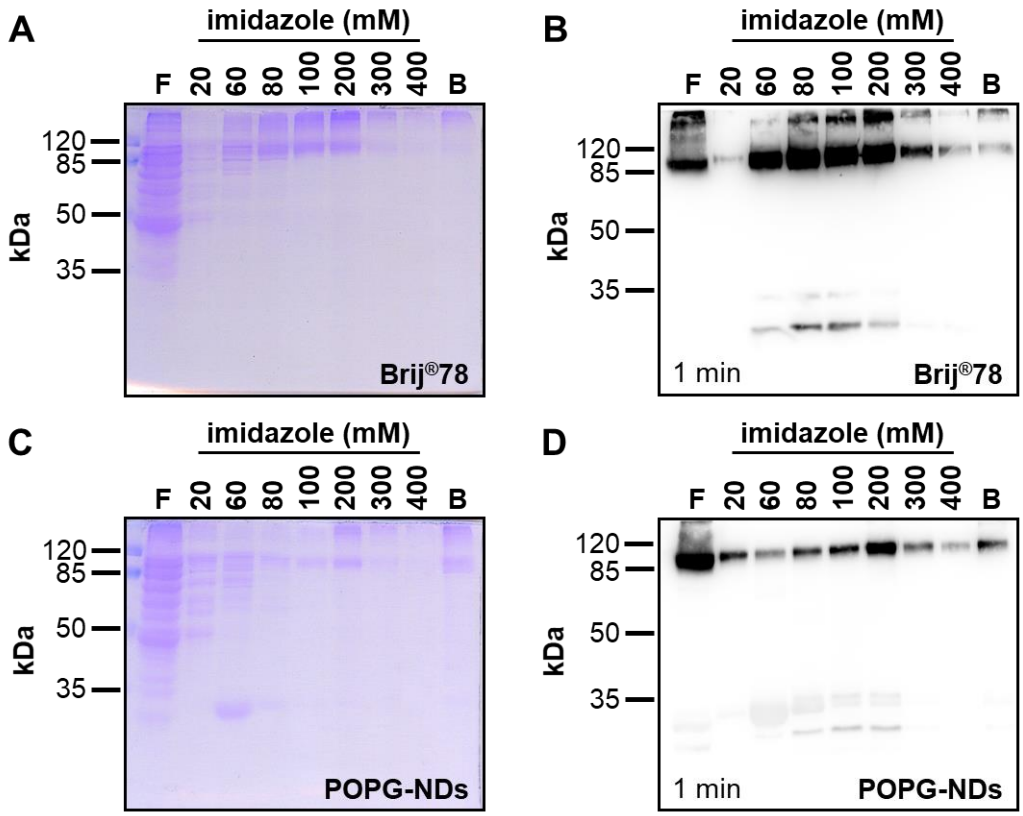

Figure 4.32. Large-scale cell-free synthesis and purification of BSG var2-MCT1 in preparative scale. Protein was synthesized and reconstituted with Brij®78 **(A, B)** or POPG-nanodiscs **(C, D)**. The elution fractions from step gradient Ni^{2+}-NTA affinity chromatography (20−400 mM imidazole) as well as the bead (B) and flow-through (F) fractions were separated by SDS-PAGE (20 µl per lane) and protein was detected with Coomassie staining **(A, C)** and Western blotting using a His-tag-targeting antibody **(B, D)**. Exposure times are indicated.

In both approaches, most of the protein was eluted with 60 to 200 mM imidazole with some of the target protein lost in the flow-through. Although the first elution fractions included several protein bands, later fractions (> 80 mM imidazole) contained highly purified protein. The protein fractions (80–400 mM imidazole) were combined and further purified using size-exclusion chromatography (Figure 4.33A, C). The size-exclusion chromatography of Brij®78- and nanodisc-reconstituted proteins equally showed three peaks eluted at high elution volumes and most likely represent imidazole as well as the protein fragments that were already observed in Western blot analysis. The purification of Brij®78-reconstituted protein additionally showed a broad and intense peak ranging from 7.5 to 12.5 ml elution volume representing at least two unresolved and overlapping peaks and a slight shoulder at 11.0 ml (arrow in Figure 4.33A). The first peak eluted after 8.5 ml contains larger molecules and emerged in both reconstitution approaches therefore most likely containing protein aggregates. In cooperation with P. Arnold (Anatomical Institute, CAU Kiel), transmission electron microscopic

(TEM) images from individual fractions were captured. TEM of the largest peak at 9.5 ml showed insufficient resolution and separation from aggregates. In contrast, TEM of the fraction collecting the peak shoulder elucidated a very homogenous probe (Figure 4.33B). Several particles of similar size were visualized and probably represent reconstituted BSG var2-MCT1. Due to the limited particle size, class-sum images to further elucidate structural properties were not calculated.

This limitation was overcome by the protein reconstitution in POPG-nanodiscs. Along with an improved protein stability, the comparably large size of protein-nanodisc particles favors structure elucidation with electron microscopic approaches [148, 149]. Size-exclusion chromatography of nanodisc-reconstituted protein showed generally smaller peaks indicating lower protein yields (Figure 4.33C). In addition to the aggregate peak at 8.5 ml, the chromatogram showed two additional, partly overlapping peak maxima at 10.5 ml and 12.0 ml. TEM of corresponding fractions revealed that the later eluted fraction probably contained non-filled nanodiscs. Along with empty nanodiscs, the 10.5 ml fraction (arrow in Figure 4.33C) suggested to additionally contain protein-filled nanodiscs with reconstituted BSG var2-MCT1 (Figure 4.33D). Single particles were subsequently analyzed to calculate class-sum images and refine structural features (Figure 4.33E). Interestingly, the particles were captured in two distinct orientations representing a top (class-sums 1−3) and a side-view (class-sums 4−6) of assembled nanodiscs.

These results laid the foundation for future attempts on structure elucidation of the basigin-MCT1 complex. In cooperation with A. Möller (Max Planck Institute of Biophysics, Frankfurt am Main), a first approach including cryo electron microscopy (cryo-EM) confirmed current observations of properly reconstituted fusion protein. Although hinting at a reconstitution of BSG var2-MCT1 as dimers, a further structure elucidation was limited given the insufficient separation of empty and protein-filled nanodiscs and an interference with class-sum calculations.

Strikingly, whilst pursuing the attempts on a structure elucidation of the basigin-MCT1 complex, a cryo-EM structure of MCT1 in association with basigin splice variant 2 was resolved at a resolution of 3.0─3.3 Å [103]. This underlines this project’s relevance and will, in the future, promote an understanding of the basigin-MCT1 interaction and transport modulation (see discussion in chapter 5).

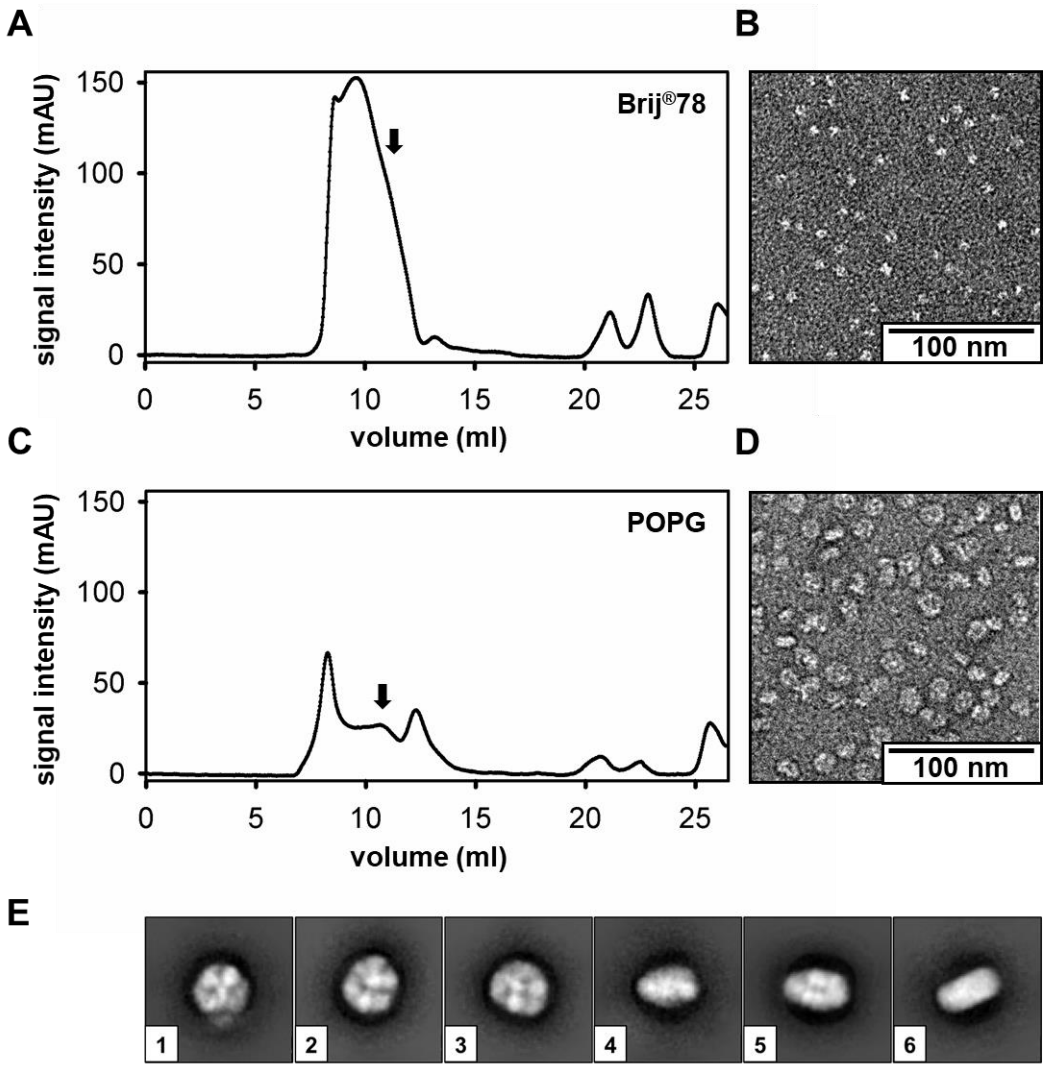

Figure 4.33. Size-exclusion chromatography and TEM of the BSG var2-MCT1 fusion protein. **(A, C)** Pooled fractions (80−400 mM imidazole) were concentrated and approximately 1.1 mg (Brij®78, **(A)**) or 0.3 mg (POPG-nanodiscs, **(C)**) of protein were injected for size-exclusion chromatography (20 mM Tris-HCl, pH 8.0, 150 mM NaCl, ± 0.05 % Brij®78 as eluent; flow rate 0.35 ml min^{-1}, detection at 280 nm). Arrows indicate fractions collected for TEM. **(B, D)** Transmission electron microscopy (TEM) of collected fractions. Representative excerpts are shown. **(E)** Class-sum images for POPG-reconstituted protein were calculated and six representative class-sums are shown.

5. Discussion and Perspective

The primal aim of this study was to investigate if basigin has a direct effect on L-lactate transport by human monocarboxylate transporter 1 (MCT1). Due to the tight dependence of the plasma membrane expression of MCT1 on basigin in commonly used mammalian cell lines and *Xenopus* oocytes, the answer to this question remained unresolved. In this study, human MCT1 was expressed using *S. cerevisiae* as the expression system. MCT1 was correctly targeted to the plasma membrane alone as well as in fusion with basigin. The unique metabolic and physiological prerequisites of *S. cerevisiae* were exploited to monitor ^{14}C-labeled substrate uptake not only in the initial phase but also in the equilibrium state of transport. Moreover, the use of MCT1 inhibitors and protein modifiers shed light on the inhibitory profile in the absence and in the presence of interacting basigin and revealed distinct transporter regions and residues crucial to maintain transporter activity.

5.1. *S. cerevisiae*: a valuable expression system for human MCT1

To study the functionality, the transport mechanism and the pharmacological properties of transmembrane transport proteins, a suitable system that either endogenously expresses or allows heterologous expression of the protein of interest is needed. Generally available systems range from prokaryotic *Escherichia coli* to eukaryotic mammalian cells with each system employing distinct (dis-)advantages. In the case of human monocarboxylate transporters, human cell lines [47, 60, 150] and *Xenopus laevis* oocytes [50, 151] are most common and have proven successful for many issues. The expression of mammalian transport proteins in their origin organism (i.e. human cell lines) profits from native protein processing, secretory pathways and trafficking. Although human cell lines represent the most natural environment, the expression of human MCTs holds several problems. Most importantly, examining transmembrane transport via MCTs in mammalian cell lines suffers from simultaneous expression of several MCT members of similar substrate specificity but differing kinetic properties (reviewed in [152]). Studies on distinct isoforms depend on the availability of cell types dedicated to the overexpression of a single isoform or the knockdown of other isoforms using e.g. small interfering RNA molecules. Moreover, the presence of up to four basigin isoforms of different function [73] interferes with basigin-related studies on MCT transport. The investigation of genetically engineered variants relies on an efficient knockdown of endogenous proteins and a heterologous expression of the desired protein construct. None of these methods fully abolishes endogenous background activity. Therefore, the distinct discrimination of heterologous and native transport activity and effects is hardly possible. For functional studies, due to the lack of an endogenous MCT homolog, *Xenopus laevis* oocytes

appeared more amendable and have primarily been employed to characterize MCTs [50, 51]. Nonetheless, work with *Xenopus* oocytes is not the standard in most laboratories [153]. Most importantly for this study, despite the absence of endogenous MCT activity, *Xenopus* oocytes do express basigin homologs (refer to [132]).

Ideally, a system used to characterize MCT functionality as well as the role of its chaperone should be devoid of any intrinsic activity. It should further enable the heterologous expression of a desired isoform as well as manufactured protein constructs. In that respect, the yeast system appeared underexploited in the field of human monocarboxylate transporters. The yeast *S. cerevisiae* is a unicellular, eukaryotic organism that has been proven valuable due to the robust phenotype, and the extensive knowledge of the genome and metabolic traits (reviewed in [154]). The cells allow for cost- and time-efficient cultivation in a broad pH range and are resistant to high osmolarities. Due to a similar intracellular organization, the yeast is a most valuable model for cells of higher eukaryotes. Most importantly, yeast cells are highly amendable to genetic modifications and distinct gene knockouts [154]. Hence, the knockout of both transporters that mediate monocarboxylate transport in yeast, namely Jen1 and Ady2 [105, 106], has been proven very useful for characterizing heterologously expressed monocarboxylate transporters with no endogenous background transport. This expression system has been used successfully for the functional characterization of non-mammalian monocarboxylate transporters including formate-nitrite transporters from *Plasmodium falciparum* (PfFNT), *Toxoplasma gondii* (TgFNT), and the bacterial formate-transporting FocA from *Escherichia coli* [155–157]. In this study, a *jen1 ady2* knockout yeast produced functional recombinant human monocarboxylate transporter 1 (MCT1). So far, only a limited number of research articles exist that used a yeast-based expression system for the functional characterization of MCTs [88, 104]. In studying MCTs, *S. cerevisiae* seems particularly suited given the lack of an intrinsic expression of basigin homologs – a unique property and an ideal prerequisite to characterize MCTs free of endogenous basigin interference. Hence, Makuc *et al.* have demonstrated the feasibility of a *jen1* knockout yeast to characterize rat MCT1 [88]. In line with the results from this study, they showed a functional expression of MCT1 at the plasma membrane of *S. cerevisiae* in the absence of an accessory protein. This is in contrast to commonly used expression systems where MCTs fully reside in intracellular compartments if basigin is absent preventing any functional characterization [69]. Likewise, in this study, the transformation of yeast cells with the coding region for human MCT1 alone led to the synthesis of functional protein at the plasma membrane (refer to Figure 4.1A and B, Figure 4.4C). Only minor protein fragmentation was visible and indicated protein degradation at the long, unstructured linker between TM6 and 7 which was shown before to be susceptible for proteolysis [53]. Confocal microscopy indicated that, indeed, some of the protein produced was trapped in intracellular membranes (compare with [88]). Nonetheless, a substantial portion

reached the plasma membrane and allowed detectable and adequate transport rates for L-lactate (refer to Figure 4.1C). The functionality of MCT1 does not depend on posttranslational modifications whereas basigin requires processing: basigin is a highly glycosylated protein and in the case of splice variant 2, it requires the formation of two disulfide bridges for correct folding of the extracellular Ig-like domains [76]. Due to their eukaryotic nature, yeasts share similarities with mammalian organisms in protein processing and offer similar membrane trafficking mechanisms [158], glycosylation [159] and disulfide bridge formation [160]. Indeed, Makuc *et al.* successfully co-expressed rat MCT1 and basigin in *S. cerevisiae* and showed an enhanced translocation of MCTs to the plasma membrane [88]. This indicated proper synthesis and functionality of both proteins and the feasibility of the yeast system in studying the MCT-basigin interplay. Affirmatively, the results from this thesis likewise showed a successful expression of MCT1 and various basigin constructs but in a fusion set-up. The protein isolated from transformed cells was detected using immunoblotting techniques and showed respective shifts to higher molecular weights with largely smaller overall expression levels (refer to Figure 4.8A). Only minor fragmentation indicated some breakage of both proteins in their linking sequence. Basigin displays at least three glycosylation sites and non-glycosylated (27 kDa) and glycosylated protein (35−66 kDa) differ in the prevailing molecular weight [73, 161]. Given the rather slight shift in molecular weight in this study (maximum of ~40 kDa for fusion of MCT1 with full-length basigin splice variant 2) and especially the appearance of well-defined protein bands, the recombinantly expressed basigin constructs appeared not or only minorly glycosylated in yeast. This is in line with previous studies [88]. A glycosylation of basigin is primarily linked to physiological responses and signaling processes and it seems rather unlikely that basigin glycosylation plays a role in MCT functionality [162]. Nonetheless, given the lack of further insight and the possibility of differences in mammalian and yeast glycosylation patterns, glycosylation-related effects would hardly be resolved in the used yeast system. More importantly, the β-sheet motifs of basigin's extracellular Ig-like domains demand stabilization by disulfide linkages. Indeed, *S. cerevisiae* assures a catalytic disulfide bond formation with specific disulfide isomerases [163]. Confirmatively, the mutation of involved cysteines to serines in this study caused a disruption of observed basigin-mediated effects indicating that basigin was properly folded beforehand (discussed in detail in section 5.4). Accordingly, the fusion of MCT1 with basigin maintained transporter function and did alter the transport properties (discussed in section 5.3).

5.2. Molecular fusion of MCT1 and its chaperone basigin

This study's set-up differs from previous approaches in the MCT research in two main aspects. First, the use of a yeast-based expression system allowed the functional expression of MCT1 alone and set the ideal grounds to elucidate unbiased, basigin-independent MCT characteristics. And second, employing the fusion technology to covalently link basigin and MCT1 disclosed further direct basigin effects on transport.

The fusion of two proteins or domains of different proteins is a valuable concept for various purposes. One of the most common uses of the fusion technology is to add small peptide tags to the N- or C-terminal end of recombinantly expressed proteins for purification and labeling purposes (reviewed in [164]). Generally, a fusion can optimize the biochemical protein characteristics such as solubility, stability, trafficking or activity (reviewed in [165]). Exemplary, the fusion technology can be used to couple two enzymes that catalyze consecutive steps in metabolism. This fusion has been shown to promote the net aldol reaction via the dihydroxy-acetone kinase and the fructose-1,6-bisphosphate aldolase by an efficient substrate shuttling between active centers [166]. In this study, an end-to-end fusion of coding regions for MCT1 and several natural or artificial constructs of its interacting basigin was employed. In contrast to a co-expression approach, the fusion profits from a permanent proximity of both proteins in a stoichiometric manner, and an increased probability of both proteins to interact. In the case of a stable fusion, this ensures an association of both proteins at all times. At the start of this study, only limited information was available on how MCTs and basigin would interact. In 2000, Kirk *et al.* used chimeras of basigin and another non-MCT-related member of the immunoglobulin-like family (CD2) to reveal that the C-terminal end and the transmembrane domain of basigin are sufficient for an interaction with MCTs [69]. Accordingly, fluorescence resonance energy transfer (FRET) studies by Wilson *et al.* confirmed a close proximity of the C-terminus of basigin and the C- and N-terminal ends of MCT1 [87]. These results were further specified by elucidating the Glu218 as a charged residue in the transmembrane domain of basigin variant 2 to be crucial for interaction [57]. The end-to-end fusion of two proteins dictates several requirements to ensure a functional protein expression. As reviewed by Yu *et al.*, the fusion of two proteins demands long and flexible C- and N-terminal ends to ensure a linking sequence of minimal constraint. These terminal ends should not exhibit a role in protein function [167]. In the case of a basigin-MCT1 fusion, the intracellular localization of MCT's termini required a fusion of basigin's intracellular C-terminus to the N-terminus of MCT1. Based on the structure data for SfMCT and secondary structure predictions for basigin, this assured a flexible linker of roughly 60 amino acids. Considering that naturally occurring and empirically designed linkers between proteins or individual domains stretch from 10 to 15 residues [168], 60 amino acids should avoid steric hindrance and provide enough flexibility for basigin and MCT1 to fall into proper interaction. The predicted spatial orientation of basigin and MCT1 in

this work is visualized in Figure 5.1A. During this study, the structure for MCT1 in complex with basigin variant 2 was resolved [103] (Figure 5.1B, discussed in detail in section 5.6). This structure perfectly mirrors the predictions made for this study. Accordingly, the transmembrane domain of basigin is in close contact with the transmembrane helix 6 of MCT1. This orientates the extracellular domain of basigin, i.e. the Ig-I domain, in a way that it “covers” the substrate entrance path of MCT1.

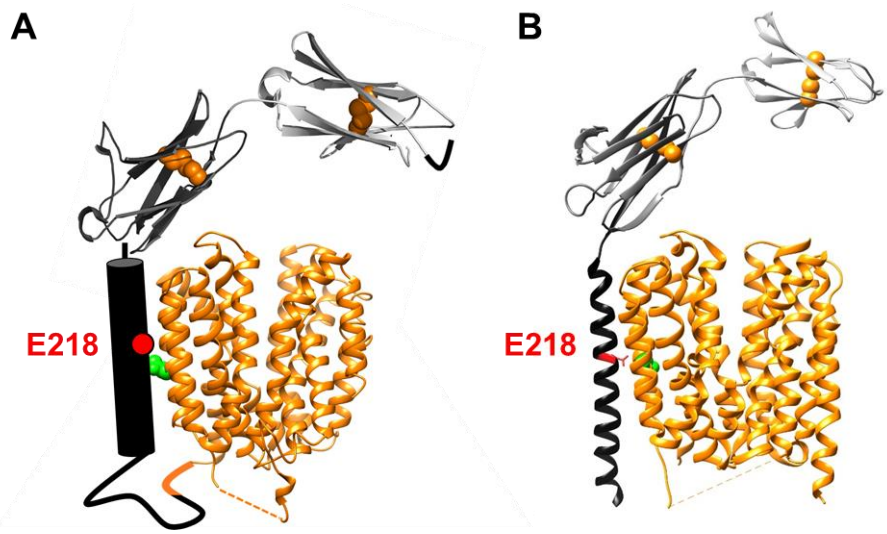

Figure 5.1. Comparison of the basigin-MCT1 fusion model and the resolved structure of the complex. **(A)** Schematic model for the fusion construct of basigin variant 2 (black/gray; PDB #3B5H; the transmembrane domain as schematic illustration) with MCT1 (orange; structure model based on SfMCT, PDB #6HCL). This figure is a modified version of Figure 4.5. **(B)** Resolved structure of MCT1 in complex with basigin variant 2 (PDB #6LZ0). In both images, disulfide bridges in the extracellular domain of basigin are shown as orange spheres. Glu218 in the transmembrane domain of basigin is highlighted in red, and the interacting Asn187 in MCT1 is marked green.

Previous literature proposed Arg86 in helix 3 of MCT1 to be in close distance to the transmembrane domain of basigin and to presumably involve in the interaction with basigin’s Glu218 – although not via a charge-pair [57]. Wang *et al.* confirmed the importance of Glu218 for interaction [103] and further claimed Asn187 of helix 6 to engage in a hydrogen bond with Glu218. In this study, a charge-reversing mutation of Glu218 to arginine (E27R in the BSGΔIg construct) prevented the MCT1 functionality although it was present at the plasma membrane (refer to Figure 4.6). In this context, it can be assumed that MCT1 and basigin were in fact interacting, and that a positive charge in basigin prevents interaction and even affects the neighbouring MCT1 – either by misfolding that is transmitted to MCT1 or due to charge-repelling effects. Although some breakage of the fusion construct between MCT1 and basigin

was observable in Western blotting (refer to Figure 4.8A), the full abolishment of transporter function by a point mutation in basigin and the lack of any residual activity that would arise from non-fused MCT1 indicates that even after molecular separation, both proteins appear to have remained associated. Afterall, these conclusions support the feasibility of this study's experimental fusion set-up.

5.3. Monitoring L-lactate transport across plasma membranes

5.3.1. General approaches and modalities

Over the years, monitoring monocarboxylate transport across plasma membranes has been intensively studied using different kinds of methodic approaches each facing its own obstacles and challenges (extensively reviewed in [169]). Generally, lactate transport across membranes is, according to the Arrhenius equation, temperature-dependent [170] and, given the proton co-transport, pH-dependent [61]. Nowadays, a sophisticated laboratory equipment easily manages stable and precise pH buffering and temperature control and allows accurate kinetic measurements. Due to the difficulties that accompany the direct tracing of monocarboxylates (see below), the MCT-mediated transport is commonly followed as the concurrent pH change. Using intra- or extracellular pH electrodes or pH-dependent fluorescent dyes (i.e. 2'-7'-bis-(carboxyethyl)-5-6-carboxy-fluorescein (BCECF)), the transport of the substrate-accompanying protons across membranes is monitored [171, 172]. In contrast to measuring the flux of the monocarboxylate of interest itself, the pH shift is a real-time and universal measure to cover transport by MCTs that exhibit a diverse spectrum of transported substrates. On the far side, the proton flux is an indirect measure of transport that might be affected by cellular pH buffering in need for diligent experimental calibration. Since MCTs convey bi-directional transport, only the net flux of protons is captured, and a mere exchange of protons can not be traced. For certain cases, the use of radiolabeled substrates appears more suitable. A substrate labeling with β-emitting radiocarbon (^{14}C) gives a sensitive and direct measure of transport. This approach has successfully been used to characterize monocarboxylate transporters of several species in- and outside the Beitz lab [54, 109, 173]. Nonetheless, in living organisms, to monitor monocarboxylate/lactate transport and characterize the functionality and kinetics of transporters is a major challenge. First, monocarboxylates all share the deprotonatable carboxylic acid function. In the protonated, non-charged form, monocarboxylates are able to cross plasma membranes in the absence of any transporter [174, 175]. Therefore, substrate diffusion across the plasma membrane might hamper accurate transport measurements. Nonetheless, with a pK_a of 3.9, lactic acid and is largely deprotonated (≈ 99.97 %) at a physiological pH of 7.4. Only at low pH values, diffusion constants get significant [175]. Nonetheless, passive diffusion does play a role and uptake

rates need adequate correction. In human cells lines and *Xenopus* oocytes, the contribution of background diffusion can be estimated by eliminating transporter-mediated flux using specific inhibitors (reviewed in [9]). In the yeast system, genetic knockout strains that do not express monocarboxylate transporters constitute an ideal system for background correction.

In co-transporters that allow an electroneutral, bi-directional substrate shuttling, transport is defined by substrate concentrations at both sides of the membrane and the prevailing concentration gradients [176]. In cell-based systems, any transport-unrelated processes affecting substrate concentrations in- and outside the cell will affect measured transport parameters. Most importantly, the substrate metabolism and its endogenous intracellular pool contribute to prevailing concentrations and inaccuracy. Explicitly, L-lactate plays a major role in the energy metabolism of mammalian cells [1]. Therefore, metabolically active cells have an undefined intracellular pool of non-radiolabeled L-lactate impairing zero-trans influx measurements. Moreover, a constant metabolic conversion of entered L-lactate maintains a dynamic steady-state preventing the establishment of a thermodynamic equilibrium. Only in a limited number of cell lines or model organisms, L-lactate metabolism is absent or can manually be repressed. These include mature red blood cells after mitochondria expulsion [177], and yeast cells [141]. In other cellular systems, the rapid metabolic clearance restricts in-deep kinetic measurements especially of substrate efflux from preloaded cells or the determination of transport equilibria. The transport measurements are essentially limited to initial transport rates within the seconds time scale (10−60 s) or to low temperatures to repress metabolic activity (reviewed in [169]).

In this study, a yeast-based system was used to monitor the zero-trans influx of an externally applied gradient of ^{14}C-labeled L-lactate into cells that are devoid of the measured substrate. For that purpose, a single MCT isoform, i.e. MCT1, was recombinantly expressed in a *jen1 ady2* knockout strain. At a stable temperature of 19 ± 1 °C and an externally buffered pH of 6.8 or 5.8, background diffusion or transport was hardly detectable. Under these conditions (pH 6.8, 1 mM L-lactate gradient), MCT1-expressing cells gave values of 200−579 cpm (depending on incubation time) with a mean background of 104 cpm (refer to section 4.1.1) which ensured a sufficient signal-to-noise ratio even with the least active transporter construct examined in this study. Nonetheless, the background was subtracted for each individual experiment (refer to Figure 4.1C). In *S. cerevisiae*, L-lactate consumption and metabolism is repressed in the presence of glucose-containing medium [141]. Moreover, yeast cells naturally rely on metabolic pathways that do not produce large amounts of L-lactate [108]. These conditions met the requirements to conduct zero-trans experiments with no substantial metabolic interference. Interestingly, a glucose supplementation throughout uptake measurements led to a generally decreased lactate accumulation in cells (refer to Figure 4.14A) suggesting that, through enforced glycolysis, a minor intracellular lactate pool

was acquired and antagonized substrate influx. Hence, to thoroughly suppress metabolic activity and deprive intracellular L-lactate reservoirs to ensure zero-trans conditions, yeast cells were early withdrawn from glucose supply and kept on ice until conducting the uptake measurements.

5.3.2. Transport rates of basigin-MCT1 fusion constructs: the need for normalization

Most available studies on transport in general and on transport via MCTs refer to initial transport rates in zero-trans influx, zero-trans efflux or equilibrium exchange experiments. In that respect, initial transport rates accomplished by one or more expressed MCT isoforms in response to applied changes in pH, substrate concentrations, or inhibitor treatment are monitored. This gives distinct information on the kinetic properties of the respective isoform. In those cases where the modalities of a single isoform are examined in a system where only external factors are to be altered, initial rates give a good and comparable measure. Nonetheless, initial transport rates are affected by the number of transporting proteins residing at the plasma membrane. In this study, the different fusion constructs of MCT1 differed in their total expression levels (refer to Figure 4.8A). Since only the proportion of protein that reaches the plasma membrane contributes to initial transport rates, normalization was essential. A common approach to estimate the protein localization in living cells is confocal microscopy. In confocal microscopy, a central plane of the cells is visualized and with the use of a fluorescent indicator, proteins can be localized and quantified [178]. The fluorescent labeling can be achieved by using tagged protein-specific antibodies and tracer dyes, or by a direct fusion of proteins to a marker, i.e. green fluorescent protein (GFP). Both techniques have been successfully used in the field of MCT research [69, 87, 88]. Here, GFP was fused to the C-terminal end of the basigin-MCT1 fusion constructs and gave a good relative measure of how much of the fusion construct was displayed at the plasma membrane (refer to Table 4.1). As expected, the membrane localization differed between constructs. Of note, the differing total expression levels between fusion proteins did not allow to discriminate whether the translocation to the plasma membrane was altered or mere differences in the overall expression of protein caused a changed membrane localization. Nonetheless, the fusion constructs from this study displayed different initial transport rates and maximum velocities (v_{max}) and largely, these variances correlated with the relative abundance of tagged protein constructs at the plasma membrane (refer to Table 4.1). Thus, the initial transport rate and the maximum velocity achievable by MCT1 appeared unaffected by a fusion with basigin. Nonetheless, a protein quantification using confocal microscopy is error prone. The confocal images displayed a rather heterogenous signal distribution with the overall intensity in part contradicting expression levels from Western blotting. The non-automated quantification and the rather small sample size contribute to the expected large errors in quantification. Notably,

the fusion of GFP to the C-terminal end resulted in non-functional MCT1 questioning conclusions made for non-GFP-tagged proteins. Interestingly, Wilson *et al.* were able to fuse GFP to the C-terminus of MCT1 without losses in protein function [87]. Makuc *et al.* produced similar GFP fusion proteins in yeast but did not check for sustained functionality [88]. Nonetheless, in this study, the abolished transporter function hints at a so far undetected importance of the large and flexible C-terminal sequence of MCT1. Despite some evidence that propose the C-terminus as an anchor for MCT-associated proteins to regulate the MCT function [179, 180], data on a direct role in the transporter function is scarce. Although it can be assumed that C-terminal fusion to GFP did not alter membrane translocation of proteins, future approaches and save conclusions on initial and maximal transport rates are in demand for accurate and confident quantification at the plasma membrane. Alternatively, cell fractionation experiments or cell surface protein biotinylation techniques may be tried [88, 181].

5.3.3. The equilibrium of transport

Generally, a channel protein facilitates diffusion of a substrate across membranes and along its concentration gradient until an equilibrium of substrate in- and outside the cell is reached [176]. In secondary active MCT transport, the prevailing gradient of a secondary substrate, i.e. protons, drives transport of the co-transported substrate, i.e. L-lactate, for accumulation [176]. MCT transport is bi-directional and works equally in both directions [169, 182] (reviewed in [9]). In a zero-trans setting, an extracellular L-lactate gradient can be applied to drive influx via the transporter. In that case, in the first seconds of transport when the gradient is maximal, L-lactate is taken up at maximum speed, i.e. with the above described initial transport rates. In a system where the substrate that is accumulated at the trans-side is neither consumed nor exported via alternative routes, the system will establish a steady state in which influx equals efflux leading to equilibrium concentrations at both sides of the transporter. This would appear as a saturation in an uptake-over-time curve and a maximal uptake capacity under the prevailing conditions. In analogy to enzymatic catalysis, a transporter accelerates the establishment of this equilibrium but it will not affect its position [1]. In an electroneutral substrate/proton co-transport, this thermodynamic equilibrium is defined by an inversely proportional relation between the concentrations of substrate (c_{eq}) and protons ($[H]^+_{eq}$) in- and outside the cells. This correlation is summarized as the “fundamental rule of co-transport” and defined by the equation $c_{eq\_in} \cdot [H^+]_{eq\_in} = c_{eq\_ex} \cdot [H^+]_{eq\_ex}$ [176] (reviewed for MCTs in [169]). According to Le Chatelier’s principle, transport can be stimulated by changes in each of the four contributors.

To date, the transport equilibrium of MCTs could not be resolved since common experimental approaches suffer from rapid metabolism of the accumulating substrate (see section 5.3.1). In this study, the use of a yeast-based system allowed to monitor L-lactate uptake for time periods

long enough to determine equilibrium concentrations for L-lactate (summarized in Table 4.1). Confirming the validity of the experimental framework, experiments at different temperatures displayed different transport rates but yielded comparable equilibrium concentrations (refer to Figure 4.3).

5.4. Basigin: a proton and substrate collecting antenna to drive L-lactate influx

So far, the role of basigin has been seen purely as a chaperone to guide MCTs to the plasma membrane [69]. Interestingly, basigin undertakes this function not only for MCTs but also for other membrane proteins, i.e. the plasma membrane Ca^{2+}-ATPase (PMCA) [183, 184]. In line with the studies on MCTs, the transmembrane domain of basigin appeared sufficient for interaction and chaperoning. In the absence of basigin, MCTs are trapped in intracellular compartments [69] and this basigin-dependent plasma membrane localization is associated with several disease-related conditions including cancer [185]. Due to this tight dependency, MCTs are not accessible for functional studies in the absence of basigin. Hence, earlier studies lack unbiased characterization of MCTs and failed to elucidate any potential direct basigin effects on MCT functionality. This direct regulation has been occasionally suggested but was never confidentially confirmed.

In this work, the use of a yeast-based expression system offered the unique property that MCTs are, indeed, properly targeted to the plasma membrane without the aid of a chaperoning basigin. This enabled the determination of intracellular L-lactate equilibrium concentrations achievable by MCT1 alone and in fusion to artificial basigin constructs of subsequently added protein domains. Strikingly, the functional fusion of MCT1 to basigin constructs that harbored the membrane-proximal Ig-I domain enabled an at least 4.5-fold accumulation of L-lactate inside the cells (refer to Table 4.1). This was associated with a slight increase in K_m that has previously been linked to an association of MCTs with basigin [88]. An impaired domain folding by mutating the cysteines that are involved in a stabilizing disulfide bridge reversed this effect (refer to Figure 4.10D). The presence of the second N-terminal Ig-C2 domain of basigin did not further affect the L-lactate accumulation (refer to Table 4.1). Of note, the Western blot analysis displayed no apparent band shift between the constructs BSG Ig-I-MCT1 and BSG Ig-I/C2-MCT1 although the additional Ig-like domain accounts for a calculated molecular weight difference of 8 kDa (refer to Figure 4.8A). Hence, an early separation of this domain from the fusion constructs cannot fully be excluded and could account for a lack of effect. Nonetheless, recognizing the Ig-C2 domain as the membrane- and MCT-distant domain [103] agrees with the Ig-I domain as the more likely candidate for any regulation of MCT1. The presence of basigin's Ig-I domain led to an L-lactate accumulation to concentrations well above those provided with the buffer, i.e. 1.8−2.1 mM (refer to Figure 4.12A). The knowledge of the

external buffer and proton concentrations as well as the experimentally determined internal pH allowed an estimation of the equilibrium constants achieved by the different constructs. MCT1 alone and in combination with basigin lacking a properly folded Ig-I domain (BSGΔIg-MCT1, BSG Ig-I C23S/C82S-MCT1) acquired a thermodynamic equilibrium with $K \approx 1$ meeting the requirements of the fundamental rule of co-transport. The presence of the extracellular Ig-I domain led to a disturbance of the equilibrium resulting in an apparent K_{app} of 4.5−5.2 (refer to Figure 4.12B). Thermodynamically, such a disturbance could be explained by locally increased concentrations at the extracellular side of the transporter. A correct calculation of equilibrium constants requires utilizing these local concentrations instead of the now underestimating buffer concentrations. According to Le Chatelier's principle, the locally increased concentrations would imply substrate accumulation at the trans side of transport, i.e. inside the cell (Figure 5.2).

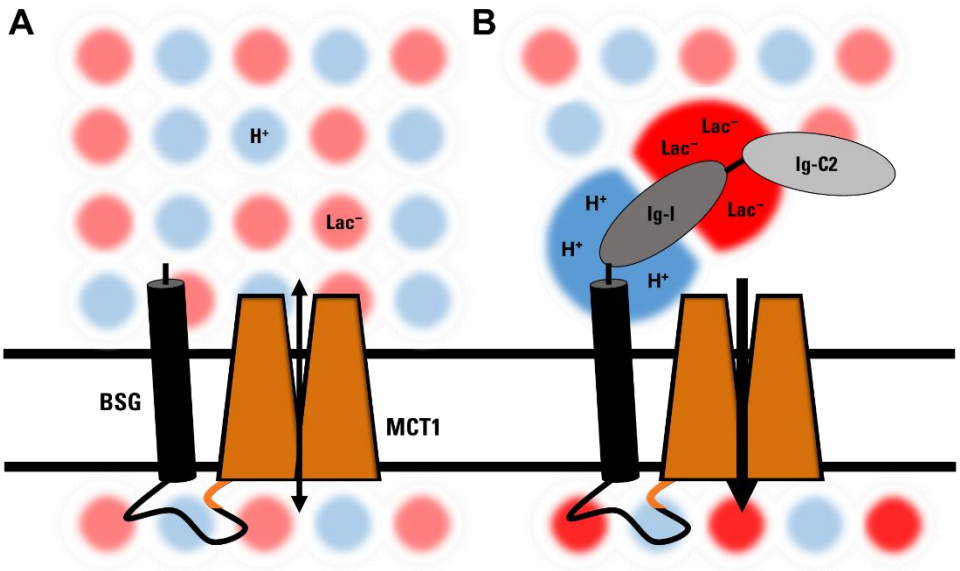

Figure 5.2. Electrostatic attraction of L-lactate and protons by the Ig-I domain of basigin. **(A)** In the absence of the extracellular BSG Ig-I domain, the buffer concentrations of L-lactate and protons determine transport and a thermodynamic equilibrium is reached. **(B)** The presence of the Ig-I domain creates a microenvironment of increased local concentrations of substrate and protons at the transporter surface. This drives substrate influx according to Le Chatelier's principle. Referring to outside buffer concentrations, an apparent equilibrium constant $K_{app} > 1$ is achievable. Substrate accumulates above concentrations provided by the buffer.

The experimental evidence of such a substrate-concentrating function of proteins or protein domains was recently provided for aquaporin 9 (AQP9) [186]. Rothert *et al.* confirmed an electrostatic attraction mechanism for lactate anions via a positive arginine cluster, driving

substrate influx [186]. For basigin, the calculation of Poisson-Boltzmann electrostatics revealed a strong positive and an adjoining negative patch within the basigin Ig-I domain (refer to Figure 4.15). An impaired domain folding and patch formation by disulfide bridge-breaking point mutations (refer to Figure 4.10D), or a dissolution of the patches by respective residue exchanges by neutral amino acids (refer to Figure 4.16) reversed the basigin-mediated effects. Residues situated closer to the transporter surface exhibited the most substantial effect. This elucidates the modalities of a bivalent proton and substrate harvesting function of basigin via its Ig-I domain. This study hypothesizes that the harvesting creates a “microenvironment” of locally pooled substrate anions and protons at the transporter surface. This, in turn, generates a steeper substrate gradient driving L-lactate influx (Figure 5.2). In this microenvironment, the thermodynamic requirements are met ($c_{eq\_in} \cdot [H^+]_{eq\_in} = c_{eq\_ex} \cdot [H^+]_{eq\_ex}$), but an apparent disturbance with respect to buffer concentrations in the overall “macroenvironment” is created. This alters the transmembrane substrate distribution and enables an intracellular substrate accumulation beyond concentrations the buffer and the pH gradient would thermodynamically allow. Interestingly, glucose-rich conditions also eliminated any basigin-mediated effect with an overall effect on cytosolic substrate accumulation (refer to Figure 4.14). This establishes the basic requirement for zero-trans conditions. In this case, an endogenously built up L-lactate pool by glucose breakdown could antagonize and exhaust the harvesting potential and much rather reflect equilibrium exchange modalities instead of a zero-trans influx.

Together, these results point to basigin as an electrostatic antenna for both, substrate and protons, and a key regulator in MCT1 function. Strikingly, Updegraff *et al.* just recently found that shedding of the extracellular domain of basigin by the action of the transmembrane protease TMPRSS11B forced a substrate efflux from MCT4-expressing cells in a physiological setting [89]. Their determined decrease in intracellular lactate content by a factor of 4 is perfectly in line with the inverse 4.5-fold shift to influx by basigin in this study. This points at an overarching mechanism of basigin that is transferable to other MCT isoforms. This notion adds perfectly to a picture that has been drawn in the past several years. Quite recently, two new interacting partners of the basigin-MCT complex, namely carbonic anhydrases (CA) II and IV, have been found to regulate lactate flux [151, 180]. Together with Forero-Quintero *et al.* [172], these studies revealed a regulating mechanism in which the CAIV binds extracellularly to the Ig-C2 domain of basigin and the CAII associates with the intracellular C-terminal end of MCT1/4 to act as electrostatic proton antennae that guide protons to the transporter entry and release them on the other side. Accordingly, CAII and CAIV enhance an efficient lactate flux through MCTs via a mechanism that is unrelated to their enzymatic function. For proton-coupled transporters, mathematic models show that mere proton diffusion in the medium is too slow to maintain the high transport rates observed for MCTs, and that the existence of proton-collecting subunits would resolve this problem [187]. In that regard, Noor *et al.* postulated a

mathematical discrepancy suggesting that MCTs require, beside CAII, additional harvesting antennae to sustain transport [180]. One of which is the CAIV, and another is here proposed to be MCT's well-known chaperone basigin. Moreover, basigin appears to act not only as the bridging proton antenna between CAIV and MCTs, but also as an additional L-lactate collector to drive L-lactate influx even more efficiently.

Given that MCT1 offers a moderate substrate affinity and is the least destined MCT isoform with respect to transport directionality, basigin is now revealed as a key determinant. This is particularly important since from a thermodynamic point of view, an enforced substrate influx at given L-lactate concentrations would require an intense shift in pH either intra- or extracellularly. Here, an outside pH shift of one unit from 6.8 to 5.8 drove substrate influx via MCT1 alone to a similar degree as fusion to basigin did at pH 6.8 (refer to Figure 4.11D). This underlines the magnitude of the substrate harvesting by basigin which was of particular importance at a pH of 6.8 (refer to Figure 4.11D). From a more macroscopic perspective, the basigin-favored substrate influx gave a physiologic benefit to expressing yeast cells that require L-lactate as carbon source (refer to Figure 4.13). In humans, MCT1 is ubiquitously expressed and can, in general, adapt a lactate-releasing and a lactate-receiving function in metabolically adapted (reverse) Warburg cancer cells. The expression of basigin and the choice of specific isoforms (note that some do not display the critical Ig-I domain [73]) might be key in defining the net directionality of MCT1 transport and in determining the fate of cancer cells. This underlines its great importance and reveals a new angle for therapeutic intervention – especially in cancer.

Collecting antennae in MCT transport: What is next?

This newly resolved regulation of transport via MCT1 has important implications on the functionality of MCTs in general. It will be interesting to test whether basigin can fulfill this harvesting function also for other MCT isoforms. Unfortunately, attempts to express other MCT isoforms in *S. cerevisiae* have failed (see Master's thesis of K. R. Jacks [188]). Nonetheless, the fusion of MCTs from other species to basigin would offer insights on a global mechanism and a transferability to other proton-coupled monocarboxylate transporters. Rat MCT1, a member that has been successfully expressed in this study in yeast, represents one interesting candidate – especially considering embigin as its genuine chaperone [56]. Moreover, given the proposed mechanism includes an electrostatic substrate anion attraction, it is most likely that substrate harvesting by basigin also drives an influx of other known transporter substrates, e.g. pyruvate or acetate. Moreover, does the yeast system allow further N-terminal anchoring of the carbonic anhydrase to the basigin-MCT fusion proteins to elucidate a potential cooperative harvesting of both antennae? In this work, the fusion of MCT1 to embigin variants as the preferred partner for MCT2 and an alternative chaperone for MCT1 led to low expression levels

and no substantial transport activity (refer to Figure 4.7 and Figure 4.9). However, sequence alignments of basigin and embigin reveal a high conservation across species but not between both family members at the charge patch-forming positions (Figure 5.3). In contrary, the transmembrane domains including the charged glutamate for MCT interaction are highly conserved between basigin and embigin. In future attempts, chimeras of the transmembrane domain of basigin for proper interaction and the extracellular portion of embigin could reveal differences in their regulatory function on MCT transport. Explicitly, does embigin similarly collect protons and substrate, or is basigin the only member equipped with an antenna function?

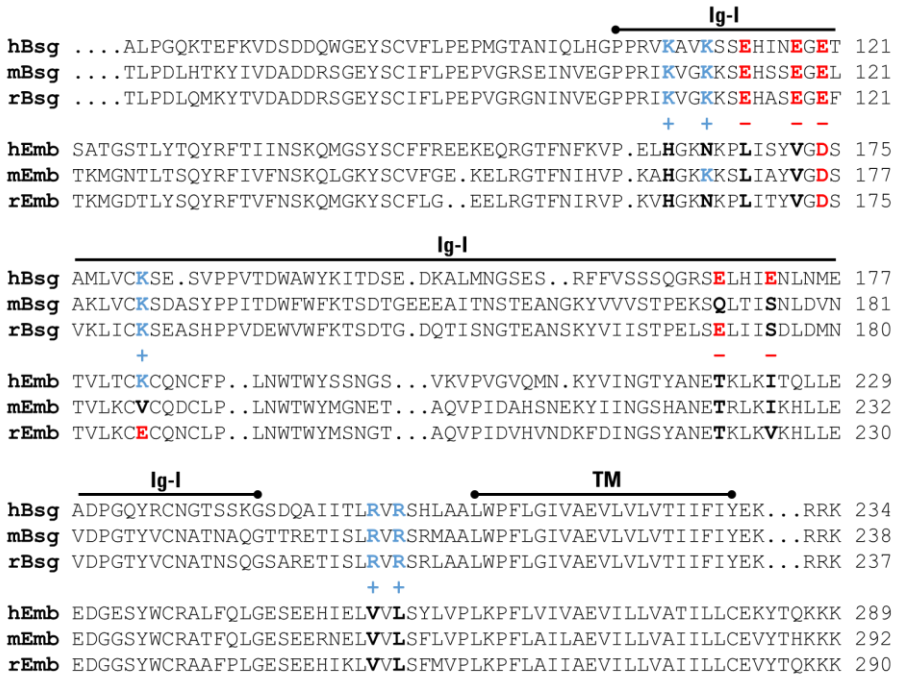

Figure 5.3. Excerpt of a sequence alignment of human, mouse and rat basigin (BSG) and embigin (EMB). Residues that contribute to the electrostatic surface potential in hBSG are highlighted in red (negative charge) and blue (positive charge).

To examine the physiological relevance of basigin's regulatory function, the here ascribed implications from yeast should be tested in the human system. In that respect, a cooperation with the Schäfer lab at the Institute of Experimental Cancer Research (UKSH Kiel) seeks to express the basigin-MCT1 fusion constructs in human cell systems.

5.5. Cys159 in the MCT1 hinge region: a molecular anchor?

MCTs are implicated as promising drug targets in anti-tumor therapy. So far, most known inhibitors are unspecific or at least lack isoform-specificity. Moreover, data on the mode of action of common inhibitors is scarce. Given the tight and retained association of MCTs and basigin or embigin at the plasma membrane [87], several studies implicate basigin/embigin association with drug efficacy and inhibition [70, 189] but reliable evidence is limited.

Although ineligible when comparing differentially expressed protein constructs, initial transport rates constitute a confidential readout in inhibitory studies. Again, the yeast system and its expression of functional MCT1 when not associated with basigin appeared most suitable and offered the opportunity to compare the efficacy of compounds in the absence and presence of basigin. Given its high transport activity and it being the variant carrying both extracellular Ig-like domains, the BSG Ig-I/C2-MCT1 fusion construct appeared most suited. MCT1 alone and in fusion with basigin exhibited sufficiently high transport rates to carry out inhibitor studies. Due to the generally low background signals (refer to Figure 4.1C), signal-to-noise ratios were high enough to permit the determination of percent activities with acceptable variances even at high degrees of inhibition. To make up for the time-dependent decrease in cell fitness and uptake capabilities (refer to Figure 4.2B), non-inhibited cells always underwent the same procedure and were assayed as controls. This assured a most reliable reference and save conclusions on efficiencies of tested substances.

Expectedly, the compound AZD3965 was found to directly inhibit MCT1 (refer to Figure 4.17A). This is in line with the recently resolved structure of MCT1 that presents AZD3965 in the substrate-binding pocket [103]. The fusion to basigin led to a comparable IC_{50} value indicating that basigin is neither essential nor does it modulate inhibitor binding (refer to Figure 4.17B). In contrast, the cysteine-modifying reagent *p*-chloromercuribenzene sulfonate (pCMBS) was long accepted as an indirect MCT inhibitor. In 2005, based on an MCT4 structure model on the *Escherichia coli* glycerol-3-phosphate transporter and the lactose permease, Wilson *et al.* predicted solvent-accessible cysteines yet a mutation of such cysteines failed to confer pCMBS resistance [70]. Accordingly, the authors proposed the covalent modification of disulfide cysteines in basigin's Ig-C2 domain and misfolding to be transmitted to the neighboring MCT. Given that, in the *Xenopus* oocytes system, misfolded basigin prevents proper MCT trafficking, concrete evidence for MCT inhibition beyond a lack of plasma membrane translocation is missing. Here, the yeast expression of MCT1 without interference from chaperoning proteins was key in elucidating that pCMBS is a direct MCT1 inhibitor with basigin having no effect on its inhibitory potential (refer to Figure 4.18). Site-directed mutagenesis revealed Cys159 as the sole target for modification by pCMBS. The available structure models for MCT1 (refer to Figure 4.19A) delineated Cys159 to be positioned in a central hinge region of MCT1. This critical position was now confirmed by the resolved cryo-

EM structure of MCT1 [103] (Figure 5.4A, B). Cys159 is situated deep in the substrate binding pocket but accessible in the outward open conformation. pCMBS transfers a very bulky side chain with a van der Waals volume of 135 Å^3 (calculated with chemicalize.org by ChemAxon). Accordingly, covalent modification of Cys159 might serve as a wedge and hinder free transporter motion locking it in the outward open conformation (Figure 5.4C).

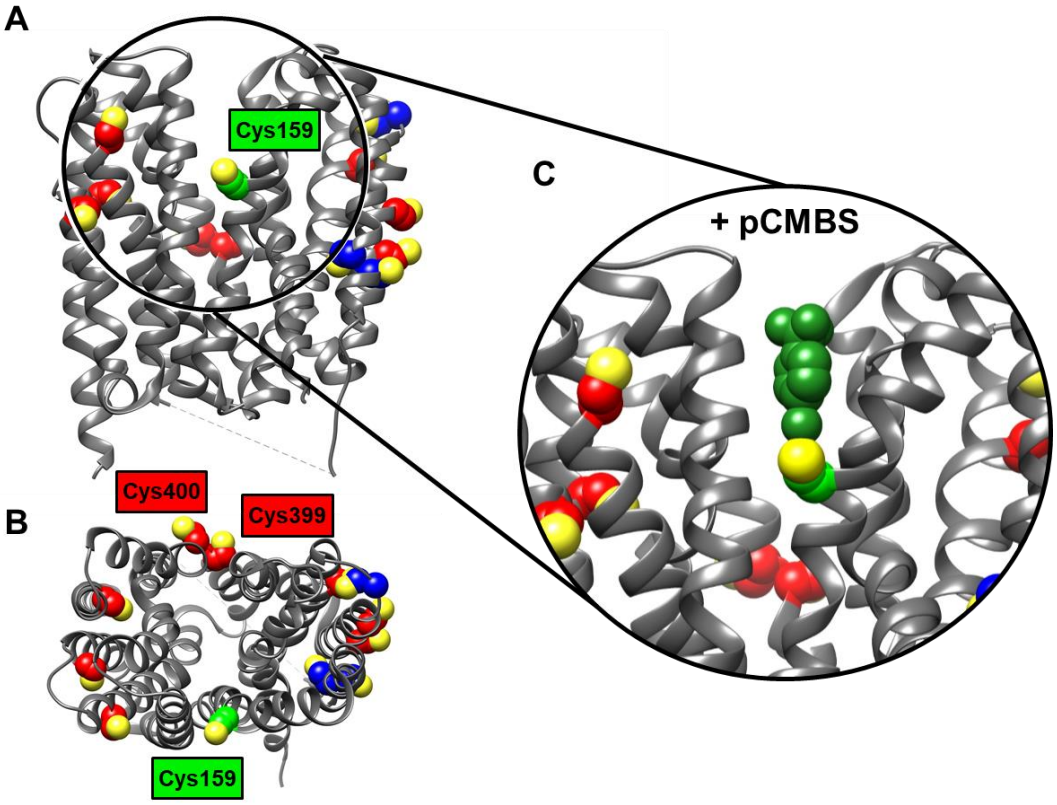

Figure 5.4. Structure of MCT1 and modification of Cys159 by pCMBS. **(A, B)** Structure of human MCT1 in the outward open conformation (PDB #6LZ0) in side-view **(A)** and in top-view (view from extracellular space) **(B)**. Cysteines are highlighted in red, blue and light green (Cys159). Color coding refers to Figure 4.19A. Sulfur atoms are marked yellow. **(C)** Magnified excerpt of the MCT1 structure showing the covalent modification of Cys159 by pCMBS (dark green) retaining MCT1 in the outward open conformation.

Affirmatively, a covalent modification with the smallest available cysteine-modifier, methyl methanethiosulfonate (MMTS, 47 Å^3), only partially decreased transport rates (refer to Figure 4.23B). MMTS modified Cys159 but was revealed as non-selective with other cysteines being additionally modified (refer to Figure 4.25). Given the small size of the transferred moiety and the membrane-permeability, it is thinkable that MMTS gains access to additional more buried cysteine residues possibly also from the intracellular site. Consecutive studies by

K. Geistlinger aimed for the complete cysteine conversion with the medium-sized MTS reagents PMTS and BMTS and confirmed a size-dependent inhibition with increasing inhibitor size correlating with a selectivity for Cys159.

In general, cysteines can play important roles in protein function. Although they are of low abundance, roughly half of the cysteines present in a protein are solvent-accessible and have implications in its functionality [190]. To date, only a limited number of studies addressed the role of cysteine residues in MCT transport. Yamaguchi *et al.* conducted studies with the cysteine-modifying reagent 5,5′-dithiobis(2-nitrobenzoic acid) (DTNB) but saw no effect on transport [66]. They concluded that cysteines in general are not accessible. Nonetheless, DTNB, and the equally non-effective MTSES from this study, are medium-sized and charged reagents. It is possible that they, due to the limited membrane-permeability, do not gain access to the transporter hinge region or other (intracellularly) targetable cysteines. Here, MCT1 emerged as attackable by cysteine-reactive compounds and engaging cysteines, i.e. Cys159, were susceptible for transporter inhibition. Of note, whilst the covalent modification of Cys159 was not tolerated by MCT1, its substitution by serine had no effect yielding almost identical transport rates compared to the wildtype protein (refer to Figure 4.20B). Other reported cysteine mutations including the ones presented by Wilson *et al.* [70] (refer to section 4.2.2), rat MCT1 Cys336 (Cys343 in human MCT1) [65] and human MCT1 Cys399 to alanine [191] were likewise without effect. With Cys362 of bacterial SfMCT, a single cysteine was revealed that did not allow an amino acid substitution and was implicated in the MCT transporter function. Single mutation of this cysteine to alanine greatly decreased SfMCT transport activity [54]. This cysteine is not conserved among human MCT members but sequence alignments locate it right next to the Cys399/Cys400 pair in MCT1. Indeed, in this study, while single substitutions of Cys399 and Cys400 did not affect transport, a Cys399/Cys400 double mutant was non-functional. Although none of the single cysteine mutations conferred complete resistance to MMTS, the complete transport abolishment by an absence of both revealed a relevance of some kind (refer to Figure 4.26). Interestingly, this pair of cysteines sits on the opposite site of Cys159 with the thiols slightly protruding into the substrate binding pocket (Figure 5.4A, B). Together, the presented data reveal several cysteines, and explicitly Cys159, that occupy a designated hinge region in the substrate path MCTs potentially pivot around in the translocation cycle. The usage of several cysteine-modifying reagents revealed cysteines to be accessible. Cys159 in the binding pocket was selectively targeted by larger reagents which allowed a full block of transporter motion.

The transporter hinge region: What is next?

The accessibility of Cys159 opens doors for covalent modification and labeling in the most critical part of the transporter. Thereof, site-specificity is key and would require knowledge of all accessible cysteines. Accordingly, the identity of additional MMTS target sites is to be resolved in future studies, specifically with regards to a first tested fluorescent MTS reagent that proved to be non-specific for Cys159. Nonetheless, future site-specific labeling with sophisticated cysteine-modifiers could shed light on the mechanistic basis of MCT-mediated substrate transport. To date, the structural data in two transporter conformations and implications on distinct residues crucial for transport delineate an alternating access mechanism of MCTs. Information on a mechanistic basis and the distinct transporter motion is scarce. Using Cys159 as an anchor for fluorescence [192, 193] or electron paramagnetic resonance (EPR) labeling [194] could report on local electrostatics and conformational changes, and provide detailed information on the transport process of MCTs including substrate recognition, attraction and the translocation cycle.

5.6. How will the three-dimensional structure help?

The elucidation of three-dimensional protein structures provides information essential to understand protein dynamics, to identify substrate binding sites, or to define inhibitor binding and targeted drug design. Today's approaches demand the production of large amounts of highly purified, rigid protein to make it accessible for structure elucidation by X-ray crystallography [195], nuclear magnetic resonance (NMR) spectroscopy [196], or cryo electron microscopy (cryo-EM) [197]. Current methodic approaches and developments are progressing fast but, still, a structure elucidation of membrane-associated, non-soluble proteins remains highly challenging. Given the tight lipid association of membrane proteins, the structure elucidation demands sophisticated protein solubilization and reconstitution (reviewed in [198]). As of today, only 4058 of a total of 175508 entries in the RCSB Protein Data Bank (RCSB PDB, data from 03/12/2021, [134, 135]) are membrane proteins. To date, most of the available protein structures relied on an *Escherichia coli* expression system (refer to the RCSB PDB). Due to an alternate codon usage, the lack of native protein processing and improper protein folding in *E. coli* (reviewed in [199]), the recombinant expression of human proteins using alternative or eukaryotic expression systems including mammalian cell lines, Sf9 insect cells or yeast cells increasingly gained interest in structure elucidation (reviewed in [200]).
Structural information on the transporter surface, the substrate binding site as well as the spatial orientation of complexed basigin and MCT1 would largely contribute to understanding the mechanistic basis of the conclusions drawn in this study. The feasibility of functional

expression of MCT1 in fusion with its chaperone basigin in a yeast-based expression system laid the foundation to launch large-scale protein synthesis for structure elucidation. Here, *Pichia pastoris* was tested for the expression of MCT1 and basigin-MCT1 fusion constructs. In general, *P. pastoris* is advantageous in a way that it allows stable genome integration, inexpensive and inducible protein production and growth to much higher cell densities – all contributing to high protein yields (reviewed in [201, 202]). Unfortunately, *P. pastoris* did not produce MCT1 in this study (refer to section 4.3.1) whereas the plasmodial formate-nitrite transporter (PfFNT) was successfully expressed (refer to Figure 4.28). Given the strong dependency on a suitable chaperone for proper MCT expression in other systems [69], their autonomy in *S. cerevisiae* might be unique, and the expression in *P. pastoris* might require the presence of a guiding chaperone. Here, the unguided MCT1 and a fusion construct with the rather uncommon basigin splice variant 1 that also lacked proper production in *S. cerevisiae* (refer to Figure 4.9) were not produced in detectable yields. In contrast, a cell-free approach for the large-scale protein synthesis appeared promising. Using a detergent- and a lipid-protein nanodisc-based strategy, MCT1 in fusion with basigin splice variant 2 was synthesized and appeared correctly folded (refer to Figure 4.30 and Figure 4.31). Generally, the cell-free production and a subsequent reconstitution in nanodiscs combines highly versatile and controllable, large-scale production in short time periods [203] (reviewed in [198]) with a reconstitution in protein-stabilizing, membrane-mimicking nanodiscs that increase particle size required for analysis by cryo-EM [148, 149] (reviewed in [204]). Protein yields were sufficient to carry out transmission electron microscopy (TEM) of nanodisc-reconstituted protein. Initial class-sum calculations indicated protein reconstitution but, primarily, samples lacked sufficient homogeneity and separation from non-protein-filled nanodiscs (refer to Figure 4.33). On the far end, a cell-free synthesis does not necessarily or even unlikely ensure eukaryotic protein processing [198] essential to produce at least basigin in its functional and native form. Still, first trials on cryo-EM and class-sum calculations elucidated initial structural features and implied a dimeric state of the basigin-MCT1 complex.

During this study, three structures of MCT member were resolved at high resolution. These include the bacterial MCT of *Syntrophobacter fumaroxidans* (SfMCT) [54], human MCT2 [55], and human MCT1 in complex with basigin in two conformational states [103]. Together, they provide a structural basis for MCT's alternating access mechanism and substrate recognition in their designated conformations. Up to six discontinuous TM helices appear to facilitate the conformational reorganization [55]. A multimeric organization declares a cooperative behavior of MCTs [55]. Using a co-expression set-up and a Sf9 insect cell-based expression system, Wang *et al.* provided information on the spatial organization of MCT1 and basigin via cryo-EM (resolution of 3.0−3.3 Å) (see Figure 5.1) [103].

This recent progress provides deep structural insights and widely confirmed the validity of the homology models that served as basis for this study (refer to Figure 5.1 and Figure 5.4). In the future, the major profit will be to bring the structural data and the functional conclusions from this study together and contribute to a detailed understanding and revelations on the exact mechanism of substrate harvesting by basigin and on the transporter toggling around the designated Cys159 hinge region. MCTs in general are a key element in human metabolism. Cancer cells rely on efficient L-lactate shuttling and deregulated expression and functionality of MCTs is a hallmark of cancer. An in-depth understanding of the mechanistic basis of transport and the combination of structural and functional data will aid and promote MCT's implications in anti-tumor therapy.

References

1. Berg, J. M., Stryer, L., and Tymoczko, J. L. (2013) Stryer Biochemie, 7th Edition, Springer Spektrum, Berlin, Heidelberg. 978-3-8274-2989-6

2. Stillwell, W. (2016) An introduction to biological membranes, 2nd Edition, Elsevier, London. 978-0-444-63772-7

3. The Human Protein Atlas (2005) The Human Protein Atlas [*database*]. Online available at: https://www.proteinatlas.org/. Last visited on 03/12/2021.

4. Uhlen, M., Oksvold, P., Fagerberg, L., Lundberg, E., Jonasson, K., Forsberg, M., Zwahlen, M., Kampf, C., Wester, K., Hober, S., Wernerus, H., Björling, L., and Ponten, F. (2010) Towards a knowledge-based Human Protein Atlas. *Nat. Biotechnol.* **28**, 1248–1250

5. Quick, M., and Javitch, J. A. (2007) Monitoring the function of membrane transport proteins in detergent-solubilized form. *Proc. Natl. Acad. Sci. U.S.A.* **104**, 3603–3608

6. Adeva-Andany, M., López-Ojén, M., Funcasta-Calderón, R., Ameneiros-Rodríguez, E., Donapetry-García, C., Vila-Altesor, M., and Rodríguez-Seijas, J. (2014) Comprehensive review on lactate metabolism in human health. *Mitochondrion* **17**, 76–100

7. Bricker, D. K., Taylor, E. B., Schell, J. C., Orsak, T., Boutron, A., Chen, Y.-C., Cox, J. E., Cardon, C. M., van Vranken, J. G., Dephoure, N., Redin, C., Boudina, S., Gygi, S. P., Brivet, M., Thummel, C. S., and Rutter, J. (2012) A mitochondrial pyruvate carrier required for pyruvate uptake in yeast, Drosophila, and humans. *Science* **337**, 96–100

8. Cornell, N. W., Lund, P., Hems, R., and Krebs, H. A. (1973) Acceleration of gluconeogenesis from lactate by lysine. *Biochem. J.* **134**, 671–672

9. Halestrap, A. P. (2013) Monocarboxylic acid transport. *Compr. Physiol.* **3**, 1611–1643

10. Cheung, S. M., Husain, E., Masannat, Y., Miller, I. D., Wahle, K., Heys, S. D., and He, J. (2020) Lactate concentration in breast cancer using advanced magnetic resonance spectroscopy. *Br. J. Cancer* **123**, 261–267

11. Howe, F. A., Barton, S. J., Cudlip, S. A., Stubbs, M., Saunders, D. E., Murphy, M., Wilkins, P., Opstad, K. S., Doyle, V. L., McLean, M. A., Bell, B. A., and Griffiths, J. R. (2003) Metabolic profiles of human brain tumors using quantitative *in vivo* 1H magnetic resonance spectroscopy. *Magn. Reson. Med.* **49**, 223–232

12. Wright, A. J., Fellows, G. A., Griffiths, J. R., Wilson, M., Bell, B. A., and Howe, F. A. (2010) *Ex-vivo* HRMAS of adult brain tumours: metabolite quantification and assignment of tumour biomarkers. *Mol. Cancer* **9**, 66

13. Hanahan, D., and Weinberg, R. A. (2011) Hallmarks of cancer: the next generation. *Cell* **144**, 646–674

14. Warburg, O., Wind, F., and Negelein, E. (1927) The metabolism of tumors in the body. *J. Gen. Physiol.* **8**, 519–530

15. Iyer, N. V., Kotch, L. E., Agani, F., Leung, S. W., Laughner, E., Wenger, R. H., Gassmann, M., Gearhart, J. D., Lawler, A. M., Yu, A. Y., and Semenza, G. L. (1998) Cellular and developmental control of O_2 homeostasis by hypoxia-inducible factor 1 alpha. *Genes Dev.* **12**, 149–162

16. Osthus, R. C., Shim, H., Kim, S., Li, Q., Reddy, R., Mukherjee, M., Xu, Y., Wonsey, D., Lee, L. A., and Dang, C. V. (2000) Deregulation of glucose transporter 1 and glycolytic gene expression by c-Myc. *J. Biol. Chem.* **275**, 21797–21800

17. Guppy, M., Greiner, E., and Brand, K. (1993) The role of the Crabtree effect and an endogenous fuel in the energy metabolism of resting and proliferating thymocytes. *Eur. J. Biochem.* **212**, 95–99

18. Pfeiffer, T., Schuster, S., and Bonhoeffer, S. (2001) Cooperation and competition in the evolution of ATP-producing pathways. *Science* **292**, 504–507

19. DeBerardinis, R. J., Lum, J. J., Hatzivassiliou, G., and Thompson, C. B. (2008) The biology of cancer: metabolic reprogramming fuels cell growth and proliferation. *Cell Metab.* **7**, 11–20

20. Faubert, B., Li, K. Y., Cai, L., Hensley, C. T., Kim, J., Zacharias, L. G., Yang, C., Do, Q. N., Doucette, S., Burguete, D., Li, H., Huet, G., Yuan, Q., Wigal, T., Butt, Y., Ni, M., Torrealba, J., Oliver, D., Lenkinski, R. E., Malloy, C. R., Wachsmann, J. W., Young, J. D., Kernstine, K., and DeBerardinis, R. J. (2017) Lactate metabolism in human lung tumors. *Cell* **171**, 358-371

21. Hui, S., Ghergurovich, J. M., Morscher, R. J., Jang, C., Teng, X., Lu, W., Esparza, L. A., Reya, T., Le Zhan, Yanxiang Guo, J., White, E., and Rabinowitz, J. D. (2017) Glucose feeds the TCA cycle via circulating lactate. *Nature* **551**, 115–118

22. Payen, V. L., Mina, E., van Hée, V. F., Porporato, P. E., and Sonveaux, P. (2019) Monocarboxylate transporters in cancer. *Mol. Metab.* **33**, 48–66

23. Végran, F., Boidot, R., Michiels, C., Sonveaux, P., and Feron, O. (2011) Lactate influx through the endothelial cell monocarboxylate transporter MCT1 supports an NF-κB/IL-8 pathway that drives tumor angiogenesis. *Cancer Res.* **71**, 2550–2560

24. Roland, C. L., Arumugam, T., Deng, D., Liu, S. H., Philip, B., Gomez, S., Burns, W. R., Ramachandran, V., Wang, H., Cruz-Monserrate, Z., and Logsdon, C. D. (2014) Cell surface lactate receptor GPR81 is crucial for cancer cell survival. *Cancer Res.* **74**, 5301–5310

25. Colegio, O. R., Chu, N.-Q., Szabo, A. L., Chu, T., Rhebergen, A. M., Jairam, V., Cyrus, N., Brokowski, C. E., Eisenbarth, S. C., Phillips, G. M., Cline, G. W., Phillips, A. J., and Medzhitov, R. (2014) Functional polarization of tumour-associated macrophages by tumour-derived lactic acid. *Nature* **513**, 559–563

26. Lu, H., Forbes, R. A., and Verma, A. (2002) Hypoxia-inducible factor 1 activation by aerobic glycolysis implicates the Warburg effect in carcinogenesis. *J. Biol. Chem.* **277**, 23111–23115

27. Sandforth, L., Ammar, N., Dinges, L. A., Röcken, C., Arlt, A., Sebens, S., and Schäfer, H. (2020) Impact of the monocarboxylate transporter-1 (MCT1)-mediated cellular import of lactate on stemness properties of human pancreatic adenocarcinoma cells. *Cancers (Basel)* **12**, 581

28. Gopal, E., Fei, Y.-J., Sugawara, M., Miyauchi, S., Zhuang, L., Martin, P., Smith, S. B., Prasad, P. D., and Ganapathy, V. (2004) Expression of slc5a8 in kidney and its role in Na^+-coupled transport of lactate. *J. Biol. Chem.* **279**, 44522–44532

29. Coady, M. J., Chang, M.-H., Charron, F. M., Plata, C., Wallendorff, B., Sah, J. F., Markowitz, S. D., Romero, M. F., and Lapointe, J.-Y. (2004) The human tumour suppressor gene SLC5A8 expresses a Na^+-monocarboxylate cotransporter. *J. Physiol.* **557**, 719–731

30. Iwanaga, T., Takebe, K., Kato, I., Karaki, S.-I., and Kuwahara, A. (2006) Cellular expression of monocarboxylate transporters (MCT) in the digestive tract of the mouse, rat, and humans, with special reference to slc5a8. *Biomed. Res.* **27**, 243–254

31. Gopal, E., Umapathy, N. S., Martin, P. M., Ananth, S., Gnana-Prakasam, J. P., Becker, H., Wagner, C. A., Ganapathy, V., and Prasad, P. D. (2007) Cloning and functional characterization of human SMCT2 (SLC5A12) and expression pattern of the transporter in kidney. *Biochim. Biophys. Acta* **1768**, 2690–2697

32. Paradies, G., and Papa, S. (1977) On the kinetics and substrate specificity of the pyruvate translocator in rat liver mitochondria. *Biochim. Biophys. Acta* **462**, 333–346

33. Halestrap, A. P. (1978) Pyruvate and ketone-body transport across the mitochondrial membrane. Exchange properties, pH-dependence and mechanism of the carrier. *Biochem. J.* **172**, 377–387

34. Hashimoto, T., Hussien, R., and Brooks, G. A. (2006) Colocalization of MCT1, CD147, and LDH in mitochondrial inner membrane of L6 muscle cells: evidence of a mitochondrial lactate oxidation complex. *Am. J. Physiol. Endocrinol. Metab.* **290**, E1237-E1244

35. Brooks, G. A., Brown, M. A., Butz, C. E., Sicurello, J. P., and Dubouchaud, H. (1999) Cardiac and skeletal muscle mitochondria have a monocarboxylate transporter MCT1. *J. Appl. Physiol.* **87**, 1713–1718

36. Bioparadigms (2013) SLC Tables [*database*]. Online available at: https://slc.bioparadigms.org/. Last visited on 03/12/2021.

37. Song, W., Li, D., Tao, L., Luo, Q., and Chen, L. (2020) Solute carrier transporters: the metabolic gatekeepers of immune cells. *Acta Pharm. Sin. B* **10**, 61–78

38. Hediger, M. A., Romero, M. F., Peng, J.-B., Rolfs, A., Takanaga, H., and Bruford, E. A. (2004) The ABCs of solute carriers: physiological, pathological and therapeutic implications of human membrane transport proteins. *Pflugers Arch.* **447**, 465–468

39. Kim, D. K., Kanai, Y., Chairoungdua, A., Matsuo, H., Cha, S. H., and Endou, H. (2001) Expression cloning of a Na^+-independent aromatic amino acid transporter with structural similarity to H^+/monocarboxylate transporters. *J. Biol. Chem.* **276**, 17221–17228

40. Friesema, E. C. H., Ganguly, S., Abdalla, A., Manning Fox, J. E., Halestrap, A. P., and Visser, T. J. (2003) Identification of monocarboxylate transporter 8 as a specific thyroid hormone transporter. *J. Biol. Chem.* **278**, 40128–40135

41. Murakami, Y., Kohyama, N., Kobayashi, Y., Ohbayashi, M., Ohtani, H., Sawada, Y., and Yamamoto, T. (2005) Functional characterization of human monocarboxylate transporter 6 (SLC16A5). *Drug Metab. Dispos.* **33**, 1845–1851

42. Hugo, S. E., Cruz-Garcia, L., Karanth, S., Anderson, R. M., Stainier, D. Y. R., and Schlegel, A. (2012) A monocarboxylate transporter required for hepatocyte secretion of ketone bodies during fasting. *Genes Dev.* **26**, 282–293

43. Suhre, K., Shin, S.-Y., Petersen, A.-K., Mohney, R. P., Meredith, D., Wägele, B., Altmaier, E., Deloukas, P., Erdmann, J., Grundberg, E., Hammond, C. J., Angelis, M. H. de, Kastenmüller, G., Köttgen, A., Kronenberg, F., Mangino, M., Meisinger, C., Meitinger, T., Mewes, H.-W., Milburn, M. V., Prehn, C., Raffler, J., Ried, J. S., Römisch-

Margl, W., Samani, N. J., Small, K. S., Wichmann, H.-E., Zhai, G., Illig, T., Spector, T. D., Adamski, J., Soranzo, N., and Gieger, C. (2011) Human metabolic individuality in biomedical and pharmaceutical research. *Nature* **477**, 54–60

44. Poole, R. C., and Halestrap, A. P. (1988) Reconstitution of the L-lactate carrier from rat and rabbit erythrocyte plasma membranes. *Biochem. J.* **254**, 385–390

45. Poole, R. C., and Halestrap, A. P. (1992) Identification and partial purification of the erythrocyte L-lactate transporter. *Biochem. J.* **283 (Pt 3)**, 855–862

46. Poole, R. C., and Halestrap, A. P. (1994) N-terminal protein sequence analysis of the rabbit erythrocyte lactate transporter suggests identity with the cloned monocarboxylate transport protein MCT1. *Biochem. J.* **303 (Pt 3)**, 755–759

47. Garcia, C. K., Goldstein, J. L., Pathak, R. K., Anderson, R. G., and Brown, M. S. (1994) Molecular characterization of a membrane transporter for lactate, pyruvate, and other monocarboxylates: implications for the Cori cycle. *Cell* **76**, 865–873

48. Halestrap, A. P. (2013) The SLC16 gene family - structure, role and regulation in health and disease. *Mol. Aspects Med.* **34**, 337–349

49. Philp, N. J., Yoon, H., and Grollman, E. F. (1998) Monocarboxylate transporter MCT1 is located in the apical membrane and MCT3 in the basal membrane of rat RPE. *Am. J. Physiol.* **274**, R1824-R1828

50. Bröer, S., Schneider, H. P., Bröer, A., Rahman, B., Hamprecht, B., and Deitmer, J. W. (1998) Characterization of the monocarboxylate transporter 1 expressed in *Xenopus laevis* oocytes by changes in cytosolic pH. *Biochem. J.* **333 (Pt 1)**, 167–174

51. Bröer, S., Bröer, A., Schneider, H. P., Stegen, C., Halestrap, A. P., and Deitmer, J. W. (1999) Characterization of the high-affinity monocarboxylate transporter MCT2 in *Xenopus laevis* oocytes. *Biochem. J.* **341 (Pt 3)**, 529–535

52. Dimmer, K. S., Friedrich, B., Lang, F., Deitmer, J. W., and Bröer, S. (2000) The low-affinity monocarboxylate transporter MCT4 is adapted to the export of lactate in highly glycolytic cells. *Biochem. J.* **350 (Pt 1)**, 219–227

53. Poole, R. C., Sansom, C. E., and Halestrap, A. P. (1996) Studies of the membrane topology of the rat erythrocyte H^+/lactate cotransporter (MCT1). *Biochem. J.* **320 (Pt 3)**, 817–824

54. Bosshart, P. D., Kalbermatter, D., Bonetti, S., and Fotiadis, D. (2019) Mechanistic basis of L-lactate transport in the SLC16 solute carrier family. *Nat. Commun.* **10**, 2649

55. Zhang, B., Jin, Q., Xu, L., Li, N., Meng, Y., Chang, S., Zheng, X., Wang, J., Chen, Y., Neculai, D., Gao, N., Zhang, X., Yang, F., Guo, J., and Ye, S. (2020) Cooperative

transport mechanism of human monocarboxylate transporter 2. *Nat. Commun.* **11**, 2429

56. Wilson, M. C., Meredith, D., Bunnun, C., Sessions, R. B., and Halestrap, A. P. (2009) Studies on the DIDS-binding site of monocarboxylate transporter 1 suggest a homology model of the open conformation and a plausible translocation cycle. *J. Biol. Chem.* **284**, 20011–20021

57. Manoharan, C., Wilson, M. C., Sessions, R. B., and Halestrap, A. P. (2006) The role of charged residues in the transmembrane helices of monocarboxylate transporter 1 and its ancillary protein basigin in determining plasma membrane expression and catalytic activity. *Mol. Membr. Biol.* **23**, 486–498

58. Lin, R. Y., Vera, J. C., Chaganti, R. S., and Golde, D. W. (1998) Human monocarboxylate transporter 2 (MCT2) is a high affinity pyruvate transporter. *J. Biol. Chem.* **273**, 28959–28965

59. Ritzhaupt, A., Wood, I. S., Ellis, A., Hosie, K. B., and Shirazi-Beechey, S. P. (1998) Identification and characterization of a monocarboxylate transporter (MCT1) in pig and human colon: Its potential to transport L-lactate as well as butyrate. *J. Physiol.* **513 (Pt 3)**, 719–732

60. Dubinsky, W. P., and Racker, E. (1978) The mechanism of lactate transport in human erythrocytes. *J. Membr. Biol.* **44**, 25–36

61. Bruijne, A. W. de, Vreeburg, H., and van Steveninck, J. (1983) Kinetic analysis of L-lactate transport in human erythrocytes via the monocarboxylate-specific carrier system. *Biochim. Biophys. Acta* **732**, 562–568

62. Bruijne, A. W. de, Vreeburg, H., and van Steveninck, J. (1985) Alternative-substrate inhibition of L-lactate transport via the monocarboxylate-specific carrier system in human erythrocytes. *Biochim. Biophys. Acta* **812**, 841–844

63. Juel, C. (1991) Muscle lactate transport studied in sarcolemmal giant vesicles. *Biochim. Biophys. Acta* **1065**, 15–20

64. Juel, C., Kristiansen, S., Pilegaard, H., Wojtaszewski, J., and Richter, E. A. (1994) Kinetics of lactate transport in sarcolemmal giant vesicles obtained from human skeletal muscle. *J. Appl. Physiol.* **76**, 1031–1036

65. Rahman, B., Schneider, H. P., Bröer, A., Deitmer, J. W., and Bröer, S. (1999) Helix 8 and helix 10 are involved in substrate recognition in the rat monocarboxylate transporter MCT1. *Biochemistry* **38**, 11577–11584

66. Yamaguchi, A., Futagi, Y., Kobayashi, M., Narumi, K., Furugen, A., and Iseki, K. (2020) Extracellular lysine 38 plays a crucial role in pH-dependent transport via human monocarboxylate transporter 1. *Biochim. Biophys. Acta Biomembr.* **1862**, 183068

67. Yamaguchi, A., Narumi, K., Furugen, A., Iseki, K., and Kobayashi, M. (2020) Identification of the essential extracellular aspartic acids conserved in human monocarboxylate transporters 1, 2, and 4. *Biochem. Biophys. Res. Com.* **529**, 1061–1065

68. Poole, R. C., and Halestrap, A. P. (1997) Interaction of the erythrocyte lactate transporter (monocarboxylate transporter 1) with an integral 70-kDa membrane glycoprotein of the immunoglobulin superfamily. *J. Biol. Chem.* **272**, 14624–14628

69. Kirk, P., Wilson, M. C., Heddle, C., Brown, M. H., Barclay, A. N., and Halestrap, A. P. (2000) CD147 is tightly associated with lactate transporters MCT1 and MCT4 and facilitates their cell surface expression. *EMBO J.* **19**, 3896–3904

70. Wilson, M. C., Meredith, D., Fox, J. E. M., Manoharan, C., Davies, A. J., and Halestrap, A. P. (2005) Basigin (CD147) is the target for organomercurial inhibition of monocarboxylate transporter isoforms 1 and 4: the ancillary protein for the insensitive MCT2 is EMBIGIN (gp70). *J. Biol. Chem.* **280**, 27213–27221

71. Philp, N. J., Ochrietor, J. D., Rudoy, C., Muramatsu, T., and Linser, P. J. (2003) Loss of MCT1, MCT3, and MCT4 expression in the retinal pigment epithelium and neural retina of the 5A11/basigin-null mouse. *Investig. Ophthalmol. Vis. Sci.* **44**, 1305–1311

72. Tachikui, H., Kurosawa, N., Kadomatsu, K., and Muramatsu, T. (1999) Genomic organization and promoter activity of embigin, a member of the immunoglobulin superfamily. *Gene* **240**, 325–332

73. Liao, C.-G., Kong, L.-M., Song, F., Xing, J.-L., Wang, L.-X., Sun, Z.-J., Tang, H., Yao, H., Zhang, Y., Wang, L., Wang, Y., Yang, X.-M., Li, Y., and Chen, Z.-N. (2011) Characterization of basigin isoforms and the inhibitory function of basigin-3 in human hepatocellular carcinoma proliferation and invasion. *Mol. Cell. Biol.* **31**, 2591–2604

74. Biswas, C., Zhang, Y., DeCastro, R., Guo, H., Nakamura, T., Kataoka, H., and Nabeshima, K. (1995) The human tumor cell-derived collagenase stimulatory factor (renamed EMMPRIN) is a member of the immunoglobulin superfamily. *Cancer Res.* **55**, 434–439

75. Ozawa, M., Huang, R. P., Furukawa, T., and Muramatsu, T. (1988) A teratocarcinoma glycoprotein carrying a developmentally regulated carbohydrate marker is a member of the immunoglobulin gene superfamily. *J. Biol. Chem.* **263**, 3059–3062

76. Yu, X.-L., Hu, T., Du, J.-M., Ding, J.-P., Yang, X.-M., Zhang, J., Yang, B., Shen, X., Zhang, Z., Zhong, W.-D., Wen, N., Jiang, H., Zhu, P., and Chen, Z.-N. (2008) Crystal structure of HAb18G/CD147: implications for immunoglobulin superfamily homophilic adhesion. *J. Biol. Chem.* **283**, 18056–18065

77. Redzic, J. S., Armstrong, G. S., Isern, N. G., Jones, D. N. M., Kieft, J. S., and Eisenmesser, E. Z. (2011) The retinal specific CD147 Ig0 domain: From molecular structure to biological activity. *J. Mol. Biol.* **411**, 68–82

78. Yurchenko, V., Zybarth, G., O'Connor, M., Dai, W. W., Franchin, G., Hao, T., Guo, H., Hung, H.-C., Toole, B., Gallay, P., Sherry, B., and Bukrinsky, M. (2002) Active site residues of cyclophilin A are crucial for its signaling activity via CD147. *J. Biol. Chem.* **277**, 22959–22965

79. Li, Y., Wu, J., Song, F., Tang, J., Wang, S.-J., Yu, X.-L., Chen, Z.-N., and Jiang, J.-L. (2012) Extracellular membrane-proximal domain of HAb18G/CD147 binds to metal ion-dependent adhesion site (MIDAS) motif of integrin β1 to modulate malignant properties of hepatoma cells. *J. Biol. Chem.* **287**, 4759–4772

80. Tang, J., Wu, Y.-M., Zhao, P., Yang, X.-M., Jiang, J.-L., and Chen, Z.-N. (2008) Overexpression of HAb18G/CD147 promotes invasion and metastasis via alpha3beta1 integrin mediated FAK-paxillin and FAK-PI3K-Ca^{2+} pathways. *Cell. Mol. Life Sci.* **65**, 2933–2942

81. Kanekura, T., Chen, X., and Kanzaki, T. (2002) Basigin (CD147) is expressed on melanoma cells and induces tumor cell invasion by stimulating production of matrix metalloproteinases by fibroblasts. *Int. J. Cancer* **99**, 520–528

82. Muramatsu, T. (2016) Basigin (CD147), a multifunctional transmembrane glycoprotein with various binding partners. *J. Biochem.* **159**, 481–490

83. Crosnier, C., Bustamante, L. Y., Bartholdson, S. J., Bei, A. K., Theron, M., Uchikawa, M., Mboup, S., Ndir, O., Kwiatkowski, D. P., Duraisingh, M. T., Rayner, J. C., and Wright, G. J. (2011) Basigin is a receptor essential for erythrocyte invasion by *Plasmodium falciparum*. *Nature* **480**, 534–537

84. Pushkarsky, T., Zybarth, G., Dubrovsky, L., Yurchenko, V., Tang, H., Guo, H., Toole, B., Sherry, B., and Bukrinsky, M. (2001) CD147 facilitates HIV-1 infection by interacting with virus-associated cyclophilin A. *Proc. Natl. Acad. Sci. U.S.A.* **98**, 6360–6365

85. Chen, Z., Mi, L., Xu, J., Yu, J., Wang, X., Jiang, J., Xing, J., Shang, P., Qian, A., Li, Y., Shaw, P. X., Wang, J., Duan, S., Ding, J., Fan, C., Zhang, Y., Yang, Y., Yu, X., Feng, Q., Li, B., Yao, X., Zhang, Z., Li, L., Xue, X., and Zhu, P. (2005) Function of

HAb18G/CD147 in invasion of host cells by severe acute respiratory syndrome coronavirus. *J. Infect. Dis.* **191**, 755–760

86. Jin, S., Ding, P., Chu, P., Li, H., Sun, J., Liang, D., Song, F., and Xia, B. (2018) Zn(II) can mediate self-association of the extracellular C-terminal domain of CD147. *Protein Cell* **9**, 310–315

87. Wilson, M. C., Meredith, D., and Halestrap, A. P. (2002) Fluorescence resonance energy transfer studies on the interaction between the lactate transporter MCT1 and CD147 provide information on the topology and stoichiometry of the complex *in situ*. *J. Biol. Chem.* **277**, 3666–3672

88. Makuc, J., Cappellaro, C., and Boles, E. (2004) Co-expression of a mammalian accessory trafficking protein enables functional expression of the rat MCT1 monocarboxylate transporter in *Saccharomyces cerevisiae*. *FEMS Yeast Res.* **4**, 795–801

89. Updegraff, B. L., Zhou, X., Guo, Y., Padanad, M. S., Chen, P.-H., Yang, C., Sudderth, J., Rodriguez-Tirado, C., Girard, L., Minna, J. D., Mishra, P., DeBerardinis, R. J., and O'Donnell, K. A. (2018) Transmembrane protease TMPRSS11B promotes lung cancer growth by enhancing lactate export and glycolytic metabolism. *Cell Rep.* **25**, 2223–2233.e6

90. Pérez-Escuredo, J., van Hée, V. F., Sboarina, M., Falces, J., Payen, V. L., Pellerin, L., and Sonveaux, P. (2016) Monocarboxylate transporters in the brain and in cancer. *Biochim. Biophys. Acta* **1863**, 2481–2497

91. Juel, C., and Halestrap, A. P. (1999) Lactate transport in skeletal muscle - role and regulation of the monocarboxylate transporter. *J. Physiol.* **517 (Pt 3)**, 633–642

92. Sonveaux, P., Végran, F., Schroeder, T., Wergin, M. C., Verrax, J., Rabbani, Z. N., Saedeleer, C. J. de, Kennedy, K. M., Diepart, C., Jordan, B. F., Kelley, M. J., Gallez, B., Wahl, M. L., Feron, O., and Dewhirst, M. W. (2008) Targeting lactate-fueled respiration selectively kills hypoxic tumor cells in mice. *J. Clin. Investig.* **118**, 3930–3942

93. Pinheiro, C., Longatto-Filho, A., Ferreira, L., Pereira, S. M. M., Etlinger, D., Moreira, M. A. R., Jubé, L. F., Queiroz, G. S., Schmitt, F., and Baltazar, F. (2008) Increasing expression of monocarboxylate transporters 1 and 4 along progression to invasive cervical carcinoma. *Int. J. Gynecol. Pathol.* **27**, 568–574

94. Pinheiro, C., Albergaria, A., Paredes, J., Sousa, B., Dufloth, R., Vieira, D., Schmitt, F., and Baltazar, F. (2010) Monocarboxylate transporter 1 is up-regulated in basal-like breast carcinoma. *Histopathology* **56**, 860–867

95. Oliveira, A. T. T. de, Pinheiro, C., Longatto-Filho, A., Brito, M. J., Martinho, O., Matos, D., Carvalho, A. L., Vazquez, V. L., Silva, T. B., Scapulatempo, C., Saad, S. S., Reis, R. M., and Baltazar, F. (2012) Co-expression of monocarboxylate transporter 1 (MCT1) and its chaperone (CD147) is associated with low survival in patients with gastrointestinal stromal tumors (GISTs). *J. Bioenerg. Biomembr.* **44**, 171–178

96. Le Floch, R., Chiche, J., Marchiq, I., Naiken, T., Ilc, K., Murray, C. M., Critchlow, S. E., Roux, D., Simon, M.-P., and Pouysségur, J. (2011) CD147 subunit of lactate/H^+ symporters MCT1 and hypoxia-inducible MCT4 is critical for energetics and growth of glycolytic tumors. *Proc. Natl. Acad. Sci. U.S.A.* **108**, 16663–16668

97. Meredith, D., and Christian, H. C. (2008) The SLC16 monocaboxylate transporter family. *Xenobiotica* **38**, 1072–1106

98. Voss, D. M., Spina, R., Carter, D. L., Lim, K. S., Jeffery, C. J., and Bar, E. E. (2017) Disruption of the monocarboxylate transporter-4-basigin interaction inhibits the hypoxic response, proliferation, and tumor progression. *Sci. Rep.* **7**, 4292

99. Guan, X., Rodriguez-Cruz, V., and Morris, M. E. (2019) Cellular uptake of MCT1 inhibitors AR-C155858 and AZD3965 and their effects on MCT-mediated transport of L-lactate in murine 4T1 breast tumor cancer cells. *AAPS J.* **21**, 13

100. Curtis, N. J., Mooney, L., Hopcroft, L., Michopoulos, F., Whalley, N., Zhong, H., Murray, C., Logie, A., Revill, M., Byth, K. F., Benjamin, A. D., Firth, M. A., Green, S., Smith, P. D., and Critchlow, S. E. (2017) Pre-clinical pharmacology of AZD3965, a selective inhibitor of MCT1: DLBCL, NHL and Burkitt's lymphoma anti-tumor activity. *Oncotarget* **8**, 69219–69236

101. Ovens, M. J., Davies, A. J., Wilson, M. C., Murray, C. M., and Halestrap, A. P. (2010) AR-C155858 is a potent inhibitor of monocarboxylate transporters MCT1 and MCT2 that binds to an intracellular site involving transmembrane helices 7-10. *Biochem. J.* **425**, 523–530

102. Nancolas, B., Sessions, R. B., and Halestrap, A. P. (2015) Identification of key binding site residues of MCT1 for AR-C155858 reveals the molecular basis of its isoform selectivity. *Biochem. J.* **467**, 192

103. Wang, N., Jiang, X., Zhang, S., Zhu, A., Yuan, Y., Xu, H., Lei, J., and Yan, C. (2021) Structural basis of human monocarboxylate transporter 1 inhibition by anti-cancer drug candidates. *Cell* **184**, 370–383.e13

104. Golldack, A., Henke, B., Bergmann, B., Wiechert, M., Erler, H., Blancke Soares, A., Spielmann, T., and Beitz, E. (2017) Substrate-analogous inhibitors exert antimalarial

action by targeting the *Plasmodium* lactate transporter PfFNT at nanomolar scale. *PLOS Pathog.* **13**, e1006172

105. Casal, M., Paiva, S., Andrade, R. P., Gancedo, C., and Leão, C. (1999) The lactate-proton symport of *Saccharomyces cerevisiae* is encoded by JEN1. *J. Bacteriol.* **181**, 2620–2623

106. Kok, S. de, Nijkamp, J. F., Oud, B., Roque, F. C., Ridder, D. de, Daran, J.-M., Pronk, J. T., and van Maris, A. J. A. (2012) Laboratory evolution of new lactate transporter genes in a *jen1*Δ mutant of *Saccharomyces cerevisiae* and their identification as ADY2 alleles by whole-genome resequencing and transcriptome analysis. *FEMS Yeast Res.* **12**, 359–374

107. Cherry, J. M., Hong, E. L., Amundsen, C., Balakrishnan, R., Binkley, G., Chan, E. T., Christie, K. R., Costanzo, M. C., Dwight, S. S., Engel, S. R., Fisk, D. G., Hirschman, J. E., Hitz, B. C., Karra, K., Krieger, C. J., Miyasato, S. R., Nash, R. S., Park, J., Skrzypek, M. S., Simison, M., Weng, S., and Wong, E. D. (2012) *Saccharomyces* Genome Database: The genomics resource of budding yeast. *Nucleic Acids Res.* **40**, D700-5

108. van Dijken, J. P., and Scheffers, W. A. (1986) Redox balances in the metabolism of sugars by yeasts. *FEMS Microbiol. Rev.* **1**, 199–224

109. Wu, B., Rambow, J., Bock, S., Holm-Bertelsen, J., Wiechert, M., Soares, A. B., Spielmann, T., and Beitz, E. (2015) Identity of a *Plasmodium* lactate/H^+ symporter structurally unrelated to human transporters. *Nat. Commun.* **6**, 6284

110. Meyer, A., Eskandari, S., Grallath, S., and Rentsch, D. (2006) AtGAT1, a high affinity transporter for gamma-aminobutyric acid in *Arabidopsis thaliana*. *J. Biol. Chem.* **281**, 7197–7204

111. Holm-Bertelsen, J. (2016) Expressionssysteme zur Gewinnung von rekombinantem PfFNT zur Reinigung, Funktionsuntersuchung und Kristallisation. *Dissertation.* Christian-Albrechts-Universität zu Kiel.
Online available at: https://nbn-resolving.org/urn:nbn:de:gbv:8-diss-191285

112. Müller-Lucks, A. (2012) Optimierung der zellfreien Proteinsynthese durch Etablierung einer schnellen *in-situ* Faltungskontrolle mittels GFP-Fusion. *Dissertation.* Christian-Albrechts-Universität zu Kiel.
Online available at: https://nbn-resolving.org/urn:nbn:de:gbv:8-diss-102165

113. Müller-Lucks, A., Bock, S., Wu, B., and Beitz, E. (2012) Fluorescent *in situ* folding control for rapid optimization of cell-free membrane protein synthesis. *PLOS ONE* **7**, e42186

114. Bock, S. (2014) Zellfreie Synthese von schwer herstellbaren Proteinen. *Dissertation.* Christian-Albrechts-Universität zu Kiel.
Online available at: https://nbn-resolving.org/urn:nbn:de:gbv:8-diss-142980

115. Soares-Silva, I., Paiva, S., Diallinas, G., and Casal, M. (2007) The conserved sequence NXXS/THXS/TQDXXXT of the lactate/pyruvate:H^+ symporter subfamily defines the function of the substrate translocation pathway. *Mol. Membr. Biol.* **24**, 464–474

116. Schwarz, D., Junge, F., Durst, F., Frölich, N., Schneider, B., Reckel, S., Sobhanifar, S., Dötsch, V., and Bernhard, F. (2007) Preparative scale expression of membrane proteins in *Escherichia coli*-based continuous exchange cell-free systems. *Nat. Protoc.* **2**, 2945–2957

117. Rues, R.-B., Gräwe, A., Henrich, E., and Bernhard, F. (2017) Membrane protein production in *E. coli* lysates in presence of preassembled nanodiscs. *Methods Mol. Biol.* **1586**, 291–312

118. Pettersen, E. F., Goddard, T. D., Huang, C. C., Couch, G. S., Greenblatt, D. M., Meng, E. C., and Ferrin, T. E. (2004) UCSF Chimera--a visualization system for exploratory research and analysis. *J. Comput. Chem.* **25**, 1605–1612

119. Hansen, C. (2019) Zellfreie Transportproteinsynthese mit Nanodisc-Technologie für Strukturuntersuchungen und phänotypisches Wirkstoffscreening in der Hefe. *Master's thesis, unpublished.* Christian-Albrechts-Universität zu Kiel.

120. Gietz, R. D. (2014) Yeast transformation by the LiAc/SS carrier DNA/PEG method. *Methods Mol. Biol.* **1205**, 1–12

121. Godwin, H. (1962) Half-life of radiocarbon. *Nature* **195**, 984

122. Damon, P., Lerman, J., and Long, A. (2003) Temporal fluctuations of atmospheric ^{14}C: causal factors and implications. *Annu. Rev. Earth Planet. Sci.* **6**, 457–494

123. Rambow, J. (2015) Characterization of PfFNT – a lactate transporter in *Plasmodium falciparum*. *Dissertation.* Christian-Albrechts-Universität zu Kiel.
Online available at: https://nbn-resolving.org/urn:nbn:de:gbv:8-diss-165273

124. Golldack, A. (2018) Entdeckung von Inhibitoren des Lactat-Transporters aus dem Malaria-Erreger *Plasmodium falciparum*. *Dissertation.* Christian-Albrechts-Universität zu Kiel.
Online available at: https://nbn-resolving.org/urn:nbn:de:gbv:8-diss-224802

125. Karbanowicz, T., Dover, E., Mu, X., Tabor, A., and Rodriguez-Valle, M. (2017) Extracellular expression of the HT1 neurotoxin from the Australian paralysis tick in two *Saccharomyces cerevisiae* strains. *Toxicon* **140**, 1–10

126. Denisov, I. G., Grinkova, Y. V., Lazarides, A. A., and Sligar, S. G. (2004) Directed self-assembly of monodisperse phospholipid bilayer Nanodiscs with controlled size. *J. Am. Chem. Soc.* **126**, 3477–3487

127. Ritchie, T. K., Grinkova, Y. V., Bayburt, T. H., Denisov, I. G., Zolnerciks, J. K., Atkins, W. M., and Sligar, S. G. (2009) Reconstitution of membrane proteins in phospholipid bilayer nanodiscs. *Meth. Enzymol.* **464**, 211–231

128. Arnold, P., Himmels, P., Weiß, S., Decker, T.-M., Markl, J., Gatterdam, V., Tampé, R., Bartholomäus, P., Dietrich, U., and Dürr, R. (2014) Antigenic and 3D structural characterization of soluble X4 and hybrid X4-R5 HIV-1 Env trimers. *Retrovirology* **11**, 42

129. Tang, G., Peng, L., Baldwin, P. R., Mann, D. S., Jiang, W., Rees, I., and Ludtke, S. J. (2007) EMAN2: an extensible image processing suite for electron microscopy. *J. Struct. Biol.* **157**, 38–46

130. US National Library of Medicine (1988) National Center for Biotechnology Information (NCBI) [*database*]. Online available at: https://www.ncbi.nlm.nih.gov/. Last visited 03/12/2021.

131. Altschul, S. F., Gish, W., Miller, W., Myers, E. W., and Lipman, D. J. (1990) Basic local alignment search tool. *J. Mol. Biol.* **215**, 403–410

132. The UniProt Consortium (2020) UniProt: The universal protein knowledgebase in 2021. *Nucleic Acids Res.* **49**, D480-D489

133. Beitz, E. (2000) T(E)Xtopo: shaded membrane protein topology plots in LAT(E)X2epsilon. *Bioinformatics* **16**, 1050–1051

134. Berman, H. M., Westbrook, J., Feng, Z., Gilliland, G., Bhat, T. N., Weissig, H., Shindyalov, I. N., and Bourne, P. E. (2000) The Protein Data Bank. *Nucleic Acids Res.* **28**, 235–242

135. Research Colloboratory for Structural Bioinformatics (RCSB) (1998) Protein Data Bank (PDB) [*database*]. Online available at: https://www.rcsb.org/. Last visited on 03/12/2021.

136. Guex, N., Peitsch, M. C., and Schwede, T. (2009) Automated comparative protein structure modeling with SWISS-MODEL and Swiss-PdbViewer: A historical perspective. *Electrophoresis* **30**, 162-173

137. Waterhouse, A., Bertoni, M., Bienert, S., Studer, G., Tauriello, G., Gumienny, R., Heer, F. T., Beer, T. A. P. de, Rempfer, C., Bordoli, L., Lepore, R., and Schwede, T. (2018)

SWISS-MODEL: Homology modelling of protein structures and complexes. *Nucleic Acids Res.* **46**, W296-W303

138. Dolinsky, T. J., Nielsen, J. E., McCammon, J. A., and Baker, N. A. (2004) PDB2PQR: an automated pipeline for the setup of Poisson-Boltzmann electrostatics calculations. *Nucleic Acids Res.* **32**, W665-W667

139. Dolinsky, T. J., Czodrowski, P., Li, H., Nielsen, J. E., Jensen, J. H., Klebe, G., and Baker, N. A. (2007) PDB2PQR: expanding and upgrading automated preparation of biomolecular structures for molecular simulations. *Nucleic Acids Res.* **35**, W522-W525

140. Baker, N. A., Sept, D., Joseph, S., Holst, M. J., and McCammon, J. A. (2001) Electrostatics of nanosystems: application to microtubules and the ribosome. *Proc. Natl. Acad. Sci. U.S.A.* **98**, 10037–10041

141. Guiard, B. (1985) Structure, expression and regulation of a nuclear gene encoding a mitochondrial protein: the yeast L(+)-lactate cytochrome c oxidoreductase (cytochrome b2). *EMBO J.* **4**, 3265–3272

142. Avers, C. J., Pfeffer, C. R., and Rancourt, M. W. (1965) Acriflavine induction of different kinds of "petite" mitochondrial populations in *Saccharomyces cerevisiae*. *J. Bacteriol.* **90**, 481–494

143. Keyhani, E., Khavari-Nejad, S., Keyhani, J., and Attar, F. (2009) Acriflavine-mediated apoptosis and necrosis in yeast *Candida utilis*. *Ann. N. Y. Acad. Sci.* **1171**, 284–291

144. Bader, A., and Beitz, E. (2020) Transmembrane facilitation of lactate/H^+ instead of lactic acid is not a question of semantics but of cell viability. *Membranes* **10**, 236

145. Hansen, M., Kun, J. F. J., Schultz, J. E., and Beitz, E. (2002) A single, bi-functional aquaglyceroporin in blood-stage *Plasmodium falciparum* malaria parasites. *J. Biol. Chem.* **277**, 4874–4882

146. Manning Fox, J. E., Meredith, D., and Halestrap, A. P. (2000) Characterisation of human monocarboxylate transporter 4 substantiates its role in lactic acid efflux from skeletal muscle. *J. Physiol.* **529 (Pt 2)**, 285–293

147. Hajek, P., Bader, A., Helmstetter, F., Henke, B., Arnold, P., and Beitz, E. (2019) Cell-free and yeast-based production of the malarial lactate transporter, PfFNT, delivers comparable yield and protein quality. *Front. Pharmacol.* **10**, 375

148. Yoshiura, C., Kofuku, Y., Ueda, T., Mase, Y., Yokogawa, M., Osawa, M., Terashima, Y., Matsushima, K., and Shimada, I. (2010) NMR analyses of the interaction between CCR5 and its ligand using functional reconstitution of CCR5 in lipid bilayers. *J. Am. Chem. Soc.* **132**, 6768–6777

149. Henderson, R., Chen, S., Chen, J. Z., Grigorieff, N., Passmore, L. A., Ciccarelli, L., Rubinstein, J. L., Crowther, R. A., Stewart, P. L., and Rosenthal, P. B. (2011) Tilt-pair analysis of images from a range of different specimens in single-particle electron cryomicroscopy. *J. Mol. Biol.* **413**, 1028–1046

150. Deuticke, B. (1982) Monocarboxylate transport in erythrocytes. *J. Membr. Biol.* **70**, 89–103

151. Klier, M., Andes, F. T., Deitmer, J. W., and Becker, H. M. (2014) Intracellular and extracellular carbonic anhydrases cooperate non-enzymatically to enhance activity of monocarboxylate transporters. *J. Biol. Chem.* **289**, 2765–2775

152. Halestrap, A. P., and Meredith, D. (2004) The SLC16 gene family-from monocarboxylate transporters (MCTs) to aromatic amino acid transporters and beyond. *Pflugers Arch.* **447**, 619–628

153. Goldin, A. L. (2006) Expression of ion channels in *Xenopus* oocytes. In: Clare, J. J., Trezise, D. J. Expression and analysis of recombinant ion channels: from structural studies to pharmacological screening, pp. 1-25. Wiley-VCH, Weinheim. 978-3527608096

154. Volkov, V. (2015) Quantitative description of ion transport via plasma membrane of yeast and small cells. *Front. Plant Sci.* **6**, 425

155. Wiechert, M., Erler, H., Golldack, A., and Beitz, E. (2017) A widened substrate selectivity filter of eukaryotic formate-nitrite transporters enables high-level lactate conductance. *FEBS J.* **284**, 2663–2673

156. Erler, H., Ren, B., Gupta, N., and Beitz, E. (2018) The intracellular parasite *Toxoplasma gondii* harbors three druggable FNT-type formate and L-lactate transporters in the plasma membrane. *J. Biol. Chem.* **293**, 17622–17630

157. Helmstetter, F., Arnold, P., Höger, B., Petersen, L. M., and Beitz, E. (2019) Formate-nitrite transporters carrying nonprotonatable amide amino acids instead of a central histidine maintain pH-dependent transport. *J. Biol. Chem.* **294**, 623–631

158. Feyder, S., Craene, J.-O. de, Bär, S., Bertazzi, D. L., and Friant, S. (2015) Membrane trafficking in the yeast *Saccharomyces cerevisiae* model. *Int. J. Mol. Sci.* **16**, 1509–1525

159. Tanner, W., and Lehle, L. (1987) Protein glycosylation in yeast. *Biochim. Biophys. Acta* **906**, 81–99

160. Nørgaard, P., Westphal, V., Tachibana, C., Alsøe, L., Holst, B., and Winther, J. R. (2001) Functional differences in yeast protein disulfide isomerases. *J. Cell Biol.* **152**, 553–562

161. Yu, X.-L., Jiang, J.-L., Li, L., Feng, Q., Xu, J., and Chen, Z.-N. (2006) The glycosylation characteristic of hepatoma-associated antigen HAb18G/CD147 in human hepatoma cells. *Int. J. Biochem. Cell Biol.* **38**, 1939–1945

162. Cui, J., Huang, W., Wu, B., Jin, J., Jing, L., Shi, W.-P., Liu, Z.-Y., Yuan, L., Luo, D., Li, L., Chen, Z.-N., and Jiang, J.-L. (2018) *N*-glycosylation by *N*-acetylglucosaminyltransferase V enhances the interaction of CD147/basigin with integrin β1 and promotes HCC metastasis. *J. Pathol.* **245**, 41–52

163. Farquhar, R., Honey, N., Murant, S. J., Bossier, P., Schultz, L., Montgomery, D., Ellis, R. W., Freedman, R. B., and Tuite, M. F. (1991) Protein disulfide isomerase is essential for viability in *Saccharomyces cerevisiae*. *Gene* **108**, 81–89

164. Terpe, K. (2003) Overview of tag protein fusions: From molecular and biochemical fundamentals to commercial systems. *Appl. Microbiol. Biotechnol.* **60**, 523–533

165. Yang, H., Liu, L., and Xu, F. (2016) The promises and challenges of fusion constructs in protein biochemistry and enzymology. *Appl. Microbiol. Biotechnol.* **100**, 8273–8281

166. Iturrate, L., Sánchez-Moreno, I., Oroz-Guinea, I., Pérez-Gil, J., and García-Junceda, E. (2010) Preparation and characterization of a bifunctional aldolase/kinase enzyme: A more efficient biocatalyst for C-C bond formation. *Chem. Eur. J.* **16**, 4018–4030

167. Yu, K., Liu, C., Kim, B.-G., and Lee, D.-Y. (2015) Synthetic fusion protein design and applications. *Biotechnol. Adv.* **33**, 155–164

168. Chen, X., Zaro, J. L., and Shen, W.-C. (2013) Fusion protein linkers: Property, design and functionality. *Adv. Drug Deliv. Rev.* **65**, 1357–1369

169. Poole, R. C., and Halestrap, A. P. (1993) Transport of lactate and other monocarboxylates across mammalian plasma membranes. *Am. J. Physiol.* **264**, C761–C782

170. Deuticke, B., Rickert, I., and Beyer, E. (1978) Stereoselective, SH-dependent transfer of lactate in mammalian erythrocytes. *Biochim. Biophys. Acta* **507**, 137–155

171. Carpenter, L., and Halestrap, A. P. (1994) The kinetics, substrate and inhibitor specificity of the lactate transporter of Ehrlich-Lettre tumour cells studied with the intracellular pH indicator BCECF. *Biochem. J.* **304 (Pt 3)**, 751–760

172. Forero-Quintero, L. S., Ames, S., Schneider, H.-P., Thyssen, A., Boone, C. D., Andring, J. T., McKenna, R., Casey, J. R., Deitmer, J. W., and Becker, H. M. (2019) Membrane-

anchored carbonic anhydrase IV interacts with monocarboxylate transporters via their chaperones CD147 and GP70. *J. Biol. Chem.* **294**, 593–607

173. Bröer, S., Rahman, B., Pellegri, G., Pellerin, L., Martin, J. L., Verleysdonk, S., Hamprecht, B., and Magistretti, P. J. (1997) Comparison of lactate transport in astroglial cells and monocarboxylate transporter 1 (MCT 1) expressing *Xenopus laevis* oocytes. Expression of two different monocarboxylate transporters in astroglial cells and neurons. *J. Biol. Chem.* **272**, 30096–30102

174. Bakker, E. P., and van Dam, K. (1974) The movement of monocarboxylic acids across phospholipid membranes: evidence for an exchange diffusion between pyruvate and other monocarboxylate ions. *Biochim. Biophys. Acta* **339**, 285–289

175. Cássio, F., Leão, C., and van Uden, N. (1987) Transport of lactate and other short-chain monocarboxylates in the yeast *Saccharomyces cerevisiae*. *Appl. Environ. Microbiol.* **53**, 509–513

176. Stein, W. D., and Litman, T. (2015) Channels, carriers, and pumps, 2nd Edition, Elsevier, London. 978-0-12-416579-3

177. Moras, M., Lefevre, S. D., and Ostuni, M. A. (2017) From erythroblasts to mature red blood cells: organelle clearance in mammals. *Front. Physiol.* **8**, 1076

178. White, J. G., Amos, W. B., and Fordham, M. (1987) An evaluation of confocal versus conventional imaging of biological structures by fluorescence light microscopy. *J. Cell Biol.* **105**, 41–48

179. Stridh, M. H., Alt, M. D., Wittmann, S., Heidtmann, H., Aggarwal, M., Riederer, B., Seidler, U., Wennemuth, G., McKenna, R., Deitmer, J. W., and Becker, H. M. (2012) Lactate flux in astrocytes is enhanced by a non-catalytic action of carbonic anhydrase II. *J. Physiol.* **590**, 2333–2351

180. Noor, S. I., Jamali, S., Ames, S., Langer, S., Deitmer, J. W., and Becker, H. M. (2018) A surface proton antenna in carbonic anhydrase II supports lactate transport in cancer cells. *eLife* **7**, e35176

181. Hurley, W. L., Finkelstein, E., and Holst, B. D. (1985) Identification of surface proteins on bovine leukocytes by a biotin-avidin protein blotting technique. *J. Immunol. Methods* **85**, 195–202

182. Wang, X., Levi, A. J., and Halestrap, A. P. (1994) Kinetics of the sarcolemmal lactate carrier in single heart cells using BCECF to measure pHi. *Am. J. Physiol.* **267**, H1759-H1769

183. Schmidt, N., Kollewe, A., Constantin, C. E., Henrich, S., Ritzau-Jost, A., Bildl, W., Saalbach, A., Hallermann, S., Kulik, A., Fakler, B., and Schulte, U. (2017) Neuroplastin and basigin are essential auxiliary subunits of plasma membrane Ca^{2+}-ATPases and key regulators of Ca^{2+} clearance. *Neuron* **96**, 827–838.e9

184. Gong, D., Chi, X., Ren, K., Huang, G., Zhou, G., Yan, N., Lei, J., and Zhou, Q. (2018) Structure of the human plasma membrane Ca^{2+}-ATPase 1 in complex with its obligatory subunit neuroplastin. *Nat. Commun.* **9**, 3623

185. Marchiq, I., Le Floch, R., Roux, D., Simon, M.-P., and Pouyssegur, J. (2015) Genetic disruption of lactate/H^+ symporters (MCTs) and their subunit CD147/BASIGIN sensitizes glycolytic tumor cells to phenformin. *Cancer Res.* **75**, 171–180

186. Rothert, M., Rönfeldt, D., and Beitz, E. (2017) Electrostatic attraction of weak monoacid anions increases probability for protonation and passage through aquaporins. *J. Biol. Chem.* **292**, 9358–9364

187. Martínez, C., Kalise, D., and Barros, L. F. (2010) General requirement for harvesting antennae at Ca^{2+} and H^+ channels and transporters. *Front. Neuroenergetics* **2**

188. Jacks, K. R. (2018) Klonierung und Expression der humanen Monocarboxylat-Transporter 2 und 4. *Master's thesis, unpublished.* Christian-Albrechts-Universität zu Kiel.

189. Ovens, M. J., Manoharan, C., Wilson, M. C., Murray, C. M., and Halestrap, A. P. (2010) The inhibition of monocarboxylate transporter 2 (MCT2) by AR-C155858 is modulated by the associated ancillary protein. *Biochem. J.* **431**, 217–225

190. Requejo, R., Hurd, T. R., Costa, N. J., and Murphy, M. P. (2010) Cysteine residues exposed on protein surfaces are the dominant intramitochondrial thiol and may protect against oxidative damage. *FEBS J.* **277**, 1465–1480

191. Futagi, Y., Kobayashi, M., Narumi, K., Furugen, A., and Iseki, K. (2019) Homology modeling and site-directed mutagenesis identify amino acid residues underlying the substrate selection mechanism of human monocarboxylate transporters 1 (hMCT1) and 4 (hMCT4). *Cell. Mol. Life Sci.* **76**, 4905–4921

192. Li, M., and Lester, H. A. (2002) Early fluorescence signals detect transitions at mammalian serotonin transporters. *Biophys. J.* **83**, 206–218

193. Mannuzzu, L. M., Moronne, M. M., and Isacoff, E. Y. (1996) Direct physical measure of conformational rearrangement underlying potassium channel gating. *Science* **271**, 213–216

194. Mchaourab, H. S., Lietzow, M. A., Hideg, K., and Hubbell, W. L. (1996) Motion of spin-labeled side chains in T4 lysozyme. Correlation with protein structure and dynamics. *Biochemistry* **35**, 7692–7704

195. Shi, Y. (2014) A glimpse of structural biology through X-ray crystallography. *Cell* **159**, 995–1014

196. Sugiki, T., Kobayashi, N., and Fujiwara, T. (2017) Modern technologies of solution nuclear magnetic resonance spectroscopy for three-dimensional structure determination of proteins open avenues for life scientists. *Comput. Struct. Biotechnol. J.* **15**, 328–339

197. Cheng, Y. (2015) Single-particle cryo-EM at crystallographic resolution. *Cell* **161**, 450–457

198. Junge, F., Schneider, B., Reckel, S., Schwarz, D., Dötsch, V., and Bernhard, F. (2008) Large-scale production of functional membrane proteins. *Cell. Mol. Life Sci.* **65**, 1729–1755

199. Rosano, G. L., and Ceccarelli, E. A. (2014) Recombinant protein expression in *Escherichia coli*: advances and challenges. *Front. Microbiol.* **5**, 172

200. Bill, R. M., and Haar, T. von der (2015) Hijacked then lost in translation: the plight of the recombinant host cell in membrane protein structural biology projects. *Curr. Opin. Struct. Biol.* **32**, 147–155

201. Byrne, B. (2015) *Pichia pastoris* as an expression host for membrane protein structural biology. *Curr. Opin. Struct. Biol.* **32**, 9–17

202. Cereghino, G. P. L., Cereghino, J. L., Ilgen, C., and Cregg, J. M. (2002) Production of recombinant proteins in fermenter cultures of the yeast *Pichia pastoris*. *Curr. Opin. Biotechnol.* **13**, 329–332

203. Klammt, C., Löhr, F., Schäfer, B., Haase, W., Dötsch, V., Rüterjans, H., Glaubitz, C., and Bernhard, F. (2004) High level cell-free expression and specific labeling of integral membrane proteins. *Eur. J. Biochem.* **271**, 568–580

204. Denisov, I. G., and Sligar, S. G. (2017) Nanodiscs in membrane biochemistry and biophysics. *Chem. Rev.* **117**, 4669–4713

Supplementary Data

In the following, sequences of the open reading frames (ORF) for used plasmid vectors are shown. Complete vector maps can be found in section 2.1.2. Detailed information on the cloning procedures for MCT constructs are summarized in section 3.1.1.

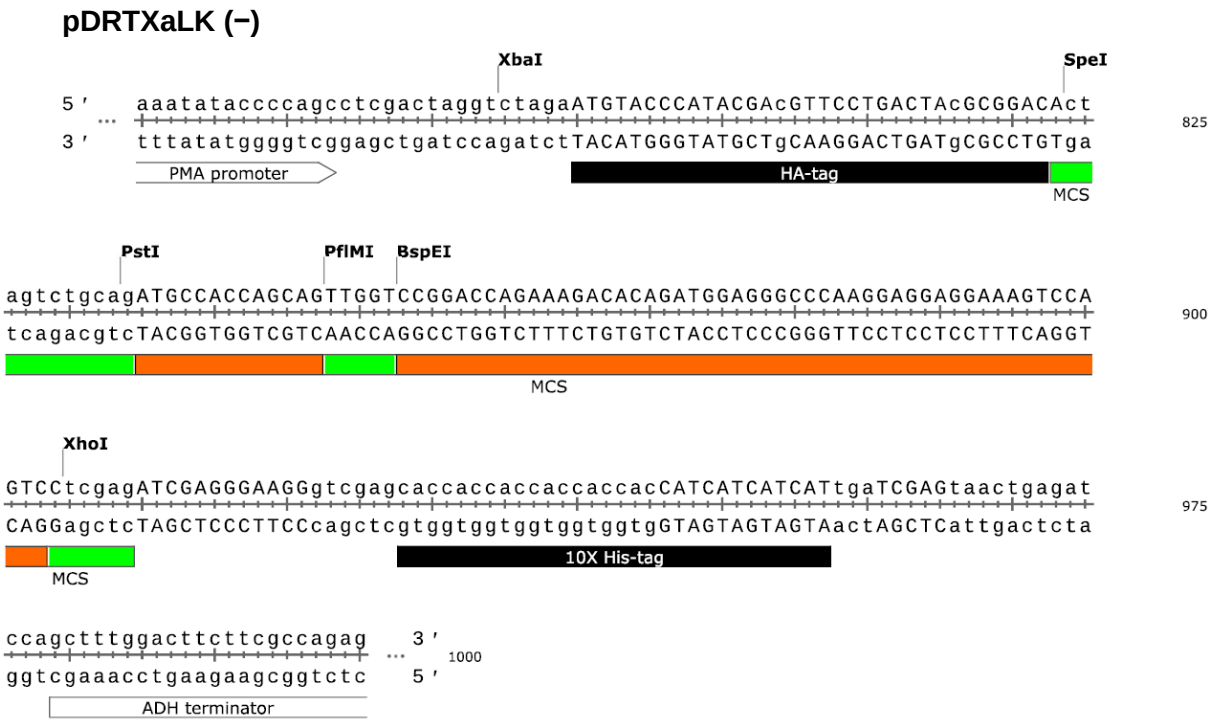

Supplementary Figure 1. Excerpt of the pDRTXaLK plasmid vector showing the open reading frame including the flanking fragments of the PMA promotor and the ADH terminator sequences. To yield pDRTXaLK, a linker sequence (green and orange) was introduced into the pDRTXa vector via a pair of oligonucleotides and includes N-terminal and C-terminal ends of MCT1 (orange). Commercial MCT1 was inserted using PflMI and BspEI restriction sites. Further relevant restriction sites are marked, and sequences for additional protein tags are highlighted. HA, hemagglutinin; MCS, multiple cloning site.

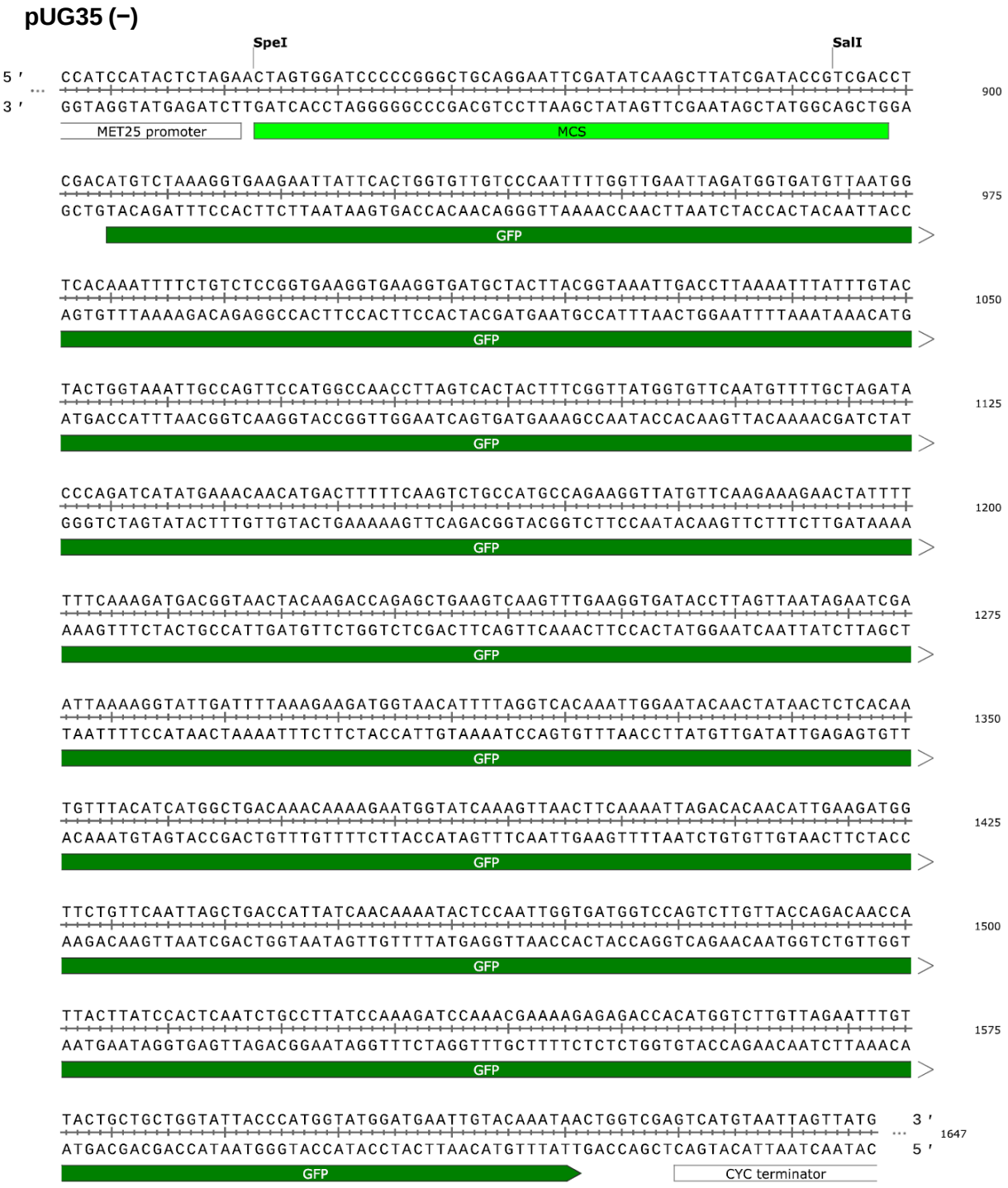

Supplementary Figure 2. Excerpt of the pUG35 (−) plasmid vector showing the open reading frame (ORF) including the flanking fragments of the MET25 promotor and the CYC terminator sequences. MCT1 was inserted using SpeI and SalI restriction sites. The ORF encodes for C-terminal GFP.

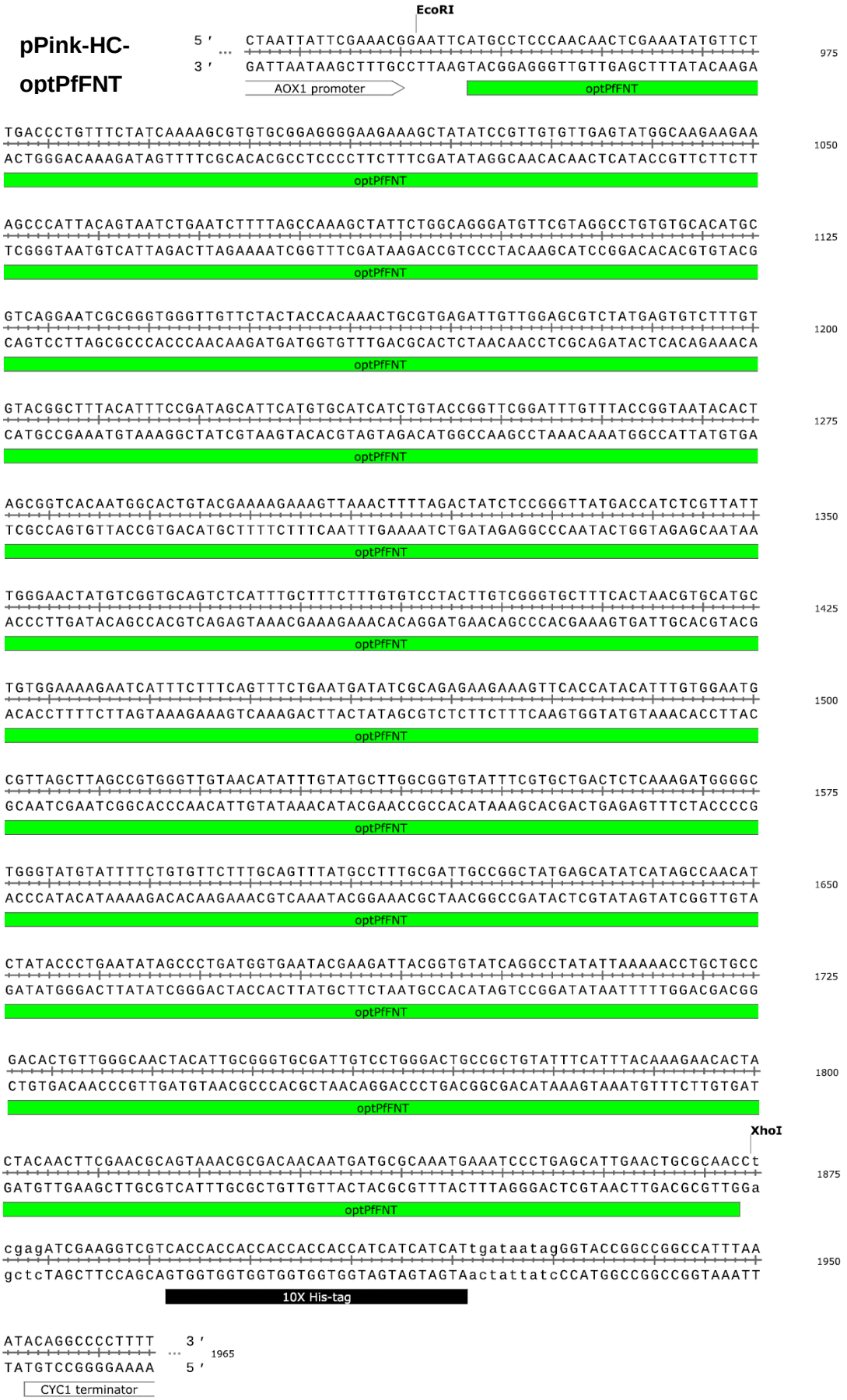

Supplementary Figure 3. Excerpt of the pPink-HC-optPfFNT plasmid vector showing the ORF including the flanking sequences of the AOX1 promotor and the CYC1 terminator and protein tags.

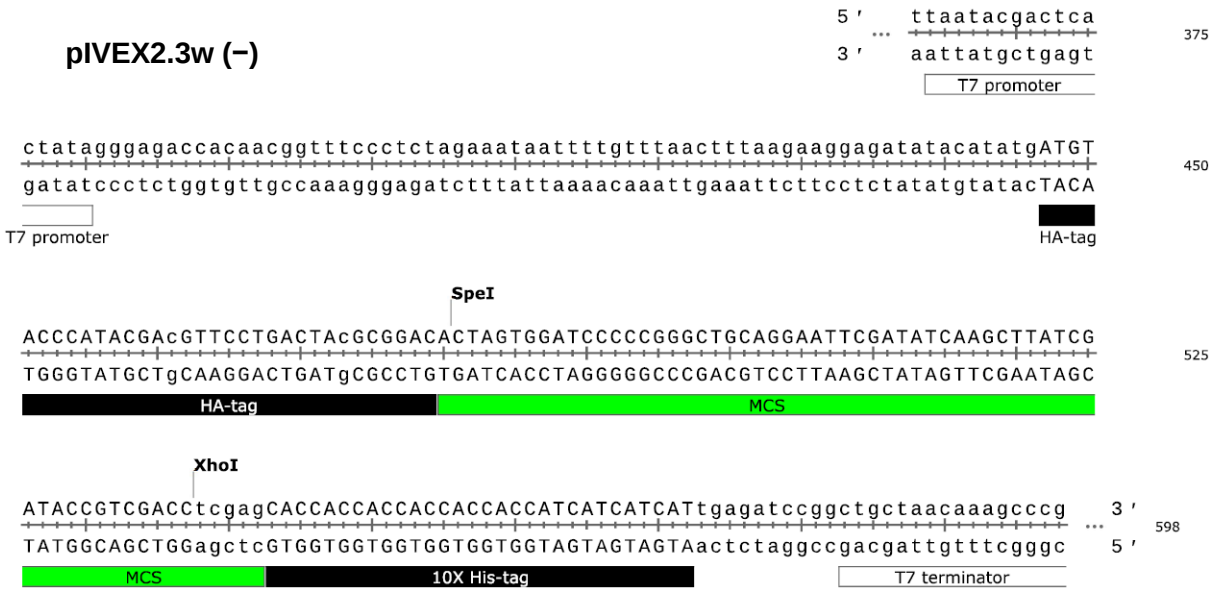

Supplementary Figure 4. Excerpt of the pIVEX2.3w (−) plasmid vector showing the open reading frame (ORF) including the flanking fragments of the T7 promotor / terminator sequences and sequences for protein tags. MCT1 constructs were inserted using SpeI and XhoI restriction sites. HA, hemagglutinin.

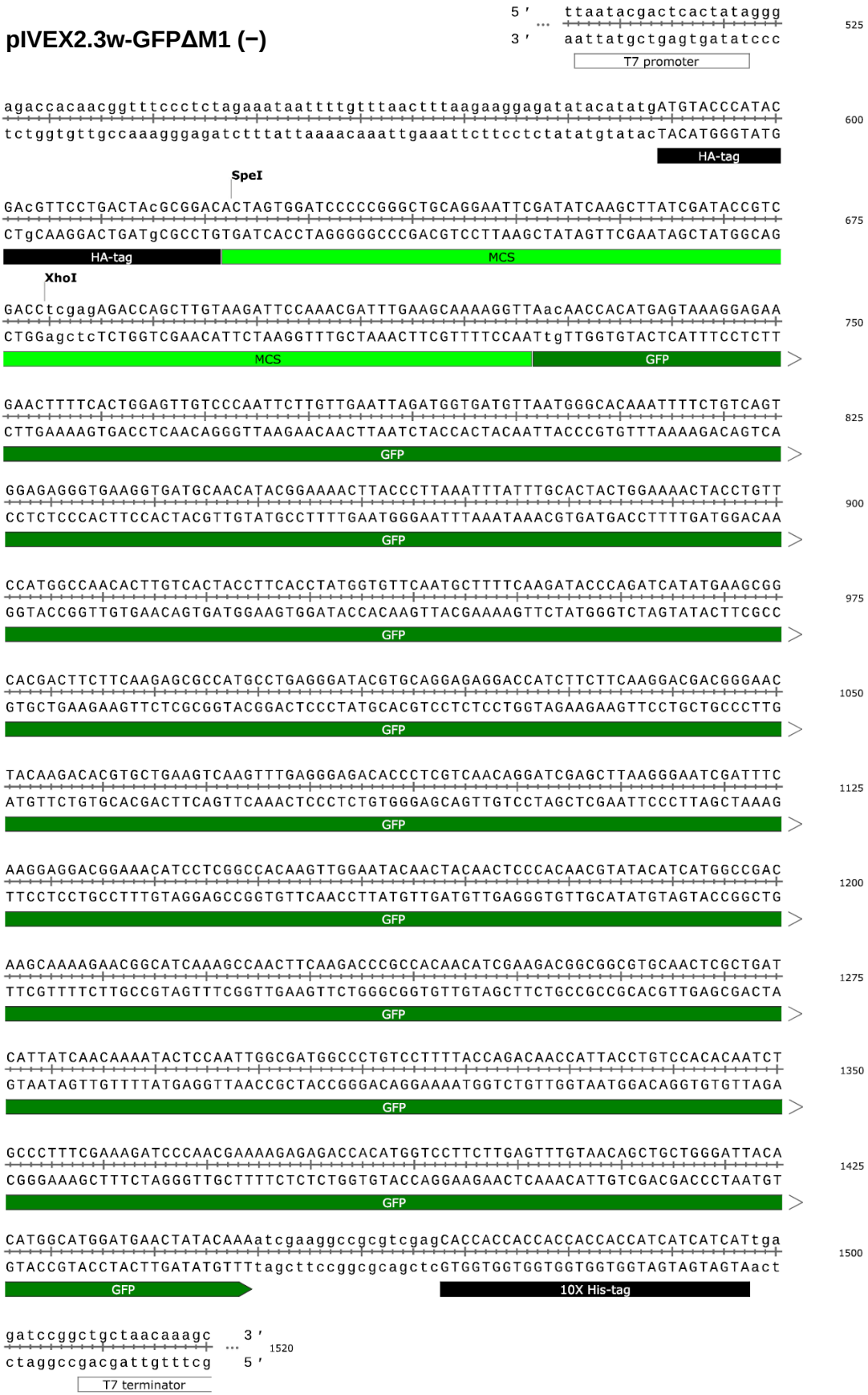

Supplementary Figure 5. Excerpt of the pIVEX2.3w-GFPΔM1 (−) plasmid vector showing the open reading frame including the flanking sequences of the T7 promotor and terminator, C-terminal GFP and protein tags. MCT1 constructs were inserted using SpeI and XhoI restriction sites. HA, hemagglutinin.

Eidesstattliche Erklärung

Hiermit erkläre ich eidesstattlich, dass ich die vorliegende Arbeit, abgesehen von der Beratung durch den Betreuer, nach Inhalt und Form selbst und selbstständig angefertigt habe und keine weiteren Quellen und Hilfsmittel als die angegebenen verwendet habe. Diese Arbeit hat weder ganz noch in Teilen im Rahmen eines Prüfungsverfahrens vorgelegen, und wurde an anderer Stelle weder veröffentlicht noch zur Veröffentlichung eingereicht. Ich habe / werde die Zulassung zur Promotion nicht mit demselben Thema zeitgleich an einer anderen Fakultät im In- oder Ausland beantragt / beantragen. Ich habe noch an keiner anderen Hochschule oder an keiner anderen Fakultät dieser Hochschule ein Promotionsvorhaben endgültig nicht bestanden, und mir wurde noch kein akademischer Grad entzogen.
Die Arbeit ist gemäß den Regeln zur guten wissenschaftlichen Praxis der Deutschen Forschungsgemeinschaft angefertigt worden.

Teile dieser Arbeit sind in Veröffentlichungen oder in Posterbeiträgen zu finden:

Köpnick, A.-L., Jansen, A., Geistlinger, K., Epalle, N. H., Beitz, E. Basigin drives intracellular accumulation of L-lactate by harvesting protons and substrate anions.
PLOS ONE (2021) **16**, e0249110. (doi: 10.1371/journal.pone.0249110)

Köpnick, A.-L., Geistlinger, K., Beitz, E. Cysteine 159 delineates a hinge region of the alternating access monocarboxylate transporter 1 and is targeted by cysteine-modifying inhibitors.
FEBS J. (2021) *Epub ahead of print.* (doi: 10.1111/febs.16024)

Posterbeiträge:

Köpnick, A. L., Beitz, E. (2019) Expression of hMCT1 and basigin as fusion protein: Role of basigin domains in lactate transport activity.
BioMedicalTransporters Conference, 2019, Luzern, Schweiz.

Kiel, 28.05.2021

Unterschrift 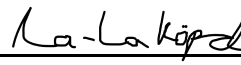

Danksagung

An dieser Stelle möchte ich allen Personen danken, die mich auf meinem Weg unterstützend begleitet haben und ohne die das Verfassen dieser Arbeit nicht möglich gewesen wäre.

In erster Linie möchte ich dabei meinem Betreuer Prof. Dr. Eric Beitz dafür danken, dass er mich in seinen Arbeitskreis aufgenommen hat, mir das Thema vorgestellt und die dynamische, freie Gestaltung und Entwicklung der Arbeit ermöglicht hat. Des Weiteren bedanke ich mich für die zahlreichen anregenden fachlichen Diskussionen und die sehr lehrreiche Zusammenarbeit beim Verfassen von Publikationen.

Prof. Dr. Axel Scheidig danke ich für die Unterstützung und das offene Ohr, die mich bei vielen wichtigen Etappen des Studiums und der Promotion seit meiner Zeit in Kiel begleitet und unterstützt haben.

Für die Kooperation auf wissenschaftlicher Ebene möchte ich mich bei Christine Desel, Steffen Riethmüller, Philipp Arnold und Arne Möller bedanken. Für die kooperative Zusammenarbeit und Unterstützung innerhalb des Arbeitskreises bedanke ich mich außerdem bei Katharina Geistlinger, Annika Jansen, Nathan Hugo Epalle und Christian Hansen. Bei Ulrich Girreser bedanke ich mich für die sehr kompetente fachliche Unterstützung bei statistischen Fragestellungen und die spaßige Zeit bei der Betreuung der Studierenden. Ein großer Dank galt Anna Fuchs und Björn Henke für die immerwährende Zusammenarbeit, auf die ich während der gesamten Zeit zählen konnte und die mich tatkräftig unterstützt hat.

Für die umfassende Unterstützung im Endspurt der Dissertation, das Korrekturlesen der Arbeit, die Beratung und die Diskussionen bedanke ich mich von ganzem Herzen bei Christian Hansen, Anna Meier, Lea Petersen, Johannes Köpnick und Bastian Höger.

Für die ebenso große Unterstützung und Ablenkung abseits der Arbeit, die spaßigen Unternehmungen, Kochabende und Tage am Strand, und den unentbehrlichen emotionalen Beistand danke ich Johannes, Nicolas, Basti, Christian, Lea und Andreas. Für die wunderbaren Unternehmungen und die tolle Arbeitsatmosphäre im Institut bedanke ich mich beim gesamten Arbeitskreis, bei allen Mitgliedern der verrückten Sozialraum-Klicke und vor allem Karl-Willi Bock und Susanne Voss.

Zuletzt und im Herzen doch zuerst: Mein allergrößter Dank galt meiner Familie. Für die bedingungslose Unterstützung, die Diskussionen, den immerwährenden Rückhalt, die gemeinsamen Urlaube, und die ununterbrochen erfahrene und empfundene Liebe möchte ich mich von ganzem Herzen bei meiner Mutter Angela, meinem Vater Holger und meinem Bruder Johannes bedanken und glücklich schätzen. Ohne euch hätte ich es nicht geschafft.